Computational modelling of surface interactions – wear, material separation and deposition

von der Fakultät Maschinenbau
der Technischen Universität Dortmund
zur Erlangung des akademischen Grades

Doktor-Ingenieur (Dr.-Ing.)

genehmigte Dissertation

von

Markus Manuel Schewe

aus Heidenheim an der Brenz

Vorsitz:	PD Dr.-Ing. T. Kaiser
Referent:	Prof. Dr.-Ing. A. Menzel
Korreferenten:	Prof. Dr. J. M. Carbonell Puigbó
	Prof. Dr.-Ing. A. Erman Tekkaya
Tag der Einreichung:	04.03.2025
Tag der mündlichen Prüfung:	24.06.2025

Bibliografische Information Der Deutschen Bibliothek
Die Deutsche Bibliothek verzeichnet diese Publikation in der Deutschen Nationalbibliografie; detaillierte bibliografische Daten sind im Internet über **http://dnb.d-nb.de/** abrufbar.

Bibliographic information published by Die Deutsche Bibliothek
Die Deutsche Bibliothek lists this publication in the Deutsche Nationalbibliografie; detailed bibliographic data is available in the Internet at **http://dnb.d-nb.de/**.

Schriftenreihe des Instituts für Mechanik

Herausgeber: Institut für Mechanik
Fakultät Maschinenbau
Technische Universität Dortmund
Leonhard-Euler-Str. 5
D-44227 Dortmund

Druck: Koffler DruckManagement GmbH

Als Manuskript gedruckt. Printed in Germany.

ISSN 2191-0022
ISBN 978-3-947323-55-5

"Still round the corner there may wait
A new road or a secret gate,
And though we pass them by today,
Tomorrow we may come this way
And take the hidden paths that run
Towards the Moon or to the Sun."

J.R.R. Tolkien, Bilbo's walking song (1954)

Acknowledgements

I wrote and developed my doctoral thesis during my time as a scientific assistant at the Institute of Mechanics, from 2017 to 2025. I chose a quote from Bilbo Baggins to open my work because it pictures this period perfectly: a journey of learning and discovery, following paths that were unknown to me. Just as Bilbo did not walk these paths alone – he had thirteen dwarves and a wizard by his side – I too had the support of many people. I would now like to take this opportunity to thank my companions.

Firstly, I would like to thank my supervisor, Andreas Menzel, for our collaboration, for everything I learnt from you and for the opportunities to work on various projects with a lot of freedom. I would also like to thank the members of the thesis committee for their valuable contributions. Josep Maria Carbonell Puigbó, thank you for examining my thesis and for travelling to Dortmund for my defence – it was a fruitful and very pleasant experience! To A. Erman Tekkaya, thank you for your time, and for the valuable practical perspective your questions provided during my examination. Tobias Kaiser, thank you for your professional and personal guidance throughout the examination process.

The IoM is a warm and supportive team, with the permanent members forming its backbone. Jörn Mosler, thank you for encouraging the two teams to work as one. Thank you, Kerstin Walter and Tina McDonagh, for keeping the team together through social events, and for your invaluable work organising financing, contracts and proofreading (I will try not to keep making the same mistakes!). Matthias Weiß, thank you for providing safe and reliable IT infrastructure. I also enjoyed our chats, from Linux to music. Thank you to Thorsten Bartel, Patrick Kurzeja, Tobias Kaiser and Lars Rose for sharing your experience, and for your commitment and courage in revising processes and courses. Special thanks go to Thorsten for your help and guidance in finishing and publishing my work, and to Lars, my office mate, for all those enjoyable discussions.

I would like to thank the entire team. Starting out as a student assistant, I learned a lot from Rolf Berhelsen, who supervised and guided me during my first years, and from Ralf Denzer, who always encouraged me when we met. I also enjoyed working on FEM courses with Dinesh Dusthakar and César Polindara. I well remember the team back then: Raphael Holtermann, Alexander Bartels, Karsten Buckmann, Tim Heitbreder, Krishnendu Haldar, Christian Sievers, Björn Kiefer, Sandra Klinge, Till Clausmeyer, Tobias Waffenschmidt, Guillermo Díaz, Maniprakash Subramanian and Richard Ostwald. It was a great time and I am grateful to all of you. Over time, many of my fellow students became my colleagues: Robin Schulte, Lars Rose, Volker Fohrmeister, Leon Sprave and Tobias Kaiser, I am thankful for sharing the way with you and for the learning and working together. And there are more members of the IoM family: Isabelle Noll, Tim

Furlan, Dilek Güzel, Merlin Böddecker, Justice Olatunbosun, Kai Langenfeld, Henning Lammen, Hendrik Wilbuer, Alexander Niehüser, Klas Feike, Marius Harnisch, Gian-Luca Geuken, Felix Rörentrop, Samuel Brabender, Lennart Sobisch, Sebastian Bencker, Carina Witt, Serhat Aygün, Tillmann Wiegold, Fabian Guhr, Philipp Scherm, Marzena Mucha, Knut Andreas Meyer and Annika Möglich. Thank you all for being such a dedicated team, for the memorable conferences and trips, and for supporting and inspiring one another.

I would also like to thank my cooperation partners on various projects for good work, valuable lessons and friendly collaboration: Alexander Meijer, Dirk Biermann, Florian Gutknecht, Till Clausmeyer, Dominik Stagnier and Philipp Müller – Philipp Retzl, Ernst Kozeschnik, Nils Schmidt, Monika Kipp, Jan Peters, Robin Roj, Christoph Böttinger, Christian Pelshenke, Josefina Ottitsch, Stefan Kaschnitz-Biegl, Harald Peherstorfer, Fritz Bleicher, Adam Kazuch and Benjamin Losert – Hamed Dardaei Joghan, Farin Weinert, Marlon Hahn, A. Erman Tekkaya and Yannis P. Korkolis.

I would like to conclude this acknowledgement by saying thank you to my family and friends for your support, love and joy. Let's see what awaits us around the corner!

Dortmund, August 2025 Markus Schewe

Zusammenfassung

In dieser Arbeit werden numerische Modellierungsansätze zur Simulation von Formänderungen durch Oberflächenwechselwirkungen entwickelt und damit ein Beitrag zur Verbesserung der Modellierung industrieller Prozesse hinsichtlich Verschleiß, Materialtrennung und additiver Fertigung geleistet.

Für die *Verschleißmodellierung* wird ein Coulomb-Reibmodell mit einer Begrenzung der maximalen Scherspannung in Verbindung mit einem modernen Archard Verschleißmodell basierend auf dissipierter Reibarbeit verwendet. Formänderungen durch Verschleiß werden in einem PYTHON-basierten Postprozessor umgesetzt, der Reibkräfte und Geschwindigkeitsdaten aus Finite Elemente Simulationen in ABAQUS verarbeitet. Simulierte und experimentelle Verschleißmuster zeigen, dass dissipationsbasierte Archard-Formulierungen realistischer sind als druckbasierte Ansätze im Fall von nicht konstanten Reibkoeffizienten. Mikrostrukturierte Werkzeugoberflächen können mit Hilfe des Modells optimiert werden, um maßgeschneiderte Mikrostrukturen zu entwerfen und deren Einlaufverhalten und Verschleißfestigkeit vorherzusagen.

Für die *Materialtrennung* wird die Partikel-Finite-Elemente-Methode (PFEM) in einem MATLAB-basierten Forschungscode adaptiert, um das adhäsionsfreie Abscheren einzelner Oberflächenerhebungen auf mikroskopischer Ebene zu simulieren. Dabei wird die Verformung der Erhebung aus Stahl mit großen volumenerhaltenden plastischen Verformungen modelliert. Eine Untersuchung zeigt, dass etablierte gemischte Elemente gut für hyperelastische, quasi-inkompressible Materialien geeignet sind, während die vorgeschlagenen quadratischen Elemente glattere Spannungsfelder unter elastoplastischen Bedingungen in PFEM liefern. Ein verbessertes lokales Übertragungsschema für Zustandsvariablen erhöht zusätzlich die numerische Robustheit. Die adaptive Vernetzung auf Basis der äquivalenten plastischen Dehnung wird durch Einfügen und Entfernen von Punkten realisiert und durch eine α-Formerkennung mit Schädigungskriterium zur Rissmodellierung in stark plastisch verformten Regionen ergänzt. Als neuer Beitrag zur PFEM-Literatur wird außerdem die Selbstkontakt-Vernetzung eingeführt.

Für den *Materialauftrag* wird ein thermomechanisches PFEM-Modell zur Simulation von Hochgeschwindigkeits-Schmelzeströmen auf kalte Substrate entwickelt. Ein neues Vernetzungskriterium für die Verbindungszone basiert auf der Verbindungsfront im Auftragsprozess. Darüber hinaus ermöglicht das entwickelte konstitutive Modell für Schmelzefluss und Erstarrung bei großen Deformationen die Analyse von Eigenspannungen während der Abkühlung und liefert wertvolle Erkenntnisse zur Prozessoptimierung beim Laser-Pulver-Auftragschweißen.

Die entwickelten Modellierungsansätze verbessern die Simulationsmöglichkeiten für Verschleißmechanismen, Materialtrennungsprozesse und additive Fertigungstechnologien.

Abstract

This thesis develops numerical modelling approaches to simulate shape changes induced by surface interactions, addressing critical challenges in wear modelling, material separation and additive manufacturing processes.

For *wear modelling*, a Coulomb friction model with a shear-stress limit is employed alongside a modern Archard law based on dissipated frictional work. Shape updates are performed by developing a PYTHON-based postprocessor that processes traction and velocity data from ABAQUS Finite Element simulations. The comparison between simulated and experimental wear patterns supports the literature's proposition that dissipation-based formulations are more realistic than the classic pressure-based relation when the friction coefficient varies. Microstructured tool surfaces are investigated, demonstrating how the modelling framework can help to design tailored microstructures for optimised effective friction properties and asses their run-in behaviour and wear resistance.

In *material separation*, the Particle Finite Element Method (PFEM) is adapted in a MATLAB-based research code to simulate adhesion-free asperity shearing at the microscopic level, targeting steel deformation under large volume-preserving plastic flow. A study of element types reveals that while established mixed formulation elements perform well for hyperelastic quasi-incompressible materials, the proposed quadratic elements provide smoother stress fields in elastoplastic conditions in PFEM. Additionally, an improved local state-variable transfer scheme enhances numerical robustness compared to traditional methods. Adaptive meshing based on equivalent plastic strain is implemented with point insertion and removal schemes, while α-shape detection is enriched with a fracture criterion for crack modelling in highly plastically deformed regions. Notably, self-contact meshing is introduced as a novel contribution to PFEM literature.

For *material deposition*, thermo-mechanical PFEM simulates high-velocity hot fluid melt streams deposited onto cold substrates. A mesh generation criterion is proposed for the bonding zone based on material progression fronts, alongside a large-strain constitutive model for melt flow and solidification using a deformation based framework. This approach enables analysis of residual stresses during cooling, providing valuable insights into process optimisation for Directed Energy Deposition with a Laser Beam technology.

The developed frameworks advance simulation capabilities in wear mechanisms, material separation processes, and additive manufacturing technologies.

Publications

Key parts of this thesis are based on peer-reviewed journal articles, which were published during the progress of this thesis.

1. M. Schewe, H. Wilbuer, and A. Menzel. Simulation of wear and effective friction properties of microstructured surfaces. *Wear*, 464-465:203491, 2021, [118].

2. M. Schewe, T. Bartel, and A. Menzel. Comparison of elements and state-variable transfer methods for quasi-incompressible material behaviour in the particle finite element method. *Computational Mechanics*, 75:755–773, 2025, [119].

3. M. Schewe, I. Noll, T. Bartel, and A. Menzel. Towards the simulation of metal deposition with the Particle Finite Element Method and a phase transformation model. *Computer Methods in Applied Mechanics and Engineering*, 437:117730, 2025, [120].

For journal article 1, the author of this thesis finalised existing numerical implementations with regard to the contact mechanics methods, carried out all the simulations, made analyses and comparisons with experimental results, deducted conclusions and prepared the article. Moreover, for journal articles 2-3, the author of this thesis contributed essential aspects with regard to the outline of the theory, carried out all of the numerical implementations, simulations and analyses, and prepared the articles. Special symbols mark the text parts in this thesis which have been pre-published in one of the aforementioned journal articles. The opening marker ${}^{\text{qtd.}}_{[118]}\{$until the closing marker $\}^{\text{qtd.}}_{[118]}$ enclose text pre-published in journal article 1. The parenthesis extends at most to the end of the respective numbered section and is repeated in the next section if necessary. The quoted pre-published text is identical word for word except for minor textual adaptations or footnotes. Accordingly, ${}^{\text{qtd.}}_{[119]}\{$to $\}^{\text{qtd.}}_{[119]}$ and ${}^{\text{qtd.}}_{[120]}\{$to $\}^{\text{qtd.}}_{[120]}$ mark text quoted from the pre-published journal articles 2 and 3.

In addition, the following publications have been produced alongside the preparation of the thesis, which are not directly covered in this thesis.

4. M. Schewe and A. Menzel. The Particle Finite Element Method for the modelling and simulation of solid body interactions. *Proceedings in Applied Mathematics and Mechanics*, 18(1):e201800110, 2018, [115].

5. M. Schewe and A. Menzel. Aspects of the Particle Finite Element Method applied to contact problems. *Proceedings in Applied Mathematics and Mechanics*, 19(1):e201900403, 2019, [116].

6. B.-A. Behrens, D. Biermann, A. Menzel, W. Tillmann, R. Krimm, A. Meijer, M. Schewe, D. Stangier, O. Commichau, P. Müller, S. Hübner, and D. Rosenbusch. Untersuchungen strukturierter Werkzeugflächen und der Einfluss auf den Werkzeugverschleiß. In M. Merklein, B.-A. Behrens, and A. E. Tekkaya, editors, *4. Workshop Blechmassivumformung*, pages 7–30, Hannover, 2020. FAU University Press, [13].

7. M. Schewe and A. Menzel. Mechanism-Based Modelling of Wear in Sheet-Bulk Metal Forming. In M. Merklein, A. E. Tekkaya, and B.-A. Behrens, editors, *Sheet Bulk Metal Forming – Research Results of the TCRC73*, pages 434–457. Springer International Publishing, Cham, 2021, [117].

8. T. Furlan, M. Schewe, P. Scherm, P. Retzl, E. Kozeschnik, and A. Menzel. Modelling and finite element simulation of martensite and bainite phase transformations during quenching under consideration of carbon repartitioning. Mechanics of Materials, 204:105275, 2025. [55]

Contents of the conference proceedings 4-5 have contributed to this thesis as basis for the understanding of contact mechanics in PFEM, but are not directly covered here. The conference proceeding 6 contains work that is methodically also covered in [118]. As final report of the Transregional Collaborative Research Center 73, the publication 7 covers aspects which are also contained in [115, 116, 118]. The journal article 8 is not contained in this thesis, but helped the author of this thesis to establish knowledge on phase transformation models.

Furthermore, the following student theses have contributed to this thesis

1. H. Wilbuer, *An inelastic finite element framework for the simulation of wear*, B.Sc. thesis, 2016.

2. M. Schewe, *Implementation of the Particle Finite Element Method*, M.Sc. thesis, 2017.

3. P. Linneweber*, *Finite-Elemente-Implementierung eines Kontaktmodells mit Dreieck-Segmenten*, B.Sc. thesis, 2018.

4. N. Zöllner*, *Viskose Materialmodelle in der Finite-Elemente-Simulation von Schmierstoffen*, B.Sc. thesis, 2019.

5. P. Araghchi*, *Regelmäßige Neuvernetzung als Strategie für Finite-Element-Simulationen bei großen Verformungen in der Festkörpermechanik.*, B.Sc. thesis, 2020.

6. A. Niehüser*, *Finite Element Simulation of Large Strain Frictional Contact with the Contact Domain Method*, M.Sc. thesis, 2020.

7. P. Scherm*, *Material Modelling and Finite Element Simulation of Quenching*, M.Sc. thesis, 2023.

8. R. Liskow, *Towards a finite strain modelling framework for additive manufacturing processes*, M.Sc. thesis, 2023.

9. J. Olatunbosun*, *Particle Finite Element Method based modelling of Laser Cladding Additive Manufacturing*, M.Sc. thesis, 2024.

Student thesis 1 together with the publication [16] laid the groundwork for the journal article [118]. Thesis 2 has been conducted by the author of the present thesis and covers a simplified version of PFEM. Student thesis 3 and 4 contributed to the publications [13, 115, 117] containing basic analyses which are not part of the present thesis. Student thesis 5 developed a remeshing scheme based on Abaqus and Gmsh with patch-recovery for state-variable mapping, which is not covered in the present thesis. Thesis 6 provided the implementation of the contact domain method which is used in the present thesis. The student thesis 7 laid the basis for [55], which is not covered in the present thesis. Student thesis 8 provided a first version of the material model and student thesis 9 provided ideas on mesh generation methods which are both extended in journal article [120]. The author of the present thesis thereby co-supervised 3, 4, 5, 6, 7 and 9 as indicated by *.

Contents

1 Introduction

The objective of this work is the development of computational models for the simulation of large deformation solid body interactions which lead to changes in the shape and topology of the bodies. Such phenomena appear for example in

- forming technologies such as extrusion or deep drawing, where a tool induces large shape changes of the workpiece by surface interactions
- subtractive manufacturing processes such as grinding or machining, where grains or cutting edges impose a large deformation and material separation by contact forces
- tool wear in one of the aforementioned manufacturing processes, where the frictional surface interaction leads to gradual removal of surface material
- microscopic wear mechanisms including adhesion and plastic deformation and breakage of surface asperities
- additive manufacturing processes such as metal deposition, where large deformation of the deposited material and a connection with the substrate material leads to the final shape of the printed part

In this work, model development is focussed on specific applications, namely on the wear of forming tools, on the material separation of single surface asperities on microscopic level and on material deposition in a laser Additive Manufacturing process. The simulation of wear is based on a phenomenological Archard wear model, whereas in the simulation of material separation and deposition, the Particle Finite Element Method (PFEM) is adapted in order to resolve the separation or connection of material with an adaptive remeshing method. Two main topics are central in this thesis, large deformation material flows and surface interactions.

Modelling of large deformation material flows The computational modelling of large deformation material flows is relevant to a wide range of engineering applications, including mechanical engineering, manufacturing processes, geomechanics, biomechanics, fluid-structure interactions and fluid dynamics. These problems involve complex material

behaviour, extreme deformations and topology changes, often requiring advanced numerical techniques to capture contact, separation, and reconnection of material domains. Based on the review articles Rodríguez et al. [110], which focuses on numerical methods for chip formation, and Cremonesi et al. [34], which provides a comprehensive review of the PFEM in comparison to other approaches, an overview of relevant computational methods is presented in the following. The main distinction is between *continuum methods*, which define governing equations for field variables such as displacements or velocities in a computational domain, and *discrete methods*, which describe the interaction of separate entities. The list of methods is not complete but shall give orientation on where to localise the present thesis.

1. Mesh-based continuum methods

   - Lagrangian methods: the standard Finite Element Method (FEM) describes the motion of the material as the movement of the discretisation points. The material behaviour is simulated in integration points to which the nodal field variables and gradients are approximated. The direct connection of mesh and material deformation allows for an accurate simulation of history-dependent material behaviour and a variety of advanced constitutive models is available – but it also limits the applicability of FEM to very large deformations because the mesh quality deteriorates. Adaptive remeshing techniques with a regeneration of the mesh and a mapping of fields and state-variables are available, see e.g. Wriggers [140].

   - Eulerian methods: Eulerian FEM describes the motion of the material based on fixed spatial grid points. Unlike Lagrangian FEM, history information can be difficult to track and the general flux-based approach is not optimal for deformation-oriented solid analysis. Computational Fluid Dynamics (CFD) is also primarily based on Eulerian descriptions. The Finite Volume Method (FVM) is a common approach in CFD, which is based on spatially fixed control volumes. Eulerian methods are mainly suitable for describing flow in a fixed domain, see Cremonesi et al. [34].

   - Hybrid methods: The Material Point Method (MPM) tracks the motion of Lagrangian material points, which correspond to the quadrature points in FEM but also contain the field variable information. The solution of the balance equations is performed on a fixed Eulerian background grid, so mesh distortion is no longer a problem. However, the Eulerian mesh makes it more difficult to define time-dependent boundary conditions and contact conditions and to adjust the mesh to strain localisation, see e.g. Ambati et al. [1]. Arbitrary Lagrangian-Eulerian (ALE) is based on a Lagrangian description, but allows for additional movement of the material relative to the mesh. The mesh is repositioned to maintain a good mesh quality, allowing the simulation of e.g. metal forming processes. However, the mesh motion can be difficult to define for unpredictable large material flows. A

detailed introduction can be found in Belytschko [14]. Another hybrid approach is the Coupled Eulerian Lagrangian (CEL), available for example in the commercial software Abaqus [40], see also the application to geomechanics in Qiu et al. [101]. Lagrangian bodies can be defined alongside Eulerian domains in CEL, improving the contact description and the accuracy of contact related information, while very large deformations can be described with the Eulerian part of the model. This makes the approach particularly suitable for fluid-structure interactions. Defining the appropriate size and density of the Eulerian domain can be difficult, especially in cases of strain localisation or unpredictable flow.

2. Mesh-free continuum methods

   - The Smoothed Particle Hydrodynamics (SPH) is a mesh-free method based on points/particles. Gradients are calculated based on all particles within a specific influence radius, denoted smoothing kernel. Contact with tools can be modelled by particle interactions similar to discrete methods. The neighbour search makes the method computationally very expensive, such that it is especially suited for high accuracy simulations with high flexibility for topological changes. Exemplary application in Additive Manufacturing can be found in Meier et al. [86] and a review is given in Bagheri et al. [6]. In this review, several extensions and similar approaches are discussed, for example the Reproducing Kernel Particle Method (RKPM), which has a different smoothing kernel than the SPH allowing for higher continuity in describing the physical equations. This also comes at higher cost for the correction of the kernel approximations.

   - The Local Maximum-entropy mesh-free method (Local max-ent) is also based on a mesh-free set of points, but applies a different spatial approximation than the SPH and RKPM. The property of maximum information-entropy is used to define shape functions which fulfil certain properties such as partition of unity and a specific interpolation continuity. The locality of this class of max-ent approximations is introduced by Arroyo and Ortiz [3], creating a direct link to mesh-based methods using Delaunay Triangulations. This connection allows for direct definition of boundary conditions while still being independent of a mesh. Further enhancements are presented for example in Kumar et al. [74], which improves applicability in solid mechanics for large elastoplastic deformation and dynamics.

3. Discrete methods

   - The Discrete Element Method (DEM) is the classic approach for discrete models which are based on inter-particle forces. Particle distances are used to specify contact interactions and elastic deformation. DEM is especially suited for simulating the flow of granular materials, where very large relative motion between particles can be efficiently simulated in this manner. For history dependent materials in solid

mechanics, the lack of continuum mechanical deformation measures can be limiting for the constitutive modelling. See Tavarez and Plesha [130] for an introduction.

- Hybrid approaches such as FEM-DEM combine both methods in a common model. Thereby, both techniques coexist in this approach and are coupled via forces to allow for more precise deformation modelling in the FEM part and efficient particle interactions in the DEM part, see e.g. Zheng et al. [150].

The PFEM is a continuum method which uses ideas from particle methods. Originally, in the PFEM all field and state-variable information was located in the particles, see e.g. Oñate et al. [98], Sabel et al. [114]. The particles correspond to the node points of the underlying FEM model and the triangular Delaunay mesh is regenerated in each calculation step. That makes a state-variable mapping necessary between integration points and nodes, when the mesh is regenerated. However, in recent PFEM models, state-variable data is directly copied or mapped between old and new quadrature points, see e.g. Carbonell et al. [28], Rodríguez et al. [111]. Therefore, the PFEM is essentially a Lagrangian FEM with remeshing, whereby the remeshing is performed very frequently on a mostly fixed set of points. The similarities to other Lagrangian remeshing methods can be seen in the work of Marusich and Ortiz [83], which presents a triangular mesh regeneration approach for a point set including mesh adaptability and the modelling of crack propagation. These methods are very similar to the PFEM approach. In PFEM, both mapping of state-variables and adaptivity of the mesh density are performed locally based on the previous mesh configuration. The high frequency of mesh regeneration thereby allows for the tracking of changes in the topology of the body and for a continuous optimisation of the mesh quality. PFEM combines relevant features of Lagrangian FEM such as accurate material modelling, direct imposition of boundary conditions and established contact models with the topological flexibility of a particle method. This makes the PFEM a choice candidate for the simulation of solid body interactions which induce large deformations and topology changes. $^{\text{qtd.}}_{[119]}\{$In solid mechanics, PFEM has for example been applied in geomechanics, see Carbonell et al. [28], Hauser and Schweiger [60], Monforte et al. [90], in metal cutting, see Carbonell et al. [26], Oliver et al. [96], Rodríguez et al. [111], and for simulating flowing hot molten metal, Bobach et al. [18], Franci et al. [54]. $\}^{\text{qtd.}}_{[119]}$

Modelling of surface interactions Surface interactions of solid bodies as well as the interaction of liquid steel melt with a solid steel surface are considered in this work. For the solid body interactions, dry contact without lubrication is considered. The contact interaction can be divided into normal contact and frictional contact. Normal contact is represented by the impenetrability condition between the bodies. Frictional contact is characterised by Wriggers [141] being governed by ploughing of the surface asperities and by adhesive forces. Adhesive forces partly arise from inter-molecular forces that cause clean metal surfaces to stick together. In a rough surface, such adhesive forces are

important at the microscopic asperity level, where adhesive bonds are formed and broken, contributing to the also present interlocking and the elastic and plastic deformation of the surface asperities, see also Straffelini [123]. These frictional phenomena are also the basis of wear simulation. The classic Archard wear model [2] has been developed for adhesive wear, i.e. wear by tearing out adhesively bonded material. The Archard model can also be applied to abrasive wear, which is characterised by a hard particle ploughing into a softer body and thereby removing material. However, wear of forming tools is considered to be adhesive wear. On this basis, wear modelling with the Archard model is considered for microstructured forming tools in Chapter 3. Furthermore, the shearing, plastic deformation and fracture of surface asperities is modelled with PFEM in Chapter 4.

Fluid-structure interaction can naturally be modelled with PFEM since the remeshing allows to describe fluid flow as demonstrated in e.g. Oñate et al. [98], Rizzieri et al. [109], Falla et al. [49], see also the review Cremonesi et al. [34] for further references. As soon as the fluid and the solid domains are close to each other, remeshing generates connection elements which can for example be modelled with the constitutive behaviour of the fluid domain. In this case, the surface of the solid domain is significantly stiffer such that the flow within the connection elements mainly consist of the movement of the fluid nodes. Therefore, the bonding automatically represents a no-slip boundary condition, which is the general boundary condition for fluid dynamics, see Cremonesi et al. [34]. For the no-slip boundary condition, the solid nodes on the surface which are connected to the fluid domain are sufficient. For slip boundary conditions, a set of fluid nodes can be added on the solid boundary in order to describe the slip by a constitutive model. Such models are referenced in the cited review [34]. In Chapter 5, a PFEM modelling approach for laser metal deposition is proposed. The liquid metal deposited on the solid baseplate represents a FSI problem which is solved in a monolithic strongly coupled manner with PFEM with a no-slip boundary condition.

After giving a general introduction to the topic of this thesis, the subsequent sections will go into more detail with respect to the three application cases and the respective state of the art in the modelling and simulation of these applications as well as the objectives of this work, respectively.

1.1 Modelling of wear

Frictional tool-workpiece interactions induce surface deterioration in form of adhesive wear which is a limiting factor for service life for metal forming tools. In the first part of the present thesis, tool wear is analysed on microstructured tool surfaces of metal forming tools. $\overset{\text{qtd.}}{\underset{[118]}{}}${Microstructured surfaces are one class of tailored surfaces which are investigated to improve the friction, wear and failure properties of tool surfaces, see Löffler et al. [81]. The considered process is called sheet-bulk metal forming, since bulk metal forming processes are applied to form functional parts like toothings or carriers

on sheet parts, see Merklein et al. [87]. Figure 1.1 shows such a process using a tool with structured surfaces taken from an experimental study of Sieczkarek et al. [122]. One of the therein applied surface structures is bionically motivated from a beetle. The application of this structure is performed using micro-milling machines with a ball end milling cutter with a 0.2 mm diameter. Other studied surfaces are deterministic patterns of grooves or dimples. Application of such surface structures allows to, e.g., locally increase or decrease the material flow in a metal forming process. Kersting et al. [69] show that surface structuring leads to a higher mould filling in tooth-forming processes on steel sheet by decreasing material flow in regions where no teeth have to be formed. The frictional properties and wear of such structures are simulated in this contribution.

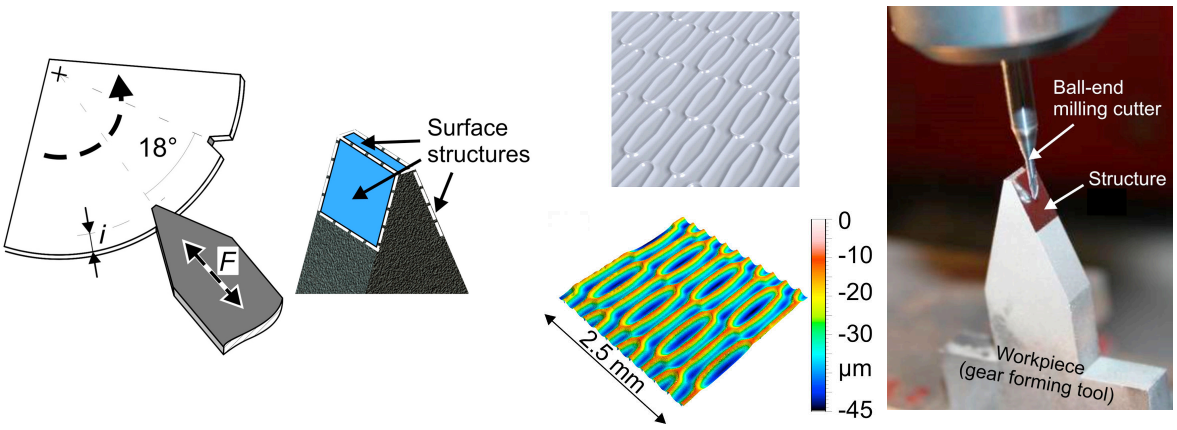

Figure 1.1: Application of microstructured surface on tooth forming tool via micro milling. Figure reprinted from [122] with permission from Elsevier.

As the length scale of one period of these microstructures is $\approx 300\,\mu m$, it is not feasible to resolve both the deformation process and the surface microstructure in one simulation. Therefore, a cut-out of surface material is considered with periodic boundary conditions on the mesoscale, where the microstructure is resolved, but where lower scale asperities are represented by a friction model. Homogenisation of frictional contact has been presented in Stupkiewicz [125] for scanned three-dimensional rough surfaces and in De Lorenzis and Wriggers [41] for fractal rough surfaces including the choice of appropriate cut-out dimensions and periodic boundary conditions for the two-dimensional case. In this work, the periodicity is exactly enforced only for the strongly deforming workpiece. For the rather stiff tool, periodicity is not strictly enforced due to the complex geometry and the contact discretisation, which cannot take periodicity into account. Temizer and Wriggers [131] used friction homogenisation with a multiscale approach to pass local loads and conditions to the micro-simulation and to obtain effective friction properties for the macro simulation. A similar scheme is presented in Stupkiewicz et al. [128] for three-dimensional anisotropic rough surfaces with a micro-to-macro-transition to provide load dependent effective coefficients for an orthotropic friction model. For the characterisation of frictional properties and wear of microstructured surfaces, this work

restricts to the mesoscale modelling without a micro-macro transition. Instead, frictional homogenisation is combined with the modelling of wear.

For the modelling of wear in metal forming applications, Volk et al. [133] review three main approaches: Physically based models include effects on the micro-scale interaction of the contacting bodies. However, these models are mainly beneficial for the understanding of the wear phenomenons, whereas the applicability for real-scale problems is limited. On the other hand, there are purely empirical models which can model complex interconnections, if sufficient data is available. This field becomes more attractive with new machine learning algorithms and increased databases. However, Volk et al. [133] currently name phenomenological models to be the most applied models to predict tool wear. These models compromise between physical motivation and empirical adjustment. The classic Archard wear relation [2] is widely used, see e.g. Öqvist [154], Hambli [57] and Hegadekatte et al. [61],Hegadekatte et al. [62] for early finite element based applications, Hoffmann et al. [63], Falconnet et al. [48], Behrens et al. [11] and Cha et al. [31] for early up to recent applications in metal forming simulation. Fouvry et al. [53] and Ramalho and Miranda [104] discussed an alternative format of the Archard relation which is based on the dissipated frictional energy. For constant Coulomb friction coefficients both models coincide. This, however, is often not the case, e.g. in the high pressure regime of forming processes. The dissipation based approach has been applied by Ersoy-Nürnberg et al. [47] and Behrens et al. [12] in metal forming and by Farah et al. [50] using modern mortar based contact algorithms with a more academic focus. Lengiewicz and Stupkiewicz [77] present the dissipation based Archard model in a continuum mechanically sound fashion which is adapted in this work. The results are compared with the classic approach since both models are recently used.

The modelled amount of worn volume has to be taken into account within the simulation. Stupkiewicz [127] mainly summarises two shape update schemes available in the literature: The widely used approach is a wear postprocessor in which the deformation problem is solved independently of the wear evolution, and in which the wear is calculated and applied via a shape update afterwards. This approach is sometimes referred to as geometry update scheme and has been used in [61], [63], [47], [48], [12], [11] and [134]. The second approach adds wear as an additional unknown to the deformation problem. This approach is developed as a monolithic scheme by Lengiewicz and Stupkiewicz [77] and Stupkiewicz [126] and as a staggered scheme by Farah et al. [50]. The postprocessor approach is much easier to implement and to apply on complex microstructured surfaces and is therefore applied in this work. As proposed e.g. in Lengiewicz and Stupkiewicz [77] the calculated wear of one passover simulation is furthermore upscaled, as wear is usually a slow process compared to the deformation timescale.

In summary, this contribution provides a pragmatic combination of frictional contact homogenisation and continuum mechanically sound phenomenological wear simulation with a postprocessor shape update scheme applied to microcstructured surfaces on the meso scale. Compared to the preliminary publication Berthelsen et al. [16], an extension to three-dimensional microstuctures with more complex periodic boundary

conditions, relative velocities and normals is elaborated. Furthermore, a combined friction model appropriate for high pressures in metal forming shall be used, see e.g. Behrens et al. [12], Wriggers [141], as well as an appropriate elasto-plastic material model. These modifications allow for directional studies as well as for application to real wear experiments in forming technologies and for a comparison of wear patterns of the classic Archard relation with the dissipation based formulation. }$^{\text{qtd.}}_{[118]}$ The model is described in Chapter 3 along with illustrative examples for microstructured surfaces and a conclusion.

1.2 Modelling of material separation

Separation of material in solid body mechanics presents a challenge for modelling approaches due to the topological shape changes. One illustrative example is machining, where chip formation has been extensively studied with several computational modelling approaches as summarised in the review Rodríguez et al. [110]. In the second part of the present thesis, material separation is considered in a smaller length-scale on the level of single asperity interactions. Figure 1.2 shows the topography of a rough surface with the detachment of a wear particle. Such measurements motivate the analysis of single asperity interactions for studying wear mechanisms on the microscopic scale.

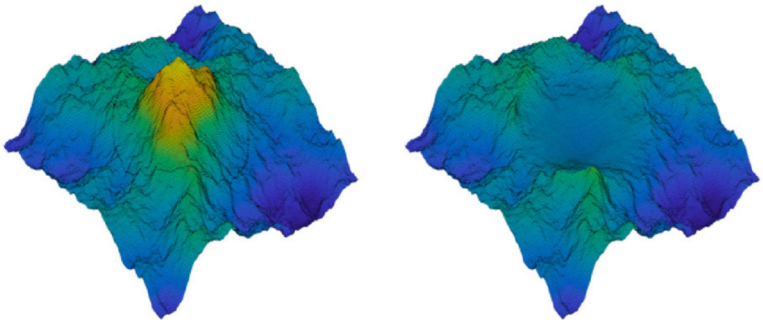

Figure 1.2: Topography of a rough surface showing the detachment of a wear particle. Reprinted from [99], licensed under CC BY 4.0.

According to Wriggers [141] and Straffelini [123], frictional contact and adhesive wear are based on formation and breakage of adhesive bonds as well as on the interlocking, elastoplastic deformation and breakage of surface asperities. Adhesive wear is extensively studied in tribology due to its importance in engineering applications. The review Zhang et al. [145] summarises modelling approaches to adhesive wear on asperities and rough surfaces. Two main analytical models for adhesive wear are the Archard model [2] and the Rabinowicz criterion [102]. The Archard model describes the amount of worn volume based on pressure and contact area, see also Section 1.1 for more recent Archard formulations based on the dissipated frictional energy. The Rabinowicz model provides a criterion for the detachment of wear particles based on a comparison of adhesive and elastic energy. While these empirical models can be of great predictive

value, numerical models account for the interaction of plasticity, crack initiation and surface interactions in order to study wear mechanisms. The review Zhang et al. [145] summarises approaches based on Molecular Dynamics (MD), DEM and FEM for the simulation of asperity interaction. The MD simulations provide insights in atomic-level wear mechanisms. Figure 1.3 shows results from Zhong et al. [151], where asperity shear is simulated between an aluminium asperity and a Lennard-Jones test-tip used as the contact reference. With strong adhesion, part of the aluminium asperity sticks to the tip after the shearing. For weak adhesion, no aluminium adheres to the tip, but the atoms are strongly deformed and rebonded within the asperity. Similar results with detailed analyses for the accordance with analytical models can be found in Molinari et al. [89], Zhao and Aghababaei [148]. DEM simulations are reported as an alternative, which also successfully were applied for the investigation of wear modes, see [145] for the respective references.

(a) Strong adhesion leads to adherence of removed aluminium on the tip.

(b) Weak adhesion leads to rebonding within the asperity (white atoms).

Figure 1.3: Molecular Dynamics simulation result for asperity shearing with strong and weak adhesion. Reprinted from [151] with permission from AIP Publishing.

FEM has the advantage of superior constitutive modelling capabilities compared to DEM, while being significantly more efficient than MD. FEM modelling approaches for asperity shear mentioned in [145] are for example an asperity interaction with elastoplastic material using Abaqus explicit, see Mulvihill et al. [92], and the simulation of sub-surface crack initiation using Abaqus, see Zhang and Etsion [144]. The latter reference mentions challenges for the FEM simulation in terms of extreme simulation times.

In this thesis, a PFEM approach is developed for the simulation of elastoplastic asperity interactions of steel surfaces. The focus is on the adhesion-free case as shown in the MD simulation in Figure 1.3b. The PFEM approach requires special element technology for the incompressible plastic flow that is common for steel. This topic is studied intensively and is therefore introduced in more detail in Section 1.2.1. Furthermore, modelling of contact, material separation and self-contact is necessary. These topics are introduced in Section 1.2.2.

1.2.1 Modelling of quasi-incompressible material behaviour in PFEM

qtd. [119]{In the PFEM, linear elements are a natural choice, however these elements restrict the usage in cases of quasi-incompressible material behaviour. In solid mechanics PFEM literature, mainly three approaches are established for dealing with quasi-incompressible material behaviour:

- first-order mixed triangular elements (P1P1) of displacement-pressure ($\boldsymbol{u}$-p) or displacement-volume-dilatation ($\boldsymbol{u}$-ϕ) type, see [18, 26, 28, 60, 90, 111]. The $\boldsymbol{u}$-p formulation is reported in Carbonell et al. [26] to produce slightly better stress distributions than the $\boldsymbol{u}$-ϕ formulation, whereas Monforte et al. [90] reports the $\boldsymbol{u}$-ϕ formulation to perform slightly better in the scatter-free representation of Lode-angles than the $\boldsymbol{u}$-p formulation. A three-field formulation $\boldsymbol{u}$-ϕ-p is also tested, but the third field is not necessary according to Monforte et al. [90]. As the $\boldsymbol{u}$-ϕ formulation does not restrict the material model formulation to a volumetric-isochoric split, this formulation is chosen in this work.

- first-order pure displacement triangular elements with strain smoothing onto the nodes and nodal integration, see Zhang et al. [146], usually referred to as smoothed PFEM, i.e. SPFEM. An edge-based smoothing version with Gauss-integration has also been proposed, see Jin et al. [67]. The smoothing prevents the element-wise calculation of the global tangent stiffness matrix contributions, which considerably complicates the finite element implementation for implicit time integration. SPFEM is therefore especially suited for explicit time integration, where no tangent stiffness matrix is needed. Furthermore, Reinold and Meschke [105] combined an edge-based smoothing with a first order mixed $\boldsymbol{u}$-p formulation.

- second-first-order mixed triangular elements of displacement-stress ($\boldsymbol{u}$-$\boldsymbol{\sigma}$) type, where the edge-mid-nodes are neglected in remeshing, see e.g. Wang et al. [135] and Zhang et al. [147]. The large number of unknowns is therein treated in a variational setting with a so-called second-order cone programming solver.

Although it has been shown in the context of standard FEM that a second-order pure displacement triangular element (TRI6) already performs considerably better than first-order displacement elements and close to more advanced element technologies, see Caylak and Mahnken [30], this option has so far not been reported in the PFEM-literature to the authors' knowledge. In this work, a TRI6 element is applied in PFEM and compared to the stabilised mixed P1P1 element of $\boldsymbol{u}$-ϕ-type under 2d plane strain conditions. Amongst the state-of-the-art formulations the P1P1 element can still straightforwardly be implemented in standard FEM-algorithms and is therefore preferred to the other mentioned formulations. The restriction to 2d plane strain represents a simplification that excludes the consideration of advanced remeshing methods necessary in 3d PFEM simulations. For example, mesh-smoothing is essential in 3d to address specially distorted tetrahedra, commonly referred to as slivers, cf. Carbonell et al. [26], Meduri et al. [85].

The frequent remeshing in the PFEM requires a transfer of state-variables. One option is the mapping of the previous stress tensor which is then additively combined with the new stress increment in a strain-rate based hypoelastic material model, see e.g. Franci et al. [54]. However, this work follows the strict deformation based approach used in Monforte et al. [90] and Carbonell et al. [26], which allows for the application of hyperelasticity-type constitutive relations. Thereby, details on the mapping of previous deformation, especially in the context of $\boldsymbol{u}$-ϕ formulations, are elaborated. The transfer of state-variables has a large influence on the stability and accuracy of the PFEM. In the present work, this transfer is done directly rather than via the node points. This contradicts the classic particle-based spirit of PFEM and the early state-of-the-art of a L2-projection of the variables onto the node points, see e.g. Oliver et al. [96], Sabel et al. [114]. However, copying state-variables directly between old and new quadrature points has become the state-of-the-art in PFEM since it avoids unnecessary variable smoothing in unchanged mesh regions, see Carbonell et al. [28], Rodríguez et al. [111]. Thereby, the information of the closest previous quadrature point is copied, so that this method is abbreviated as closest point mapping (CPM) in the following. Especially for coarse meshes and large spatial changes of state-variables, the CPM introduces a considerable error in the transfer. To improve the transfer quality, the interpolation of state-variables from three of the previous quadrature points has been proposed in Hu and Randolph [65] and used in Zhang et al. [147]. In Hu and Randolph [65], two such schemes are proposed: the arbitrary linear interpolation method interpolates from the three nearest quadrature points in the reference mesh, whereas the unique element method uses the previous element which contains the new quadrature point and interpolates or extrapolates from the quadrature points of this unique element. The unique element method makes use of the high smoothness of the variables within one element which yielded the best results in Hu and Randolph [65]. However, in this work the arbitrary linear interpolation method is applied in a straightforward implementation by using a background-triangulation of all previous quadrature points where it is only necessary to interpolate by standard shape functions. The method is abbreviated as background triangle mapping (BTM). Furthermore, the interpolation in the BTM mapping can furthermore be improved by transfer operators suggested in Camacho and Ortiz [25] which preserve incompressible deformation states in linear operations such as interpolation. Since it involves a spectral decomposition it will be evaluated as to whether the effort is justified for the numerical examples. $\}^{\text{qtd.}}_{[119]}$ The both element formulations and the extended state-variable mapping is presented and analysed with numerical studies in Section 4.1.

1.2.2 Modelling of contact and material separation

Contact modelling has a long history in FEM, see e.g. the monograph Wriggers [141]. Considering the aspect of contact discretisation, the main methods mentioned in [141] are classic projections (Node-to-Segment, Segment-to-Segment) based on both surface meshes, Mortar methods which define one surface as the mortar surface on which the other surface

is projected, and smooth discretisations based on Isogeometric Analysis (IGA). In a more recent overview, Wriggers [142] adds Third Media Approaches and the Contact Domain Method (CDM), which both consider a third mesh of continuum elements between the contacting bodies which are given special properties. The CDM is particularly popular in the PFEM literature due to its similarities in mesh generation to the techniques required for bulk meshing. Therefore, the CDM is chosen in the present thesis. The main ideas of the CDM with respect to the contact discretisation are introduced in Oliver et al. [96]. Improved constraint enforcement with a Nitsche-type approach, referred to as the Smoothed Lagrange Multiplier Method (SLMM), as well as robust analytical derivations of the contact contributions are then presented in the two-part paper Hartmann et al. [58], Oliver et al. [97]. A 3d extension is given in Hartmann et al. [59] and a comparison of the SLMM with a classic penalty formulation is given in Weyler et al. [139], where the SLMM generally shows more robust results. Recent applications of the CDM in PFEM can be found in Bakhshan et al. [7], for vibration-assisted micromachining using the penalty formulation and in Carbonell et al. [28] for geotechnical applications using the SLMM formulation. In the present thesis, the SLMM formulation is applied and briefly summarised in Section 4.2.

With respect to the modelling of material separation, the review Rodríguez et al. [110] gives a good overview on computational methods for material separation in the context of chip formation. It shows examples for Eulerian and DEM approaches as well as for Lagrangian FEM with remeshing. Among the Lagrangian FEM approaches, Rodríguez et al. [110] distinguishes geometric criteria and physical criteria for chip separation. An example of a geometric criterion is a predefined layer of duplicated nodes along which the distance to the tool tip is used to release the node coupling in order to allow cutting and chip separation, see Komvopoulos and Erpenbeck [72]. For the physical criteria, a similar layer of coupled nodes is used in Strenkowski and Carroll [124], but combined with a fracture criterion based on the effective plastic strain. Another approach is presented in Marusich and Ortiz [83], where adaptive remeshing is coupled with a fracture criterion based on critical effective plastic strain and the mesh is adapted to allow for a discretisation of the crack formation. In the PFEM literature, full material separation in cutting processes is not in the focus but rather the simulation of the metal cutting and chip formation itself. In Sabel et al. [114], the cutting is induced by a stretching of the elements close to the tool tip such that the α-shape deletes elements and generates a cut. In this approach, the α-shape technique detects topological changes, e.g. in the formation of cracks by detecting new surfaces in stretched areas. Large topological changes lead to a large deviation from the equilibrium state and consequently to convergence issues, which can be limiting for this method. In contrast, Rodríguez et al. [111] and Carbonell et al. [26] model the chip formation as a plastic flow around the tool tip, which requires mesh refinement in the cutting zone to account for the large plastic deformations. Therefore, PFEM methods have been extended with several techniques. Firstly, a point density dependent α-test radius makes inhomogeneous mesh densities possible, cf. Carbonell et al. [27]. Furthermore, the boundary polygon of the

previous step is preserved by using a Constrained Delaunay triangulation (CDT), cf. Carbonell et al. [27] and by inserting additional particles in regions, where boundary segments are largely stretched, cf. Rodríguez et al. [111]. Minimising the deviation from the equilibrium state in each remeshing step by adapted mesh densities and the CDT yields a better numerical robustness of the model. Therefore, in the present thesis the extended remeshing methods are adapted to the application of asperity shearing.

A limiting factor of modelling topological changes solely by plastic deformations and adaptive remeshing is the inability to simulate full material separation, e.g. chip breakage in a machining simulation. In Sabel et al. [114], material separation is modelled based on the stretch of surface segments detected by the α-shape method alone. However, this approach is only meaningful as long as the element shape is directly related to the material deformation. As soon as the connectivity changes under shear deformation, or when points are inserted and removed, the local deformation state becomes unrelated to the element shape. Therefore, the addition of a damage criterion supplements the abilities of the α-shape method for detecting topological changes. Furthermore, self-contact simulation is a feature that is often not modelled in PFEM contact simulations. Once a crack occurs in the body discretisation, special remeshing techniques are required for a successful generation of the bulk and contact meshes. This novel feature is discussed in Section 4.3 along with the material separation criterion and the adapted PFEM methods.

1.3 Modelling of material deposition

Due to the ability to simulate Fluid Structure Interaction, the PFEM is considered in the third part of this thesis for the modelling of an Additive Manufacturing (AM) process. [120]qtd.{The particular application respectively process considered in this work, i.e. directed energy deposition with a laser beam (DED-LB), is depicted in Figure 1.4. The directed energy from the laser beam melts powder particles which are continuously deposited on a substrate surface. The present work aims to establish a simulation framework for the deposition and solidification of the steel melt by adapting the PFEM remeshing capabilities and by combining these with appropriate phase transformation material models. The overall goal of the simulation approach is the investigation of process induced part properties regarding residual stresses and distortion by taking into account the full interaction of the molten metal and the substrate during the deposition. Therefore, established simulation approaches for DED need to be extended and adapted to this goal. Part-scale simulation of DED is usually performed by using element activation in FEM with a predefined weld bead geometry, see e.g. [32, 51, 103]. An advanced scheme where the weld bead geometry is calculated by optimisation and where the interface is described by a cut-off function is presented in [149]. However, these approaches do not explicitly resolve the full interaction of the melt with the substrate, which motivates a more advanced approach in the present work. On the other hand, among particle based methods many approaches exist which feature a very high precision level. The

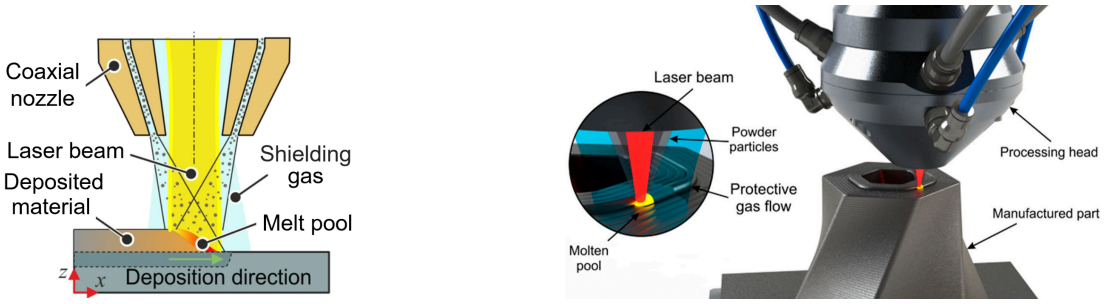

(a) Process sketch, modified from [37] under CC BY 4.0.

(b) Application example, excerpt from [8] under CC BY 4.0.

Figure 1.4: Illustration of the DED-LB process.

smoothed particle hydrodynamics is one example, see e.g. [35, 36, 86]. However, the computational cost is very high, especially if a good resolution of the stress distribution is desired. The PFEM is chosen in this work as a compromise of including sufficient details but keeping the numerical cost manageable. This method was originally designed for free surface fluid flows, see [98], and has since been adapted for many applications, see [34] for a comprehensive review. Relevant examples of these applications are the simulation of classic manufacturing technologies, see [26, 96, 111, 114], as well as the simulation of additive manufacturing processes. In this context, [19] simulate the melt pool dynamics of a spot welding process with PFEM. The DED process is modelled in [91] by the gradual growth of material on a surface in the form of node insertion based on the laser power and particle distribution. The mesh is then regenerated using PFEM methods. A comparable approach is presented in [143]. Full featured deposition simulation is established for concrete printing in several research groups, cf. [106, 108]. While these concrete deposition approaches present very advanced remeshing schemes in 3d, the simulations are not thermomechanically coupled and the extreme temperature gradients in the DED-LB process pose additional challenges for the simulation of the connection zone. With respect to thermomechanical simulations, the modelling of melt and solidification in [54] shows that PFEM is generally capable of capturing melt flow and solidification, whereas the focus in the reference lies on remelting and failure of process-plant walls.

Therefore, this work advances the PFEM approach to modelling deposition of hot metal, which is not yet thorougly discussed in the PFEM literature with regard to the high temperature gradients in the thermomechanically coupled problem, especially for modelling of the connection zone. A 2d simulation approach is chosen for clearly establishing the necessary methods, without yet adding the amount of additional mesh complexity of the 3d version, e.g. the control of bad-shaped sliver elements discussed in [85, 106, 136]. Despite the necessary assumptions for a 2d simulation, one advantage is a better observability of the mesh quality and mesh evolution during the deposition and connection. In addition to the already mentioned PFEM references, several relevant

publications in the PFEM research are mentioned in the following. The basis of the PFEM is a repeated remeshing of the point cloud describing the bodies by using a Delaunay triangulation and subsequently using the α-shape method to determine the shape of the bodies. This allows changes in the shape of the bodies to be modelled, which is not possible in conventional FEM. The described basic approach is well established, see e.g. [26]. In the deposition simulation, the meshing of the connection zone is of special interest as the α-shape will connect two bodies when they are close to each other, which generates a layer of connection elements between the bodies and thereby artificially adds mass to the simulation. The approach by [108] prevents the creation of a connection layer by merging the node points of the concrete stream and the baseplate when they come in contact. However, this approach is not suitable when both nodes have vastly different temperatures. Therefore, in this work the connection layer will be accepted for modelling the temperature gradient while the thickness of this layer is reduced by special techniques. Therefore, a distance threshold from [106] is extended with a novel progression criterion to prevent holes in the connection zone while keeping this zone sufficiently thin. The very large material flow furthermore makes an improvement of the point distribution during the simulation necessary. This has been targeted with basic point insertion and removal schemes in [111], whereas [49] as well as [78] recently proposed advanced insertion methods with regards to the location of inserted points and a prescribed mesh density function. Methods from these references are combined with emphasis on good applicability without modifying the triangulation algorithms of the Delaunay library.

The PFEM will provide the numerical framework, whereas a suitable material model is needed to describe the fluid flow as well as the solidification. The model is supposed to describe the change in the constitutive behaviour upon transformation along with accompanying stretches and heat sources. Resolving very fine microstructural details such as nucleation, dendrite growth and grain formation is therefore not necessary in the model – the interested reader is referred to applications of e.g. the phase-field approach, summarised in the review [75]. At the other end of the modelling spectrum, simplified local material models are applied on the macroscale which do not explicitly distinguish separate phases but rather use temperature dependent material parameters to also cover the changes upon phase transformation. Underlying quantities, such as the heat capacity, therefore capture non-smooth transitions which can lead to numerical instabilities. One example for this approach is [107], where in a purely thermal model the melt pool is investigated for a Laser Powder Bed Fusion (LPBF) process by using non-smooth temperature dependent parameters. Furthermore, [24] combine a weakly coupled thermomechanical approach with temperature dependent properties of a small strain viscoplastic material model with the resetting of plastic strains and stresses upon reaching the solidus temperature in order to simulate LPBF. The approach presented in [138] is based on a large strain thermoelastic model including a deletion of the deviatoric deformation component upon reaching the melt temperature along with temperature dependent parameters as a rough estimate of an irreversible melt flow. A further example

for the approach of using temperature dependent material parameters is [54], where a small strain viscoplastic relation for the melt regime is levelled via temperature dependent parameters with a viscoelastic relation in the solid regime, and where a switch between both models is applied at the melt temperature.

The present work uses phase fractions in order to locally cover the phase transition more precisely which allows for a higher modelling flexibility and a natural incorporation of transformation stretches, latent heat and jumps in material parameters. The approach originates in the simulation of shape memory alloys where both, stresses and temperature, drive the phase transformation. An energy-convexification approach is therefore applied in [9] in order to determine the energetically favourable phase-mixture. In [10, 95], such a framework is applied to the powder-melt-solid phase transformations in the LPBF. The results indicate that the liquid-solid phase transformation of metals in AM processes is mainly temperature driven in contrast to shape memory alloys. This motivates the adaptation of a phenomenological temperature dependent phase transformation function for the evolution of the phase fractions in the present work by using a smoothed step function. A similar approach can be found in [17], where a smoothed liquid-fraction function describes the latent heat release and also influences the mechanical model. A further example is [113], where a hyperbolic tangent phase transition function governs the transformation stretches in powder melting and averages the parameters in a LPBF simulation. A similar phase change function is applied in [73] within a space-time FEM for the purely thermal simulation of LPBF. Likewise, in [100] a thermal LPBF simulation with temperature and phase dependent parameters is based on a smooth liquid fraction function and an advanced adaptive layer activation scheme. In the present work, the melt material is modelled with a large-strain viscoelastic model based on the model presented in [4, 5] for electro-viscoelasticity, adapted to the thermomechanical use case with phase-appropriate modifications. More precisely, a Maxwell model is adopted for the isochoric deformation in the melt phase, making the model suitable for describing the melt flow. The model is thus well suited to describe a Newtonian fluid type response despite being based on a Lagrangian parametrisation and the transition to solid material is straightforward. The phase transformation model then consistently couples the melt and solid phase and provides a sound constitutive framework. Large strain models are required for processes such as DED-LB, while constitutive models in the AM literature are mainly developed for small strain applications. This critical extension is one objective of the present contribution. The approach of using phase fractions rather than a pure temperature dependence allows for physically well motivated material modelling and also serves as a framework which can be enriched by including additional material response phenomena in future research work. }$^{\text{qtd.}}_{[120]}$

The basic continuum thermomechanical theory is introduced along with the main PFEM methods in Chapter 2. The phase-transformation model and the extension of the PFEM for the connection zone treatment, as well as numerical examples and a conclusion are given in Chapter 5.

1.4 Objective of this work

The objective of this work is the development of numerical modelling approaches for shape changes induced by surface interactions. A macroscopic wear post-processor is developed for the specific application to microstructured forming tools. Therefore, modern dissipation based Archard models are applied because these are more naturally combined with a combined friction model. For the microstructured tools, effective friction properties are derived by friction homogenisation on a representative periodic cut-out of the tool and workpiece surfaces. The focus then shifts towards microscopic consideration of friction and wear in modelling the shearing and separation of microscopic asperities. A PFEM modelling approach is developed, which includes a physical fracture criterion enhancing the shape detection algorithm to model crack initiation and material separation by complete fracture of the material. The approach is coupled with an adaptive mesh density to provide a sufficiently fine discretisation of the crack. Furthermore, a major extension of PFEM is the modelling of self contact after material separation. While sticking with a PFEM modelling approach, the third application is an AM process of hot metal deposition, where PFEM methods are extended for specialised treatment of the connection layer between the solid and the fluid part of the model. Another main highlight is the large strain material model for melt flow and solidification which is developed for describing the deposited material which solidifies on the cold base plate.

The thesis continues with the basic theory of continuum mechanics, the Finite Element Methods for thermo-mechanical problems, the incorporation of constraint equations and with the main PFEM methods. Furthermore, the three key applications are focussed in one chapter each along with conclusions summarising the findings and possible future extensions. A final conclusion summarises the overall insights and model developments provided by this thesis.

2 Theoretical and computational concepts for solid body interactions

The modelling approaches in this thesis share a common theoretical basis, namely continuum mechanics and a Lagrangian Finite Element Method. This chapter first introduces continuum mechanics, hyperelastic material modelling and large strain finite element methods, as well as constraint equations in FEM in the form of quasi-incompressibility and mechanical contact. Most of these methods are used in the first application Chapter 3, modelling and simulation of wear, but the commercial FE software ABAQUS is used so that the focus is on the simulation of wear rather than on the finite element modelling itself. The other two application cases, modelling and simulation of material separation and material deposition, presented in Chapters 4 and 5, are based on the Particle Finite Element Method implemented in an in-house research MATLAB code. Therefore, a detailed description of the theoretical background in this chapter is important for the specific models in the respective chapters, and therefore this chapter is rounded off with the main PFEM remeshing methods.

2.1 Continuum Mechanical basis

qtd. [120] {The nonlinear kinematics of the large deformation model is introduced in the reference configuration $\mathcal{B}_0$ with placements $\boldsymbol{X}$ and in the current configuration $\mathcal{B}_t$ with placements $\boldsymbol{x}$. The deformation is described by the displacement field $\boldsymbol{u}$ such that $\boldsymbol{x} = \boldsymbol{X} + \boldsymbol{u}$. The deformation gradient is defined as $\boldsymbol{F} = \partial \boldsymbol{x} / \partial \boldsymbol{X}$. As a basis for the Updated Lagrangian formulation of the finite element formulation, furthermore a previous configuration $\mathcal{B}_n$ is introduced, in which the finite element discretisation has been regenerated. The configurations are visualised in Figure 2.1. The time t is discretised into time steps $\Delta t = t_{n+1} - t_n$ where the placements $\boldsymbol{X}_n$ of the previous time step t_n are given as

$$\boldsymbol{X}_n = \boldsymbol{X} + \boldsymbol{u}_n \tag{2.1}$$

and the displacement field up to $\mathcal{B}_n$ is denoted by $\boldsymbol{u}_n$. The total displacement is therefore decomposed into

$$\boldsymbol{u} = \boldsymbol{u}_n + \Delta \boldsymbol{u} \tag{2.2}$$

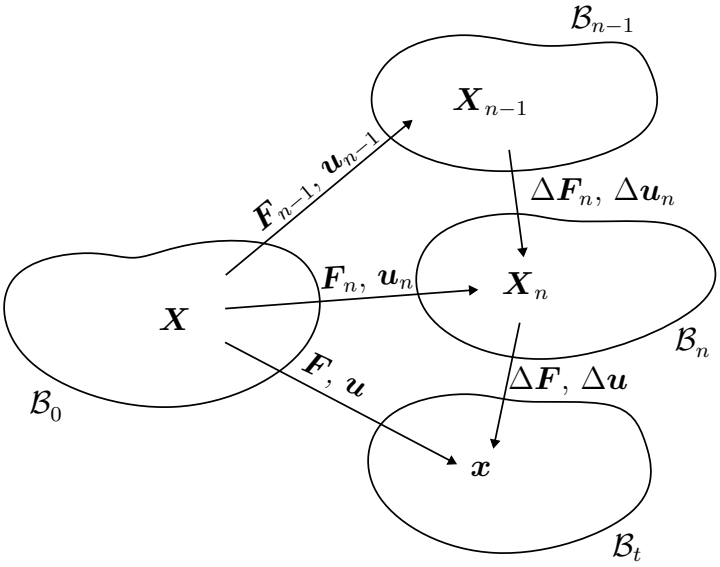

Figure 2.1: Configurations in updated Lagrangian formulation. Reprinted from [119], licensed under CC BY 4.0.

with the displacement increment $\Delta\boldsymbol{u}$. Consequently, the deformation gradient is similarly decomposed as

$$\boldsymbol{F} = \frac{\partial \boldsymbol{x}}{\partial \boldsymbol{X}_n} \cdot \frac{\partial \boldsymbol{X}_n}{\partial \boldsymbol{X}} = \Delta\boldsymbol{F} \cdot \boldsymbol{F}_n \tag{2.3}$$

As this work proceeds, $\boldsymbol{F}_n$ shall be transferred as a state-variable during remeshing in order to preserve a fully displacement based Lagrangian description. Moreover, time derivatives are introduced with respect to a fixed material point, i.e. as a material time derivative as $\dot{\bullet} = \mathrm{d}\bullet/\mathrm{d}t|_{\boldsymbol{X}}$ and $\ddot{\bullet} = \mathrm{d}^2\bullet/\mathrm{d}t^2|_{\boldsymbol{X}}$. For the derivation of the constitutive equations of the phase transformation model, only the total deformation gradient is of interest. Here, a multiplicative decomposition according to $\boldsymbol{F} = \boldsymbol{F}^{\mathrm{vol}} \cdot \boldsymbol{F}^{\mathrm{iso}}$ is used with the volumetric deformation $\boldsymbol{F}^{\mathrm{vol}} = J^{1/3}\,\boldsymbol{I}$ consisting of the volume dilatation $J = \det(\boldsymbol{F}) > 0$ and the second order identity tensor $\boldsymbol{I}$, so that the isochoric deformation reads $\boldsymbol{F}^{\mathrm{iso}} = J^{-1/3}\,\boldsymbol{F}$. The corresponding right Cauchy-Green stretch tensor $\boldsymbol{C} = \boldsymbol{F}^{\mathrm{t}} \cdot \boldsymbol{F}$ equivalently decomposes into $\boldsymbol{C}^{\mathrm{iso}} = J^{-2/3}\,\boldsymbol{C}$ and $\boldsymbol{C}^{\mathrm{vol}} = J^{2/3}\,\boldsymbol{I}$.

The displacement field $\boldsymbol{u}$ is furthermore coupled to the absolute temperature field θ and both fields are governed by continuum mechanics based balance relations, see e.g. [79, 82] for more details. The local form of the balance of linear momentum in referential format reads

$$\rho_0\,\ddot{\boldsymbol{u}} = \nabla_{\boldsymbol{X}} \cdot \boldsymbol{P} + \rho_0\,\boldsymbol{b} \tag{2.4}$$

with the referential mass density ρ_0, the Piola stress tensor $\boldsymbol{P}$ and with the body force vector $\boldsymbol{b}$. The referential format of the balance of energy in temperature format reads

$$c_0\,\dot{\theta} = -\nabla_{\boldsymbol{X}} \cdot \boldsymbol{Q} + r^{\mathrm{ext}} + r^{\mathrm{mec}} \tag{2.5}$$

with the referential heat capacity c_0, the referential heat flux vector $\boldsymbol{Q}$ and the external and mechanical volumetric heat sources r^{ext} and r^{mec}. The second law of thermodynamics is applied so as to derive thermodynamical restrictions to the formulation based on a mass-specific Helmholtz free energy density $\Psi(\boldsymbol{F}, \theta, \mathcal{V})$, which generally depends on $\boldsymbol{F}$ and θ, as well as on internal variables $\mathcal{V}$. Standard derivations result in the hyperelastic format of the Piola stresses and the specific referential heat capacity

$$\boldsymbol{P} = \rho_0 \frac{\partial \Psi}{\partial \boldsymbol{F}} \qquad\qquad c_0 = -\theta \frac{\partial^2 \rho_0 \Psi}{\partial \theta \, \partial \theta} \tag{2.6}$$

Furthermore, thermodynamic restrictions on the constitutive models are derived as two dissipation inequalities

$$\mathcal{D}_{\text{thm}} = -\frac{1}{\theta} \boldsymbol{Q} \cdot \nabla_{\boldsymbol{X}} \theta \geq 0 \qquad\qquad \mathcal{D}_{\text{mec}}^{\text{red}} = -\rho_0 \frac{\partial \Psi}{\partial \mathcal{V}} \bullet \dot{\mathcal{V}} \geq 0 \tag{2.7}$$

where $\mathcal{D}_{\text{thm}} \geq 0$ is preserved by the heat conduction model and where $\mathcal{D}_{\text{mec}}^{\text{red}} \geq 0$ imposes constraints to the mechanical material model. The mechanical heat source furthermore follows as

$$r^{\text{mec}} = \theta \frac{\partial \boldsymbol{P}}{\partial \theta} \colon \dot{\boldsymbol{F}} + \left[\mathcal{D}_{\text{mec}}^{\text{red}} - \theta \frac{\partial \mathcal{D}_{\text{mec}}^{\text{red}}}{\partial \theta} \right] \tag{2.8}$$

where the first part is related to thermoelastic heat and the second part to dissipation due to the evolution of internal variables. $\}^{\text{qtd.}}_{[120]}$

The hyperelastic material modelling framework in (2.6) allows the derivation of stresses and multiphysical coupling from the Helmholtz free energy function in a thermodynamically consistent manner. Objectivity under large deformations is naturally guaranteed and path dependent material behaviour can be described by internal variables which are governed by the dissipation restriction (2.7). This provides a solid basis for the simulation of the application examples in this work. The specific Helmholtz free energy functions and path dependent model extensions are described in the respective application chapters.

2.2 Updated Lagrangian Finite Element formulation of thermomechanics

For the Finite Element solution of the balance equations (2.4) and (2.5), multiplication with admissible test function $\delta \boldsymbol{u}$ and $\delta\theta$, integration by parts and application of the Gauss theorem lead to the weak forms of the balance equations

$$\mathcal{W}_{\boldsymbol{u}} = \int_{\mathcal{B}_0} \rho_0 \, \delta \boldsymbol{u} \cdot \ddot{\boldsymbol{u}} + \nabla_{\boldsymbol{X}} \delta \boldsymbol{u} \colon \boldsymbol{P} - \rho_0 \, \delta \boldsymbol{u} \cdot \boldsymbol{b} \, \mathrm{d}V - \int_{\partial \mathcal{B}_0^{\boldsymbol{t}}} \delta \boldsymbol{u} \cdot \boldsymbol{t}_0 \, \mathrm{d}A = 0 \tag{2.9}$$

$$\mathcal{W}_{\theta} = \int_{\mathcal{B}_0} c_0 \, \delta\theta \, \dot{\theta} - \nabla_{\boldsymbol{X}} \delta\theta \cdot \boldsymbol{Q} - \rho_0 \, \delta\theta \left[r^{\text{ext}} + r^{\text{mec}} \right] \mathrm{d}V - \int_{\partial \mathcal{B}_0^{Q}} \delta\theta \, Q_{\text{sur}} \, \mathrm{d}A = 0 \tag{2.10}$$

with the surface traction $\boldsymbol{t}_0$ and the surface heat flux Q_{sur}. The integration of these equations in the reference domain $\mathcal{B}_0$ is the standard approach but, given the mesh adaptation in the remeshing framework, an integration in a deformed mesh is preferred.

qtd. [120] {The Updated Lagrangian Finite Element formulation is applied in the present work, since it provides a framework for using the regenerated mesh and still preserves the advantage of a constant integration and interpolation space in $\mathcal{B}_n$ during the solution iteration. The framework is documented in [74] for the mechanical case, whereas the thermomechanical formulation is summarised in the following. The domain $\mathcal{B}_n$ is subdivided in n_{el} finite elements. The nodal degrees of freedom, i.e. displacement $\boldsymbol{u}^{eA}$ and temperature θ^{eC} of nodes A and C in element e, are used for field and gradient approximation in standard manner as

$$\boldsymbol{u}^e = \sum_{A=1}^{n_{\text{en}}} \boldsymbol{u}^{eA}\, N^A \qquad \frac{\partial \Delta \boldsymbol{u}}{\partial \boldsymbol{X}_n} = \sum_{A=1}^{n_{\text{en}}} \Delta \boldsymbol{u}^{eA} \otimes \frac{\partial N^A}{\partial \boldsymbol{X}_n} \tag{2.11}$$

$$\theta^e = \sum_{C=1}^{n_{\text{en}}} \theta^{eC}\, N^C \qquad \frac{\partial \theta}{\partial \boldsymbol{X}_n} = \sum_{C=1}^{n_{\text{en}}} \theta^{eC}\, \frac{\partial N^C}{\partial \boldsymbol{X}_n} \tag{2.12}$$

with nodal shape functions N and their gradients. Herein, identical shape functions are used for the approximation of all fields and, moreover, also applied to the approximation of the related test function contributions and the discretisation of the geometry. The term $\partial \Delta \boldsymbol{u} / \partial \boldsymbol{X}_n$ is required for the incremental deformation gradient according to (2.3). The weak form of the balance equations (2.4) and (2.5) follows from standard derivations together with the assembly operator $\mathbf{A}_{e=1}^{n_{\text{el}}}$ as

$$\mathbf{r}^{\boldsymbol{u}} = \mathbf{A}_{e=1}^{n_{\text{el}}} \Big[\boldsymbol{M}^{eAB} \cdot \ddot{\boldsymbol{u}}^B + \boldsymbol{f}_{\text{int}}^{\boldsymbol{u}eA} - \boldsymbol{f}_{\text{vol}}^{\boldsymbol{u}eA} - \boldsymbol{f}_{\text{sur}}^{\boldsymbol{u}eA} \Big] = \mathbf{0} \tag{2.13}$$

$$\mathbf{r}^{\theta} = \mathbf{A}_{e=1}^{n_{\text{el}}} \Big[C^{eCD}\, \dot{\theta}^D + f_{\text{int}}^{\theta eC} - f_{\text{vol}}^{\theta eC} - f_{\text{sur}}^{\theta eC} \Big] = 0 \tag{2.14}$$

where the local nodal quantities are the force vectors $\boldsymbol{f}_{\text{int,vol,sur}}^{\boldsymbol{u}eA}$, the mass matrix $\boldsymbol{M}^{eAB}$, the scalar of the heat capacity C^{eCD} and the heat fluxes $f_{\text{int,vol,sur}}^{\theta eC}$. All nodal quantities are assembled first as elemental lists and subsequently collated in global arrays and matrices, which are denoted with upright bold symbols, e.g. $\mathbf{r}^{\boldsymbol{u}}$ and $\mathbf{r}^{\theta}$. Additional node counters B and D are introduced for defining nodal interactions. The contributions are given as

$$\boldsymbol{M}^{eAB} = \int_{\mathcal{B}_n^e} \rho_0\, N^A\, \boldsymbol{I}\, N^B\, J_n^{-1}\, \mathrm{d}V_n \qquad C^{eCD} = \int_{\mathcal{B}_n^e} c_0\, N^C\, N^D\, J_n^{-1}\, \mathrm{d}V_n \tag{2.15}$$

$$\boldsymbol{f}_{\text{int}}^{\boldsymbol{u}eA} = \int_{\mathcal{B}_n^e} \boldsymbol{P} \cdot \boldsymbol{F}_n^{\text{t}} \cdot \nabla_{\boldsymbol{X}_n} N^A\, J_n^{-1}\, \mathrm{d}V_n \quad f_{\text{int}}^{\theta eC} = -\int_{\mathcal{B}_n^e} \nabla_{\boldsymbol{X}_n} N^C \cdot \boldsymbol{F}_n \cdot \boldsymbol{Q}\, J_n^{-1}\, \mathrm{d}V_n \tag{2.16}$$

$$\boldsymbol{f}_{\mathrm{vol}}^{\boldsymbol{u}eA} = \int\limits_{\mathcal{B}_n^e} \rho_0\, N^A\, \boldsymbol{b}\, J_n^{-1}\, \mathrm{d}V_n \qquad f_{\mathrm{vol}}^{\theta eC} = \int\limits_{\mathcal{B}_n^e} \rho_0\, N^C \left[r^{\mathrm{ext}} + r^{\mathrm{mec}}\right] J_n^{-1}\, \mathrm{d}V_n \tag{2.17}$$

$$\boldsymbol{f}_{\mathrm{sur}}^{\boldsymbol{u}eA} = \int\limits_{\partial\mathcal{B}_n^{e\boldsymbol{t}}} N^A\, \boldsymbol{P}\cdot\boldsymbol{F}_n^{\mathrm{t}}\cdot\boldsymbol{N}_n\, J_n^{-1}\, \mathrm{d}A_n \qquad f_{\mathrm{sur}}^{\theta eC} = \int\limits_{\partial\mathcal{B}_n^{eQ}} N^C\, Q_{n,\mathrm{sur}}\, \mathrm{d}A_n \tag{2.18}$$

Herein, the contributions $\boldsymbol{P}$, $\boldsymbol{Q}$, c_0, $Q_{n,\mathrm{sur}}$ and r^{mec} are to be defined by constitutive relations. }$^{\mathrm{qtd.}}_{[120]}$ The Updated Lagrangian formulation is integrated in the previous configuration $\mathcal{B}_n$ instead of the reference configuration $\mathcal{B}_0$. $^{\mathrm{qtd.}}_{[119]}${For the push forward $J_n = \det(\boldsymbol{F}_n) > 0$ is used for the volume transformation, $\boldsymbol{F}_n$ is used for gradient transformations and $\mathrm{cof}(\boldsymbol{F}_n) = J_n\,\boldsymbol{F}_n^{-\mathrm{t}}$ is used for area transformations according to

$$\mathrm{d}V = J_n^{-1}\,\mathrm{d}V_n \tag{2.19}$$

$$\nabla_{\boldsymbol{X}}(\bullet) = \nabla_{\boldsymbol{X}_n}(\bullet)\cdot\boldsymbol{F}_n \tag{2.20}$$

$$\mathrm{d}\boldsymbol{A} = J_n^{-1}\,\boldsymbol{F}_n^{\mathrm{t}}\cdot\boldsymbol{N}_n\,\mathrm{d}A_n \tag{2.21}$$

}$^{\mathrm{qtd.}}_{[119]}$ such that the integrals and gradients can be computed in the newly remeshed previous configuration.

$^{\mathrm{qtd.}}_{[120]}${Time integration of the differential equations (2.13) and (2.14) is performed with a standard implicit Euler scheme according to

$$\ddot{\boldsymbol{u}} \approx \frac{\dot{\boldsymbol{u}} - \dot{\boldsymbol{u}}_n}{\Delta t} = \frac{\boldsymbol{u} - \boldsymbol{u}_n}{\Delta t^2} - \frac{\dot{\boldsymbol{u}}_n}{\Delta t} \qquad \dot{\theta} \approx \frac{\theta - \theta_n}{\Delta t} \tag{2.22}$$

The coupled residuum equations are solved monolithically by means of a Newton-Raphson scheme for the global list of unknowns $\mathbf{u}$ and $\boldsymbol{\theta}$. The global tangent is assembled from the elements as

$$\mathbf{J} = \begin{bmatrix} \dfrac{\mathrm{d}\mathbf{r}^{\boldsymbol{u}}}{\mathrm{d}\mathbf{u}} & \dfrac{\mathrm{d}\mathbf{r}^{\boldsymbol{u}}}{\mathrm{d}\boldsymbol{\theta}} \\ \dfrac{\mathrm{d}\mathbf{r}^{\theta}}{\mathrm{d}\mathbf{u}} & \dfrac{\mathrm{d}\mathbf{r}^{\theta}}{\mathrm{d}\boldsymbol{\theta}} \end{bmatrix} = \mathbf{A}_{e=1}^{n_{\mathrm{el}}} \left[\frac{1}{\Delta t^2} \begin{bmatrix} \boldsymbol{M}^{eAB} & \mathbf{0} \\ \mathbf{0} & 0 \end{bmatrix} + \frac{1}{\Delta t} \begin{bmatrix} \mathbf{0} & \mathbf{0} \\ \mathbf{0} & C^{eCD} \end{bmatrix} + \begin{bmatrix} \boldsymbol{K}^{\boldsymbol{uu}eAB} & \boldsymbol{K}^{\boldsymbol{u}\theta eAD} \\ \boldsymbol{K}^{\theta\boldsymbol{u}eCB} & K^{\theta\theta eCD} \end{bmatrix} \right] \tag{2.23}$$

In order to compensate for variations in the large material flows, an automatic time-stepping scheme is implemented. A fixed output time step Δt_{out} is defined for writing postprocessing files and restart files, which can be larger than the currently needed calculation time step Δt. Upon reaching an output step, the number of global iteration steps is evaluated and if less than six iteration steps were necessary, the calculation time step is increased by $\Delta t = 2\,\Delta t$ as long as $\Delta t < \Delta t_{\mathrm{out}}$. Upon any indication of diverging

algorithms on either local or global level, e.g. divergence of the local constitutive iteration or the global FE iteration, a try-catch control structure is used to reduce the calculation time step by $\Delta t = \Delta t/2$ and the simulation is resumed from the last output step by using the respective restart file. The changed Δt also needs to be passed to a viscous material relation, and the time integration scheme has to be able to work with changing time step sizes. Here, the applied implicit Euler scheme in the form of (2.22) by using $\dot{\boldsymbol{u}}_n$ as the history array works well, because it only depends on the time step size of the new calculation step. }$^{\text{qtd.}}_{[120]}$

Linearisation of the Finite Element formulation

For hyperelastic material with no internal variables, $^{\text{qtd.}}_{[120]}${the nonzero components of the global FE tangent are given as

$$\boldsymbol{K}^{\boldsymbol{uu}eAB} = \int_{\mathcal{B}_n^e} \nabla_{\boldsymbol{X}_n} N^A \cdot \boldsymbol{F}_n \circ \frac{\partial \boldsymbol{P}}{\partial \boldsymbol{F}} \cdot \boldsymbol{F}_n^{\mathrm{t}} \cdot \nabla_{\boldsymbol{X}_n} N^B \; J_n^{-1} \, \mathrm{d}V_n \tag{2.24}$$

$$\boldsymbol{K}^{\boldsymbol{u}\theta eAD} = \int_{\mathcal{B}_n^e} \nabla_{\boldsymbol{X}_n} N^A \cdot \boldsymbol{F}_n \cdot \frac{\partial \boldsymbol{P}}{\partial \theta} \, N^D \; J_n^{-1} \, \mathrm{d}V_n \tag{2.25}$$

$$\boldsymbol{K}^{\theta \boldsymbol{u}eCB} = \int_{\mathcal{B}_n^e} \rho_0 N^C \, \frac{\partial r^{\mathrm{mec}}}{\partial \boldsymbol{F}} \cdot \left[\nabla_{\boldsymbol{X}_n} N^B \cdot \boldsymbol{F}_n \right] \; J_n^{-1} \, \mathrm{d}V_n \tag{2.26}$$

$$K^{\theta\theta eCD} = K^{\theta\theta eCD}_{\mathrm{int}} + K^{\theta\theta eCD}_{\mathrm{vol}} + K^{\theta\theta eCD}_{\mathrm{sur}} \tag{2.27}$$

with

$$K^{\theta\theta eCD}_{\mathrm{int}} = - \int_{\mathcal{B}_n^e} \nabla_{\boldsymbol{X}_n} N^C \cdot \boldsymbol{F}_n \cdot \frac{\partial \boldsymbol{Q}}{\partial \nabla_{\boldsymbol{X}} \theta} \cdot \left[\nabla_{\boldsymbol{X}_n} N^D \cdot \boldsymbol{F}_n \right] \; J_n^{-1} \, \mathrm{d}V_n \tag{2.28}$$

$$K^{\theta\theta eCD}_{\mathrm{vol}} = \int_{\mathcal{B}_n^e} \rho_0 N^C \, \frac{\partial r^{\mathrm{mec}}}{\partial \theta} \, N^D \; J_n^{-1} \, \mathrm{d}V_n \tag{2.29}$$

$$K^{\theta\theta eCD}_{\mathrm{sur}} = \int_{\mathcal{B}_n^e} N^C \, \frac{\partial Q_{n,\mathrm{sur}}}{\partial \theta} \, N^D \, \mathrm{d}V_n \tag{2.30}$$

whereby use of the multiplication operator $[\boldsymbol{T} \circ \mathsf{A}]_{ijkl} = T_{jm} \, \mathsf{A}_{imkl}$ is made. For a good modelling flexibility, the derivatives can be determined by using exact numerical tangents provided by complex step derivative approximation (CSDA), see [129] for the application to constitutive tangent moduli. In contrast to classic finite difference approximations, the perturbation is applied to the respective imaginary parts, e.g. for the perturbed temperature as $\theta^* = \theta + \mathrm{i}\,\epsilon$ with the imaginary unit $\mathrm{i}^2 = -1$ and the perturbation ϵ. The

coefficients of the derivatives are then achieved by evaluating the imaginary part Im () of the function as

$$\frac{\partial r^{\mathrm{mec}}}{\partial \theta} = \frac{\mathrm{Im}\left(r^{\mathrm{mec}}(\boldsymbol{F}, \theta^*, \mathcal{V})\right)}{\epsilon} \qquad \frac{\partial \boldsymbol{P}}{\partial \theta} = \frac{\mathrm{Im}\left(\boldsymbol{P}(\boldsymbol{F}, \theta^*, \mathcal{V})\right)}{\epsilon} \tag{2.31}$$

For derivatives with respect to $\boldsymbol{F}$, a component-wise perturbation is used. From the perturbation of one component related to the indices kl according to $\boldsymbol{F}^* = \boldsymbol{F} + \mathrm{i}\,\epsilon\,\boldsymbol{e}_k \otimes \boldsymbol{e}_l$, the components of the tangent are derived as

$$\frac{\partial r^{\mathrm{mec}}}{\partial F_{kl}} = \frac{\mathrm{Im}\left(r^{\mathrm{mec}}(\boldsymbol{F}^*, \theta, \mathcal{V})\right)}{\epsilon} \qquad \frac{\partial P_{ij}}{\partial F_{kl}} = \frac{\mathrm{Im}\left(P_{ij}(\boldsymbol{F}^*, \theta, \mathcal{V})\right)}{\epsilon} \tag{2.32}$$

Due to the calculation of the sensitivity on the imaginary axis, no round-off errors occur and a very small perturbation can be used, e.g. $\epsilon = 10^{-16}$, which delivers numerically exact tangent approximations. For the application of this scheme, the implementation of the constitutive relations has to properly handle complex numbers [1]. }$^{\text{qtd.}}_{[120]}$ The FE tangent equations extend to inelastic material by switching to total derivatives which does not change the numerical tangents. However, for analytical linearisation, further contributions based on the evolution of internal variables need to be taken into account. In the present thesis, analytical tangents are used for the elastoplastic material model in Chapter 4 and the exact numerical tangents are used for the melt flow and solidification model in Chapter 5.

2.3 Incorporation of constraint equations in the FEM

In this work, two types of constraint equations are considered in the Finite Element formulation. Methods for quasi-incompressible material behaviour couple additional global field variables to local quantities by using constraint equations. Similarly, contact mechanics are based on contact constraints, namely impenetrability and stick constraints. Both types of constraint equations are expressed as an extension of the weak form of the balance of linear momentum (2.9). Therefore, the following derivations are restricted to a mechanical problem without the coupling to the balance of energy (2.10). As explained in [22] the weak form (2.9) can be obtained either by derivation from the strong form (2.4) with the principle of virtual work, or from the minimisation of a total potential energy function in the case of a conservative and static system. Such a variational formulation

[1] As an example of possible difficulties, in MATLAB, the matrix transpositions need to be performed with the non-conjugate rather than the standard transpose operator in order to work for both real and complex numbers.

of the FEM serves as a framework for the introduction of the constraint equations in the following subsections. The potential energy of a conservative and static system reads

$$\Pi(\boldsymbol{u}) = \underbrace{\int_{\mathcal{B}_0} \Psi \, \mathrm{d}V}_{=: \, \Pi_{\mathrm{int}}} - \underbrace{\left[\int_{\mathcal{B}_0} \rho_0 \, \boldsymbol{u} \cdot \boldsymbol{b} \, \mathrm{d}V + \int_{\partial \mathcal{B}_0^t} \boldsymbol{u} \cdot \boldsymbol{t}_0 \, \mathrm{d}A \right]}_{=: \, \Pi_{\mathrm{ext}}} \tag{2.33}$$

The stationarity condition $\delta \Pi_{\boldsymbol{u}} = 0$ yields an identical format as the weak form (2.9), i.e.

$$\delta \Pi_{\boldsymbol{u}} = \mathcal{W}_{\boldsymbol{u}} = 0 \tag{2.34}$$

In such manner, additional constraint equations can be introduced according to the theory of constraint optimisation in the form of

$$\min_{\boldsymbol{u}} \Pi(\boldsymbol{u}) \quad \text{subject to} \quad h = 0 \quad \text{and} \quad g \geq 0 \tag{2.35}$$

where the minimisation problem is subjected to a general equality constraint h and a general inequality constraint g.

2.3.1 Incorporation of quasi-incompressibility

Treatment of almost incompressible material behaviour is challenging in Finite Element methods because of the associated artificially stiff response denoted as volumetric locking. As explained in [22], the incompressibility constraint is not easily satisfied by a purely displacement based FE discretisation, especially for low order shape functions. While the problem partly vanishes for higher order shape functions, a general solution approach involves mixed formulations with additional global field variables. A general approach for quasi-incompressible material behaviour is the Hu-Washizu variational principle which will be summarised in the following based on [22]. The related extended potential function reads

$$\Pi_{\mathrm{HW}}(\boldsymbol{u}, \phi, p) = \int_{\mathcal{B}_0} \left[\Psi^{\mathrm{iso}}(\boldsymbol{C}^{\mathrm{iso}}) + \Psi^{\mathrm{vol}}(\phi) + p \, [J - \phi] \right] \mathrm{d}V \; - \; \Pi_{\mathrm{ext}} \tag{2.36}$$

where Π_{int} is defined with a volumetric-isochoric decomposition. Herein, ϕ is an additional field variable which describes the volume change and thus facilitates the representation of the incompressible deformation. The potential (2.36) represents a Lagrangian functional for minimising the potential energy under fulfilment of the equality constraint $h_{\mathrm{HW}} = J - \phi = 0$. The constraint is enforced by the Lagrange multiplier p which represents the pressure. In such a way, the determinant J of the deformation gradient is coupled to the

new field variable ϕ enforced by the third field variable p. The stationarity conditions of (2.36) follow as

$$\delta \Pi_{\mathrm{HW}\,\boldsymbol{u}} = \int_{\mathcal{B}_0} \frac{\partial \Psi^{\mathrm{iso}}}{\partial \boldsymbol{u}} \cdot \delta \boldsymbol{u} + p\, \delta J \,\mathrm{d}V \;-\; \delta \Pi_{\mathrm{ext}} = 0 \tag{2.37}$$

$$\delta \Pi_{\mathrm{HW}\,\phi} = \int_{\mathcal{B}_0} \left[\frac{\partial \Psi^{\mathrm{vol}}}{\partial \phi} - p \right] \delta \phi \,\mathrm{d}V = 0 \tag{2.38}$$

$$\delta \Pi_{\mathrm{HW}\,p} = \int_{\mathcal{B}_0} [J - \phi]\, \delta p \,\mathrm{d}V = 0 \tag{2.39}$$

It can be shown that (2.37) corresponds to the weak form $\mathcal{W}_{\boldsymbol{u}} = 0$ from (2.9) for the case of an isochoric-volumetric split, cf. [22]. Equation (2.38) defines a constitutive relation for the pressure and (2.39) kinematically defines the field ϕ. In the literature, variations of this approach are presented which make use of only two fields, i.e. $\boldsymbol{u}$-ϕ or $\boldsymbol{u}$-p formulations, see e.g. [90]. One such method is discussed in more detail in the context of PFEM in Section 4.1, namely the $\boldsymbol{u}$-ϕ formulation which features the advantage of not requiring an isochoric-volumetric split of the energy function. Furthermore, details regarding the application of the mixed formulation in low order triangular elements in PFEM are given therein.

2.3.2 Incorporation of contact constraints

The basic concepts of contact mechanics are summarised in the following based on [141], [76] and [97], starting with the contact constraints in normal direction of the contact surface and adding tangential constraints afterwards.

Normal contact

The basic constraint equation of contact mechanics is the impenetrability condition $g_{\mathrm{N}} \geq 0$, where g_{N} is the normal gap between two contacting bodies. Consequently, from

$$\min_{\boldsymbol{u}} \Pi(\boldsymbol{u}) \quad \text{subject to} \quad g_{\mathrm{N}} \geq 0 \tag{2.40}$$

follows a Lagrange formulation of the potential energy from (2.33) for normal contact as

$$\Pi_{\mathrm{cN}}(\boldsymbol{u}, \lambda_{\mathrm{N}}) = \Pi_{\mathrm{int}} - \Pi_{\mathrm{ext}} + \int_{\partial \mathcal{B}_0^{\mathrm{cN}}} \lambda_{\mathrm{N}}\, g_{\mathrm{N}} \,\mathrm{d}A \tag{2.41}$$

where the contact contribution only appears on the boundary which experiences active contact, denoted as $\partial \mathcal{B}_0^{\mathrm{cN}}$. In addition, the optimality conditions are

$$g_{\mathrm{N}} \geq 0\,, \quad \lambda_{\mathrm{N}} \leq 0, \quad \lambda_{\mathrm{N}}\, g_{\mathrm{N}} = 0 \tag{2.42}$$

commonly known as the Hertz-Signorini-Moreau conditions. The Lagrange multiplier λ_N can hereby be interpreted as normal contact traction which has to be negative in the case of contact and zero otherwise. The stationarity conditions follow as

$$\delta \Pi_{\mathrm{cN}\,\boldsymbol{u}} = \delta \Pi_\mathrm{int} - \delta \Pi_\mathrm{ext} + \int\limits_{\partial \mathcal{B}_0^\mathrm{cN}} \lambda_\mathrm{N}\, \delta g_\mathrm{N}\, \mathrm{d}A = 0 \tag{2.43}$$

$$\delta \Pi_{\mathrm{cN}\,\lambda_\mathrm{N}} = \int\limits_{\partial \mathcal{B}_0^\mathrm{cN}} g_\mathrm{N}\, \delta \lambda_\mathrm{N}\, \mathrm{d}A = 0 \tag{2.44}$$

where (2.43) equals the weak form of the balance of linear momentum (2.9) extended by a contact traction contribution on the contact surface. Furthermore, (2.44) is the constraint equation which has to hold for active contact. Direct solution of the system of equations for the variables $\boldsymbol{u}$ and λ_N is generally challenging, since a zero matrix appears in the Jacobian matrix from (2.44) being independent of λ_N. More importantly, the response of this contact formulation is immediate and infinitely stiff upon penetration of a discretised surface, such that the set of active contact elements as well as the solution of the system of equations is numerically difficult to solve. Consequently, numerous methods for the discretisation of contact as well as for variants of the formulation of the constraint equation have been suggested in the literature, see e.g. [76, 141].

Frictional contact

For frictional contact including a stick-slip formulation, the variational formulation is based on a friction law following the explanations in [76] and [97]. In this work, a Coulomb friction law is considered in form of a slip function Φ_S which reads

$$\Phi_\mathrm{S} = \|\boldsymbol{\lambda}_\mathrm{T}\| - \mu\, |\lambda_\mathrm{N}| \leq 0 \tag{2.45}$$

where μ is the Coulomb friction coefficient and where $\boldsymbol{\lambda}_\mathrm{T}$ is the tangential contact traction vector with $\| \bullet \| = \sqrt{\bullet \cdot \bullet}$. The minimisation problem follows as

$$\min_{\boldsymbol{u}} \Pi(\boldsymbol{u}) \quad \text{subject to} \quad g_\mathrm{N} \geq 0 \quad \text{and} \quad \Phi_\mathrm{S} \leq 0 \tag{2.46}$$

with a Lagrange formulation of the potential energy from (2.33) for normal and frictional contact as

$$\Pi_\mathrm{cNT}(\boldsymbol{u}, \lambda_\mathrm{N}, \boldsymbol{\lambda}_\mathrm{T}) = \Pi_\mathrm{int} - \Pi_\mathrm{ext} + \int\limits_{\partial \mathcal{B}_0^\mathrm{cN}} \lambda_\mathrm{N}\, g_\mathrm{N}\, \mathrm{d}A + \int\limits_{\partial \mathcal{B}_0^\mathrm{cT}} \boldsymbol{\lambda}_\mathrm{T} \cdot \boldsymbol{g}_\mathrm{T}\, \mathrm{d}A \tag{2.47}$$

Here, the tangential slip distance is measured with the tangential gap vector $\boldsymbol{g}_\mathrm{T}$. In a 2d setting, the scalar tangential traction λ_T and the tangential slip distance g_T are sufficient

for the formulation, such that the notation is simplified to the scalar quantities in the remainder of this work. The stationarity conditions follow as

$$\begin{aligned}\delta \Pi_{\mathrm{cNT}\,\boldsymbol{u}} = \delta \Pi_{\mathrm{int}} - \delta \Pi_{\mathrm{ext}} + \int\limits_{\partial \mathcal{B}_0^{\mathrm{cN}}} \lambda_{\mathrm{N}}\, \delta g_{\mathrm{N}}\, \mathrm{d}A \\ + \int\limits_{\partial \mathcal{B}_0^{\mathrm{cT}}} \lambda_{\mathrm{T}}\, \delta g_{\mathrm{T}}\, \mathrm{d}A + \int\limits_{\partial \mathcal{B}_0^{\mathrm{cS}}} \mathcal{T}\, \delta g_{\mathrm{T}}\, \mathrm{d}A = 0\end{aligned} \tag{2.48}$$

$$\delta \Pi_{\mathrm{cNT}\,\lambda_{\mathrm{N}}} = \int\limits_{\partial \mathcal{B}_0^{\mathrm{cN}}} g_{\mathrm{N}}\, \delta \lambda_{\mathrm{N}}\, \mathrm{d}A = 0 \tag{2.49}$$

$$\delta \Pi_{\mathrm{cNT}\,\lambda_{\mathrm{T}}} = \int\limits_{\partial \mathcal{B}_0^{\mathrm{cT}}} g_{\mathrm{T}}\, \delta \lambda_{\mathrm{T}}\, \mathrm{d}A = 0 \tag{2.50}$$

Hereby, the whole contact surface $\partial \mathcal{B}_0^{\mathrm{cN}}$ is subject to normal contact constraints, whereas the active stick domain $\partial \mathcal{B}_0^{\mathrm{cT}}$ and the slip domain $\partial \mathcal{B}_0^{\mathrm{cS}} = \partial \mathcal{B}_0^{\mathrm{cN}} \setminus \partial \mathcal{B}_0^{\mathrm{cT}}$ are complementary subsets depending on the state of the slip function. The optimality conditions for friction read

$$\Phi_{\mathrm{S}} \leq 0\,, \quad g_{\mathrm{T}} \geq 0\,, \quad \Phi_{\mathrm{S}}\, g_{\mathrm{T}} = 0 \tag{2.51}$$

such that in the sliding case, the tangential traction is defined as

$$\mathcal{T} = \mu\, |\lambda_{\mathrm{N}}|\, \mathrm{sign}\,(\lambda_{\mathrm{T}}) \tag{2.52}$$

2.4 PFEM – Particle Finite Element Method

{qtd. [119] In PFEM simulations, the cloud of points which represents the body under consideration is frequently remeshed and the shape of the boundary is redefined. In other remeshing schemes, the boundaries are preserved and the points are regenerated. Within the PFEM, the preservation of the points has the advantage of more straightforward state-variable transfer schemes. The redefinition of the boundary makes PFEM flexible for boundary changes, especially as the remeshing is usually performed for every time step to track possible shape changes. }qtd. [119]

2.4.1 Mesh regeneration and shape detection

{qtd. [119] The converged global displacement list of the last time step $\mathbf{u}_n$ defines the placements $\mathbf{X}_n = \mathbf{X} + \mathbf{u}_n$ of the new previous configuration, which is used for the mesh generation. The discretisation is performed by a Delaunay triangulation of the points, originally introduced by [43]. Figure 2.2a shows the triangulation, whereby the algorithm includes

the boundary polygon of the previous mesh, here by applying a Constrained Delaunay Triangulation (CDT). This prevents undesired mesh distortion in the surface region. The Delaunay triangulation discretises the convex hull of the body. To remove all elements outside the actual shape of the body, the α-shape method introduced by [46] is applied in a modified version, which has become standard in PFEM, see [27, 52]. Thereby, the α-shape detection is based on a preceding Delaunay triangulation which already enforces that each triangle circumcircle contains no further points. Testing the circumcircles for emptiness by verifying that they do not contain any other vertices, which was a component of the original α-shape method, is therefore obsolete. In summary, all elements

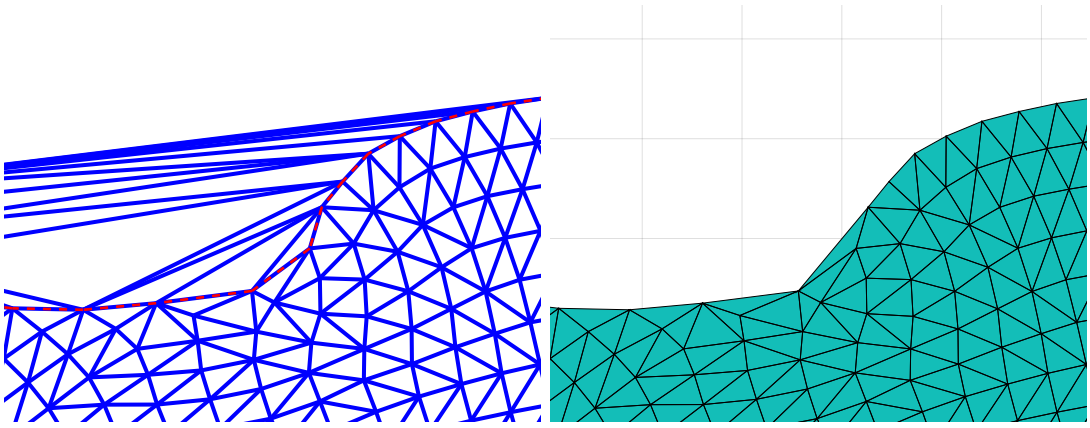

(a) Illustration of constrained Delaunay triangulation of the convex hull of a point cloud. Previous boundary polygon (dashed) has to be contained in the discretised region.

(b) Discretisation after applying the α-shape detection method with a point-density dependent test radius.

Figure 2.2: Constrained Delaunay triangulation and α-shape detection of the point cloud representing the body. Reprinted from [119], licensed under CC BY 4.0.

of the constrained Delaunay triangulation are subjected to the α-test

$$r_\alpha = \alpha\, l_{\text{char}} < r_{\text{circum}\,T} \quad \Rightarrow \quad \text{reject } T \tag{2.53}$$

i.e. when the test radius r_α fits into the circumcircle radius $r_{\text{circum}\,T}$ of a triangle T, the element is not considered to be part of the body. As test radius, a characteristic mesh size l_{char} is used and multiplied by the α value. For homogeneous mesh densities, a constant l_{char} can be used, e.g. $l_{\text{char}} = l_{\text{min}}$, the minimal particle distance in the cloud, see [114]. For inhomogeneous mesh-densities, [27] proposed a local characteristic length $l_{\text{char}}^{\text{loc}}$. The average point distance of the node-point p to its n_{nb} neighbour nodes is calculated in the previous mesh as

$$d_{\text{avg}}^{p} = \sum_{i=1}^{n_{\text{nb}}} \frac{\| \boldsymbol{X}_{n,i} - \boldsymbol{X}_{n,p} \|}{n_{\text{nb}}} \tag{2.54}$$

For each triangle in the new mesh, the average point-distances d^p_{avg} are further averaged over the three element nodes via

$$l^{\text{loc}}_{\text{char}} = \frac{1}{3}\sum_{p=1}^{3} d^p_{\text{avg}} \tag{2.55}$$

This value is used in the α-test (2.53) for the respective triangle. Thereby, it is important to use the previous mesh for the calculation of d^p_{avg}. The newly generated mesh may still contain potentially very large, distorted triangles as shown in Figure 2.2a, which are subsequently removed by the α-shape algorithm. Including these elements in the calculation of d^p_{avg} would artificially increase the averaged point distance, resulting in inaccuracies in the α-shape detection.

A resulting mesh after application of the α-shape method is shown in Figure 2.2b. All edges that appear only once in the connectivity define the boundary polygon which needs to be stored for the Constrained Delaunay Triangulation of the next remeshing. }$^{\text{qtd.}}_{[119]}$

2.4.2 Transfer of state-variables

$^{\text{qtd.}}_{[119]}${Two options are considered here for the transfer of the state variables – a direct copying of the variables from the closest quadrature point in the old mesh (CPM), see [65, 111], and an interpolation from three old quadrature points in a background triangle mesh (BTM) as also used in [147] and [65]. Both schemes only change the history data if the global position of a quadrature point changes. Where the previous and new quadrature points occupy the same spatial position, the copying operation does, in general, not alter an equilibrium state. Due to the very frequent remeshing within PFEM, the connectivities and quadrature point positions often undergo localised adjustments within small areas of the mesh. Hence these schemes prevent unnecessary smoothing which can be seen in the standard least-square mapping approach which has been used in early PFEM publications, e.g. [96, 114].

Closest point mapping (CPM) For the direct transfer of state-variables between meshes, a background triangulation connecting the old integration points is used. Triangulations simplify the search of a nearest neighbour. The method is illustrated in Figure 2.3a. Due to a simple copy, nonlinear properties of the mapped deformation gradient, such as the determinant, are preserved which is important for incompressible deformation states.

Background triangulation mapping (BTM) By analogy with the CPM, the BTM is constructed based on a background triangulation of the old integration points. In the BTM, interpolation from the three quadrature points of the enclosing background triangle is employed when the new quadrature point does not coincide with an existing old quadrature point, as illustrated in Figure 2.3b. Such algorithm preserves beneficial properties of the CPM, i.e. smoothing of variables is not activated in regions where the

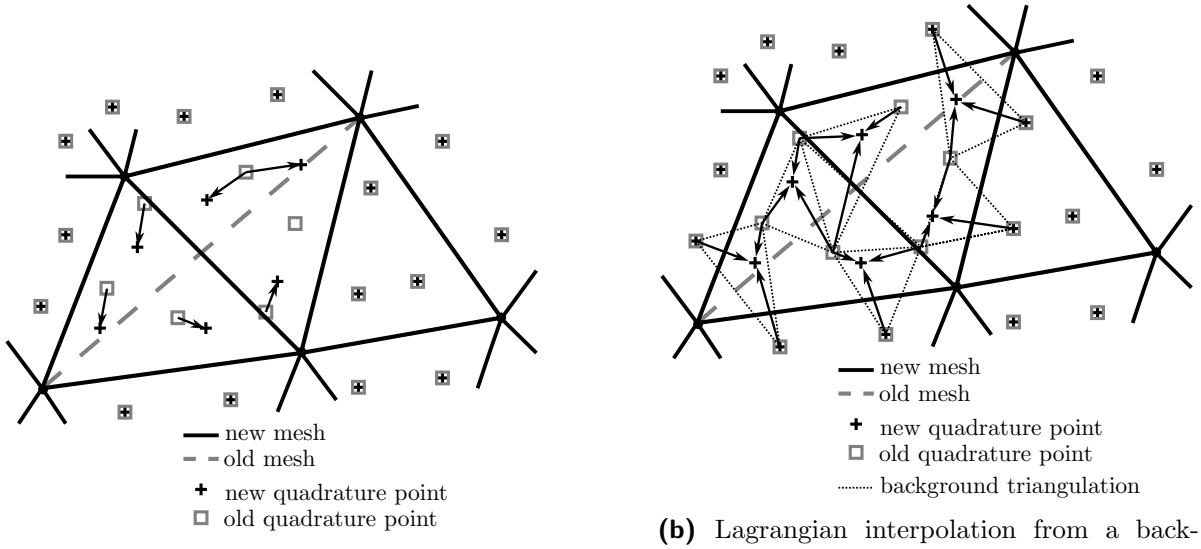

(a) Copy data of closest old quadrature point (CPM).

(b) Lagrangian interpolation from a background triangle of three old quadrature points (BTM).

Figure 2.3: Illustration of mapping methods for a typical edge-flip connectivity change when the mesh is reconstructed for the same point positions after deformation. Both considered elements, TRI6 and P1P1, need three quadrature points per element. Reprinted from [119], licensed under CC BY 4.0.

mesh does not change. In regions experiencing mesh changes, interpolation is intended to reduce transfer errors compared to the CPM, particularly for coarser discretisations.

The BTM coincides with the algorithm denoted arbitrary Lagrangian interpolation in [65], whereas the denomination BTM refers to the use of a background triangulation, here a Delaunay triangulation. In [147] a slightly different version, also suggested in [65], is applied in PFEM, where the data is mapped from the quadrature points of one unique old element. This element contains the new quadrature point. This motivates the denomination of the algorithm as unique element method. In this work only the interpolation from the three quadrature points of the background triangle, independent of the corresponding old element, is considered.

The interpolation is based on linear shape functions N^A, where

$$\mathbf{s}_q = \sum_{A=1}^{3} \mathbf{s}_A \, N^A(\boldsymbol{\xi}_q) \tag{2.56}$$

interpolates background-point state-variables $\mathbf{s}_A$ to new quadrature point state-variables $\mathbf{s}_q$. Here, the points of the background mesh A are the old quadrature points. The new quadrature point q therefore lies within this triangle. For the interpolation (2.56) the natural coordinates $\boldsymbol{\xi}_q$ are calculated from rearranging

$$\boldsymbol{X}_{n,q} = \sum_{A=1}^{3} \boldsymbol{X}_{n,A} \, N^A(\boldsymbol{\xi}_q) \tag{2.57}$$

Since all physical coordinates of old quadrature points $\boldsymbol{X}_{n,A}$ and of the new quadrature point $\boldsymbol{X}_{n,q}$ are known, the solution for $\boldsymbol{\xi}_q$ can be derived analytically for specific shape functions. At the boundary of the body, the background triangulation may contain rather distorted triangles, which leads to poor interpolation weights. Furthermore, a new quadrature point can lie outside of any background triangle. In both cases, the data of the closest old quadrature point is copied instead of using an interpolation. As a quality threshold for the background triangles, the radius ratio

$$\frac{r_{\text{in}\,T}}{r_{\text{circum}\,T}} < 0.005 \tag{2.58}$$

of insphere radius $r_{\text{in}\,T}$ to circumsphere radius $r_{\text{circum}\,T}$ is used, as introduced by [29], see also [70] for further information on element quality measures. The algorithmic treatment of the BTM is further illustrated in Figure 2.4 for a linear triangular mesh along with the respective interpolation weights.

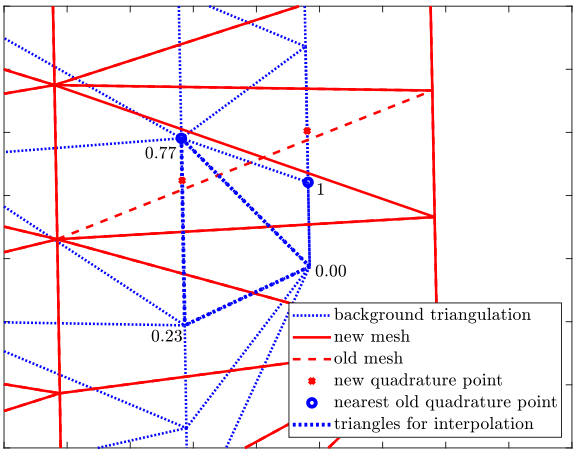

Figure 2.4: Illustration of BTM for linear triangles with one quadrature point. Left new quadrature point receives interpolated values with weights from shape functions. Right new quadrature point receives data from closest quadrature point since background triangle is too distorted at the boundary. For coinciding quadrature points, the data is copied without smoothing. Reprinted from [119], licensed under CC BY 4.0.

The interpolation of variables from nearby points is a linear averaging operation. Nonlinear operations, such as the determinant, are in general not preserved by these interpolations. This aspect is critical for almost incompressible deformation states. An algorithm introduced by [25] uses the logarithm of the polar decomposition $\boldsymbol{F} = \boldsymbol{R} \cdot \boldsymbol{U}$ to preserve isochoric deformation states. The basic idea is to formulate $\det(\boldsymbol{F})$ in eigenstretches $\lambda_{1,2,3}$, i.e.

$$\det(\boldsymbol{F}) = \det(\boldsymbol{R} \cdot \boldsymbol{U}) = \det(\boldsymbol{R})\ \det(\boldsymbol{U}) = \prod_{i=1}^{3} \lambda_i \tag{2.59}$$

and, thereafter, application of the logarithm operation. The determinant then transforms to the sum of eigenstretches, namely

$$\log(\det(\boldsymbol{F})) = \log\left(\prod_{i=1}^{3}\lambda_i\right) = \sum_{i=1}^{3}\log(\lambda_i) = \mathrm{tr}(\log(\boldsymbol{U})) \tag{2.60}$$

The resulting sum is a linear operator which is preserved within the linear interpolation. }$^{\text{qtd.}}_{[119]}$ In the case of path dependent material behaviour, additional tensorial state-variables need to be mapped. The following mapping steps are exemplary for $\boldsymbol{F}$ as unsymmetric deformation gradient and $\boldsymbol{C}^{\text{iso}}_{\text{mel,v}}$ as a symmetric state-variable of the viscous deformation in a melt phase considered in Chapter 5.

- $^{\text{qtd.}}_{[120]}${Calculate the global coordinates of the quadrature points in the previous mesh and create a background Delaunay triangulation of these points.
- Loop the elements in the new mesh and calculate the new global quadrature point positions.
- Search for the nearest neighbour[2] to detect whether a previous quadrature point coincides with the new one and copy the state variable data in that case.
- If no previous point coincides, search for the background triangle containing the new point for interpolation. For special cases (bad aspect ratios of the background triangles, no containing triangle found near the surface) resort to copying the data from the closest old quadrature point.
- Calculate the logarithm of the polar decomposition of $\boldsymbol{F}$, i.e. $\log(\boldsymbol{R})$ and $\log(\boldsymbol{U})$, as well as the logarithm of the stretch tensor $\log\left(\boldsymbol{C}^{\text{iso}}_{\text{mel,v}}\right)$ from the symmetric and rotation-free $\boldsymbol{C}^{\text{iso}}_{\text{mel,v}} = \boldsymbol{U}^{\text{iso}}_{\text{mel,v}} \cdot \boldsymbol{U}^{\text{iso}}_{\text{mel,v}}$.
- Interpolate the decomposed tensors using standard shape functions and the natural coordinates of the new quadrature points.
- Recover $\boldsymbol{F} = \boldsymbol{R} \cdot \boldsymbol{U}$ from the interpolated $\log(\boldsymbol{R})$ and $\log(\boldsymbol{U})$, as well as $\boldsymbol{C}^{\text{iso}}_{\text{mel,v}}$ from the interpolated $\log\left(\boldsymbol{C}^{\text{iso}}_{\text{mel,v}}\right)$.}$^{\text{qtd.}}_{[120]}$

2.4.3 Mesh adaptivity

$^{\text{qtd.}}_{[120]}${Although the PFEM regenerates the connectivities in each time step, the point distribution in a large deformation problem can become unbalanced which leads to very large and highly distorted elements as well as to point accumulation. Therefore, a simple

[2] The present implementation is based on the MATLAB function `delaunayTriangulation()` which provides nearest neighbour and containing triangle searches similar to other open sources mesh generation libraries.

geometry based point insertion scheme is adapted from [111]. A more advanced scheme has recently been presented by [78]. However, the implementation requires considerable effort and control over the Delaunay algorithm, since the interpolation of the node data cannot be done on an element-by-element basis. This is because the insertion of a single point also changes the connectivity of neighbouring elements, requiring edge swaps to restore the Delaunay property before a next point can be inserted. Based on these considerations, a simpler elementwise approach is used in this work.

Point insertion is performed in the centre of the triangle T if the circumsphere radius r_{cT} exceeds a global threshold value $r_{\mathrm{c}}^{\max}$, i.e.

$$r_{cT} > r_{\mathrm{c}}^{\max} \implies \begin{cases} \text{insert point in element centre} & \texttt{if} \quad T \text{ is inside} \\ \text{insert point on longest bound. edge} & \texttt{else} \end{cases} \tag{2.61}$$

The size threshold is chosen from the circumcircle radius of an equilateral triangle featuring the edge length of the characteristic seed size l_{seed} of the initial point cloud, multiplied by a heuristic factor a, i.e. $r_{\mathrm{c}}^{\max} = a\, l_{\mathrm{seed}}/\sqrt{3}$, where the quotient $\sqrt{3}$ stems from the radius calculation of an equilateral triangle. The factor $a = 2$ has proven to provide good results for the point insertion. This criterion is applied to the previous triangulation which is already α-shaped from the last time step, using the updated placements $\mathbf{X}_n$. Furthermore, a distinction is made with respect to elements containing boundary nodes. Only elements with maximum one boundary node are treated with point insertion in the element centre. Otherwise the point distribution quality close to the boundary deteriorates. When the considered element contains one or two boundary edges, a point is inserted on the middle of the longest boundary edges. The point on the boundary edge is not inserted if the edge-length is smaller than the threshold for the point-removal scheme. In that regard, the minimum edge-length criterion has priority over the point insertion scheme on boundaries[3]. The detailed insertion algorithm is presented in Algorithm 1 along with the subsequently described point removal scheme. At first glance this criterion seems to be in conflict with the α-test (2.53). However, the α-test is based on a local mesh-density measure in order to detect changes in the shape of the bodies, whereas the point insertion scheme is based on a global threshold value to restrict the maximum size of the elements.

Point removal is similarly based on a geometrical criterion, i.e. a minimum edge length as proposed by [111], whereas the exact point removal strategy is adopted from [78]. The edge length l_{ed} of each edge in the mesh connectivity is checked against a global minimum edge length $l_{\mathrm{ed}}^{\min}$ according to

$$l_{\mathrm{ed}} < l_{\mathrm{ed}}^{\min} \implies \begin{cases} \text{remove inside point of edge} & \texttt{if} \quad \text{edge has one bound. node} \\ \text{collapse edge to midpoint} & \texttt{else} \end{cases} \tag{2.62}$$

[3]To stop points being removed from the same edge in the next step, choose $l_{\mathrm{ed}} > 2\, l_{\mathrm{ed}}^{\min}$ as stricter exclusion criterion e.g. on contact surfaces

whereby, as adopted from [78], collapsing means the insertion of a point in the centre of the edge and removal of both end points. This usually yields better mesh quality and is easier to implement than a decision criterion on which point has to be removed. The threshold value is chosen as $l_{\mathrm{ed}}^{\mathrm{min}} = b\, l_{\mathrm{seed}}$ where $b = 0.4$ is a reasonable heuristic value. Since the edge collapsing scheme inserts a point in the middle of the edge in exchange for deleting the end points, unwanted side-effects can occur if several adjacent edges are collapsed. This happens when the mesh is locally well shaped but finer than the specified edge length tolerance. In this case, several adjacent edges are collapsed at the same time, resulting in even shorter edges that are again targeted by the criterion. In order to terminate the algorithm, [78] propose a criterion based on a minimum circumradius. This is realised in the current work by checking the termination criterion

$$r_{\mathrm{c}}^{\mathrm{adj}} < r_{\mathrm{c}}^{\mathrm{min}} \quad \forall \text{ adjacent elements} \quad \Longrightarrow \quad \text{do not collapse the edge} \tag{2.63}$$

i.e. the circumradii $r_{\mathrm{c}}^{\mathrm{adj}}$ of all triangles adjacent to the edge should not be smaller than a threshold value $r_{\mathrm{c}}^{\mathrm{min}}$. This simple check makes it unlikely that the neighbouring edges are also collapsed without actually checking their lengths individually. Once more, the threshold radius is derived from the circumradius of an equilateral triangle featuring a fraction of the seed size as edge length, i.e. $r_{\mathrm{c}}^{\mathrm{min}} = c\, l_{\mathrm{seed}}/\sqrt{3}$ where $c = 0.7$ yielded good results in the examples investigated as this work proceeds. Algorithm 1 summarises the detailed algorithm along with the treatment of Dirichlet boundary conditions. In a procedural programming style, removal of nodes makes an adaptation of the node numbers from boundary conditions necessary and, moreover, boundary conditions need to be transferred for point insertion on boundary edges. Here, only Dirichlet boundary conditions are considered since the transfer of nodal Neumann boundary conditions is not straightforward. $\}_{[120]}^{\mathrm{qtd.}}$ If surface flux conditions are needed, a surface element is recommended.

For the application of the point insertion and removal for contact problems with material separation and crack formation, special treatment of boundary information and additional data checks are necessary which are explained in Section 4.3.1.

Algorithm 1: Point insertion and removal in PFEM remeshing.
Reprinted from [120], licensed under CC BY 4.0.

Input : Global arrays: points $\mathbf{X}$, displacements $\mathbf{u}_n$, velocities $\dot{\mathbf{u}}_n$, point-densities $\mathbf{d}^p_{\text{avg}}$, temperatures $\boldsymbol{\theta}$, furthermore element connectivity conn, boundary info boundinfo, edgelist edges, boundary conditions drlt, parameter l_{seed}

Output : Updated global arrays $\mathbf{X}$, $\mathbf{u}_n$, $\dot{\mathbf{u}}_n$, $\mathbf{d}^p_{\text{avg}}$, $\boldsymbol{\theta}$, drlt

Initialise parameters: $r_{\text{c}}^{\max} \leftarrow 2\,l_{\text{seed}}/\sqrt{3}$, $\quad l_{\text{ed}}^{\min} \leftarrow 0.4\,l_{\text{seed}}$, $\quad r_{\text{c}}^{\min} \leftarrow 0.4\,l_{\text{seed}}/\sqrt{3}$;

Point insertion: for *each element e in* conn **do**
- Calculate circumradius r_{cT} of triangle T;
- **if** $r_{cT} > r_{\text{c}}^{\max}$ **then**
  - **if** *at most one point is a boundary point* **then**
    - Insert new point at element centre;
  - **else**
    - Check minimal edge-length criterion[3];
    - **if** $l_{\text{ed}} > l_{\text{ed}}^{\min}$ **then**
      - Insert new point at centre of longest boundary edge;
      - Store edge for Dirichlet recovery;
  - Interpolate $\mathbf{X}$, $\mathbf{u}_n$, $\dot{\mathbf{u}}_n$, $\mathbf{d}^p_{\text{avg}}$, $\boldsymbol{\theta}$ to the new point;

Point removal: for *each edge in* edges **do**
- Calculate edge length l_{ed} and circumradius of adjacent triangles $r_{\text{c}}^{\text{adj}}$;
- **if** $l_{\text{ed}} < l_{\text{ed}}^{\min}$ **and** *termination criterion* $r_{\text{c}}^{\text{adj}} > r_{\text{c}}^{\min}$ **then**
  - **if** *edge has only one node on the boundary* **then**
    - Remove the inside node of the edge;
  - **else**
    - Insert a point in the middle of the edge;
    - Remove both end points of the edge;
    - Store edge for Dirichlet recovery;
    - Interpolate $\mathbf{X}$, $\mathbf{u}_n$, $\dot{\mathbf{u}}_n$, $\mathbf{d}^p_{\text{avg}}$, $\boldsymbol{\theta}$ to the new point;

Update mesh and data arrays;

Recovery of Dirichlet boundary conditions:

Loop all stored edges: transfer Dirichlet conditions on inserted point;

Loop new node list: transfer Dirichlet conditions from identical coordinates in old mesh;

3 Modelling and simulation of wear

The frictional interaction of solid bodies such as forming tools and workpiece surfaces leads to wear that accumulates on the tool surfaces, resulting in a loss of geometric accuracy and thus limiting tool life. In Section 1.1 this topic is introduced in the context of wear of microstructured tool surfaces. In this chapter, a wear post-processor is presented which adapts the surface geometry of the tool microstructure after a runover simulation. It also focuses on the homogenisation of the frictional surfaces by considering a microstructured surface in a representative surface cut-out using periodic boundary conditions. In this way, the wear behaviour of this surface structure can be analysed and the effective frictional properties of the microstructured surface can be deduced. In addition, the evolution of the effective frictional properties during the evolution of wear can be investigated.

Apart from minor adaptations, this chapter is a textual reproduction of the journal article Schewe et al. [118], with directly quoted passages marked in each numbered subsection using $\overset{\text{qtd.}}{_{[118]}}\{$to $\}^{\text{qtd.}}_{[118]}$.

3.1 Continuum mechanical formulation of the Archard wear model

$\overset{\text{qtd.}}{_{[118]}}\{$Due to wear, the geometry of the considered bodies is updated. As wear evolves rather slowly after several loading cycles, two timescales are defined following [77]: slow timescale t describes wear over time, fast timescale τ describes one deformation problem. In the deformation problem two bodies $\mathcal{B}^i$, i=1, 2 are considered with reference configuration $\mathcal{B}^i_0(t, \tau{=}\tau_0)$ and current configuration $\mathcal{B}^i_\tau(t, \tau{>}\tau_0)$. The deformation mapping $\boldsymbol{\varphi}$ is introduced as

$$\boldsymbol{x}^i = \boldsymbol{\varphi}^i_t(\boldsymbol{X}^i, \tau)\,, \qquad t \in [0, T]\,,\ \tau \in [t, t + \Delta\tau] \tag{3.1}$$

as well as the deformation gradient $\boldsymbol{F}^i = \nabla_{\boldsymbol{X}} \boldsymbol{\varphi}^i_t$ with $\boldsymbol{X}^i \in \mathcal{B}^i_0$ and $\boldsymbol{x}^i \in \mathcal{B}^i_\tau$. The final time of wear evolution is denoted by T and the duration of one deformation problem by

$\Delta\tau$. After reaching $t + \Delta\tau$, wear is evaluated and applied to update the geometry and to obtain a new reference configuration, i.e.

$$\boldsymbol{X}^i_{t+\Delta\tau} = \boldsymbol{X}^i_t - V^i_W \, \boldsymbol{N}^i \,, \quad \text{on } \partial\mathcal{B}^i_0 \tag{3.2}$$

with the wear volume per unit referential surface area V^i_w and the referential outward surface normal vector $\boldsymbol{N}^i$. To account for the slow nature of wear, a speedup- or upscaling-factor M is usually applied so that

$$\boldsymbol{X}^i_{n+1} = \boldsymbol{X}^i_n - M \, V^i_W \, \boldsymbol{N}^i \quad \text{on } \partial\mathcal{B}^i_0 \tag{3.3}$$

and only at certain points in time $t_{n+1} = t_n + \Delta t$ the deformation problem is solved. In the case of path-dependent material behaviour a choice of $M > 1$ introduces additional modelling errors. According to the Archard wear model [2], worn volume v_W is proportional to the normal pressure load p and to the sliding distance s, i.e.

$$v_W \propto p \, s \,. \tag{3.4}$$

If Coulomb friction is assumed, the relation can be reformulated in terms of tangential surface tractions t_T

$$v_W \propto \frac{1}{\mu} \, t_T \, s \,. \tag{3.5}$$

More recently, the Archard wear model has been formulated based on the dissipation rate density $\dot{D}$, i.e. the rate density of the dissipated work through friction, e.g. [53], [104], [77], i.e.

$$\dot{v}^i_{W(\dot{D})} = k^i \, \boldsymbol{t}^*_T \cdot \dot{\boldsymbol{\varphi}}^*_T \tag{3.6}$$

where $\boldsymbol{t}^*_T$ is the tangential contact traction and where $\dot{\boldsymbol{\varphi}}^*_T$ is the relative tangential velocity of both bodies. The material time derivative is defined as $\dot{\bullet} = \partial \bullet (\boldsymbol{X}, \tau)/\partial\tau$. Following Cauchy's theorem, the spatial contact tractions are based on Cauchy stresses $\boldsymbol{\sigma}$ via

$$\boldsymbol{t}^* = \boldsymbol{\sigma} \cdot \boldsymbol{n} \,, \quad \boldsymbol{t}^*_N = [\boldsymbol{t}^* \cdot \boldsymbol{n}] \, \boldsymbol{n} = t^*_N \, \boldsymbol{n} \,, \quad \boldsymbol{t}^*_T = \boldsymbol{t}^* - \boldsymbol{t}^*_N \,, \tag{3.7}$$

where $t^*_N = p$, and $\boldsymbol{n}$ denotes the spatial outward surface normal vector. Equation (3.6) describes the rate of worn volume per unit spatial area with Archard proportionality parameter k^i of body i. Clearly, the time integral of this formulation is equivalent to the classic approach assuming Coulomb friction (3.5) if k^i and $\boldsymbol{t}^*_T$ are constant. Formulating (3.4) as rate equation for non-stationary processes yields

$$\dot{v}^i_{W(p)} = \widetilde{k}^i \, t^*_N \, \|\dot{\boldsymbol{\varphi}}^*_T\| \tag{3.8}$$

where $\widetilde{k}^i = k^i \, \mu$ is the relation of the wear coefficients if Coulomb's law holds true. If alternative friction models are used, which are e.g. non-linear in the normal pressures, the

dissipation-based formulation (3.6) is well motivated. Ramalho and Miranda [104] show that the energy based approach delivers good results by using a constant energy-based Archard parameter k^i. If μ is not constant, or if Coulomb's law is not applicable, the assumption of a constant original Archard coefficient $\widetilde{k}^i$ is not reasonable. However, considering wear of microstructured surfaces, Archard law based on pressures may deliver different wear patterns and is considered as an alternative model.

The geometry update (3.3) is performed in the reference space where $\boldsymbol{N}^i$ is constant, whereas each point in time comprises a deformation dependent $\boldsymbol{n}^i$. Similar to [77], the pull back of $\dot{v}_W^i$ is applied by using the area transformation j^i. Area and volume transformations are given by

$$j^i = \mathrm{d}a^i/\mathrm{d}A^i = \boldsymbol{n}^i \cdot \mathrm{cof}(\boldsymbol{F}^i) \cdot \boldsymbol{N}^i \,, \qquad J^i = \mathrm{d}v^i/\mathrm{d}V^i = \det(\boldsymbol{F}^i) \,. \tag{3.9}$$

Referential and spatial wear coefficients transform via the volume transformation $k^i = J^i\, K^i$ and $\widetilde{k}^i = J^i\, \widetilde{K}^i$, where the referential coefficients are assumed to be constant, cf. [77] or [127]. This yields

$$\dot{V}^i_{W(\dot{D})} = K^i\, j^i\, \boldsymbol{t}^*_T \cdot \dot{\boldsymbol{\varphi}}^*_T \,, \qquad \dot{V}^i_{W(p)} = \widetilde{K}^i\, j^i\, t^*_N\, \|\dot{\boldsymbol{\varphi}}^*_T\| \,. \tag{3.10}$$

Applying time integration, the worn volume per referential unit area finally results in

$$V^i_{W(\dot{D})} = \int_t^{t+\Delta\tau} \dot{V}^i_{W(\dot{D})}\, \mathrm{d}\tau \,, \qquad V^i_{W(p)} = \int_t^{t+\Delta\tau} \dot{V}^i_{W(p)}\, \mathrm{d}\tau \,. \tag{3.11}$$

Since these worn volumes are measured per unit referential area, they represent wear depths d_W. This can be seen in (3.3). A purely mechanical boundary value problem is considered, whereas the local form of the balance of linear momentum in the spatial configuration reads

$$\nabla_{\boldsymbol{x}} \cdot \boldsymbol{\sigma} = \boldsymbol{0} \quad \text{in} \quad \mathcal{B}^i_\tau \,, \tag{3.12}$$

neglecting body and inertia forces. Boundary conditions are prescribed as

$$\boldsymbol{u}^i = \bar{\boldsymbol{u}}^i \quad \text{on} \quad \partial\mathcal{B}^{i,\boldsymbol{u}}_\tau \,, \quad \boldsymbol{t}^i = \bar{\boldsymbol{t}}^i \quad \text{on} \quad \partial\mathcal{B}^{i,\boldsymbol{t}}_\tau \,, \tag{3.13}$$

with $\boldsymbol{u}^i = \boldsymbol{x}^i - \boldsymbol{X}^i$. Furthermore, contact conditions are enforced on the contact surfaces, hence contact tractions $\boldsymbol{t}^*$ arise which enter the aforementioned wear equations. Details on the Finite-Element formulation as well as the contact problem are not carried out here, since the commercial software Abaqus is used for this purpose. For details, refer to the manual [39] or the monographs of Bonet and Wood [22], Wriggers [140] and Wriggers [141] }$^{\text{qtd.}}_{[118]}$ or the Section 2.2.

3.2 Spatial homogenisation of friction

qtd. [118]{To study the friction and wear of microstructured tool surfaces, a contact homogenisation procedure is applied, as proposed in De Lorenzis and Wriggers [41] for the two-dimensional case. Figure 3.1 shows the experimental setup of a wear experiment carried out in a collaborative work, see [13]. In this experiment several plateaus with different microstructures are placed on a forming tool. Each plateau represents the tip of a tooth forming tool as shown in Figure 1.1. These plateaus are pressed into sheet material to investigate wear of the surface structures.

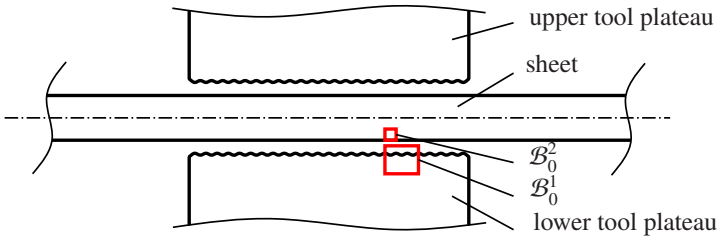

Figure 3.1: Setup of wear experiment with microstructured tools. Representative friction problem (red boxes) with tool cut-out $\mathcal{B}_0^1$ and sheet cut-out $\mathcal{B}_0^2$. Reprinted from [118], licensed under CC BY 4.0.

To study the microstructured surfaces with repetitive deterministic patterns of approximately 200-400 μm width and 20-30 μm depth, only a representative surface cut-out is considered. According to [41] sample dimensions are chosen dependent on the length of one period λ of the microstructure in sliding direction x: sample length $\Delta x = 3\,\lambda$, width $\Delta z = \lambda_{\text{lat}}$ and height $\Delta y = 0.75\,\lambda$. Here, λ_{lat} is the lateral length of one period, since most three-dimensional periodic surface structures have different periodic lengths in both directions depending on the orientation of the cut-out. The counterbody, i.e. a cut-out of sheet material, measures $\lambda \times \lambda_{\text{lat}} \times 0.75\,\lambda$ and hence covers one period of the microstructured surface in both directions. Figure 3.2 shows the loads and measurements for an exemplary boundary value problem of an angular cut-out from a sinusoidal surface structure.

Periodic boundary conditions are applied to represent the ambient material. Figure 3.3 shows the sheet cut-out $\mathcal{B}_0^2$ with its surfaces. The top surface $\partial\mathcal{B}_0^{2t}$ is coupled in y-direction using a multipoint constraint on the master node N_M. On this node, the total force $\boldsymbol{F}_{\text{ext}}$ is applied. It is assumed that deeper areas of the sheet material do not contribute to the friction and deformation behaviour of the surface region. The contact surface $\partial\mathcal{B}_0^{2c}$ is free and used in the contact definition. The two surfaces in sliding direction on the left side $\partial\mathcal{B}_0^{2l}$ and on the right $\partial\mathcal{B}_0^{2r}$ are coupled with periodic boundary conditions as well as are the two lateral surfaces on the front $\partial\mathcal{B}_0^{2f}$ and on the back $\partial\mathcal{B}_0^{2b}$. The periodic boundary conditions read

$$\begin{aligned} \boldsymbol{u}^l = \boldsymbol{u}^r, \quad \boldsymbol{t}^l = -\,\boldsymbol{t}^r \quad \text{on} \quad \partial\mathcal{B}_\tau^{2l} \cup \partial\mathcal{B}_\tau^{2r}\,, \\ \boldsymbol{u}^f = \boldsymbol{u}^b, \quad \boldsymbol{t}^f = -\,\boldsymbol{t}^b \quad \text{on} \quad \partial\mathcal{B}_\tau^{2f} \cup \partial\mathcal{B}_\tau^{2b}\,, \end{aligned} \tag{3.14}$$

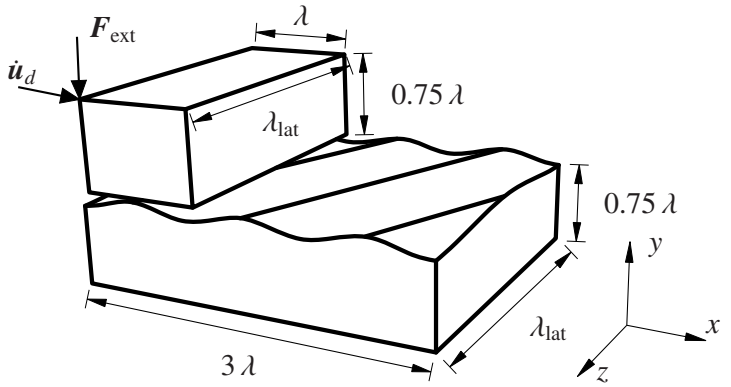

Figure 3.2: Boundary value problem of three-dimensional surface cut-out with dragging velocity $\dot{\boldsymbol{u}}_d$ and pressure force $\boldsymbol{F}_{\text{ext}} = \lambda\,\lambda_{\text{lat}}\,\boldsymbol{t}_{\text{ext}}$ applied on sheet cut-out using a multi-point constraint. Periodic boundary conditions detailed in Figure 3.3 and Eq. (3.14) and (3.15). Reprinted from [118], licensed under CC BY 4.0.

which enforce periodicity in placements $\boldsymbol{x}$ or displacements $\boldsymbol{u}$ respectively, and antiperiodicity in the tractions $\boldsymbol{t}$, cf. [41].

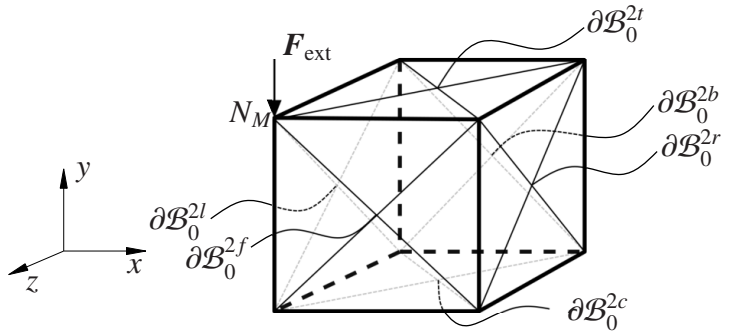

Figure 3.3: Sheet-cut-out with periodic boundary conditions coupling $\partial\mathcal{B}_0^{2l}$ with $\partial\mathcal{B}_0^{2r}$ as well as $\partial\mathcal{B}_0^{2f}$ with $\partial\mathcal{B}_0^{2b}$. Multipoint constraints applied to $\partial\mathcal{B}_0^{2t}$ to couple all surface nodes to the masternode N_M on which the force $\boldsymbol{F}_{\text{ext}}$ is applied. Contact conditions on $\partial\mathcal{B}_0^{2c}$. Reprinted from [118], licensed under CC BY 4.0.

Identical periodic boundary conditions mirrored at the $x-z$ plane can be applied on the tool cut-out $\mathcal{B}_0^1$. However, technically the meshes and therefore the application of periodic boundary conditions on tools with a resolved microstructure are much more complex. Furthermore, the tool experiences much smaller deformations than the elastoplastic sheet material. On the tool

$$\begin{aligned} u_z = 0 \quad &\text{on} \quad \partial\mathcal{B}_\tau^{1f}, \quad u_z = 0 \quad \text{on} \quad \partial\mathcal{B}_\tau^{1b}, \\ u_x = 0 \quad &\text{on} \quad \partial\mathcal{B}_\tau^{1l}, \quad u_x = 0 \quad \text{on} \quad \partial\mathcal{B}_\tau^{1b} \end{aligned} \tag{3.15}$$

is therefore prescribed. For inclined cut-outs, such as the one shown in Figure 3.2, lateral sliding occurs. This causes the workpiece to slide over the edge of the tool. Since this

leads to divergence in the contact simulation, an adjustment of the tool width is necessary. The applied contact discretisation mentioned in Section 3.3 does not take into account the periodicity. Due to these adaptions, the periodicity is only exactly enforced on the workpiece where large deformations occur.

Frictional characterisation of surfaces The homogenisation of contact friction enables the resolving of asperities or structured surfaces. However, in process simulations these effects cannot be incorporated via a geometrical resolution of these features. De Lorenzis and Wriggers [41] therefore use an effective friction coefficient calculated in the microscale simulation. Using Hill's meso-macro work equality, local frictional tractions and sliding velocities can be averaged to obtain the macroscopic quantities and vice versa, i.e.

$$\langle \boldsymbol{t} \rangle \cdot \langle \dot{\boldsymbol{\varphi}} \rangle = \langle \boldsymbol{t} \cdot \dot{\boldsymbol{\varphi}} \rangle \quad \text{on} \quad \partial \mathcal{B}_\tau^{ic} \,, \tag{3.16}$$

where $\langle \bullet \rangle$ is the average operator

$$\langle \bullet \rangle^i = \frac{1}{a^i} \int\limits_{\partial \mathcal{B}_\tau^{ic}} (\bullet) \, \mathrm{d}a \,, \tag{3.17}$$

with a^i being the total spatial surface area of $\partial \mathcal{B}_\tau^{ic}$. With this at hand, time averaging of summed up reaction forces F_T and F_N on the tool's fixed surfaces can be used to represent macroscopic effective friction coefficients via

$$\bar{\mu} = \frac{1}{\Delta\tau} \int\limits_{t}^{t+\Delta\tau} \frac{F_T}{F_N} \, \mathrm{d}\tau \,. \tag{3.18}$$

A multiscale approach with local evaluation of the micro problem and usage of effective quantities in the macro simulation is not the focus of this work. Such a scheme, however, can be found in [131] and [128]. }$^{\text{qtd.}}_{[118]}$

3.3 Simulation framework of the wear postprocessor

$^{\text{qtd.}}_{[118]}${The wear simulation is carried out in a Python-framework which invokes Abaqus Standard [39] as Finite-Element-solver, TetGen 1.5.1 [121] as remeshing library for tetrahedral meshes and the developed wear postprocessor. The following section presents the simulation model as well as the flowchart of the simulation framework.

A crucial component of the simulation of friction and wear is the modelling of contact for large displacements and large sliding distances. Here, the surface to surface contact definition with finite sliding of Abaqus Standard is used which allows for controlling penetration on both the master and the slave surface. Furthermore, this formulation introduces some smoothing of the contact discretisation. This is beneficial for a discretised

geometry with a microstructured surface, where sharp feature edges occur. The contact enforcement is carried out with an Augmented Lagrangian approach which exactly fulfils the constraints while introducing numerical robustness compared to classic Lagrange multiplier methods. For details of the contact algorithms please refer to the Abaqus manual [39] and the monograph [141].

The periodic boundary conditions (3.14) are enforced by using node-pairs which have to lie exactly opposite to each other on the respective surfaces. Conditions are set up by using the Abaqus equation-utility for each degree of freedom of each node pair, cf. [39]. The external force and dragging velocity depicted in Figure 3.2 are applied successively: at first, the contact is closed with a small vertical displacement of the workpiece. On the closed contact, the force $\boldsymbol{F}_{\text{ext}}$ is applied and in a third step, the sheet cut-out is dragged over the surface with a constant dragging velocity $\dot{\boldsymbol{u}}_d$.

Constitutive relations The microstructure represents the surface topology on a meso-scale, where the manufactured features are resolved but smaller scale asperities are not. To account for the frictional behaviour on smaller scales, two friction laws are considered: for frictional characterisation of microstructured surfaces, a pure Coulomb friction model is used. This allows direct correlations of local friction coefficients and effective friction coefficients evaluated via (3.18). For the application in metal forming, a linear relation of pressures and frictional tractions overestimates the surface resistance. In literature on forming technologies a state-of-the-art approach is to limit the frictional stresses with the shear yield strength k_f, see e.g. [12], [141] and [45]. The different models are summarised below. Coulomb's law reads

$$t_T^* = \mu\, t_N^* \,, \tag{3.19}$$

a constant shear friction model uses

$$t_T^* = m\, k_f \tag{3.20}$$

with friction factor m, and a combined friction model results in

$$t_T^* = \min\left[\mu\, t_N^*,\, m\, k_f\right] \,. \tag{3.21}$$

Several other friction models have been introduced in the literature, amongst them a smoothed version of (3.21) known as the Shaw-law, see [141] or [45]. The combined model accounts for appropriate pressure dependency in the low pressure regime as well as for a limit due to the material flow in the high pressure regime. In Abaqus this model is available as an additional shear stress limit when defining a Coulomb friction law, [39]. The shear yield strength k_f can be calculated from the uniaxial yield strength depending on the choice of a yield surface. Assuming a von Mises type yield surface, the equivalent stress of a pure shear load k_f is $\sigma_{\text{vM}} = \sqrt{3}\, k_f$. Therefore, the shear yield strength is related to the initial yield limit via $k_f = \sigma_{\text{vM}}^{y0}/\sqrt{3}$.

Similar to $\bar{\mu}$ in (3.18) an effective friction factor $\bar{m}$ is defined as

$$\bar{m} = \frac{1}{\Delta\tau} \int_{t}^{t+\Delta\tau} \frac{F_T}{A\, k_f}\, \mathrm{d}\tau\,, \tag{3.22}$$

where the effective tangential traction is calculated as the tangential reaction forces with respect to the surface area A on the top of the sheet cut-out, i.e. an approximation of the contact surface. Since the contact surface for microstructured surfaces is larger in the case of high pressures where the structures are filled and smaller when low pressures do not fill the structures, this effective friction factor is only an approximation in order to illustrate the structural resistance.

To model the sheet material, finite isotropic elasto-plasticity with a von Mises flow surface is applied. As the simulation is designed to model an experimental setup from [13], the sheet material is modelled as steel with parameters corresponding to dual phase steel DP600. Isik et al. [66] use a Swift type curve to fit measurements from uniaxial tension tests. The Swift ansatz is

$$\sigma^{y}_{\mathrm{vM}} = K\, \left[\varepsilon_0 + \varepsilon_p\right]^n \tag{3.23}$$

with the material parameters $K = 619\mathrm{MPa}$, $\varepsilon_0 = 0.00939$ and $n = 0.296$ and the accumulated plastic strain ε_p. The Swift curve is used in Abaqus as a table to define the von Mises flow curve with assuming isotropic hardening. For both the elastic part of the sheet material and the constitutive relation for the tool material, a Neo Hooke model is used. According to the Abaqus manual [39] the strain energy function reads

$$\psi_0 = \frac{\lambda}{2}\, \left[J_e - 1\right]^2 + \frac{\mu}{2}\, \left[\bar{I}_{e1} - 3\right] \tag{3.24}$$

wherein J_e is the determinant of the elastic part of the deformation gradient, $\boldsymbol{F}_e = \boldsymbol{F} \cdot \boldsymbol{F}_p^{-1}$, and $\bar{I}_{e1} = \mathrm{tr}\, \bar{\boldsymbol{C}}_e$ with $\bar{\boldsymbol{C}}_e = J_e^{-2/3}\, \boldsymbol{F}_e^{\mathrm{t}} \cdot \boldsymbol{F}_e$. Moreover, λ is the bulk modulus and μ denotes the shear modulus. This energy function is usually used for nearly incompressible material behaviour. However, in Abaqus the simple elastic material which uses logarithmic strains in large strain is not recommended for strains exceeding 5%. The hyperelastic law is also recommended for compressible materials by choosing a Poisson ratio $\nu < 0.5$, [39].

Calculation of normals and relative velocities The main components of the Archard wear relations in (3.10) are normal vectors $\boldsymbol{N}$ and $\boldsymbol{n}$, contact tractions $\boldsymbol{t}^*$ with the respective components, see (3.7), relative velocities $\dot{\boldsymbol{\varphi}}^*$ and area and volume transformations j^i and J^i. All quantities are needed on every node of the contact surface in every time increment.

To compute the outward surface normal vector $\boldsymbol{n}$ of node q, all adjacent body elements ea are considered. An illustration for the subsequent steps is provided in Figure 3.4.

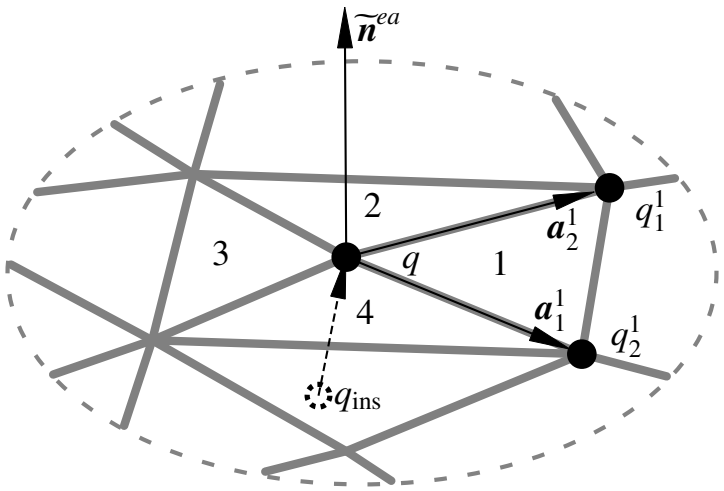

Figure 3.4: Detail of surface mesh to show calculation of outward normal vectors of point q based on $ea = 1, 2, 3, 4$ surface elements. Example is shown for $ea = 1$, normal vectors obtained by vector product are averaged and outward property is enforced by using inside point q_{ins}. Reprinted from [118], licensed under CC BY 4.0.

For each adjacent body element, two of its surface nodes q_1^{ea} and q_2^{ea} are used to define tangent vectors

$$\boldsymbol{a}_i^{ea} = \boldsymbol{x}_{q_i^{ea}} - \boldsymbol{x}_q \tag{3.25}$$

and the corresponding normal vector

$$\widetilde{\boldsymbol{n}}^{ea} = \boldsymbol{a}_1^{ea} \times \boldsymbol{a}_2^{ea} \,. \tag{3.26}$$

A neighbouring inside node q_{ins} is used to check that the vector points outwards, i.e.

$$\widetilde{\boldsymbol{n}}_{\text{out}}^{ea} = \text{sign}\left(\widetilde{\boldsymbol{n}}^{ea} \cdot [\boldsymbol{x}_q - \boldsymbol{x}_{q_{\text{ins}}}]\right) \; \widetilde{\boldsymbol{n}}^{ea} \,. \tag{3.27}$$

The normal vector is then averaged and normalised by

$$\widetilde{\boldsymbol{n}} = \sum_{ea=1}^{n_{ea}} \widetilde{\boldsymbol{n}}_{\text{out}}^{ea} \qquad \text{and} \qquad \boldsymbol{n} = \frac{\widetilde{\boldsymbol{n}}}{\|\widetilde{\boldsymbol{n}}\|} \,. \tag{3.28}$$

Due to not normalised vectors $\widetilde{\boldsymbol{n}}_{\text{out}}^{ea}$ entering the summation, larger elements contribute more to the normal direction. This is an appropriate weighting for linear tetrahedrons where $\|\widetilde{\boldsymbol{n}}^{ea}\|$ equals the surface area of the element.

The relative velocity of a surface node q with respect to the counter surface at time step m is based on sliding distances over the time step. The nearest node on the counter surface as well as all of its surface neighbour nodes are considered so as to obtain a robust calculation. For each node p in this list of n_{cn} counter nodes, the relative sliding distance is

$$\widetilde{\boldsymbol{s}}_{q,p} = \left[\boldsymbol{x}_p^2(\tau_m) - \boldsymbol{x}_q^1(\tau_m)\right] - \left[\boldsymbol{x}_p^2(\tau_{m-1}) - \boldsymbol{x}_q^1(\tau_{m-1})\right] \tag{3.29}$$

and an averaged weighted sliding distance of node q is

$$\boldsymbol{s} = \sum_{p=1}^{n_{cn}} \widetilde{\boldsymbol{s}}_{q,p}\, w_p \left[\sum_{p=1}^{n_{cn}} w_p\right]^{-1} . \tag{3.30}$$

Weights are chosen as $w_p = \|\boldsymbol{x}_p^2 - \boldsymbol{x}_q^1\|^{-1}$, i.e. the inverse distance to node q. The relative velocity then is approximated by

$$\dot{\boldsymbol{\varphi}}_T \approx \frac{\boldsymbol{s}}{[\tau_m - \tau_{m-1}]} . \tag{3.31}$$

Calculation of tractions and wear volumes Tractions in (3.7) are based on $\boldsymbol{\sigma}$, area and volume transformations in (3.9) on $\boldsymbol{F}$, which both are integration point values needed at the surface node points. As detailed in [16], a simple approach is the extrapolation using inverse shape functions together with a volume weighted average. Linear tetrahedrons are used in this work to allow for easy remeshing of the tool. Hence, the element-wise constant integration point values simply have to be averaged on the nodes with a volume weighting of all adjacent body elements. Time integration of (3.11) is performed by a summation over all n_{ts} time steps so that

$$\begin{aligned} V^i_{W(\dot{D})} &= \int_t^{t+\Delta\tau} \dot{V}^i_{W(\dot{D})}\, \mathrm{d}\tau \approx \sum_{m=1}^{n_{ts}} \dot{V}^i_{W(\dot{D})}\, [\tau_m - \tau_{m-1}] , \\ V^i_{W(p)} &= \int_t^{t+\Delta\tau} \dot{V}^i_{W(p)}\, \mathrm{d}\tau \approx \sum_{m=1}^{n_{ts}} \dot{V}^i_{W(p)}\, [\tau_m - \tau_{m-1}] , \end{aligned} \tag{3.32}$$

where the time step $\tau_m - \tau_{m-1}$ in large strain contact simulations varies. Due to the approximation of $\dot{\boldsymbol{\varphi}}_T$ in (3.31) based on the sliding distance and the time step, the time step can be cancelled out. Hence, the wear relation of one node q can be written based on an incrementally evaluated sliding distance, to be specific

$$V^i_{W(\dot{D})} \approx \sum_{m=1}^{n_{ts}} K^i\, j^i_m\, \boldsymbol{t}^*_{T\,m} \cdot \boldsymbol{s}^*_m , \qquad V^i_{W(p)} \approx \sum_{m=1}^{n_{ts}} \widetilde{K}^i\, j^i\, t^*_{N\,m}\, \|\boldsymbol{s}^*_m\| . \tag{3.33}$$

The value of the upscaling factor M in the geometry update (3.3) is coupled to a specific mesh size l_e via

$$M\, V^i_w \leq \delta_{\max}\, l_e , \tag{3.34}$$

where $\delta_{\max} \in (0, 1]$ is a user defined limit and l_e is the smallest element size. In this work, $\delta_{\max} = 0.02$ is chosen.

Setup of simulation framework The simulation framework is depicted in Figure 3.5. All steps are controlled by a main PYTHON script which invokes the respective subscripts and programs. The new model of the displacement problem at $\tau \in [t, t+\Delta\tau]$ is set up by using PYTHON scripting for ABAQUS CAE. Afterwards, the simulation of one passover is submitted to the ABAQUS Standard solver. The generated output database is evaluated using ABAQUS-PYTHON again. All quantities necessary for the evaluation of wear are calculated, and wear volumes are nodewise summed up on the reference domain according to (3.33). Within the postprocessor, the possible upscaling factor M is calculated subject to user defined limits, see (3.34). The respective cycles which correspond to the possible upscaling factor of the considered displacement problem are added to the total number of cycles. If the maximum desired number of cycles is not yet reached, the updated surface mesh of the tool geometry is passed to the TETGEN remeshing library to remesh the inner domain of the tool. }$^{\text{qtd.}}_{[118]}$

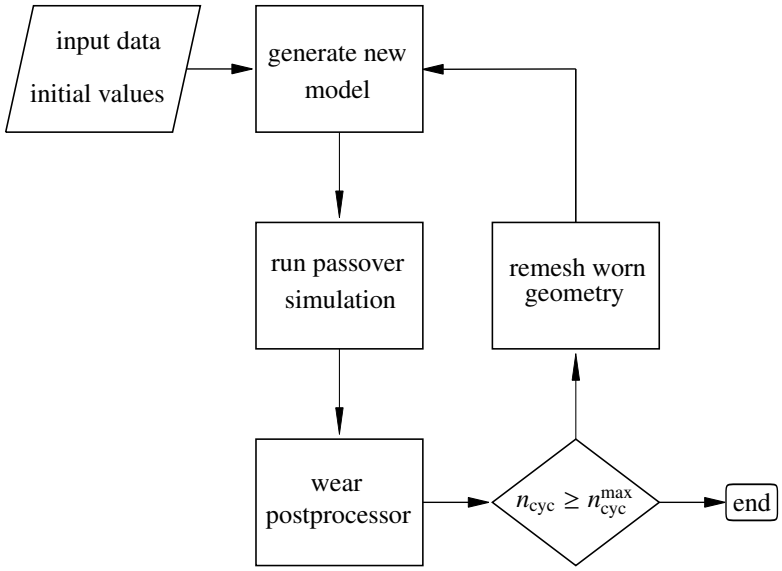

Figure 3.5: Flowchart of wear simulation framework as a geometry update scheme. Reprinted from [118], licensed under CC BY 4.0.

3.4 Results and Discussion

$^{\text{qtd.}}_{[118]}${In this section the presented framework is applied to practical examples. Firstly, a parameter study is carried out on a sinusoidal surface-structure under idealised conditions. The focus in that section lies on the frictional characterisation and the evolution of this characteristics when wear progresses. Secondly, a wear experiment conducted within a collaborative work, see [13], is simulated by using realistic material and friction models as well as the full load from the experiment for a bionic surface structure. For all simulations a constant referential energy-wear coefficient of $K^1 = 10^{-9}\,\text{mm}^2/\text{N}$ is used

for the tool. Based on the measurements from the wear experiment in [13], this factor could not be identified experimentally. Wear is not calculated on the sheet, i.e. $K^2 = 0$. Furthermore, the tool is modelled as a deformable body in all subsequent simulations with an hyperelastic constitutive relation given in (3.24). Young's Modulus $E = 210\,\mathrm{GPa}$ and Poisson ratio $\nu = 0.3$ are chosen for the tool steel. $\}^{\text{qtd.}}_{[118]}$

3.4.1 Sinusoidal surface structures

$^{\text{qtd.}}_{[118]}\{$Sinusoidal structures are produced via micromilling to adapt to local friction characteristics on metal forming tools, see [13]. In addition to the practical application, these structures are well suited for parameter studies due to their simplicity. To be able to separate influences more clearly, a hyperelastic-perfect-plastic material model is used in the workpiece by using Young's Modulus $E = 210\,\mathrm{GPa}$, Poisson ratio $\nu = 0.3$ and $\sigma^{y0}_{\mathrm{vM}} = 400\,\mathrm{MPa}$. Furthermore, the friction model is reduced to pure Coulomb friction with $\mu = 0.15$. This simplifies the understanding of the local friction behaviour and enables a clear quantification of the effect of structural resistance. To stay in the permissible regime of Coulomb's law, the load is reduced to 20 % of the load applied in the wear experiment, i.e. $\|\boldsymbol{t}_{\mathrm{ext}}\| = 250\,\mathrm{MPa}$ and a constant dragging velocity of $\|\dot{\boldsymbol{u}}_d\| = 0.01\,\mathrm{mm/s}$. The influence of sliding direction and load level shall be studied with respect to the effective friction coefficients as well as to how they change due to wear.

The sinusoidal structure is depicted in Figure 3.6 where the considered sliding directions α are depicted. Along these directions a cut-out is generated according to the rules given in section 3.2, based on results from [41]. Practically, the structures are produced using

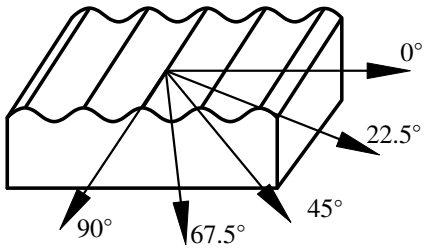

Figure 3.6: Sinusoidal surface microstructure with five sliding directions to be considered in separate simulations. The structure measures $\lambda = 200\,\mu\mathrm{m}$ with an amplitude of $10\,\mu\mathrm{m}$. Reprinted from [118], licensed under CC BY 4.0.

Python scripting for Abaqus, i.e. a sinusoidal profile is extruded and the respective angular cuts are applied. The periodic length of the structures is measured along the sliding direction, hence increases with cut-out angle. Furthermore, the structures also need to be periodic in the lateral direction. The structure adapted from the experiments in [13] exhibits a wavelength of $200\,\mu\mathrm{m}$ and an amplitude of $10\,\mu\mathrm{m}$. Element sizes l_e discussed below are defined along the 0° wave-direction and the 90° extrusion direction, as well as along the cutting direction stretched by $1/\cos(\alpha)$. Towards the bottom of the geometries a coarsening of the mesh is applied up to $5\,l_e$. The sheet cut-out as counter

body is generated as rectangular prism with element sizes of $0.8\,l_e$ on the contact surface and a coarsening up to $3\,l_e$.

A mesh density study shows differences of up to 10% in the effective friction coefficients and their development due to wear. In Figure 3.7, element sizes of $l_e = 7\,\mu$m, $l_e = 10\,\mu$m and $l_e = 13\,\mu$m are compared. All discretisations show initial effective friction coefficients of $\bar{\mu} = 0.26 \ldots 0.27$ and a decrease to $\bar{\mu} = 0.17 \ldots 0.18$ after 300000 cycles. The trend for both finer discretisations $l_e = 7\,\mu$m and $10\,\mu$m is identical despite the offset. Therefore, $l_e = 10\,\mu$m is chosen for subsequent calculations which is a good compromise between the resolution of the geometry and the computational cost. For 67.5°, $l_e = 15\,\mu$m is chosen instead in order to reduce the considerably long computation time. A comparison for the first 70 k cycles merely shows approximately 1% difference in $\bar{\mu}$ for both discretisations.

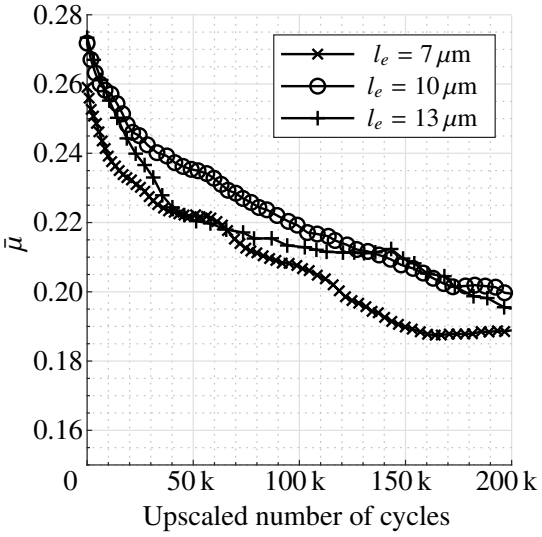

Figure 3.7: Mesh density dependence of effective friction coefficient $\bar{\mu}$ for 0° sliding direction. Reprinted from [118], licensed under CC BY 4.0.

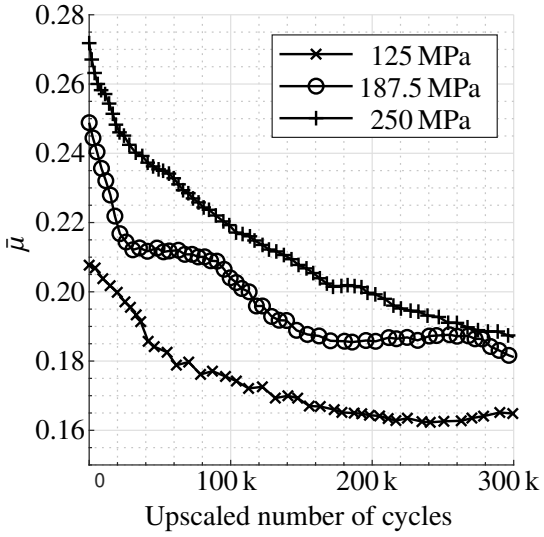

Figure 3.8: Load level dependence of effective friction coefficient $\bar{\mu}$ for 0° sliding direction. Reprinted from [118], licensed under CC BY 4.0.

The total value of the effective friction coefficients depends on the load level. Figure 3.8 shows the progress of $\bar{\mu}$ for external tractions of 125 MPa, 187.5 MPa and 250 MPa, i.e. 10%, 15% and 20% of the load applied in the wear experiment described in the next section in more detail. The absolute value of $\bar{\mu}$ clearly depends on the load level: a higher load leads to more structural resistance since a larger portion of the wave-structure is filled with elastoplastic material and resists the deformation. The progress of $\bar{\mu}$ shows a tendency towards the local value $\mu = 0.15$ used in the simulation. Clearly the simulation with the smallest load is fastest to approach this perfectly flat limit case. As soon as the part of the wave which produces the resistance is worn off, the effective friction answer converges to the local one. For the use of an effective friction coefficient on the macroscale it is therefore necessary to either provide load-dependent tabular data or to implement a multiscale approach taking into account all dependencies, see [131] and [128].

For the following investigation of different sliding directions a load of $\|\boldsymbol{t}_{\text{ext}}\| = 250\,\text{MPa}$ is chosen in order to obtain a notable structural resistance and to better discriminate the directions.

A similar dependency can be seen with respect to the bulk material model. When the swift yield relation (3.23) is scaled by factors $y_{\text{scl}} = 0.8$, $y_{\text{scl}} = 0.9$ and $y_{\text{scl}} = 1.1$, the resulting effective friction coefficients vary accordingly. This dependence is visualised in Figure 3.9. In summary, a higher load or a softer workpiece material lead to more structural resistance.

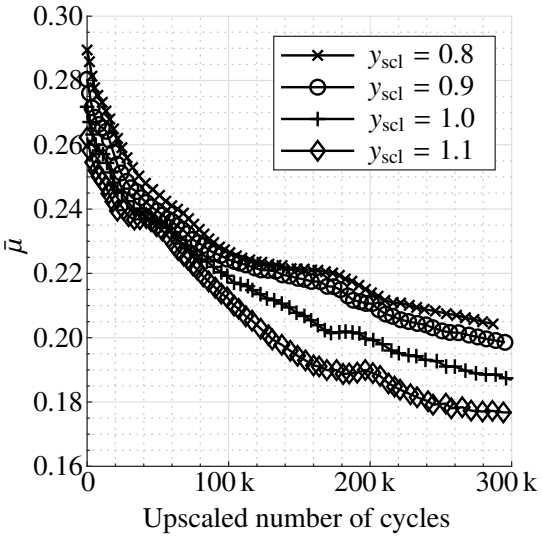

Figure 3.9: Bulk material model influence of effective friction coefficient $\bar{\mu}$ for 0° sliding direction. The yield relation σ^{y}_{vM}, cf. (3.23), is scaled by y_{scl}=0.8, 0.9, 1.0, 1.1.. Reprinted from [118], licensed under CC BY 4.0.

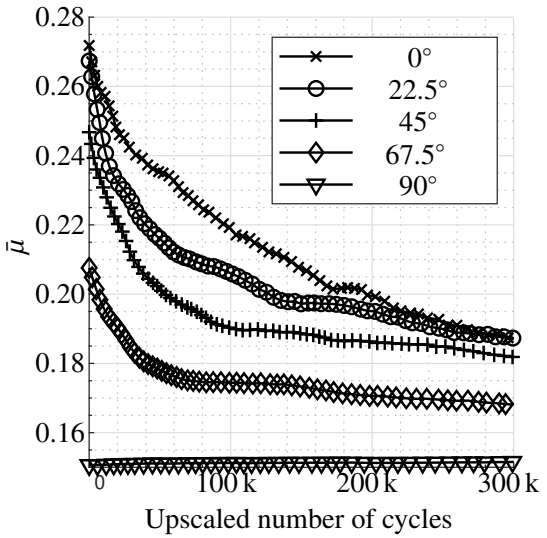

Figure 3.10: Sliding direction dependence of effective friction coefficient $\bar{\mu}$ for $\|\boldsymbol{t}_{\text{ext}}\| = 250\,\text{MPa}$ and $l_e = 10\,\mu\text{m}$. Reprinted from [118], licensed under CC BY 4.0.

The final discretised boundary value problems are given in Figure 3.12. The periodicity of the stress states is preserved in both, sliding and lateral direction due to the application of periodic boundary conditions. This can be seen in the contour plot of the von Mises equivalent stress which shows identical values at the edges. In the angular cut-outs of 22.5°, 45° and 67.5° the sheet cut-out measures exactly λ_{lat} in width, whereas the tool cut-outs have been made wider. This allows the notable lateral sliding of $0.02\,\lambda_{\text{lat}}$ for 22.5°, $0.05\,\lambda_{\text{lat}}$ for 45° and $0.08\,\lambda_{\text{lat}}$ for 67.5° induced by the angular structure. When the tool width exactly matches λ_{lat}, the sheet material slides over the tool edge which yields extremely high contact stresses and the divergence of the algorithm. The contact discretisation can not be defined in a periodic manner, and an extension of the tool width is therefore chosen. The tool width is selected as $1.025\,\lambda_{\text{lat}}$ for 22.5°, $1.06\,\lambda_{\text{lat}}$ for 45° and $1.10\,\lambda_{\text{lat}}$ for 67.5°.

The five simulations in different sliding directions show a gradation of the friction behaviour visualised in Figure 3.10. The sliding direction along the waves is preferred

by a constant and low effective friction coefficient which equals the local $\mu = 0.15$. The transverse directions exhibit increasing friction coefficients with a maximum for the 0° direction of initially $\bar{\mu} = 0.272$. This characteristic is preserved in the development of wear, where only the 0° and 22.5° direction equalise. The effective friction coefficients in the initial state and after 300 k cycles are summarised in Table 3.1.

Table 3.1: Effective friction coefficients of sinusoidal surface structures for $\|\boldsymbol{t}_{\text{ext}}\| = 250\,\text{MPa}$ and $l_e = 10\,\mu\text{m}$ at initial state and after 300 k cycles. Reprinted from [118], licensed under CC BY 4.0.

	0°	22.5°	45°	67.5°	90°
$\bar{\mu}_0$	0.2718	0.2673	0.2468	0.2092	0.1506
$\bar{\mu}_{300\,\text{k}}$	0.1874	0.1873	0.1819	0.1681	0.1515

The aforementioned effective friction coefficients are measured in sliding direction x, cf. Figure 3.2. Angular cut-outs result in anisotropic friction behaviour, i.e. lateral reaction forces appear. The initial effective friction coefficients are further detailed in Table 3.2, where the effective friction coefficient $\bar{\mu}^x$ in sliding direction x, the effective friction coefficient $\bar{\mu}^z$ in lateral direction z and the effective friction coefficient $\bar{\mu}^{\text{res}}$ in direction of the resulting tangential force in the x-z plane are distinguished. The orientation of this resulting tangential reaction force lies between the sliding direction and the direction orthogonal to the waves and is measured by α^{res} with respect to the sliding direction. The lateral reaction forces increase from 22.5° to 67.5° sliding direction. The described effects of larger structural resistance for more crosswise sliding directions is also visible in the differences of $\bar{\mu}^{\text{res}}$ in Table 3.2 although less pronounced than for $\bar{\mu}^x$. During the evolution of wear, the angle of the resulting force reduces due to the reduction of the lateral reaction forces. This is exemplary shown for the 45° direction in Figure 3.11. For the 22.5° direction, the lateral forces are smaller and hence, the difference of $\bar{\mu}^x$ and $\bar{\mu}^{\text{res}}$ is also smaller than for the 45° direction. For the 67.5° direction the lateral forces as well as the difference of $\bar{\mu}^x$ and $\bar{\mu}^{\text{res}}$ are higher than for the 45° direction. For all intermediate directions, $\bar{\mu}^x$ and $\bar{\mu}^{\text{res}}$ equalize during the evolution of wear.

Table 3.2: Effective friction coefficients of sinusoidal surface structures for $\|\boldsymbol{t}_{\text{ext}}\| = 250\,\text{MPa}$ and $l_e = 10\,\mu\text{m}$ at initial state detailed concerning the friction anisotropy. Reprinted from [118], licensed under CC BY 4.0.

	0°	22.5°	45°	67.5°	90°
$\bar{\mu}^x$	0.2718	0.2673	0.2468	0.2092	0.1506
$\bar{\mu}^z$	0.0000	0.0501	0.1014	0.1288	0.0000
$\bar{\mu}^{\text{res}}$	0.2718	0.2721	0.2671	0.2446	0.1506
α^{res}	0.00°	10.50°	22.09°	31.58°	0.00°

Figure 3.13 shows the distributions of wear depth d_W for all sliding directions after 300 k loading cycles. There is only a small region of homogeneous wear distribution measuring approximately one period in the middle of the sliding path. The results indicate

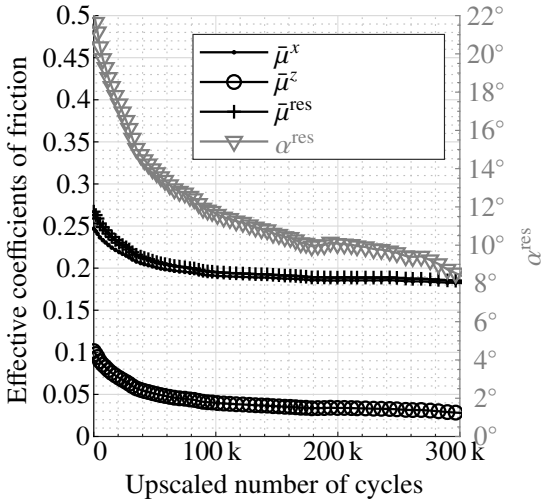

Figure 3.11: Development of friction anisotropy for sinusoidal structure under 45°. Directional effective friction coefficients $\bar{\mu}^x$, $\bar{\mu}^z$ and $\bar{\mu}^{\mathrm{res}}$ and orientation of resulting tangential reaction force α^{res}. Reprinted from [118], licensed under CC BY 4.0.

that only in this region a steady state sliding is present within the passover situation. The rest of the simulation is influenced by contact closing and opening. Furthermore, the angular cut-outs presented in Figure 3.13 show a wear pattern which does not reach the edges of the tool. This is due to the extension of the tools in width to allow for lateral sliding of the sheet cut-out. However, within the width of one lateral period, the wear distribution is homogeneous in the steady state region. As the considered amplitude measures 10 μm, the wear depths after 300 k cycles show an abrasion of 45% to 83% of the amplitude. The results in Figure 3.13 indicate that an increase in the sliding direction angle yields a larger wear depth after the same number of cycles for angular cut outs despite lower effective coefficients of friction. Consequently, the local tangential tractions and relative velocities are increased for angular sliding directions despite of lower global reaction forces. $\}^{\mathrm{qtd.}}_{[118]}$

3.4.2 Bionic scarab beetle surface structures

$^{\mathrm{qtd.}}_{[118]}\{$Tailored surfaces have been investigated in [81] for the use in sheet-bulk metal forming processes. Figure 1.1 in the introduction shows the application of a bionic structure onto toothing tools. The scarab beetle surface structure is another bionic structure to adapt the tribological behaviour of tool surfaces. Originally, the honeycomb-like structures shown in Figure 3.14 were found and investigated on a scarab beetle, see [152]. The scarab structure is produced on tool surfaces via micromilling with a ball end milling-cutter of $d = 0.3$ mm diameter, see [132] for details. The structure was investigated during a wear test in [13] which is summarised in A. The structures were applied to six plateaus measuring 4×10 mm on the active components of the tools to obtain defined contact pairs. The assembly of the tools and the ram stroke curve are

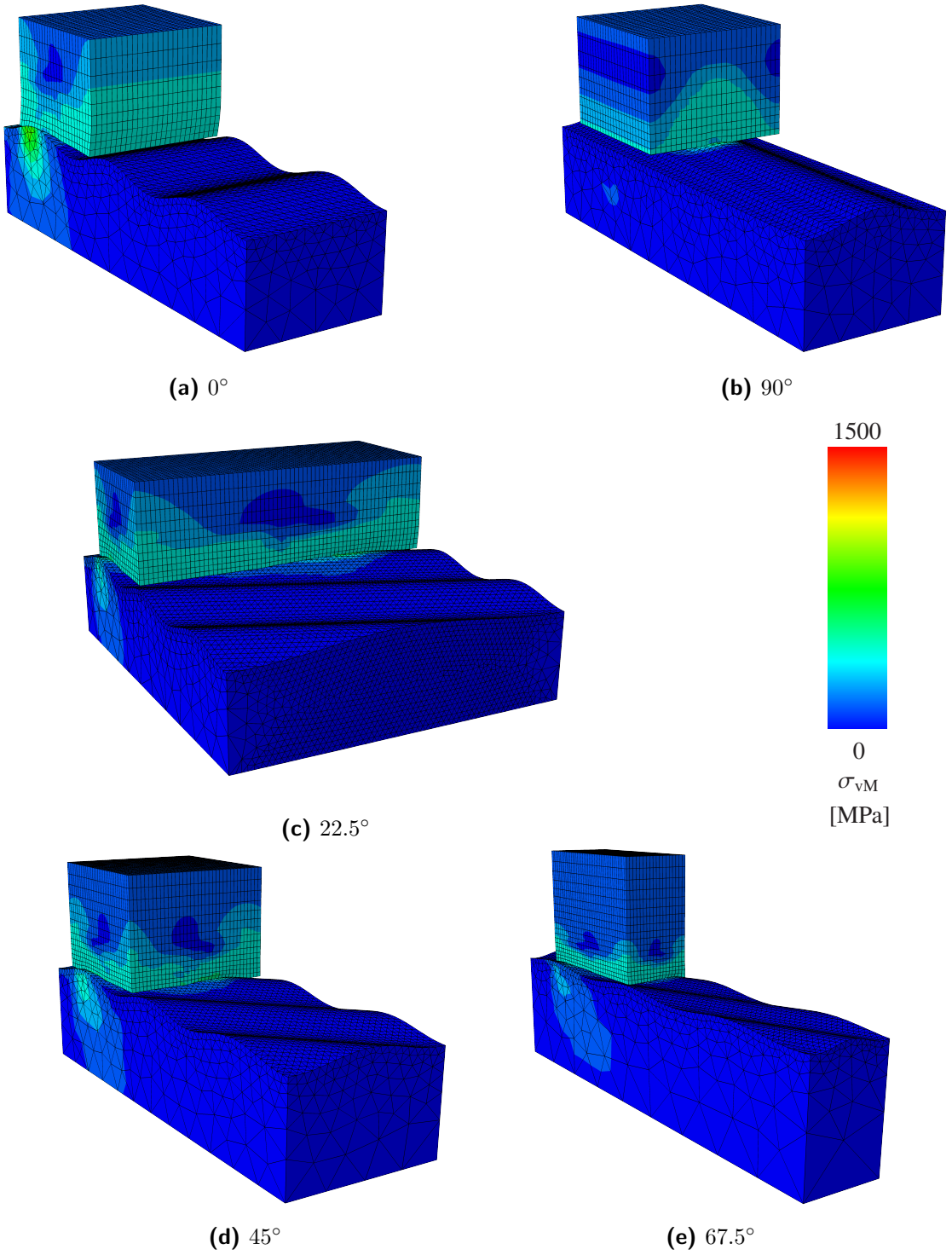

(a) 0° **(b)** 90°

(c) 22.5°

(d) 45° **(e)** 67.5°

Figure 3.12: Spatially homogenised contact friction simulation of sinusoidal surface structure in five sliding directions. Contour plots of von Mises equivalent stress. Reprinted from [118], licensed under CC BY 4.0.

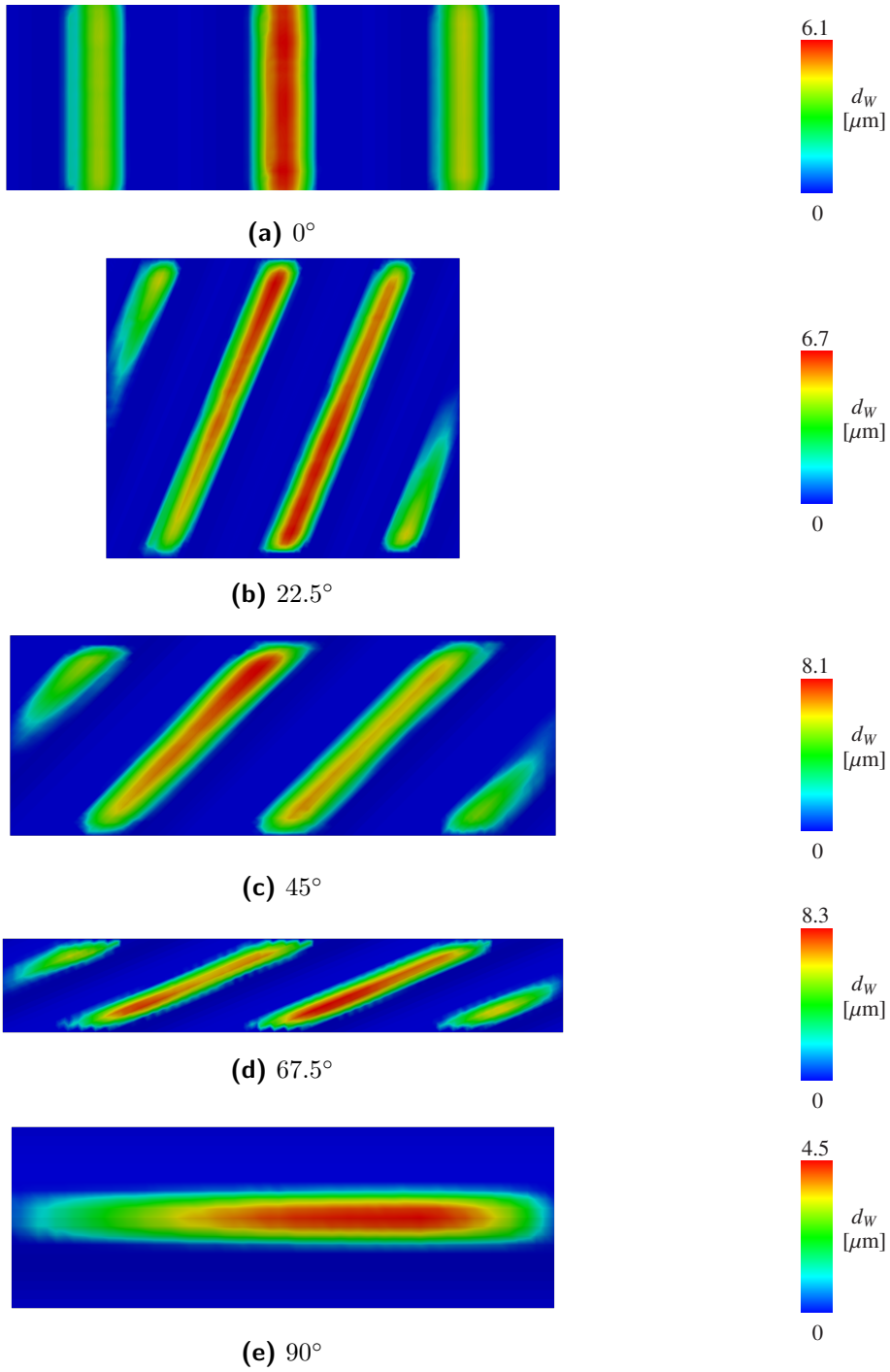

(a) 0°

(b) 22.5°

(c) 45°

(d) 67.5°

(e) 90°

Figure 3.13: Wear distribution for sinusoidal surface structure for five sliding directions after 300000 cycles. Plots are scaled differently. Reprinted from [118], licensed under CC BY 4.0.

depicted in Figures 3.20 and 3.21. The tools were pressed into a DP600 sheet with 300 kN, the pressure load on the structures on the plateaus therefore is $\|\boldsymbol{t}_{\text{ext}}\| = 1250\,\text{MPa}$. The tools were installed at an angle of 4° to increase tangential sliding of the material. Here, a constant flow of sheet material over the tool surface with $\|\dot{\boldsymbol{u}}_d\| = 0.01\,\text{mm/s}$ is assumed on the mesoscale. Due to the high pressures, Coulomb friction is no longer applicable since the resulting extreme tangential forces prevent any sliding. A combined friction model (3.21) is therefore applied by using $\mu = 0.15$ and $m = 0.34$ locally. The friction factor has been determined for a DP600 workpiece material using ring compression tests in Müller et al. [93]. The isotropic hyperelastic-plastic material model for the dual phase steel DP600 sheet material includes work hardening and is given in (3.23). The scarab beetle structure is depicted in Figure 3.14. This structure is used if an isotropic adaption of the friction properties is desired, [13]. However, geometrically, there are two sliding angles which differ by 30° and which repeat alternately. These angles shall be investigated separately.

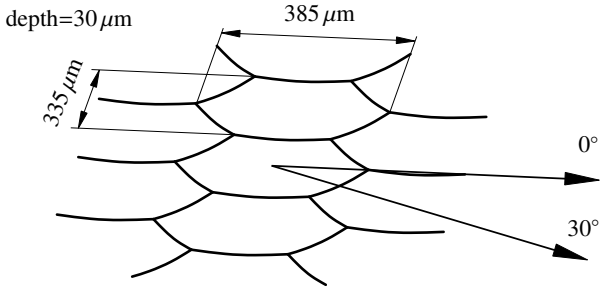

Figure 3.14: Isometric view of scarab beetle surface structure consisting of equilateral hexagonal dimples. Two characteristic sliding directions differing by 30° which repeat six times each. Reprinted from [118], licensed under CC BY 4.0.

Figure 3.15 shows the two resulting boundary value problems in the first passover simulation. Due to the high external pressure, the surface structure is almost completely filled with sheet material. Dragging over the surface induces high plastic deformations as the sheet material has to flow around each surface feature. This yields high local equivalent stresses of up to 3500 MPa.

Initially, both sliding directions show slightly different effective friction behaviour as summarised in Table 3.3. The difference can be seen in both the effective friction factors $\bar{m}$ as well as in the effective Coulomb friction coefficients $\bar{\mu}$. However, the friction factor is more relevant since, on the macroscale as well, the pressures exceed the regime where a purely pressure dependent friction law is admissible.

For the simulation of wear, both the dissipation based (3.6) and the pressure based Archard relation (3.8) are considered. Figure 3.16a shows the development of effective friction factors due to wear. In the progress of wear calculated with the dissipation based Archard relation, the 30° direction retains more of its resistance, whereas the 0° direction finally has a lower $\bar{m}$ value. By using the pressure based Archard relation, the inversion is not visible but the 0° direction shows more resistance and the difference even

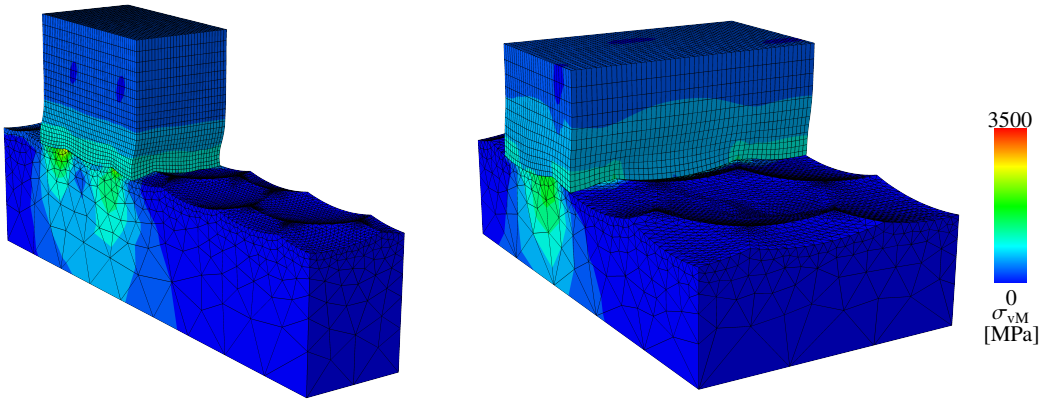

(a) 0° **(b)** 30°

Figure 3.15: Spatially homogenised contact friction simulation of scarab beetle hexagonal surface structure in two sliding directions. Contour plots of von Mises equivalent stress. Reprinted from [118], licensed under CC BY 4.0.

Table 3.3: Initial effective friction factors and Coulomb friction coefficients of scarab beetle surface structures for $\|\boldsymbol{t}_{\text{ext}}\| = 1250\,\text{MPa}$. Reprinted from [118], licensed under CC BY 4.0.

	0°	30°
$\bar{m}$	0.9167	0.8964
$\bar{\mu}$	0.1520	0.1486

increases due to strong reduction for the 30° direction. However, the comparison of both wear relations Figures 3.16a and 3.16b is influenced by different wear coefficients. They are only adapted to each other within the low-pressure regime where Coulomb's law is admissible, see section 3.3.

To compare both Archard relations, it is preferable to use a graph with respect to total worn volume and to compare sliding directions separately. Despite of different wear coefficients and relations this guarantees approximately equal wear states. Figure 3.17 shows this comparison where the dissipation based relation yields a faster reduction of structural resistance in the progress of wear for both considered directions. Figure 3.18 shows contour plots of the wear depths for both models to illustrate the different wear distributions. The wear distribution is not identical at different geometrically equal positions, since the boundary value problem does not represent a steady state sliding. Besides the contact closing and opening phase in the dragging phase this is caused by work-hardening of the sheet material. Hardening reduces formability and therefore increases the contact forces which are necessary to make the sheet material flow around the surface features. Additionally due to plastic deformations, the contact zone of the workpiece does not reach the end of the sliding path when the top surface does. Consequently, the zone of approximately steady state conditions additionally reduces. Nevertheless, the wear plots show, that the dissipation based model mainly shows wear

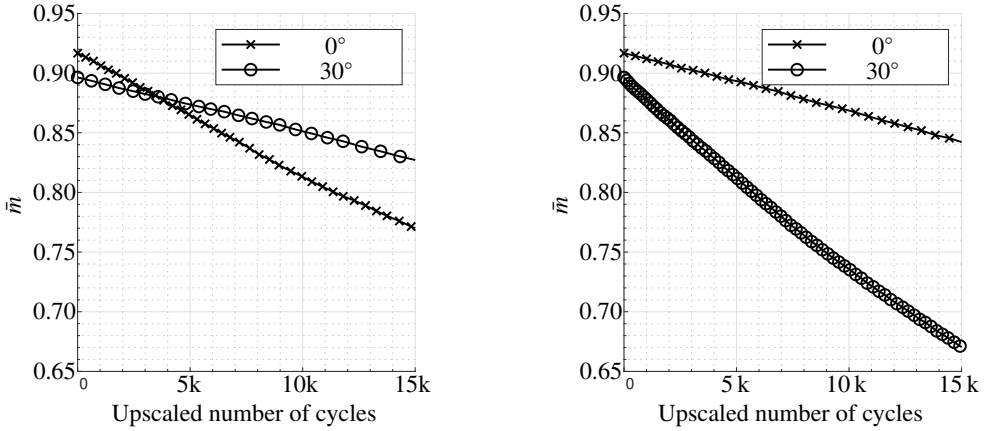

(a) Dissipation based Archard relation. **(b)** Pressure based Archard relation.

Figure 3.16: Direction dependence of effective friction factor $\bar{m}$ for scarab surface structures for both wear relations. Reprinted from [118], licensed under CC BY 4.0.

on all the edges of the surface structure, whereas the pressure based model delivers more distributed wear concentrating in front of the peaks. As the edges are preserved, the pressure based relation consequently retains more resistance.

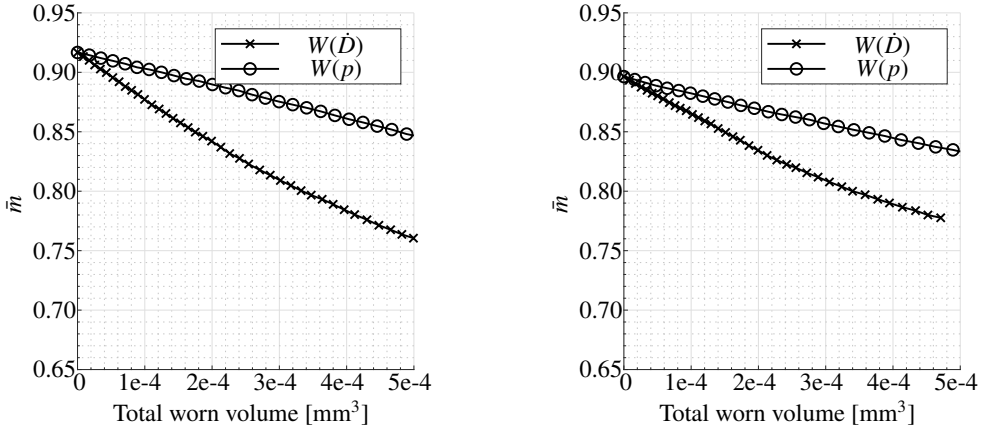

(a) 0° **(b)** 30°

Figure 3.17: Wear relation dependence of effective friction factor $\bar{m}$ with respect to total worn volume for both directions. Reprinted from [118], licensed under CC BY 4.0.

Figure 3.19 shows experimental results of the wear experiment [13], see also A, for a 20 μm depth flat variant of the scarab surface structure. The height plots in Figure 3.19a and Figure 3.19b show the initial and the worn geometry. The initial geometry exhibits burrs on the edges, whereas after 10 k cycles the burrs are gone and the surface structures are slightly rounded. The difference plot in Figure 3.19c shows the wear of the structure where the subtraction operation removes the structural shape and shows the wear effects. The fact that the honeycombs are clearly visible on the subtraction, and

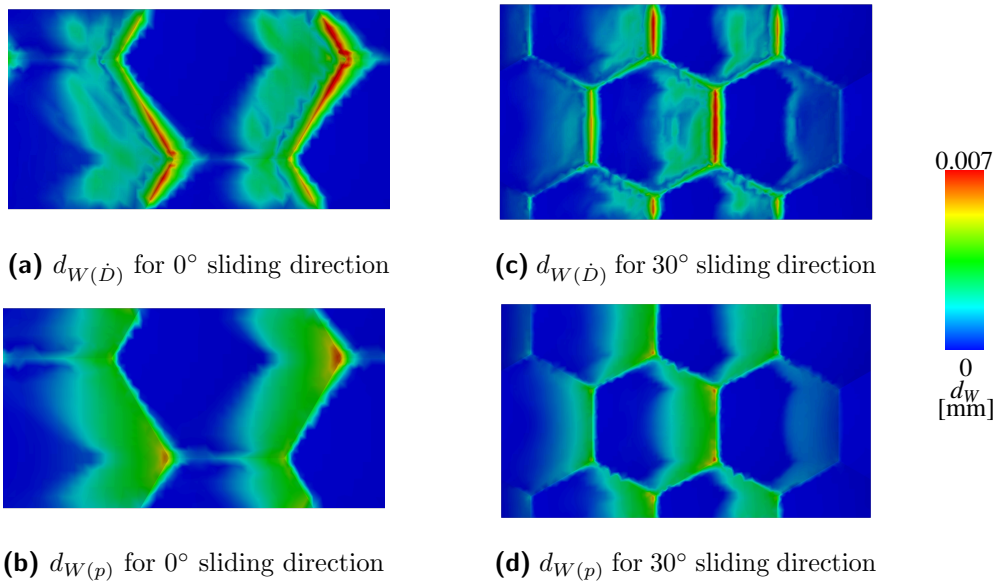

(a) $d_{W(\dot{D})}$ for 0° sliding direction

(c) $d_{W(\dot{D})}$ for 30° sliding direction

(b) $d_{W(p)}$ for 0° sliding direction

(d) $d_{W(p)}$ for 30° sliding direction

Figure 3.18: Wear distribution for scarab beetle hexagonal surface structure at 4.5e-4 mm^3 total worn volume. Contour plots of wear depth d_W for the dissipation based and the pressure based Archard relation and two sliding directions 0° and 30°. Reprinted from [118], licensed under CC BY 4.0.

that the height increases slightly towards the edges, shows that the wear distribution exhibits a concentration on the edges. A clear concentration on the peaks is not visible. Due to the burrs stemming from the machining operation, it is not possible to gain clear evidence, but there are hints that the dissipation based relation in Figure 3.18a and 3.18c shows better agreement. Therefore, the dissipation based simulation results after 10 k cycles are shown in Figure 3.19d for comparison with the measured difference in Figure 3.19c. Indeed, the height range is identical. However, the measurements are stemming from a flat variant with 20 μm depth and the burrs increase the worn height significantly. Therefore most probably the wear coefficient has to be reduced and the real number of upscaled cycles is much higher respectively. However, clear quantitative statements are not possible with the available measurements but the qualitative agreement is quite good.

From a practical viewpoint it is important to mention that the amount of wear is changed by structuring the forming tools. A reference simulation is carried out in which the tool surface is completely flat. All other parameters are identical to the scarab surface simulations and the dissipation based wear relation is used. The maximum wear depth $d_W^{\max}$ is highly increased due to the application of a surface structuring. For the 0° sliding direction, the structured tool exhibits $d_W^{\max} = 6.2\,\mu$m and the unstructured tool $d_W^{\max} = 0.9\,\mu$m after 10 k cycles. For the 30° sliding direction, $d_W^{\max} = 4.7\,\mu$m on the structured tool indicates less wear than for 0°, which is consistent with the smaller reduction of structural resistance visible in Figure 3.16a. In summary, the increase in

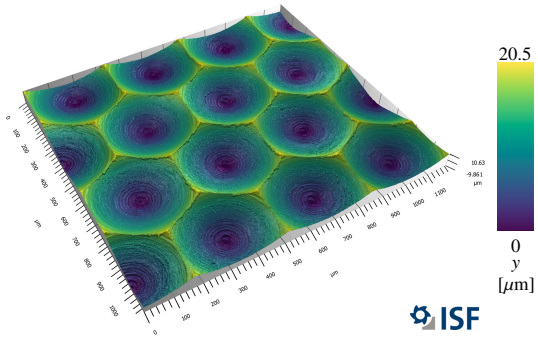

(a) Height plot of machined surface with burrs on the edges.

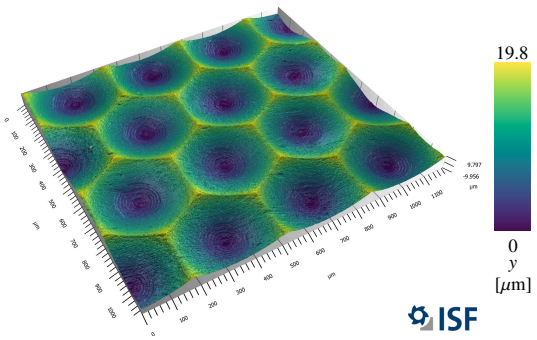

(b) Height plot after 10 k cycles in wear experiment.

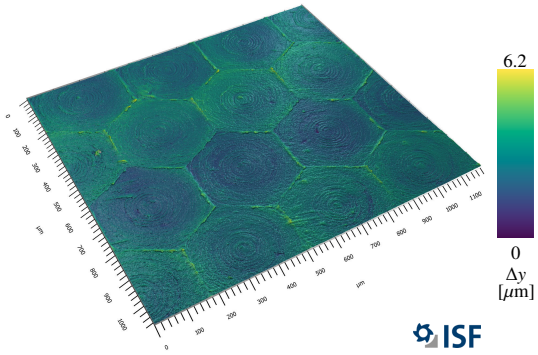

(c) Height difference of (a) and (b) filtering out structural shape.

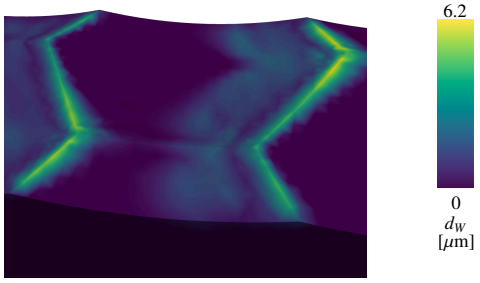

(d) Simulation results for wear depth after 10 k upscaled cycles in 0° direction.

Figure 3.19: Experimental results of wear experiment presented in A or [13] of a flat variant (20 μm depth) of the scarab structure. Height plots kindly provided by the Institute of Machining Technology ISF at TU Dortmund. Experiment shows wear along the edges in good agreement to simulation although burrs restrict quantitative comparison. Reprinted from [118], licensed under CC BY 4.0.

friction due to the structuring results in a significantly increased maximum wear depth. }qtd. [118]

3.5 Modelling and simulation of Wear – Conclusion

The simulation of wear based on the dissipated frictional work is an important approach to characterise surface interactions and the influence on the properties and operational capabilities of these surfaces. qtd. [118]{This work combines the continuum mechanics based application of the phenomenological Archard wear law with frictional contact homogenisation to filigree microstuctured surfaces on the meso scale. The wear simulation is implemented within a Python postprocessor including automatic remeshing and setup of the passover simulations in Abaqus. The procedure is detailed out for the sake of reproducibility. For the application in a real wear experiment with tailored metal forming tools,

appropriate constitutive laws are applied, i.e. isotropic large strain hyperelastic-plastic material behaviour and a combined friction model.

A study of sinusoidal surface structures reveals parameter dependencies of effective friction coefficient $\bar{\mu}$. The structural resistance represented by $\bar{\mu}$ increases for higher pressure loading and for more crosswise sliding directions, whereas wear depths decrease due to the decrease of lateral sliding. The spectrum of structural resistance for different directions makes the sinusoidal structures well suited for the anisotropic adaption of friction characteristics of surfaces. The effect is retained during the progress of wear. The investigation of an isotropic bionic surface structure adapted from the scarab beetle shows quasi-isotropic characteristics. The effective friction characteristics differ for two sliding directions which repeat every 30°. Sliding along the edge direction furthermore induces a faster reduction of structural resistance due to wear as sliding across the edges. This shows how to best apply these structures when a quasi-anisotropic adaption of friction is desired. All the investigations are conducted using aspect ratios of the cut-outs given in [41]. However, the results show only a quite short region of steady state behaviour visible in the wear distributions. Due to the use of a work hardening plasticity model and the influence of contact closing and opening, longer cut-outs should be investigated.

The experimental results from the collaborative work in [13] revisited for the wear distribution in this article supply hints that a dissipation based Archard relation is more realistic than a pressure based one. Theoretical considerations, e.g. [50] and [104] indicate this when the friction coefficients are not constant. This is the case in high pressure metal forming applications for which a combined friction model is applied in this work. Comparison of the dissipation based approach with the experimental results shows good qualitative agreement. Due to burrs stemming from machining, quantitative comparisons are limited and the wear coefficients can not be fitted. The data indicates that the wear coefficient should be reduced, or that the number of simulated cycles is actually higher. More experiments with probes, that have been given a finishing treatment before the actual wear experiments, are necessary in the future. These could give more evidence as to which wear relation is more realistic and could allow to fit the wear coefficient. However, qualitatively this work provides conclusions on the frictional characteristics of microstructured surfaces and their development in the progress of wear. Furthermore, the influence of lubrication as well as temperature effects, such as temperature induced residual stresses resulting from the application of surface structures or coatings, should be taken into account in the future. From a practical viewpoint, this study shows how surface structuring increases friction in an isotropic or anisotropic manner. The effect of this adaption is a highly increased wear depth. However, as indicated in [69], surface structuring may be necessary to enable the precise manufacturing of a part in the first place, e.g. by locally increasing the form filling. }$^{\text{qtd.}}_{[118]}$

A Appendix – Description of the wear experiment

qtd. [118]{The wear experiment used for validating the simulation has been conducted within a research collaboration published in German language in [13]. The experiment is shortly summarised in the following. A servo-mechanical knee lever press MSC-2000 of the Schuler company is used in an automated operation. The active component comprises six plateaus on which microstructures are manufactured using micro-milling operations. The active component is made of 1.3344 steel with a hardness of 63±1 HRC. This active component is installed in a tiltable tool-table, see Figure 3.20. A second identical tool-table is installed on the upper side in order to emboss the sheet metal from both sides.

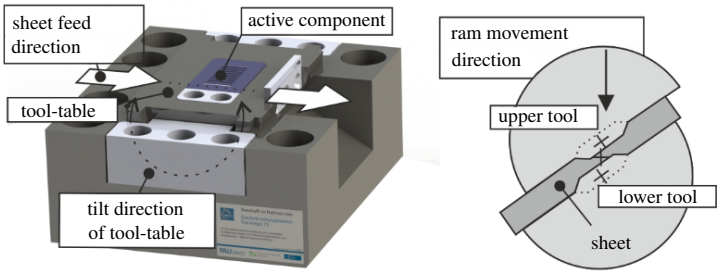

Figure 3.20: Concept of tiltable tool-table. Reprinted with translated labels from [13], licensed under CC BY 4.0.

The experimental set-up is shown in Figure 3.21 along with the ram stroke curve. The sliding of sheet metal along the tool surface is increased through tilting of the tool-table by 4°. A DP600 sheet coil with a width of 50 mm and a thickness of 3 mm has been used.

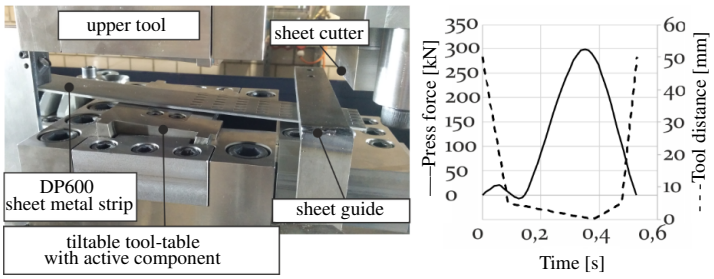

Figure 3.21: Assembled tool with applied ram stroke curve. Reprinted with translated labels from [13], licensed under CC BY 4.0.

Closing and opening of the tool is fast, whereas the embossing is slow and a maximum press force of 300 kN is applied. In total, 10000 operations have been performed with a ram stroke frequency of 30/min. The experiment was conducted once.

The surface measurements have been performed using the confocal white-light microscope Nanosoft μsurf before and after the wear experiment. The measurements show a

small reduction of surface roughness parameters as well as a slight change in the material percentage curve. In the experiment, a variant of the scarab surface with a depth of 20 μm is considered. The surface roughness is specified with the line-wise roughness average R_a and the surface roughness average S_a. Both roughness parameters represent the averaged height of the measured points with respect to the mean height. The reduction of these roughness measures due to wear can be seen in Figure 3.22a. The error bars for R_a show that this line-wise measure has a high variation over the surface. The surface measure S_a gives a more reliable quantification of the roughness and its reduction due to wear. The material percentage curve in Figure 3.22b shows the amount of area filled with material for each height level. The material percentages are reduced especially between 20 μm and 15 μm profile height. Below 10 μm profile height no change in the material percentage is visible.

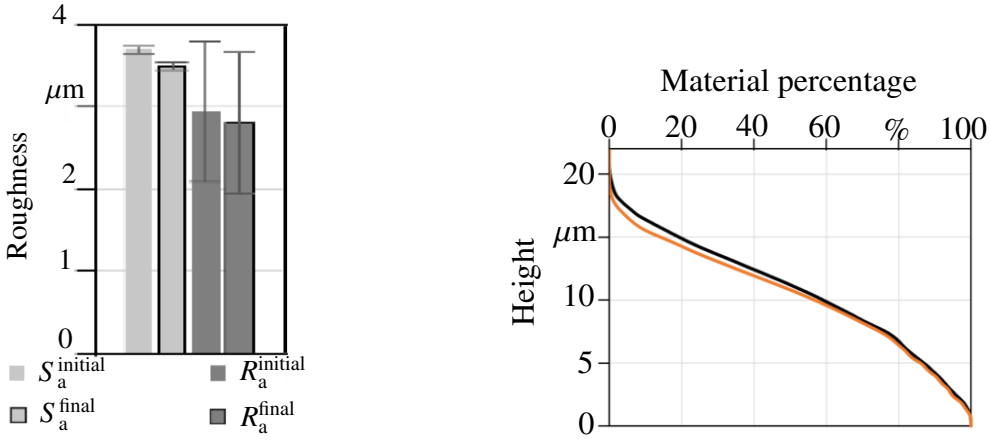

(a) Roughness parameters reduce due to wear.

(b) Material percentage curves for initial (black) and final state (orange) show reduction due to wear.

Figure 3.22: Comparison of geometrical measurements of wear experiment in initial state and after 10000 ram strokes. Reprinted in cropped form with translated labels from [13], licensed under CC BY 4.0.

Height plots provide a visual comparison of experiment and simulation to allow for a qualitative comparison. The height plots of the measured surface point-clouds are presented in Figure 3.19. }$^{\text{qtd.}}_{[118]}$

4 Modelling and simulation of material separation

Solid body contact interactions in metal forming involve changes in the shape of tools and workpieces. While the workpiece forming is intended to produce the desired part shape, tool surfaces suffer from loss of geometric accuracy due to wear. In the previous chapter, wear is simulated on a macroscopic scale, where the volume of wear is calculated in a post-processor that adjusts the mesh geometry for the next run over simulation. However, at the microscopic level, interactions of surface asperities contribute to the evolution of friction and wear. The aim of this chapter is to model asperity shearing including plastic deformation and fracture and the separation of the asperity. The methodology is based on the Particle Finite Element Method and is generally applicable to the simulation of macroscopic chip separation as well.

Special emphasis is placed on the role of point insertion in PFEM remeshing. PFEM is generally capable of simulating crack initiation and separation because it does not require a closed and topologically persistent surface description for remeshing. In other words, the change in topology induced by crack formation and material separation can be handled by PFEM. The α-shape detection takes over the role of deciding when a new surface, e.g. a crack, is generated, as analysed in [114] for a notched plate under tension. On the other hand, very large deformations in metal cutting operations require an adaptive remeshing including point insertion and removal in order to maintain a good mesh quality and resolve the material flow at the cutting edge as shown in [111], [110] and [26]. Point insertion in regions of large local deformation prevents α-shape detection from modelling crack initiation. Therefore, the main contribution of this chapter is to show how point adaptivity can be used to resolve the material flow and how the addition of a fracture criterion to the α-shape detection can still allow crack initiation. The simulation of self-contact after material separation is also presented.

For the simulation of large incompressible plastic deformations, a major limitation of PFEM is the volumetric locking of the constant strain triangular elements. Therefore, the first part of this chapter is dedicated to a study of two element formulations for quasi-incompressible material behaviour in PFEM. Apart from minor adaptations, the first section is a textual reproduction of the journal article [119], with directly quoted passages marked in each numbered subsection using ${}^{\text{qtd.}}_{[119]}\{$to $\}^{\text{qtd.}}_{[119]}$. The work analyses the

performance of these element formulations for quasi-incompressible hyperelasticity and also presents an extension of the state-variable transfer scheme. For contact simulation, the contact domain method introduced by [97] and [58] is used. The main focus thereafter is the presentation of the extended PFEM methods and numerical analyses including the simulation of an asperity shearing.

4.1 Treatment of quasi-incompressibility in PFEM

$^{\text{qtd.}}_{[119]}\{$This section compares two element-formulations for quasi-incompressible material behaviour in a deformation based updated Lagrangian formulation. Moreover, a comparative analysis of different variable transfer schemes is conducted. While the general concept of the discussed element types and state-variable transfer methods is extendible to 3d, this work is restricted to 2d plane strain conditions for conceptual simplicity. The model is yet restricted to a purely mechanical formulation in order to provide insight into the selection of a set of methods.

For the application of PFEM in the context of quasi-incompressible material behaviour, the two compared element types are illustrated in Figure 4.1 $\}^{\text{qtd.}}_{[119]}$

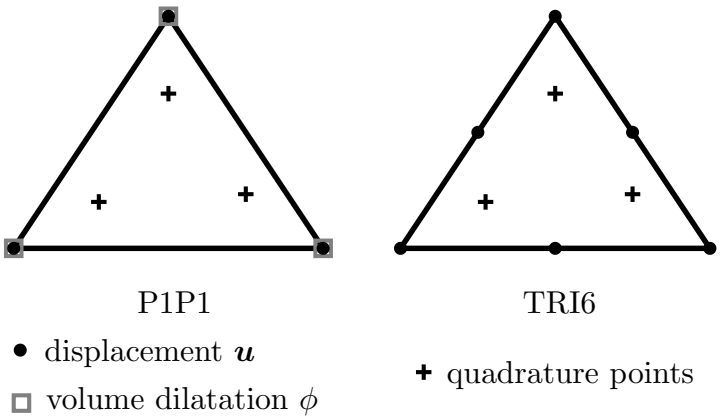

Figure 4.1: Illustration of P1P1 element with 9 degrees of freedom and TRI6 element with 12 degrees of freedom in 2d. To avoid introducing additional errors from numerical integration of non-constant integrands, three quadrature points are selected for both elements. Reprinted from [119], licensed under CC BY 4.0.

4.1.1 Quadratic TRI6 triangular elements

$^{\text{qtd.}}_{[119]}\{$The TRI6 element depicted in Figure 4.1 is a standard triangular displacement element with biquadratic shape functions. However, in the context of PFEM remeshing, some particularities occur. The TRI6 formulation shares some methodologies with the only mentioned higher order element used in PFEM, i.e. the mixed second order displacement first order stress element, cf. [135, 147]. These references mention the

edge-mid-nodes being neglected during remeshing – further details will be complemented in the following. PFEM is a remeshing method that preserves nodal points. When considering a point cloud which includes the edge-mid-nodes of the TRI6 element, no standard remeshing algorithm can directly fit a new TRI6 element into the existing point configuration. Instead, the remeshing algorithm typically constructs a linear triangular element first and then introduces edge-mid-nodes. These edge-mid-nodes serve their purpose of improving the element behaviour within a single calculation step and are subsequently erased and regenerated during the remeshing process. It is important to consider the following details:

- additional nodes during the Finite Element solution make a double book-keeping necessary for implementation, i.e. one data structure for the cloud of real particles and one data structure for the mesh with all corner- and mid-nodes and their degrees of freedom, placements etc.
- before remeshing, nodal data is stored in the cloud data-structure and the edge-mid-nodes are erased. Element data has to be kept for the state-variable mapping.
- after remeshing and variable mapping, cloud-data is interpolated onto the new edge-mid-nodes which are placed on the straight line between corner-nodes. During the subsequent time step iteration, the element edges can be curved and thus represent the quasi-incompressible deformation better than a linear triangular element.
- boundary conditions need to be enforced at the edge-mid-nodes located between corner-nodes where boundary conditions are specified. For example, on a Dirichlet boundary, if boundary conditions are not enforced, the edge-mid-nodes may protrude from the surface. Neglecting to apply boundary conditions on the edge-mid-nodes on a Neumann boundary significantly reduces the robustness of the calculation. A pragmatic solution is the application of linear constraints to fix the edge-mid-nodes m to the geometrical midpoint between two corner-nodes c_1 and c_2 according to

$$\boldsymbol{u}_m = \frac{\boldsymbol{u}_{c_1} + \boldsymbol{u}_{c_2}}{2} \tag{4.1}$$

  for all boundary edges with prescribed boundary conditions. $\}^{\text{qtd.}}_{[119]}$

4.1.2 Mixed stabilised P1P1 element formulation

$^{\text{qtd.}}_{[119]}\{$The use of stabilised low-order mixed elements is well established throughout the PFEM literature, e.g. [18, 26, 28, 60, 90, 105, 111]. The P1P1 element depicted in Figure 4.1 does not require the handling of additional edge-mid-nodes as the TRI6 element, making it more straightforward to implement in the PFEM remeshing strategy. However, an additional global balance equation needs to be solved by analogy with other

multiphysics FE implementations of coupled problems. Furthermore, a stabilisation technique is required because both fields are approximated with low-order shape functions, which can lead to violation of the LBB stability conditions. The Polynomial Pressure Projection method introduced by [20] is frequently applied in the context of PFEM, as detailed in [26, 105], and will be adapted here. An overview of stabilisation techniques can be found in [153], while [18] presents the application of an alternative method within the context of PFEM.

In this work, the $\boldsymbol{u}$-ϕ formulation is adopted which uses the volume dilatation ϕ as a primary global variable, which is coupled to the local quantity $J = \det(\boldsymbol{F})$ via an additional balance equation. Based on [90] the referential weak form of the system of two balance equations reads

$$\mathcal{W}_{\boldsymbol{u}} = \int_{\mathcal{B}_0} \nabla_{\boldsymbol{X}} \delta\boldsymbol{u} \colon \tilde{\boldsymbol{P}} \, \mathrm{d}V + w_{\mathrm{sur}} + w_{\mathrm{vol}} + w_{\mathrm{dyn}} = 0 \tag{4.2}$$

$$\mathcal{W}_{\phi} = \int_{\mathcal{B}_0} \delta\phi \, [\phi - J] \, \mathrm{d}V = 0 \tag{4.3}$$

with the test functions $\delta\boldsymbol{u}$ and $\delta\phi$. In comparison to the stationarity conditions of a Hu-Washizu three-field functional for incompressibility, see Section 2.3.1, the pressure-condition (2.38) is neglected. Furthermore, the test function δp from the dilatation condition (2.39) is replaced with $\delta\phi$ yielding a dimensionless format of the constraint-equation (4.3). In this section, the referential format is chosen for simplicity and the push forward transformation to the previous configuration $\mathcal{B}_n$ is based on (2.19), (2.20) and (2.21). In contrast to the standard balance of linear momentum (2.9), a modified Piola stress tensor $\tilde{\boldsymbol{P}}(\tilde{\boldsymbol{F}})$ is used, with the definition of the modified deformation gradient as

$$\tilde{\boldsymbol{F}} = \left[\frac{\phi}{J}\right]^{1/3} \boldsymbol{F} = \phi^{1/3} \, \boldsymbol{F}^{\mathrm{iso}} \tag{4.4}$$

whereby $\boldsymbol{F}^{\mathrm{iso}} = J^{-1/3} \, \boldsymbol{F}$ is the isochoric part of the deformation gradient. The volumetric part $\boldsymbol{F}^{\mathrm{vol}} = J^{1/3} \, \boldsymbol{I}$ is replaced by the global volume dilatation variable, i.e. $\tilde{\boldsymbol{F}}^{\mathrm{vol}} = \phi^{1/3} \, \boldsymbol{I}$. In an updated Lagrangian setting according to (2.3) a decomposition into history $\boldsymbol{F}_n$ and increment $\Delta\boldsymbol{F}$ of the deformation gradient is made. This yields the modified deformation gradient to take the representation

$$\tilde{\boldsymbol{F}} = \left[\frac{\phi}{\det(\Delta\boldsymbol{F} \cdot \tilde{\boldsymbol{F}}_n)}\right]^{1/3} \Delta\boldsymbol{F} \cdot \tilde{\boldsymbol{F}}_n \tag{4.5}$$

The use of $\tilde{\boldsymbol{F}}_n$ as the history variable is motivated by its spatial smoothness, which contributes to improved solution convergence. On the point-level, both $\boldsymbol{F}_n$ and $\tilde{\boldsymbol{F}}_n$ yield identical isochoric parts, as demonstrated by

$$\tilde{\boldsymbol{F}}_n^{\mathrm{iso}} = \frac{\tilde{\boldsymbol{F}}_n}{\det(\tilde{\boldsymbol{F}}_n)^{1/3}} = \frac{\phi^{1/3} \, \boldsymbol{F}_n^{\mathrm{iso}}}{\phi^{1/3}} = \boldsymbol{F}_n^{\mathrm{iso}} \tag{4.6}$$

However, significant spatial oscillations are exhibited by $\boldsymbol{F}$ making it unsuitable as history variable. These spatial oscillations stem from $\boldsymbol{F}^{\mathrm{vol}} = J^{1/3}\,\boldsymbol{I}$, which is no longer used in the element formulation. In contrast, the distribution of $\tilde{\boldsymbol{F}}$ is much smoother than the distribution of $\boldsymbol{F}$ and aligns better with the nodal field of ϕ, leading to a more robust implementation.

The P1P1 element does not satisfy the LBB stability conditions because both, the primary field $\boldsymbol{u}$ and the constraint field ϕ are approximated using identical first-order shape functions. The LBB condition conceptually requires that the primary field $\boldsymbol{u}$ exhibits a higher degree of continuity compared to the constraint field ϕ to ensure a well-defined coupled system of equations (4.2)-(4.3), cf. [153]. In a linear triangular element, the displacement gradient and consequently the Piola stress in (4.2) are constant. Therefore, reducing the order of continuity for the constraint field ϕ – a common approach used for other element formulations – is not applicable to satisfy the continuity requirements in this context. Hence, an extension of (4.3) is required to stabilise the formulation. Without this stabilisation, the mixed element formulation may exhibit apparent solution convergence during implementation, but volumetric locking and pressure oscillations still persist.

The Polynomial Pressure Projection, cf. [26, 105, 153], extends the constraint equation (4.3) to

$$\widetilde{\mathcal{W}}_{\phi} = \int_{\mathcal{B}_0} \delta\phi\,[\phi - J]\,\mathrm{d}V + \int_{\mathcal{B}_0} \frac{\alpha_{\mathrm{s}}^{\phi}}{G}\,\left[\delta\phi\,\phi - \delta\breve{\phi}\,\breve{\phi}\right]\,\mathrm{d}V = 0 \tag{4.7}$$

Hereby, the shear modulus G is measured in Pascals (Pa). Similarly, the stabilisation factor $\alpha_{\mathrm{s}}^{\phi}$ is assigned units of Pa to maintain the dimensionless nature of the constraint equation, as introduced in [90]. Moreover, $\breve{\phi}$ is a discontinuous projection of ϕ. The motivation of this approach is an L2-projection of the $C0$ continuous ϕ-field onto an elementwise constant and discontinuous field $\breve{\phi}$ in order to compensate for the interpolation mismatch. The L2 mapping reads

$$\int_{\mathcal{B}_0} \frac{1}{2}\,\left[\phi - \breve{\phi}\right]^2\,\mathrm{d}V \;\rightarrow\; \mathrm{Min} \qquad \Rightarrow \quad \int_{\mathcal{B}_0} \delta\breve{\phi}\,\left[\phi - \breve{\phi}\right]\,\mathrm{d}V = 0 \tag{4.8}$$

which is mentioned in [105, 153] to be solved element-wise for the unknown $\breve{\phi}$. However, the L2-mapping (4.8) can alternatively be directly inserted into (4.7) to condense $\breve{\phi}$ from the equations, cf. [26, 105, 153]. With identical linear shape functions N^A for both fields the discretisations reads

$$\boldsymbol{u}^e = \sum_{A=1}^{3} \boldsymbol{u}^{eA}\,N^A \qquad\qquad \frac{\partial \boldsymbol{u}}{\partial \boldsymbol{X}} = \sum_{A=1}^{3} \boldsymbol{u}^{eA} \otimes \frac{\partial N^A}{\partial \boldsymbol{X}} \tag{4.9}$$

$$\phi^e = \sum_{A=1}^{3} \phi^{eA}\,N^A \qquad\qquad \breve{\phi}^e = \sum_{A=1}^{3} \breve{\phi}^{eA}\,\breve{N}^A \tag{4.10}$$

with the shape functions formulated in the natural coordinates $\xi_\bullet$ of the master-element as

$$N^1 = 1 - \xi_1 - \xi_2\,, \qquad N^2 = \xi_1\,, \qquad N^3 = \xi_2 \tag{4.11}$$

$$\breve{N}^1 = 1/3\,, \qquad \breve{N}^2 = 1/3\,, \qquad \breve{N}^3 = 1/3 \tag{4.12}$$

The stabilisation term of the constraint equation (4.7) is discretised on element level as

$$\widetilde{\mathcal{W}}_{\phi\,\mathrm{stab}} = \delta\phi^A \int\limits_{\mathcal{B}_0^e} \frac{\alpha_\mathrm{s}^\phi}{G} \left[N^A N^B \, \phi^B - \breve{N}^A \breve{N}^B \breve{\phi}^B \right] \mathrm{d}V \tag{4.13}$$

with nodes A and B, where the nodal test function values of the last term has been interchanged from $\delta\breve{\phi}^A$ to $\delta\phi^A$ as mentioned in [153]. Now, the discretised form of the L2-Mapping (4.8) on element level results in

$$\delta\breve{\phi}^A \int\limits_{\mathcal{B}_0^e} \breve{N}^A N^B \,\mathrm{d}V \, \phi^B = \delta\breve{\phi}^A \int\limits_{\mathcal{B}_0^e} \breve{N}^A \breve{N}^B \,\mathrm{d}V \, \breve{\phi}^B \tag{4.14}$$

The direct solution of this mapping at the element level, as proposed in [105, 153], is not possible because the smoothing matrix, which results from the assembly process and precedes the solution vector $\breve{\boldsymbol{\phi}}^e$ of the element, becomes singular due to the shape functions (4.12). However, by inserting (4.14) into (4.13), the unknown discontinuous pressure variable $\breve{\phi}^B$ is condensed.

The discretised residual force contributions take the representations

$$\begin{aligned} \boldsymbol{f}_{\boldsymbol{u}}^{eA} = & \int\limits_{\mathcal{B}_0^e} \tilde{\boldsymbol{P}} \cdot \nabla_{\boldsymbol{X}} N^A \,\mathrm{d}V - \int\limits_{\mathcal{B}_0^e} \rho_0 \, N^A \, \boldsymbol{b} \,\mathrm{d}V \\ & - \int\limits_{\partial\mathcal{B}_0^{e\boldsymbol{t}}} N^A \, \boldsymbol{t}_0 \,\mathrm{d}A + \int\limits_{\mathcal{B}_0^e} \rho_0 \, N^A \, \boldsymbol{I} \, N^B \,\mathrm{d}V \;\cdot \ddot{\boldsymbol{u}}^B \end{aligned} \tag{4.15}$$

$$\begin{aligned} \boldsymbol{f}_{\phi}^{eA} = & - \int\limits_{\mathcal{B}_0^e} N^A \, J \,\mathrm{d}V \\ & + \Bigg[\int\limits_{\mathcal{B}_0^e} N^A N^B \,\mathrm{d}V + \underbrace{\int\limits_{\mathcal{B}_0^e} \frac{\alpha_\mathrm{s}^\phi}{G} \left[N^A N^B - \breve{N}^A N^B \right] \mathrm{d}V}_{K_{\phi\phi\,\mathrm{stab}}^{eAB}} \Bigg] \phi^B \end{aligned} \tag{4.16}$$

In (4.15), $\tilde{\boldsymbol{P}}$ depends nonlinearly on ϕ according to (4.6), which is why the internal contribution and its linearisations are integrated with three quadrature points. The

elemental stabilisation matrix $\mathbf{K}^{e}_{\phi\phi\,\mathrm{stab}}$ assembled from (4.16) consists of two mass-like matrices. The first is also integrated with three quadrature points because using only one quadrature points yields a zero matrix in the subtraction. In the references [26, 90, 105], the second mass-like contribution $\breve{N}^A N^B$ is given as $\breve{N}^A \breve{N}^B$ which does not fit into the above given derivation. In practice both matrices are identical due to identical constant $\breve{N}^A$ and the partition of unity property of N^B.

The linearisation of the residual contributions yields

$$\boldsymbol{K}^{eAB}_{\boldsymbol{uu}} = \int_{\mathcal{B}^e_0} \nabla_{\boldsymbol{X}} N^A \circ \frac{\partial \tilde{\boldsymbol{P}}}{\partial \tilde{\boldsymbol{F}}} : \frac{\partial \tilde{\boldsymbol{F}}}{\partial \boldsymbol{F}} \cdot \nabla_{\boldsymbol{X}} N^B \,\mathrm{d}V \tag{4.17}$$

$$\boldsymbol{K}^{eAB}_{\boldsymbol{u}\phi} = \int_{\mathcal{B}^e_0} \nabla_{\boldsymbol{X}} N^A \circ \frac{\partial \tilde{\boldsymbol{P}}}{\partial \tilde{\boldsymbol{F}}} : \boldsymbol{F} \left[\frac{1}{3} \frac{\phi^{[1/3-1]}}{J^{1/3}}\right] N^B \,\mathrm{d}V \tag{4.18}$$

$$\boldsymbol{K}^{eAB}_{\phi\boldsymbol{u}} = -\int_{\mathcal{B}^e_0} N^A \, J \, \boldsymbol{F}^{-\mathrm{t}} \cdot \nabla_{\boldsymbol{X}} N^B \,\mathrm{d}V \tag{4.19}$$

$$\boldsymbol{K}^{eAB}_{\phi\phi} = \int_{\mathcal{B}^e_0} N^A N^B \,\mathrm{d}V + \int_{\mathcal{B}^e_0} \frac{\alpha^{\phi}_{\mathrm{s}}}{G} \left[N^A N^B - \breve{N}^A N^B\right] \mathrm{d}V \tag{4.20}$$

with the notation $\circ$ being introduced in Section 2.2 and the deriviative in (4.17) follows from (4.6) as

$$\frac{\partial \tilde{\boldsymbol{F}}}{\partial \boldsymbol{F}} = \left[\boldsymbol{I} \,\overline{\otimes}\, \boldsymbol{I} - \frac{1}{3} \boldsymbol{F} \otimes \boldsymbol{F}^{-\mathrm{t}}\right] \left[\frac{\phi}{J}\right]^{1/3} \tag{4.21}$$

wherein $[\boldsymbol{I} \,\overline{\otimes}\, \boldsymbol{I}]_{ijkl} = \delta_{ik}\,\delta_{jl}$ and δ_{ij} denoting the Kronecker delta.

The stabilising contributions in (4.16) and (4.20) are governed by the stabilisation factor $\alpha^{\phi}_{\mathrm{s}}$, which will be discussed further in the following paragraph. In [90], a different stabilisation parameter α^{p}_{s} is introduced for the $\boldsymbol{u}$-p formulation compared to $\alpha^{\phi}_{\mathrm{s}}$ for the $\boldsymbol{u}$-ϕ formulation, and specific values for these factors are not provided. According to [26], an identical stabilisation factor $\alpha_{\mathrm{s}} = 1$ can be chosen for both formulations. However, to be precise, the units of the stabilisation factors differ between the two formulations. References [28, 111, 153] recommend $\alpha^{p}_{\mathrm{s}} \approx 1$ as a stabilisation factor for the $\boldsymbol{u}$-p formulation. This work proposes to use a stabilisation factor in the order of magnitude of the compression modulus, i.e. $\alpha^{\phi}_{\mathrm{s}} = K$. This choice is motivated by a simplified relation between the pressure p and the volume dilatation ϕ for nearly incompressible hyperelastic materials, as discussed in [22]. Thereby, the pressure p can be derived from the volumetric Helmholtz free energy density ψ^{vol} as

$$\psi^{\mathrm{vol}} = \frac{1}{2} K \,[J-1]^2 \qquad \Rightarrow \quad p = \frac{\partial \psi^{\mathrm{vol}}}{\partial J} = K\,[J-1] \tag{4.22}$$

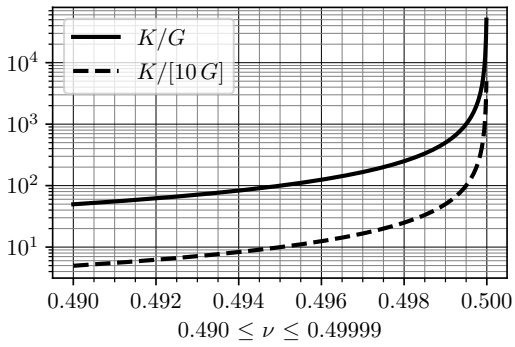

Figure 4.2: Ratio of compression modulus K and shear modulus G proposed as stabilisation prefactor. Reprinted from [119], licensed under CC BY 4.0.

which shows that J, and thus ϕ, is related to the pressure p via K. Therefore, $\alpha_{\mathrm{s}}^{\phi} = K$ should be suitable for the $\boldsymbol{u}$-ϕ formulation, while references [28, 111, 153] recommend $\alpha_{\mathrm{s}}^{p} \approx 1$ for the $\boldsymbol{u}$-p formulation. Interestingly, this leads to

$$\frac{\alpha_{\mathrm{s}}^{\phi}}{G} = \frac{K}{G} = \frac{2}{3}\frac{[1+\nu]}{[1-2\,\nu]} \tag{4.23}$$

as a prefactor for the stabilisation term in (4.16). This can be interpreted as a dimensionless factor scaling the amount of stabilisation according to the incompressibility of the material. The function is visualised in Figure 4.2 alongside a reduced prefactor of $K/[10\,G]$, both of which will be tested in the subsequent examples with respect to the influence on the solution quality and the stability of the element formulation.

Material model

A compressible Neo-Hooke-type hyperelastic material model is used with the Helmholtz free energy density

$$\psi_0 = \frac{1}{2}\,\lambda\,\ln^2(J) + \frac{1}{2}\,\mu\,[\boldsymbol{F}\colon\boldsymbol{F} - 3] - \mu\,\ln(J) \tag{4.24}$$

and the Lame parameters λ and μ which are related to the Young's modulus E and the Poisson ratio ν via

$$\lambda = \frac{E\,\nu}{[1+\nu][1-2\,\nu]}\,, \quad \mu = \frac{E}{2\,[1+\nu]} \tag{4.25}$$

as well as to the compression modulus K and shear modulus G via

$$\lambda = K - \frac{2\,G}{3}\,, \quad \mu = G \tag{4.26}$$

Resulting from a hyperelastic form, the Piola stresses $\boldsymbol{P}$ are expressed as

$$\boldsymbol{P} = \frac{\partial \psi_0}{\partial \boldsymbol{F}} = [\lambda \ln(J) - \mu] \, \boldsymbol{F}^{-\mathrm{t}} + \mu \, \boldsymbol{F} \tag{4.27}$$

$\}^{\text{qtd.}}_{[119]}$

4.1.3 Analysis of mapping methods and element formulations

$^{\text{qtd.}}_{[119]}\{$The performance of the element formulations and mappings is analysed in this section for 2d examples under plane strain conditions. A quasi-incompressible rubber block under compression is considered. The first example depicts a block strongly constrained in deformation by Dirichlet boundary conditions, with a Poisson ratio very close to $\nu = 0.5$. This example compares to literature results and investigates the influence of the stabilisation factor $\alpha_{\mathrm{s}}^{\phi}$ for the P1P1 formulation, along with a short element comparison to the TRI6 element. A second example compares the element performance of the P1P1 and the TRI6 element and the influence of the transfer-methods on a less constrained block with reduced incompressibility and relaxed geometric constraints compared to the first example.
The abbreviations used in the parameter studies are

- TRI6: six-noded 2d quadratic triangular element
- P1P1: mixed three-noded 2d linear triangular element with additional node variable ϕ, coupled to the local contribution $\det(\boldsymbol{F})$
- CPM: closest point mapping – state-variables are copied from the closest quadrature point of the previous mesh
- BTM: background triangle mapping – state-variables are interpolated from a background triangulation of the old quadrature points. Direct data copy for coinciding points.
- ISO1 (for BTM) – $\boldsymbol{F}^{\mathrm{vol}}$ and $\boldsymbol{F}^{\mathrm{iso}}$ are interpolated separately to approximately preserve isochoric deformations
- ISO2 (for BTM) – $\log(\boldsymbol{U})$ and $\log(\boldsymbol{R})$ are interpolated to exactly preserve isochoric deformations

In case of the P1P1 element, the modified deformation gradient $\tilde{\boldsymbol{F}}_n$ is used as the history variable instead of the deformation gradient $\boldsymbol{F}_n$ used in the TRI6 element. This also applies to the ISO1 and ISO2 decompositions. $\}^{\text{qtd.}}_{[119]}$

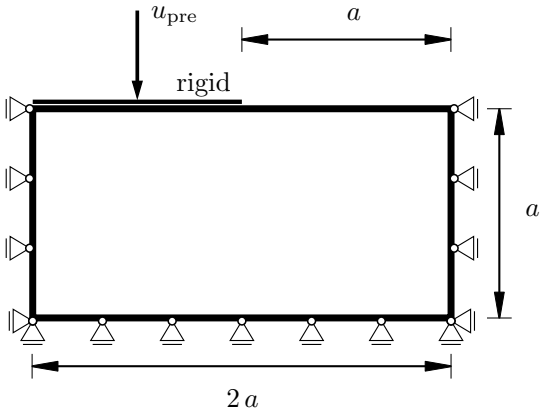

(a) Sketch of the boundary value problem.

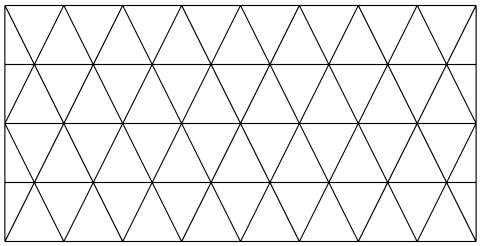

(b) Initial mesh with improved point distribution resulting in well shaped triangles.

Figure 4.3: Highly constrained rubber block under compression with $\nu = 0.49999$ and unit length $a = 1$ mm, after [21]. Reprinted from [119], licensed under CC BY 4.0.

4.1.3.1 Highly constrained rubber block under compression

qtd. [119]{The boundary-value problem depicted in Figure 4.3a is used as first benchmark, taken from [21, 84], to analyse the influence of the stabilisation factor α_{s}^{ϕ} and to find a suitable value for α_{s}^{ϕ}. A prescribed displacement of $u_{\text{pre}} = 0.2$ mm on the left half of the top surface is applied. The load represents a frictionless rigid indenter inducing a stress singularity at the middle of the top surface. The material is described by the Neo-Hooke model from (4.24) with a compression modulus $K = 10^5$ MPa and shear modulus $G = 2$ MPa, i.e. Young's modulus $E = 5.99996$ MPa and Poisson ratio $\nu = 0.49999$. Selecting a Poisson ratio close to the incompressible limit and enclosing the rubber blocks to both sides results in a quasi-incompressible deformation state. Simulating such behaviour is challenging within a finite element setting. A mesh grid is constructed with a resolution of 4×8 element edges by defining a regular arrangement of nodes. However, to improve mesh quality during deformation, the node distribution is further improved. In alternating rows, nodes are shifted by half an edge-length relative to the underlying regular grid. Additionally, endpoints are inserted in these rows to maintain a good boundary description. This refined mesh configuration enhances the grid's regularity, leading to significantly fewer unnecessary connectivity changes in the subsequent remeshing operations. The resulting mesh can be seen in Figure 4.3b. Since the grid is mostly regular, a constant $l_{\text{char}} = 0.2$ mm is used for the α-shape method along with $\alpha = 1.1$ for the α-test, cf. (2.53). The displacement is applied linearly in 200 steps of $\Delta u_{\text{pre}} = 0.001$ mm. The CPM variable mapping is chosen for this study, because connectivity changes occur only for low stabilisation parameters $\alpha_{\text{s}}^{\phi} \leq 100$ MPa and only for time, respectively load steps subsequent to $u_{\text{pre}} = 0.168$ mm. Consequently, the choice of mapping has minimal impact on the results and conclusions drawn from this example.

The stabilisation factor $\alpha_{\mathrm{s}}^{\phi}$ in the P1P1 formulation is analysed in Figure 4.4 by comparing the related force-displacement curves. Increasing the factor leads to softer behaviour. The value for $\alpha_{\mathrm{s}}^{\phi} = 1$ MPa reported in [26] yields a very stiff behaviour along with slight deviations from the smooth curves starting at $u_{\mathrm{pre}} = 0.168$ mm when the connectivities start to change and variable mapping becomes influential. These connectivity changes only occur in this example for small stabilisation factors $\alpha_{\mathrm{s}}^{\phi} \leq 100$ MPa and the resulting non-smooth deformations. The oscillations of the related force-displacement diagrams, which can be seen in the detail view in Figure 4.4, are a result of the transfer error of the CPM mapping. This can be seen in comparison with the FEM reference curve shown in the detail view of Figure 4.4, where these oscillations do not occur. The choice of $\alpha_{\mathrm{s}}^{\phi} = \{1, 2, 5, 10, 100\}$ MPa does not show a significant influence and the related curves quasi coincide. Choosing higher factors $\alpha_{\mathrm{s}}^{\phi} = \{10^3, 10^4, 10^5\}$ MPa leads to increasingly softer material behaviour. Hereby, $\alpha_{\mathrm{s}}^{\phi} = 10^4$ MPa $= K/10$ yields a final reaction force which is very similar to the results reported in [21, 84]. The references report final reaction force levels of approximately $F_{\mathrm{reac}} = 6.5$ N for different advanced finite element formulations. A comparison of pressure contour plots for $\alpha_{\mathrm{s}}^{\phi} = 1$ MPa and $\alpha_{\mathrm{s}}^{\phi} = 10^4$ MPa in Figure 4.5 shows the importance of increasing the stabilisation factor to avoid locking and pressure oscillations for such extreme quasi-incompressibility. The results indicate that an appropriate stabilisation factor might be $\alpha_{\mathrm{s}}^{\phi} = K/10$. This leads to a complete prefactor in the P1P1 formulation (4.16) of $\alpha_{\mathrm{s}}^{\phi}/G = K/[10\,G]$ which is a function of ν as depicted in Figure 4.2.

To compare the results for $\alpha_{\mathrm{s}}^{\phi} = K/10$ to the proposed TRI6 element, Figure 4.6 shows a comparison of both element formulations. The results show a stiffer behaviour for the TRI6 element, until the PFEM simulation no longer converges at $u_{\mathrm{pre}} = 0.172$ mm. The last converged time step is indicated with the $\times$-symbol in Figure 4.6. To enable a comparison nonetheless, Figure 4.6 also shows a comparison of both element formulations with their FEM version without remeshing. In these two PFEM simulations, no connectivity changes occurred and hence, the CPM preserves the state-variables perfectly and the simulation results are identical for the P1P1 element. However, the TRI6 PFEM-element bears another difference to its FEM counterpart apart from variable mapping, which is the resetting of the edge-mid-nodes to the straight edges between the corner-nodes. The resulting impact of the differing movability of the edge-mid-nodes is evident in the smoothness of the bulge curvature shown in Figure 4.7. This yields a loss of robustness which leads to divergence of the Finite Element solver of the PFEM-TRI6 simulation, as indicated in Figure 4.6. The FEM-TRI6 simulation converges without problems and shows an appropriate, but slightly stiffer behaviour compared to the P1P1 element. As the elements shall be applied in PFEM, the next section will show whether the TRI6 element is suitable for use in another test case. }$^{\text{qtd.}}_{[119]}$

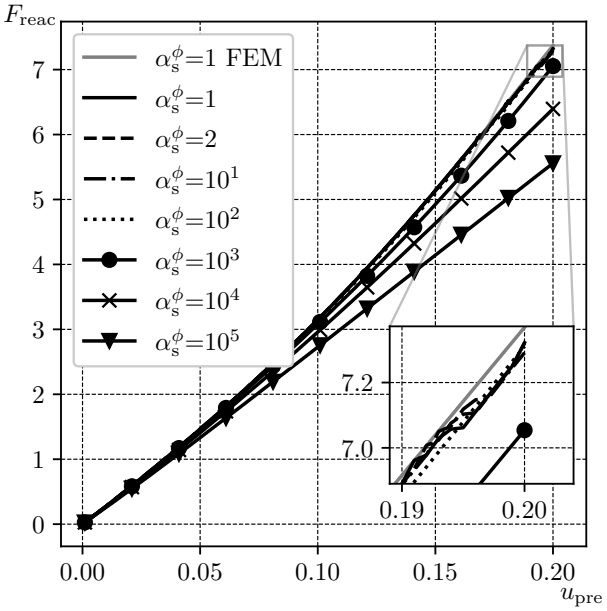

Figure 4.4: Influence of α_{s}^{ϕ} values in MPa on behaviour of P1P1 element with CPM mapping in PFEM. The reference FEM solution, visible in the detail view, shows that oscillations for small stabilisation values occur only when PFEM remeshing is used. Reprinted from [119], licensed under CC BY 4.0.

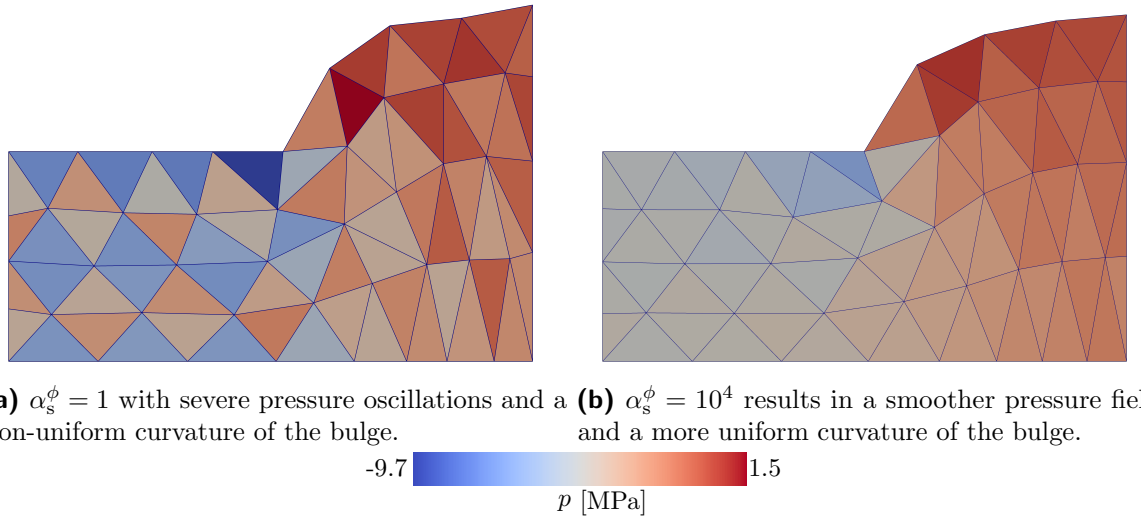

(a) $\alpha_{\text{s}}^{\phi} = 1$ with severe pressure oscillations and a non-uniform curvature of the bulge.

(b) $\alpha_{\text{s}}^{\phi} = 10^4$ results in a smoother pressure field and a more uniform curvature of the bulge.

Figure 4.5: Influence of stabilisation factor for P1P1 element on pressure distribution and surface curvature of the bulge. Reprinted from [119], licensed under CC BY 4.0.

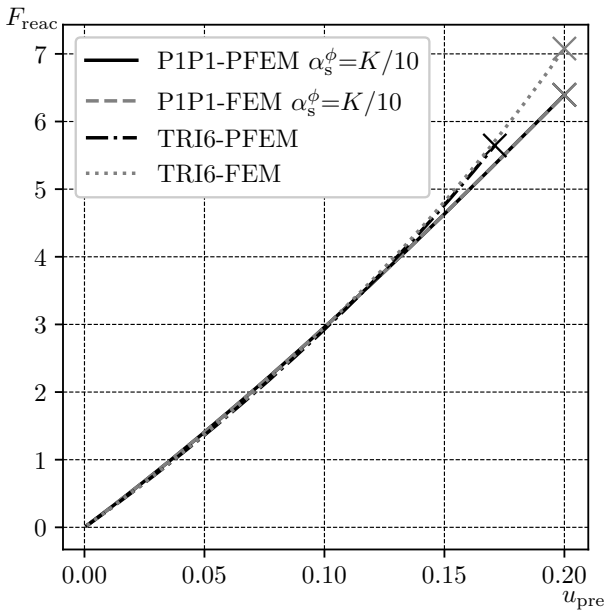

Figure 4.6: Comparison of P1P1 and TRI6 formulations and respective FEM formulations without remeshing. ×-symbol indicates last converged time step. Reprinted from [119], licensed under CC BY 4.0.

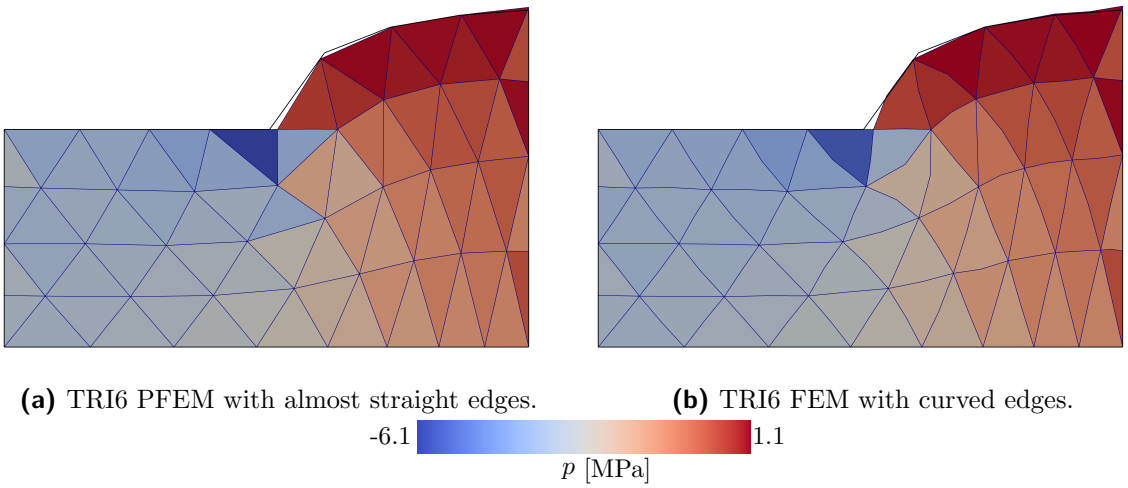

(a) TRI6 PFEM with almost straight edges. **(b)** TRI6 FEM with curved edges.

Figure 4.7: Influence of resetting the edge-mid-nodes in PFEM remeshing of the TRI6 element on the curvature of the bulge. Pressure plots at $u_{\text{pre}} = 0.172$ mm with grey outlines from P1P1 simulation with $\alpha_{\text{s}}^{\phi} = K/10$ MPa as reference. Reprinted from [119], licensed under CC BY 4.0.

4.1.3.2 Moderately constrained rubber block under compression

qtd. [119]{This section will investigate whether the choice of $\alpha_s^\phi = K/10$ also applies for less constrained boundary value problems and whether the element performance differences are similar to the previously analysed example. Furthermore, the influence of the variable mapping will be analysed for large deformations with significant connectivity changes which did not occur in the previous example. The influence of the mesh-density is also analysed. The following example is taken from [21] but reduced to 2d plane strain conditions. This indicates that the subsequent results are not quantitatively comparable with the reference, since the suppression of out-of-plane deformation increases the geometrical stiffness of the problem. The boundary value problem is illustrated in Figure 4.8. The material parameters are adopted from [21] as bulk modulus $K = 501$ MPa and shear modulus $G = 3.2296$ MPa, which is equivalent to a Young's modulus of $E = 9.6482$ MPa and a Poisson ratio of $\nu = 0.4968$. Moreover, boundary and incompressibility constraints are significantly weakened compared to the first example in Section 4.1.3.1. To be specific, the boundary on the right is considered as a free surface, a traction load is applied instead of prescribed displacements and a lower Poisson ratio is chosen. A time step size of $\Delta t = 0.1$ ms was tested for a majority of the parameter variations, resulting in robust solution convergence with only small deviations from finer time step sizes in the solution fields. However, for a more detailed resolution of the displacement vs. time step diagrams, which are essential for the analysis, a very fine time step of $\Delta t = 0.01$ ms is applied over 1000 steps. Smaller time steps result in more frequent remeshing and state-variable transfer, amplifying their effects. This emphasises the differences between the mapping methods, making the analysis simpler and clearer. The vertical traction load is defined in the reference configuration according to the Cauchy theorem as $\boldsymbol{t}_0 = \boldsymbol{P} \cdot \boldsymbol{N}$, representing a dead load. The magnitude of the traction load is linearly increased to the maximum of 30 MPa. Although the grid is regular at first, large deformations lead to significant stretching at the right edge of the traction load and compression on the left side. Therefore, the local characteristic length $l_{\text{char}}^{\text{loc}}$ from (2.55) is used for the α-shape method along with $\alpha = 2.5$ for the α-test, cf. (2.53). The high value of α allows for the preservation of highly stretched elements within the mesh. Typically, under such conditions, the shape of the body would change – however, this example focuses specifically on bulk behaviour rather than on surface changes.

The vertical displacement u_y^{mid} of the left-most node on the top surface is analysed, which corresponds to the midpoint considering symmetry boundary conditions at the left edge. The influence of the stabilisation factor α_s^ϕ is observed to be less significant in this example compared to the first case in Section 4.1.3.1. Figure 4.9 illustrates the resulting midpoint vertical displacements u_y^{mid} over time steps for a 32×32 discretisation. The compression of the block leads in general to a stiffening behaviour which can be seen in the reduction of the displacement slope. The displacement vs. load step curves for different values of α_s^ϕ are almost identical – a close-up view shows that the behaviour is slightly softer with increasing values of α_s^ϕ. However, for $\alpha_s^\phi = K = 501$ MPa the

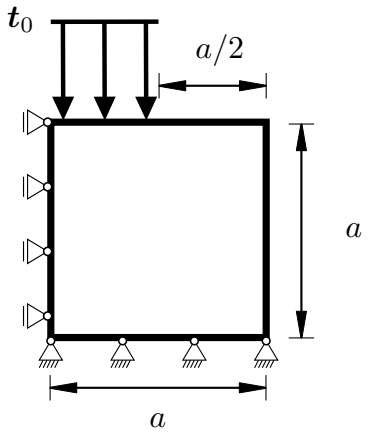

Figure 4.8: Moderately constrained rubber block under compression from vertical traction $\boldsymbol{t}_0$, with $\nu = 0.4968$ and length $a = 50$ mm – plane strain version of example considered in [21]. Reprinted from [119], licensed under CC BY 4.0.

connectivity-changes occurring in the remeshing tend to flip back and forth from one step to the next, leading to result deviations and finally to divergence of the solution algorithm. The displacement vs. time step curve in Figure 4.9 for $\alpha_{\mathrm{s}}^{\phi} = 501$ MPa shows the resulting transfer error in minimal deviations from a smooth path, with slight oscillations evident along its length. In Figure 4.10 the corresponding flipping of the mesh edges can be seen for a representative set of time steps. A study of the pressure fields reveals that $\alpha_{\mathrm{s}}^{\phi} = 1$ on the other hand is too small to suppress oscillations of the pressure field especially for small deformations at time step 10, see Figure 4.11. Interestingly, deformation and pressure field are almost identical when comparing the last time step for $\alpha_{\mathrm{s}}^{\phi} = 1$ MPa and $\alpha_{\mathrm{s}}^{\phi} = 50.1$ MPa, which can be seen in Figure 4.12. Mostly oscillation-free pressure fields throughout the load-path and no instabilities that occur for higher values support the conclusion of the previous example in Section 4.1.3.1 in proposing $\alpha_{\mathrm{s}}^{\phi} = K/10$ as stabilisation factor for P1P1 elements of $\boldsymbol{u}$-ϕ type.

After an appropriate stabilisation factor for the P1P1 element has been determined from the above analysis, the performance of the two element formulations, along with the influence of state-variable transfer methods and mesh size, will be investigated. Regarding mesh-size, increasing the mesh density leads to problems in this example due to the stress concentration at the right edge of the traction load. The finer mesh resolves this stress concentration instead of smoothing it. Therefore a comparison of mesh sizes is limited, e.g. a 64×64 mesh did not deliver more insight but would have required advanced remeshing techniques such as point-insertion, which are not in the focus of this work, see e.g. [111]. However, the two mesh-sizes 16×16 and 32×32 delivered comprehensive results without the singularity influencing the comparison. Figure 4.13 shows the resulting displacements of the top surface's midpoint u_y^{mid} of a 16×16 and a 32×32 grid for all elements and state-variable transfer methods. The finer discretisation shows quite smooth curve profiles for most parameters as illustrated in Figure 4.13c and Figure 4.13d with

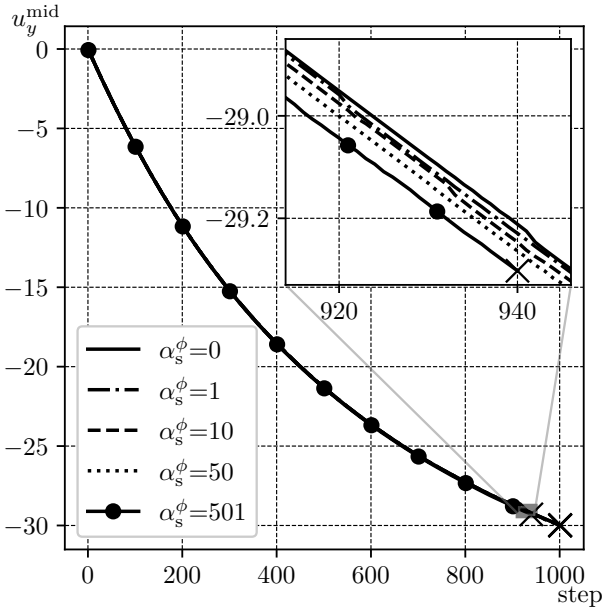

Figure 4.9: Influence of α_s^ϕ on behaviour of P1P1 element with CPM mapping for moderate test. Increasing α_s^ϕ yields slightly softer response, instabilities for α_s^ϕ=K=501, ×-symbol indicates last converged time step. Reprinted from [119], licensed under CC BY 4.0.

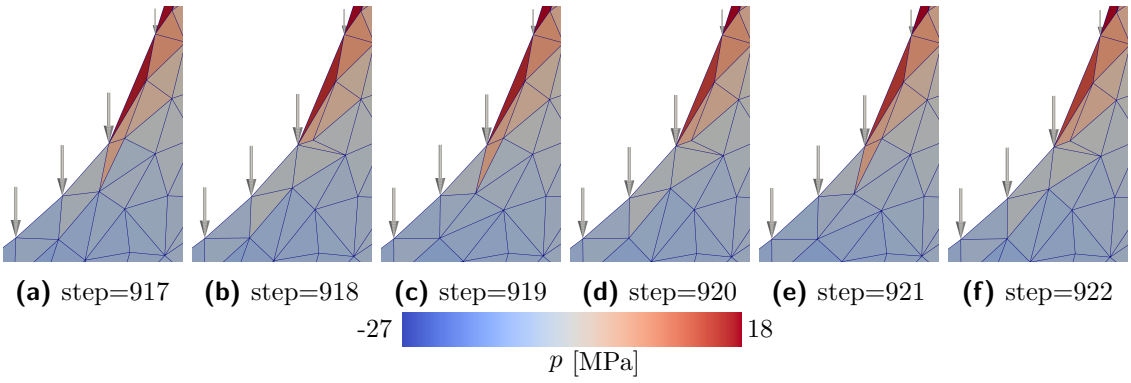

Figure 4.10: Section of the mesh close to the right edge of the nodal traction load area for representative time steps. Arrows show the nodal surface forces which represent the vertical traction load $\boldsymbol{t}_0$. P1P1 Element with CPM and $\alpha_s^\phi = K = 501$ MPa reveals back and forth flipping of the connectivities. Reprinted from [119], licensed under CC BY 4.0.

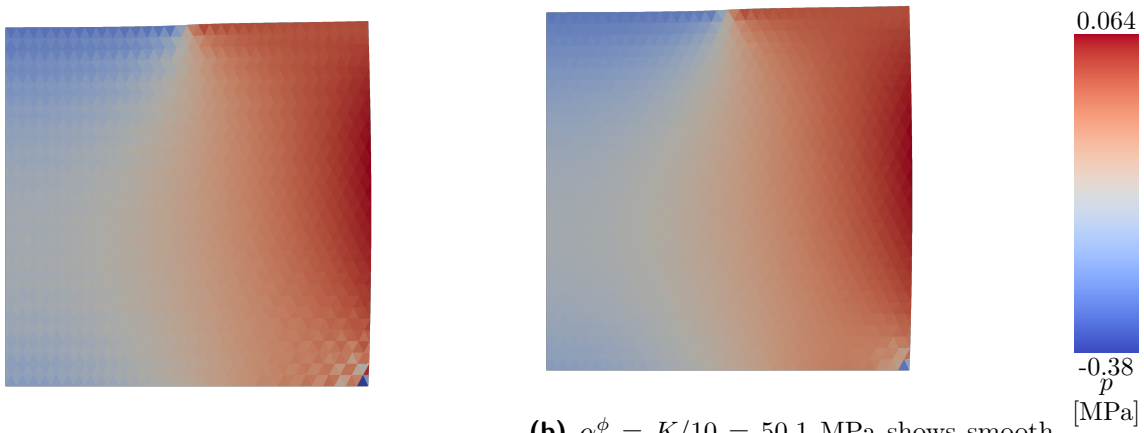

(a) $\alpha_s^\phi = 1$ MPa shows pressure oscillations

(b) $\alpha_s^\phi = K/10 = 50.1$ MPa shows smooth pressure field

Figure 4.11: Comparison of pressure field for P1P1 element with CPM at time step 10 of 1001. Reprinted from [119], licensed under CC BY 4.0.

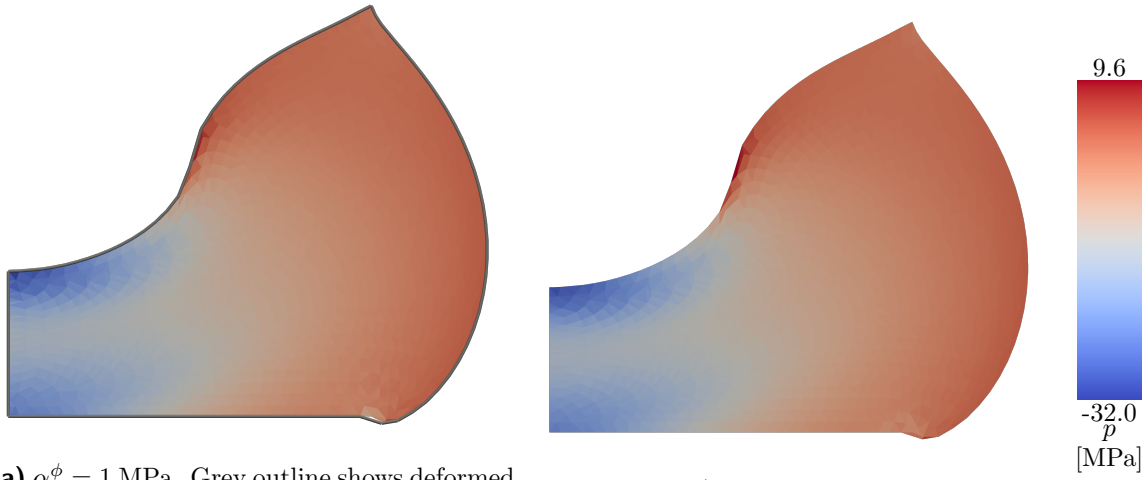

(a) $\alpha_s^\phi = 1$ MPa. Grey outline shows deformed contour of $\alpha_s^\phi = 50.1$ MPa for comparison

(b) $\alpha_s^\phi = K/10 = 50.1$ MPa

Figure 4.12: Comparison of deformation and pressure field for P1P1 element with CPM at last time step 1001 shows almost identical results for both factors. Reprinted from [119], licensed under CC BY 4.0.

some clear distinctions. To be specific, the CPM mapping produces more deviations from the smooth curve paths due to the variable mapping than the BTM mapping. For the fine discretisations, the treatment of the isochoric states with the ISO1 and ISO2 approach during BTM-interpolation yields almost identical curves. However, using no treatment of isochoric states (BTM-ISO0) leads to algorithmic divergence in the P1P1 formulation visible in Figure 4.13d. Also for the coarse discretisation, a BTM mapping with a simple interpolation of the variables (BTM-ISO0) leads to early divergence of the solution algorithm and to large deviations from the solution path in both, the TRI6 formulation in Figure 4.13a and the P1P1 formulation in Figure 4.13b. Interpolating $\boldsymbol{F}^{\text{vol}}$ and $\boldsymbol{F}^{\text{iso}}$ separately (BTM-ISO1) leads to better convergence, although the TRI6 element still shows large deviations towards the end. The special interpolation scheme introduced in (2.60) (BTM-ISO2) yields a smooth curve progression superior to the CPM method and the BTM method with ISO0 or ISO1. Comparing the two element types, especially for the coarse discretisation a clear advantage in robustness is visible for the P1P1 element in the sense of a regularity in the progression of the result curve. Even with the best mapping (BTM-ISO2) the TRI6 element still shows deviations from a smooth curve. For the fine discretisation, the TRI6 element is clearly also suitable for use and yields similar results to the P1P1 element when using the BTM transfer scheme. $\}^{\text{qtd.}}_{[119]}$

4.1.3.3 Calculation times

$^{\text{qtd.}}_{[119]}\{$From a theoretical perspective, the TRI6 element is expected to require more calculation time than the P1P1 element due to the presence of 12 elemental degrees of freedom (TRI6), compared to 9 (P1P1) within a 2d setting. In a practical test of the present implementation in MATLAB conducted on identical computer hardware, the TRI6 element demonstrated a 90% increase in computation time for the 16×16 mesh and a 40% increase for the 32×32 mesh. The overhead associated with deleting and inserting edge-mid-nodes in the TRI6 formulation appears to diminish with finer discretisation, primarily attributing the longer calculation times to the difference in the number of degrees of freedom. For the different state-variable transfer methods, the overall time step calculation-time did not vary significantly. Especially for increased deformation, the simulations featuring the BTM-ISO1 or -ISO2 mappings tend to need less iteration steps in the global FEM solution which compensates for the higher numerical cost of the variable mapping. $\}^{\text{qtd.}}_{[119]}$

4.1.4 Quasi-Incompressibility in PFEM – Conclusion

$^{\text{qtd.}}_{[119]}\{$The previous sections investigated the applicability of the TRI6 element for quasi-incompressible elasticity in the context of the Particle Finite Element Method under 2d plane strain conditions. The element was compared with the established P1P1 element in the less investigated but beneficial $\boldsymbol{u}$-ϕ version, which does not necessitate a volumetric-isochoric split in the material model. Both element formulations were

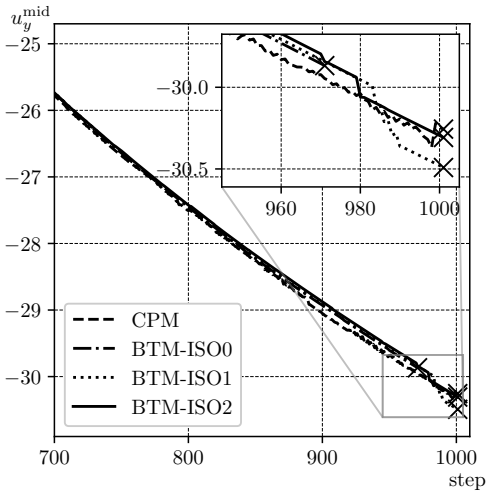

(a) 16×16 TRI6 elements – algorithmic divergence of BTM-ISO0 at time step 971

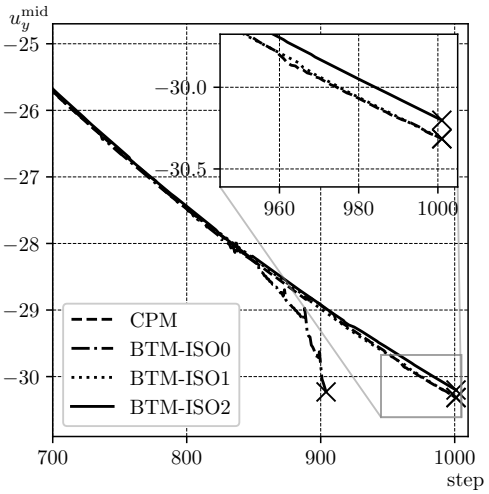

(b) 16×16 P1P1 elements – algorithmic divergence of BTM-ISO0 at time step 904

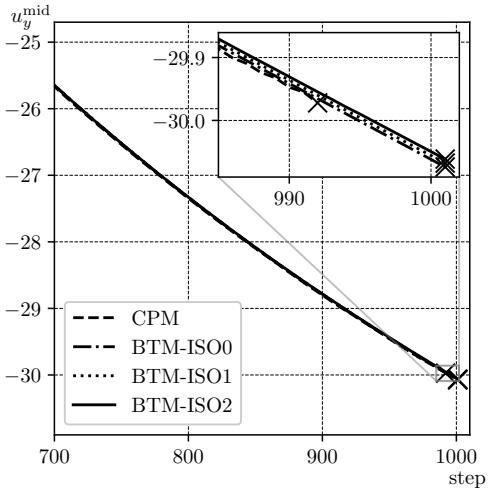

(c) 32×32 TRI6 elements – algorithmic divergence of CPM at time step 992

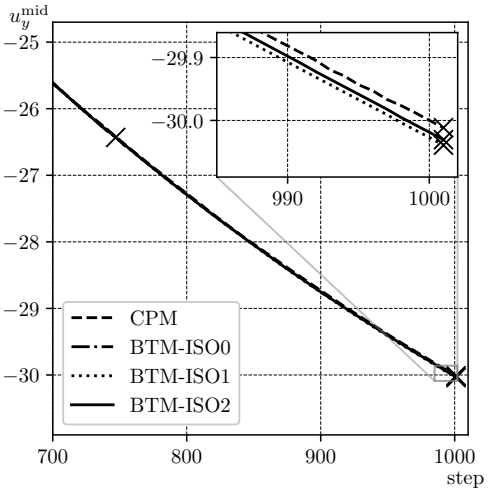

(d) 32×32 P1P1 elements – algorithmic divergence of BTM-ISO0 at time step 747

Figure 4.13: Performance of both element types depending on meshsize and state-variable transfer schemes. The coarse mesh in subfigures (a) and (b) shows the advantage of the BTM-ISO2 mapping for better stability and the overall better performance of the P1P1 element. The TRI6 element shows similar performance as the P1P1 element in the fine discretisation in subfigures (c) and (d). The last converged time step is indicated with a ×-symbol for each time-series. Reprinted from [119], licensed under CC BY 4.0.

embedded into PFEM, which involves the frequent remeshing of the node points, a shape-detection, the transfer of state-variables and an updated Lagrangian FE-formulation. For the state-variable transfer, an improved algorithm using an interpolation from the previous quadrature points was investigated along with approaches to preserve the quasi-incompressible deformation states during interpolation. The element formulations were described with details for the handling of edge-mid-nodes in the TRI6 element and complemented the P1P1 literature with respect to the choice of the deformation history tensor and the stabilisation factor.

The following conclusions can be drawn from the investigations:

- the stabilisation factor for the P1P1 formulation is advised not be set to $\alpha_{\mathrm{s}}^{\phi} = 1$ MPa, as suggested in [26]. Instead, a value $\alpha_{\mathrm{s}}^{\phi} = K/10$ MPa is recommended, which has demonstrated good agreement with literature reaction-force values, smooth progression of result curves during the simulation and avoiding pressure-oscillations. This recommendation is summarised in a simple equation for the stabilisation factor based on the Poisson ratio. Hereby, the results showed that an adjustment of the theoretically motivated equation is advisable, yielding

$$\frac{\alpha_{\mathrm{s}}^{\phi}}{G} = \frac{K}{10\,G} = \frac{2}{30}\frac{[1+\nu]}{[1-2\,\nu]} \tag{4.28}$$

  as the proposed prefactor for the stabilisation term in the P1P1 formulation, see (4.7). Therefore, the stabilisation can be automatically adjusted to the degree of quasi-incompressibility of the considered hyperelastic problem.

- for Poisson ratios very close to 0.5 along with high geometrical constraints in the boundary value problem under consideration, the P1P1 element clearly outperforms the TRI6 element when an appropriate stabilisation factor $\alpha_{\mathrm{s}}^{\phi}$ is chosen.

- for less severe quasi-incompressibility and less geometrical constraints in the considered boundary value problem, both elements perform equally for a fine discretisation. For a coarser discretisation the P1P1 element again performs better.

- the state-variable transfer which is currently most established in the literature is the CPM mapping, cf. [28, 111]. The mapping results in severe oscillations of representative displacement vs. time step curves due to the repeated remeshing. Especially coarse discretisations benefit considerably from the more advanced transfer scheme BTM. Apart from [147], such algorithm has not yet been established in the PFEM literature. The results clearly show that the BTM is best combined with a special interpolation operation, where the scheme based on a polar decomposition (ISO2) performs very well, but also the separate interpolation of $\boldsymbol{F}^{\mathrm{vol}}$ and $\boldsymbol{F}^{\mathrm{iso}}$, denoted as ISO1, yields results superior to the established CPM mapping.

It has been shown that a TRI6 element is indeed applicable in PFEM simulations with quasi-incompressible deformation states. In view of the higher number of degrees of

freedom in the TRI6 element compared to the P1P1 element leading to a higher computational cost, due to the more involved handling of variables in the TRI6 formulation, and especially due to the overall better performance of the P1P1 element, the already established P1P1 formulation is recommended. For this formulation implemented in a strict deformation based Updated-Lagrange PFEM formulation, this work adds important details on history variable handling and brings a rarely used advanced transfer method, the BTM mapping, into focus. Especially coupled with interpolation operators preserving the isochoric deformation states, the additional effort of the mapping pays out in a reduced number of iteration steps, better algorithmic convergence and smoother progression of solution-quantities during the simulation, especially for coarser meshes.

The adaption of PFEM to 3d simulations significantly increases the complexity of the geometric meshing and required re-meshing methods, cf. [26, 85]. Therefore, the application of PFEM in 3d simulations has not been addressed in this work. However, the element formulations and state-variable transfer methods discussed here are directly applicable to 3d simulations. Nevertheless, the conclusions drawn from this study should be validated through 3d simulations in future research.

For inelastic material models with more state-variables and high strain levels, future work shall investigate the optimal remeshing frequencies in order to find a compromise between the mapping errors and the resolution of material deformation and shape changes. Moreover, in future applications, e.g. the simulation of Direct Energy Deposition and the incompressible flow of molten metal, it will be necessary to reassess whether the P1P1 element continues to outperform the TRI6 element. The stabilisation factor for the P1P1 element needs to be readjusted to the problem because the proposed relation (4.28) is only valid for hyperelasticity. Here, the TRI6 element can be an alternative since it does not rely on a stabilisation factor. Furthermore, the TRI6 element can be an alternative when the P1P1 element is not applicable in a specific programming environment or software package. }$^{\text{qtd.}}_{[119]}$

4.2 The contact domain method

The contact simulation in this work is an application of the Contact Domain Method (CDM) as presented in [58, 97]. The contact domain consists of elements of the same spatial dimensionality as the base bodies which are spanned between the surfaces of the contact partners. These elements provide the discretisation of the gap function on which the solution of the contact constraints is based, here with a stabilised Lagrange multiplier approach. The contact model is summarised below on the basis of the references cited. The main difference in the current work is the application in PFEM which requires the transfer of some contact related quantities. The CDM has already been applied in PFEM in e.g. [26, 28]. Furthermore, in the current work the bulk bodies are not modelled by linear triangular elements as in [58, 97], but by a mixed formulation P1P1 and a

quadratic triangle TRI6, which will be discussed in relation to the non-constant stresses within these elements.

4.2.1 Nitsche-type contact constraint enforcement

The contact constraints of impenetrability and stick friction represent inequality constraints for the solution of the linear momentum balance as presented in Section 2.3.2. Since the direct solution of a Lagrange multiplier approach suffers from numerical instabilities, [58, 97] propose a Stabilised Lagrange Multiplier Method (SLMM) which yields a similar formulation to the Nitsche approach. The SLMM defines the Lagrange multiplier of normal contact λ_N based on the normal traction t_N of the material at the surface, which is a function of the Piola stress $\boldsymbol{P}$ and the normal surface vector. Similarly, the stick friction Lagrange multiplier λ_T is coupled to the tangential traction t_T. In this way, the contact model is coupled to the bulk material model of the underlying finite elements, resulting in a more robust formulation. A visualisation of a contact domain discretisation is shown in Figure 4.14.

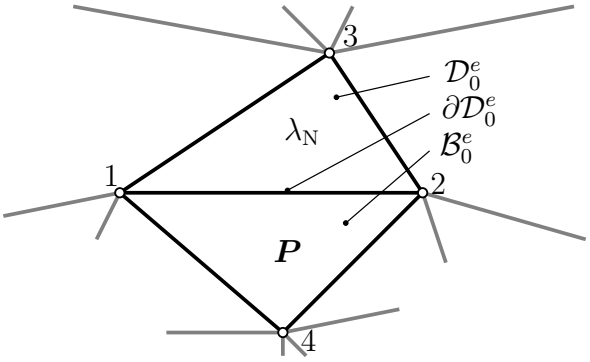

Figure 4.14: A contact domain element where λ_N is defined, associated with the underlying bulk element where $\boldsymbol{P}$ is defined.

The weak form of the linear momentum balance extended by the contact contributions is generally introduced in (2.48), (2.49) and (2.50). For the CDM formulation, the boundary integrals are formulated in the contact domain, which has the same dimensionality as the bulk bodies. In addition, the solution with SLMM adds stabilisation contributions to the constraint equations, so that the coupled system of equations becomes

$$\delta\Pi_\mathrm{int} - \delta\Pi_\mathrm{ext} + \int\limits_{\mathcal{D}_0^{\mathrm{cN}}} \lambda_\mathrm{N}\,\delta\overline{g}_\mathrm{N}\,\mathrm{d}V + \int\limits_{\mathcal{D}_0^{\mathrm{cT}}} \lambda_\mathrm{T}\,\delta\overline{g}_\mathrm{T}\,\mathrm{d}V + \int\limits_{\mathcal{D}_0^{\mathrm{cS}}} \mathcal{T}\,\delta\overline{g}_\mathrm{T}\,\mathrm{d}V = 0 \tag{4.29}$$

$$\int_{\mathcal{D}_0^{\mathrm{cN}}} \overline{g}_{\mathrm{N}}\, \delta\lambda_{\mathrm{N}}\, \mathrm{d}V + \int_{\partial\mathcal{D}_0^{\mathrm{cN}}} \tau\, [t_{\mathrm{N}} - \lambda_{\mathrm{N}}]\, \delta\lambda_{\mathrm{N}}\, \mathrm{d}A = 0 \tag{4.30}$$

$$\int_{\mathcal{D}_0^{\mathrm{cT}}} \overline{g}_{\mathrm{T}}\, \delta\lambda_{\mathrm{T}}\, \mathrm{d}V + \int_{\partial\mathcal{D}_0^{\mathrm{cT}}} \tau\, [t_{\mathrm{T}} - \lambda_{\mathrm{T}}]\, \delta\lambda_{\mathrm{T}}\, \mathrm{d}A = 0 \tag{4.31}$$

where the coupling of the Lagrangian multipliers λ_{N} and λ_{T} to the tractions t_{N} and t_{T} is controlled by the interior penalty parameter τ, and the traction for sliding friction $\mathcal{T}$ is defined in (2.52). As the equilibrium solution already aims for the bulk traction vector to be equal to the contact traction vector, this interior penalty parameter does not need to be as large as in classic penalty parameter methods. Instead of the physical gaps, strain-like quantities $\overline{g}_{\mathrm{N}}$ and $\overline{g}_{\mathrm{T}}$ are used as gap measures. The contact domain experiencing active normal contact is denoted by $\mathcal{D}_0^{\mathrm{cN}}$, which in turn is divided into the active stick domain $\mathcal{D}_0^{\mathrm{cT}}$ and the slip domain $\mathcal{D}_0^{\mathrm{cS}} = \mathcal{D}_0^{\mathrm{cN}} \setminus \mathcal{D}_0^{\mathrm{cT}}$. Furthermore, the coupling contributions are defined at the boundary between the contact domain and the underlying bulk domain, denoted by $\partial\mathcal{D}_0$, as shown in Figure 4.14.

Remark: The Nitsche approach can also be defined with a potential

$$\Pi_{\mathrm{cN}}(\boldsymbol{u}, \lambda_{\mathrm{N}}) = \Pi_{\mathrm{int,ext}} + \int_{\partial\mathcal{B}_0^{\mathrm{cN}}} t_{\mathrm{N}}\, g_{\mathrm{N}}\, \mathrm{d}A + \int_{\partial\mathcal{B}_0^{\mathrm{cN}}} \frac{1}{2}\, \tau\, g_{\mathrm{N}}^2\, \mathrm{d}A \tag{4.32}$$

and a direct constitutive assumption on the normal traction t_{N}, coupling it to the adjacent bulk stresses, see [141]. This leads to a similar extension of the weak form without the need to first derive the condensation of the Lagrangian multipliers. However, the derivation in [97] is used in the present work as it is common in the PFEM literature.

4.2.2 Contact kinematics

The kinematics of the contact formulation are visualised in Figure 4.15. All quantities are based on the previous configuration $\mathcal{B}_n$ in which the contact mesh is regenerated. The current gap vector $\boldsymbol{g}$ is calculated from the incremental deformation gradient $\Delta\boldsymbol{F}$ as

$$\boldsymbol{g} = \Delta\boldsymbol{F} \cdot \boldsymbol{G} = g_{\mathrm{N}}^{(0)} \left[\boldsymbol{I} + \frac{\partial \Delta\boldsymbol{u}}{\partial \boldsymbol{X}_n}\right] \cdot \boldsymbol{N} \tag{4.33}$$

with the incremental displacement $\Delta\boldsymbol{u}$ and the normal gap in the previous configuration $g_{\mathrm{N}}^{(0)}$. The normal and tangential components follow as

$$g_{\mathrm{N}} = \boldsymbol{n} \cdot \boldsymbol{g} \quad \text{and} \quad g_{\mathrm{T}} = \boldsymbol{t} \cdot \boldsymbol{g} \tag{4.34}$$

Consequently, the gap function is defined in the entire contact domain in theory, which is reasonable given the volume integrals of the contact contributions in the weak form

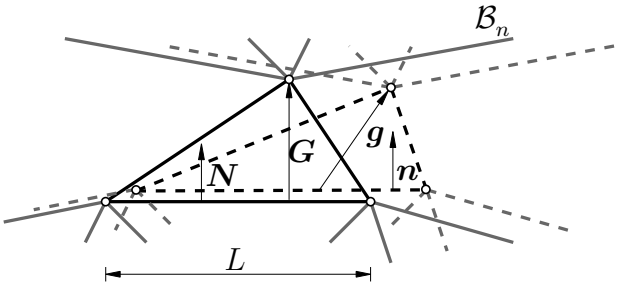

Figure 4.15: A contact domain element deforming based on the previous configuration $\mathcal{B}_n$ with the previous gap vector $\boldsymbol{G}$ and the deformed gap vector $\boldsymbol{g}$ with respect to node 3 as well as the previous normal vector $\boldsymbol{N}$ and the current normal vector $\boldsymbol{n}$.

(4.29), (4.30) and (4.31). However, by restricting the formulation to linear triangular elements, the formulation can be greatly simplified, and the method becomes much more robust through the analytical solutions that are possible by this restriction. The evaluation of gap vectors is restricted to the opposite node 3, which also represents the physical gap in the considered element. Quantities related to node 3 are denoted $(\bullet)_3$. The previous gap vector $\boldsymbol{G}$, the base side length L, the height H and the normal and tangential vectors $\boldsymbol{N}$ and $\boldsymbol{T}$ can be calculated directly from the nodal positions $\mathbf{X}_n^e$ of the element. The current discrete gap measures of node 3 are then defined as

$$(g_{\mathrm{N}})_3 = \left(g_{\mathrm{N}}^{(0)}\right)_3 \boldsymbol{n} \cdot \left[\boldsymbol{I} + \frac{\partial \Delta \boldsymbol{u}}{\partial \boldsymbol{X}_n}\right] \cdot \boldsymbol{N} \tag{4.35}$$

$$(g_{\mathrm{T}})_3 = \left(g_{\mathrm{N}}^{(0)}\right)_3 \boldsymbol{t} \cdot \left[\boldsymbol{I} + \frac{\partial \Delta \boldsymbol{u}}{\partial \boldsymbol{X}_n}\right] \cdot \boldsymbol{N} \tag{4.36}$$

and the strain like gap quantities follow as $\overline{g}_{\mathrm{N}} = (g_{\mathrm{N}})_3/H$ and $\overline{g}_{\mathrm{T}} = (g_{\mathrm{T}})_3/H$. The gap measures still depend on the displacement gradient, which is constant in the triangle, but must be calculated by using the inverse Jacobian $\boldsymbol{J}^{-1} = \partial \boldsymbol{\xi}/\partial \boldsymbol{X}_n$ with the natural coordinates $\boldsymbol{\xi}$ of the master element. To avoid problems with the singularity of the Jacobian for the near-zero thickness of the contact elements, [58] uses the linear shape functions N_A to define the gradient of the incremental displacement

$$\Delta \boldsymbol{u}^e = \sum_{A=1}^{3} \Delta \boldsymbol{u}_C \otimes \frac{\partial N_A}{\partial \boldsymbol{X}_n} \cdot \boldsymbol{N} \tag{4.37}$$

and derives analytical expressions for the directional derivatives $[\partial N_A/\partial \boldsymbol{X}_n] \cdot \boldsymbol{N}$. These analytical derivatives are purely based on the geometry and displacement of the contact element and are therefore robust and independent of the shape and height of the element. The specific terms are given in the reference. The linearisation of the gap quantities also uses these analytical derivatives, but requires the linearisation of the normal and tangential vectors, which are given in the appendix of [97]. Please refer to [58, 97] for the linearisation of the kinematic gap quantities.

4.2.3 Condensation of the Lagrange multipliers

A further simplification of the CDM formulation by using linear triangles are the resulting constant integrands of the weak form integrals. The elemental contact domain integrals for the 2d case therefore follow as

$$\int_{\mathcal{D}_0^e} \bullet \, \mathrm{d}V = \frac{1}{2} L \, H \bullet \qquad\qquad \int_{\partial\mathcal{D}_0^e} \bullet \, \mathrm{d}A = \bullet \, L \tag{4.38}$$

by assuming a unit thickness of the plane problem. By applying this analytical integration to the stabilised constraint equations (4.30) and (4.31), by elimination of the variations $\delta\lambda_\mathrm{N}$ and $\delta\lambda_\mathrm{T}$ and by using the gap strains $\overline{g}_\mathrm{N} = (g_\mathrm{N})_3/H$ and $\overline{g}_\mathrm{T} = (g_\mathrm{T})_3/H$ this yields scalar relations defining the element-wise constant Lagrange multipliers

$$\lambda_\mathrm{N} = \frac{(g_\mathrm{N})_3}{2\,\tau} + t_\mathrm{N} \tag{4.39}$$

$$\lambda_\mathrm{T} = \frac{(g_\mathrm{T})_3}{2\,\tau} + t_\mathrm{T} \tag{4.40}$$

as a purely displacement-dependent formulation. The interior penalty parameter τ therefore has the units mm^3/N and [58] therefore couples the parameter to the elastic properties and the local mesh density by defining

$$\tau = \frac{\alpha_\mathrm{stab}}{E_\mathrm{min}} L \tag{4.41}$$

where E_min is the minimum Young's modulus of the contacting bodies and α_stab is an adjustment parameter that controls the amount of contact regularisation but has little effect on the accuracy of constraint enforcement.

Remark: For the closed-form derivation of (4.39) and (4.40), t_N and t_T must also be constant along $\partial\mathcal{D}_0$. As mentioned in [97], otherwise the boundary integral has to be integrated numerically. In the present work, the P1P1 element provides a non-constant correction of the deformation gradient by the global ϕ-field, see (4.6), and the TRI6 generally has a non-constant deformation gradient. Therefore, the stresses and consequently also the traction vectors are not constant in the bulk elements. However, in the present work, for the sake of simplicity, the stresses and their linearisation are recalculated in the contact element routine for the underlying bulk elements. For the recalculation in the P1P1 element, the incremental deformation gradient is evaluated at the element centre and combined with state-variables of the first quadrature point in the data structure, i.e. with any of the three quadrature points available. The TRI6 element is treated similarly, but only the corner point displacements are used for the incremental deformation gradient. The formulation is a simplification but still provides a reasonable approximation of tractions and linearisations leading to a functional Nitsche formulation.

4.2.4 Discrete contact force contribution for normal contact

By condensing the Lagrange multipliers, the global system of equations for the mechanical contact problem is reduced to (4.29). The contact contributions are now explicitly defined by the contact kinematics and by the coupling of the contact traction to the underlying bulk stresses. The normal contact contribution to the weak form at the elemental level is

$$\delta \Pi^e_{\mathrm{cN}} = \int\limits_{\mathcal{D}_0^{\mathrm{cN}}} \lambda_{\mathrm{N}}\, \delta \overline{g}_{\mathrm{N}}\, \mathrm{d}V \tag{4.42}$$

The variation of the normal gap is derived in [97] as

$$\delta \overline{g}_{\mathrm{N}} = \overline{g}_{\mathrm{N}}\, \boldsymbol{n} \cdot \frac{\partial (\delta \Delta \boldsymbol{u})}{\partial \boldsymbol{x}} \cdot \boldsymbol{n} \tag{4.43}$$

where the spatial gradient is approximated by linear nodal shape functions N_A as

$$\delta \Delta \boldsymbol{u}^e = \sum_{A=1}^{3} \delta \Delta \boldsymbol{u}_C \otimes \frac{\partial N_A}{\partial \boldsymbol{x}} \cdot \boldsymbol{n} \tag{4.44}$$

Similar to (4.37), directional derivatives are derived analytically as given in [58] to circumvent ill-posedness of the coordinate transformation for zero-volume or inverted contact elements. With the use of analytical integration (4.38) and the directional derivatives, the discrete elemental normal contact contribution follows as

$$\delta \Pi^e_{\mathrm{cN}} = \sum_{A=1}^{3} \delta \Delta \boldsymbol{u}_A \cdot \underbrace{\left[\frac{L}{2}\, \lambda_{\mathrm{N}}\, (g_{\mathrm{N}})_3 \left[\frac{\partial N_A}{\partial \boldsymbol{x}} \cdot \boldsymbol{n} \right] \boldsymbol{n} \right]}_{\boldsymbol{f}^{\boldsymbol{u}eA}_{\mathrm{cN}}} \tag{4.45}$$

The contact force contribution $\boldsymbol{f}^{\boldsymbol{u}eA}_{\mathrm{cN}}$ can be added to the mechanical residual equation (2.13). Similar but more elaborate contributions are given for the frictional contact, for which the reader is referred to [58].

4.2.5 Active constraint indicators and contact prediction

Based on the optimality conditions of normal and stick contact (2.42) and (2.51) the active normal contact is defined by $\lambda_{\mathrm{N}} < 0$ and the active stick by $\Phi_{\mathrm{S}} < 0$. Numerically, these indicators are not very robust, especially in terms of initialisation for a new load step after remeshing. Therefore, in [97] the active set is based on displacement-based indicators that rely only on the node positions of the contact element and the tractions of the underlying bulk element. Multiplying the definitions of the Lagrange multipliers (4.39) and (4.40) by $2\,\tau > 0$ leads to the definition of these indicators

$$g^{\mathrm{eff}}_{\mathrm{N}} := (g_{\mathrm{N}})_3 + 2\,\tau\, t_{\mathrm{N}} = 2\,\tau\, \lambda_{\mathrm{N}} \qquad\qquad g^{\mathrm{eff}}_{\mathrm{T}} := (g_{\mathrm{T}})_3 + 2\,\tau\, t_{\mathrm{T}} = 2\,\tau\, \lambda_{\mathrm{T}} \tag{4.46}$$

denoted as effective gaps. In this way, the active normal contact is indicated by $g_{\mathrm{N}}^{\mathrm{eff}} < 0$ and, inserting the effective gaps into the slip function, the active stick is indicated by $|g_{\mathrm{T}}^{\mathrm{eff}}| - \mu\,|g_{\mathrm{N}}^{\mathrm{eff}}| < 0$.

In addition, the robustness of these indicators can be used in order to derive an extrapolated prediction of the active set in a newly generated contact mesh. A linear extrapolation is computed as a prediction of the effective gaps, denoted as $\tilde{g}_{\bullet}^{\mathrm{eff}}$ indicating that it is valid for normal and tangential quantities. It is

$$\tilde{g}_{\bullet}^{\mathrm{eff}} = g_{\bullet}^{\mathrm{eff}}(t_n) + \frac{\Delta t_{n+1}}{\Delta t_n}\left[g_{\bullet}^{\mathrm{eff}}(t_n) - g_{\bullet}^{\mathrm{eff}}(t_{n-1})\right] \tag{4.47}$$

For this prediction, it is necessary to store the traction history related to the boundary edges, which also involves a transfer of these quantities in the case of point insertion or removal on the boundary, see Section 4.3.1. The nodal placement history is readily available. In particular, the geometrical gap quantities $(g_{\mathrm{N}})_3$ and $(g_{\mathrm{T}})_3$ are recalculated based on the old placements with the new contact connectivity, which further improves the prediction capabilities.

4.3 PFEM methods for contact and material removal

Section 2.4 introduces the main PFEM methods for the adaptive remeshing, shape detection and data transfer which is required for the simulation of very large deformations. The present section extends the theory to details on contact related remeshing aspects, i.e. the mesh generation for contact between bodies as well as self contact and the boundary preservation during remeshing. Furthermore, specific aspects of point adaptivity for the material separation are discussed.

The remeshing strategy for PFEM of a contact problem consists of a sequence of methods. Despite the general possibility to apply the PFEM remeshing only at specific time intervals or based on a mesh quality criterion, the remeshing is generally performed in each time step. The advantage is a fine resolution of changes in the topology of the bodies, the contact situation in sliding contact and a control of the degeneration of element connectivities by mesh adaptivity and regeneration of Delaunay triangulations. Furthermore, the remeshing introduces a deviation from the equilibrium state which is smaller when the remeshing is performed in every time step than compared to remeshing after several time steps. Thus, in each time step the following steps are performed

1. *Application of displacement increment* on the previous mesh to calculate the new previous configuration, $\mathbf{X}_n = \mathbf{X} + \mathbf{u}_n$.

2. *Calculation of point quantities:* The local characteristic point distance d_{avg}^{p} is calculated with (2.54). Furthermore, state variables which are needed for the material separation criterion are mapped with a volume-weighted average from all adjacent elements onto each node. The remaining state-variables are mapped later.

3. *Point insertion and removal* according to Section 2.4.3, where a physically motivated mesh refinement criterion is added as explained in Section 4.3.1.

4. *Constrained Delaunay Triangulation (CDT) and α-shape* are performed separately for both contacting bodies. Thereby, special treatment is necessary for self-contact nodes, see Section 4.3.5. Furthermore, the material separation criterion is evaluated during the α-shape detection, see Section 4.3.3.

5. *Boundary preservation* with the previous boundary is realised by refinement techniques based on the previous boundary information, see Section 4.3.2.

6. *Deletion of free nodes* which are no longer part of the connectivity due to the α-shape detection, the material separation criterion or the boundary preservation refinement. Boundary related information required for contact prediction, see Section 4.2.5, has to be adapted accordingly as well as node-indices in e.g. boundary condition arrays.

7. *Detection of new boundary polygon* consisting of all element edges which are not repeated in the connectivity. Calculation of the related geometrical boundary information necessary for contact meshing and the mesh generation in the subsequent time step (for steps 3., 4. and 5.).

8. *Data transfer* of state-variables to the new quadrature points according to Section 2.4.2. Also for the TRI6 element, nodal data has to be interpolated to the edge-mid nodes and boundary information has to be extended and adapted accordingly.

9. *Mesh generation of contact elements* based on the new boundary information, see Section 4.3.4.

With the newly generated mesh the time step solution can be computed. The presented methods are discussed in the subsequent sections.

4.3.1 Point insertion and removal for contact and material separation

Point insertion and removal as techniques for adaptive remeshing in PFEM are introduced in Section 2.4.3, applied with small adaptions for the contact and material separation modelling in the present chapter. For the contact discretisation and solution, several methods are implemented which require boundary information. Therefore an extended *data mapping* is necessary:

- *Interpolation or deletion of node data* for inserted and deleted points. Thereby, also the local characteristic point distance d^p_{avg} is approximated because it is required within the α-shape detection and cannot straightforwardly be recalculated after point adaptivity. An average generated from the related nodes proved to work well, especially since a manipulation of the value can lead to unexpected element deletion.

For example, a reduction of d^p_{avg} upon point insertion intended to approximate the real value can lead to a deletion of neighbouring slightly larger triangles.

- *Transfer of boundary information* by addition or removal of boundary points and by splitting or updating of boundary edges. Furthermore, a simple averaging for the outward normal vector and element height of the underlying bulk element is sufficient as approximation for the subsequent meshing methods of boundary refinement and self contact.

- *Transfer of the edge related traction data* for the contact prediction explained in Section 4.2.5 to the new edges by averaging upon point removal and copying upon point insertion.

- *Updating of node labels* upon point removal when working with numbered arrays rather than objects.

Another extension to Section 2.4.3 is the necessity for rigorous *data checks* in the point insertion algorithm. In Algorithm 1, distinctions with respect to boundary edges are based on the number of boundary nodes of a targeted edge or element. However, this assumes a well ordered mesh which can not be expected in the case of crack formation and element deletion where also holes can be generated. Therefore, the following extended checks are implemented:

- For point insertion on a boundary, the number of boundary nodes is not reliable for detecting whether element edges are boundary edges. Therefore, a check is included to see if the element edges are members of the boundary edge list. If an element consists of two or three boundary nodes but the edges are not boundary edges, it is likely to be an element between holes or cracks. In the case of two boundary nodes without a boundary edge, the point is inserted in the centre of the element. In the case of three boundary nodes and no boundary edges the point insertion is skipped.

- To remove points from an edge consisting of two boundary nodes, it is checked whether the edge is a true boundary edge and whether the points are connected to only one other boundary edge. The edge is only then collapsed to a midpoint. Otherwise the edge is connected to holes or cracks and an edge collapse cannot be handled correctly for these special cases.

Furthermore, a main extension is a *physically based point insertion criterion*. In [111], points are inserted when the plastic dissipation of an element is significantly larger than the average dissipation in the surrounding elements. However, [64] showed that the equivalent plastic strain is also a suitable refinement criterion. In the case of isotropic hardening plasticity, the accumulated plastic strain $\varepsilon_{\text{p}}^{\text{eq}}$ is equivalent to the hardening variable k which therefore is used within the α-shape detection. Since the α-shape is

performed before the transfer of state-variables, the values are calculated by a volume weighted average from all adjacent elements for each node and then averaged in the newly generated triangulation. The resulting locally smoothed quantity is denoted as $\overline{\varepsilon}_{\mathrm{p}}^{\mathrm{eq}}$. In an opposite sense to the α-shape test, a point is inserted when a test radius is smaller than the circumcircle radius, i.e. when $r_{\mathrm{c}}^{\max} < r_{cT}$. The point insertion prevents the α-shape from erasing the element upon further deformation. Now, the test radius for point insertion is made dependent on a global mesh density according to

$$r_{\mathrm{c}}^{\max} = \alpha^{\mathrm{ins}}\, l_{\mathrm{seed}} \tag{4.48}$$

with the global mesh seed size l_{seed} which can be an approximate average for the relevant region in a graded mesh. The insertion α-parameter α^{ins} is now made dependent on the averaged equivalent plastic strain $\overline{\varepsilon}_{\mathrm{p}}^{\mathrm{eq}}$ of the considered element with a piecewise linear function visualised in Figure 4.16, such that evolving plastic deformation triggers a mesh refinement.

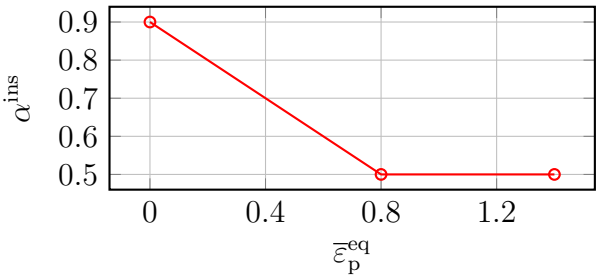

Figure 4.16: Reduction of the test radius parameter α^{ins} for point insertion depending on the equivalent plastic strain leads to an adaptive mesh refinement.

Remark: In general, the α-test for point insertion (4.48) can be made dependent on a local average point distance $l_{\mathrm{char}}^{\mathrm{loc}}$ similar to (2.55). However, this can have a self-amplifying effect as the refined mesh triggers refinement of neighbouring elements as well, eventually leading to an unwanted amount of refinement.

4.3.2 Mesh generation with boundary preservation

In contact mechanics simulations, generally the previously defined contact surface is preserved during remeshing. While a point insertion or removal on the surface polygon is possible with proper transfer of node- and edge-related variables, see Section 4.3.1, an edge flip on the surface that significantly changes the shape of the surface polygon may lead to an unsolvable violation of the current equilibrium state. The generation of a crack is also possible, but the modelling of the crack initiation or propagation should be based on a remeshed connectivity that preserves the previous boundary polygon. The first key method to achieve this is Constrained Delaunay Triangulation (CDT), which enforces the

boundary polygon to be part of the connectivity. In addition, in curved regions of the boundary polygon, elements appear that lie outside the previous boundary but are not deleted by the α-shape test, see Figure 4.17a for an example. While this may be negligible for fine meshes, it can lead to unwanted stiffening or a rejoining of previously separated material. This is particularly problematic when modelling material separation where crack boundaries are very close together. Therefore, a so-called boundary refinement scheme is proposed in [27]. The term boundary refinement does not refer to a refinement of the surface mesh density, but rather consists of a clean-up of elements that remain outside the boundary polygon after α-shape detection.

Figure 4.17a shows a detail of a boundary area mesh after the α-shape detection, with the previous boundary marked in red. Candidates for elements lying outside the previous shape are identified by being composed only of boundary nodes from the previous mesh. Boundary refinement is based on the outer normal vectors and the detected element can be deleted, see Figure 4.17b.

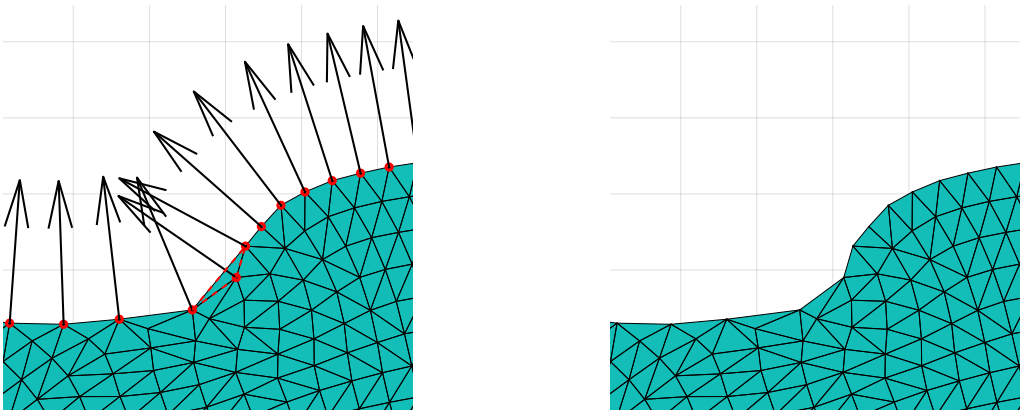

(a) α-shaped mesh with red marking of the boundary from the previous time step. An element outside the previous boundary (red) is targeted for refinement.

(b) Final mesh after refinement criterion based on normal vectors of the previous mesh deleted the outside element.

Figure 4.17: Detail of a boundary mesh after α-shaping and after additional boundary refinement.

The original boundary refinement criterion from [27] is visualised in Figure 4.18a. For each vertex of the triangle, the centre-vertex vectors are projected onto the outward normal vector of the respective vertex. If at least one of these projections is negative, the element is considered to be outside the shape. An alternative criterion is proposed in this work and visualised in Figure 4.18b. The element is rejected if an outward normal vector points into the element. The detection is based on angles between edges and normal vectors. Two special cases are discussed here, where the criteria do not work optimally. In Figure 4.19a a rough surface with a corner element inside the previous boundary is considered. With Criterion 1, nodes 1 and 2 give negative projections, i.e. the element is recognised to be outside of the previous boundary and deleted. Criterion 2 is less sensitive to such rough surfaces. However, a second scenario visualised in Figure 4.19b is

a potential self-contact scenario. Here, Criterion 1 can delete the critical element while Criterion 2 fails because no vertex normal vector points into the unwanted element. As a compromise, this work uses a combination of both criteria, which may be too strict in some special cases, but guarantees a robust boundary refinement for material separation examples. The combined method is summarised in Algorithm 2.

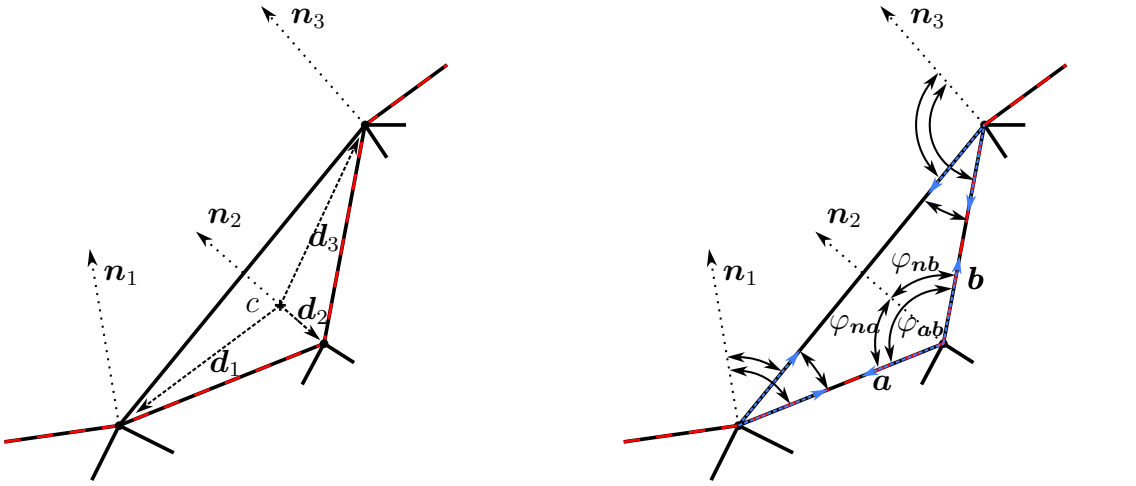

(a) Criterion 1: delete element when projection of centre-vertex vector $\boldsymbol{d}_k$ onto outward normal $\boldsymbol{n}_k$ is negative, cf. [27]. Here, nodes 1 and 2 lead to rejection of the element.

(b) Criterion 2: delete element when outward normal vector points into the element. The detection is based on angles between edge vectors. Here, only node 2 leads to rejection of the element.

Figure 4.18: Detail of boundary area with previous boundary (red). Two criteria for boundary refinement for detecting elements which lie outside the previous boundary are sketched.

4.3.3 Simulation of material separation

For the modelling of material separation, a physically motivated extension of the α-shape method is proposed in this work. The test radius of the α-shape method is made dependent on a damage criterion which makes the shape detection more sensitive in damaged regions. In such manner, the shape detection models a crack formation in damaged regions. As a deformation based criterion for the damage of the material, the averaged equivalent plastic strain $\overline{\varepsilon}_{\mathrm{p}}^{\mathrm{eq}}$ is used in this work. This represents a simplified ductile damage evolution based on the plastic strain which is also one driving factor in classic ductile damage models such as [68]. The dependence of the α-shape parameter α on $\overline{\varepsilon}_{\mathrm{p}}^{\mathrm{eq}}$, or k respectively, is visualised in Figure 4.20 exemplarily for a maximum value of $\alpha = 1$ which will be used in the subsequent numerical example. If a different value of α is desired, the function can also be used as a scaling factor of the maximum value. The approach has similarities with a simple element deletion as soon as α tends towards zero. However, the gradual reduction of the shape detection sensitivity provides more control

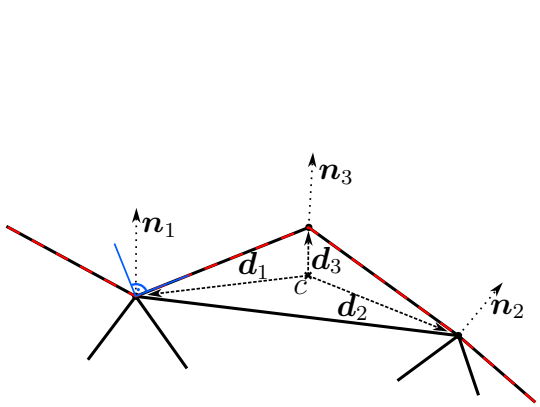

(a) Refinement Criterion 1 rejects an interior element on a rough surface because the angle between $\boldsymbol{d}_1$ and $\boldsymbol{n}_1$ is $< 90°$. Criterion 2 accepts the element because no normal vectors point into the element.

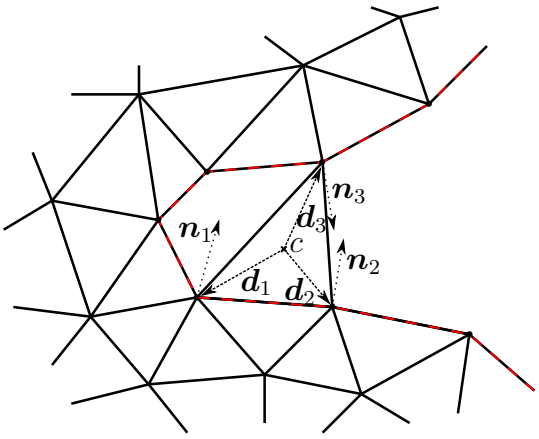

(b) In potential self-contact situation Criterion 2 fails to delete the highlighted element, since no normal vector is pointing into the element. Criterion 1 performs better in this case.

Figure 4.19: Critical cases for boundary refinement.

Algorithm 2: Combined boundary refinement scheme with Criterion 1 from [27] extended by a second criterion.

detect elements consisting of only boundary nodes of the previous boundary
Criterion 1: calculate vectors from center to vertex $\boldsymbol{d}_k = \boldsymbol{x}_k - \boldsymbol{x}_c$ and the projection onto outward normal vector $\boldsymbol{n}_k$ as $p_k = \boldsymbol{d}_k \cdot \boldsymbol{n}_k$
Criterion 2: calculate edge-vectors $\boldsymbol{a}$ and $\boldsymbol{b}$ from node k to the other nodes a and b as $\boldsymbol{a} = \boldsymbol{x}_a - \boldsymbol{x}_k$ and $\boldsymbol{b} = \boldsymbol{x}_b - \boldsymbol{x}_k$
calculate angles between vectors, $\varphi_{\boldsymbol{ab}}$, $\varphi_{\boldsymbol{na}}$ and $\varphi_{\boldsymbol{nb}}$, e.g. $\varphi_{\boldsymbol{ab}} = \cos^{-1}(\boldsymbol{a} \cdot \boldsymbol{b} / \|\boldsymbol{a}\| \, \|\boldsymbol{b}\|)$
calculate Boolean b_k for each vertex $b_k = [\varphi_{\boldsymbol{na}} < \varphi_{\boldsymbol{ab}} \;\; \text{AND} \;\; \varphi_{\boldsymbol{nb}} < \varphi_{\boldsymbol{ab}}]$
Combined criterion
if *at least one* $(p_k < 0)$ ***or*** *at least one* $(b_k == \mathit{false})$ **then**
    reject element

over the process, and the mesh quality also has a slight influence on the deletion of the elements.

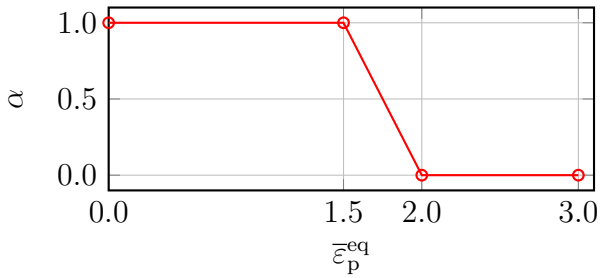

Figure 4.20: Reduction of the α-shape parameter based on the equivalent plastic strain makes the shape detection more sensitive in highly deformed and probably damaged regions.

4.3.4 Mesh generation of elements for contact and self contact

For the generation of the contact domain mesh, a triangulation of the space between the contacting bodies is required. The gap between the bodies is close to zero in the case of contact. Therefore, based on [58], the following steps are performed for the *contact mesh generation*.

- After generating the bulk mesh, the boundary information is derived. To do this, all element edges in 2d that are only contained once in the bulk connectivity are stored as boundary edges and from these, information regarding boundary points and outward normal vectors are derived.
- A shrinkage is applied to the boundary polygon for mesh generation, see Figure 4.21a. Thereby, all boundary nodes are moved inwards along their normal vectors to create a gap between the bodies.
- The boundary points are meshed with a Constrained Delaunay Triangulation, see Figure 4.21b. This guarantees that the actual boundary edges are similar to the bulk surface mesh and that no edge flips occur.
- The α-shape method can be used in an opposite sense in order to detect the shape of the contact patches, i.e. those contact patches where the bodies are close to each other, see Figure 4.21c. This reduces the number of contact elements to those which probably come into contact.
- Finally, the generated connectivity is used on the real coordinates, see Figure 4.21d. The shrinkage is only applied for mesh generation purposes.

The shrinkage factor highly influences the quality of the contact mesh. In curved regions of the contact surfaces, a large shrinkage leads to poor mesh quality when the connectivity is

used on the real point coordinates. Therefore, the shrinkage is implemented as an iterative process. The shrinkage depth is initially chosen to be very small, e.g. 1/100 of the local element height, and subsequently increased by a factor 2 until a CDT can successfully be generated without edge-intersections. A disadvantage of the small shrinkage depth is that the α-shape method tends to create holes in the contact mesh. Therefore, the α-parameter has to be chosen rather high, e.g. $\alpha = 6$ in order to achieve a filled contact domain mesh. For the α-shape of the contact mesh a global averaged characteristic length turned out to create contact meshes without voids. From the connectivity of the contact mesh the average distance of all edge lengths $l_{\text{ed}}^{\text{ave}}$ is mixed in a heuristic manner with the minimal edge length $l_{\text{ed}}^{\text{min}}$ according to

$$l_{\text{char}}^{\text{glob}} = \frac{2\, l_{\text{ed}}^{\text{ave}} + l_{\text{ed}}^{\text{min}}}{3} \tag{4.49}$$

and the standard α-test (2.53) deletes all elements with $r_\alpha = \alpha\, l_{\text{char}}^{\text{glob}} < r_{\text{circum}\,T}$.

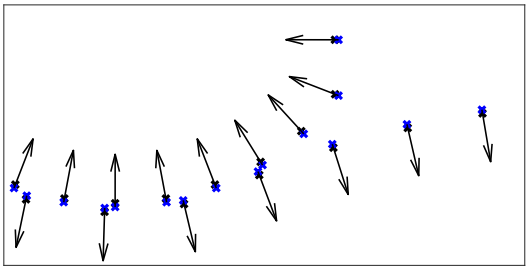

(a) Shrinkage of boundary nodes along inward normal vector makes room for intermediate mesh.

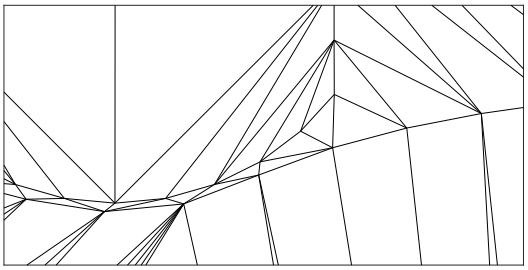

(b) Constrained Delaunay triangulation of boundary nodes automatically includes boundary polygon.

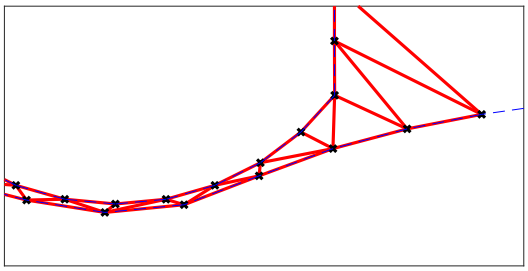

(c) The α-shape reduces the mesh to the likely active contact region.

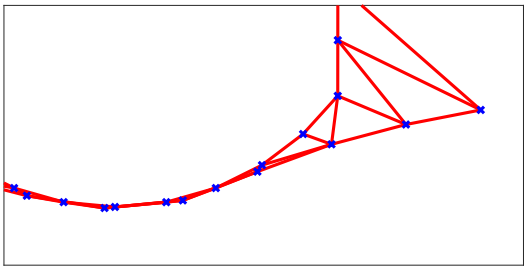

(d) Generated mesh is used on real coordinates.

Figure 4.21: Mesh generation of the contact domain consisting of elements that are spanned between the surfaces of the contacting bodies.

Further filtering of the contact element mesh is proposed in order to reduce the number of possible self-contact nodes and to exclude elements with invalid features. Candidate self-contacts are subjected to a special treatment described in the following section 4.3.5, which is undesirable for an unnecessarily large number of nodes. Furthermore, incorrect contact forces may occur for contact elements with invalid features. The contact mesh

filtering procedure identifies and removes invalid contact elements based on the newly generated boundary information. First, elements with zero or two boundary edges are discarded because they do not provide a proper base-side for the contact patch. For elements with exactly one boundary edge, the orientation of the third node is checked to ensure that it lies in the outer normal direction of the boundary edge in shrunken coordinates. The normal direction is determined by the normal to the boundary edge, where the outward direction is derived from the average of the vertex outward normal vectors. If a vector from the base side to the third node has a negative projection on the outward normal vector, the element is removed. This process ensures that only valid contact elements, with correct orientation and boundary conformity, remain in the mesh. Figure 4.22 illustrates this filtering technique.

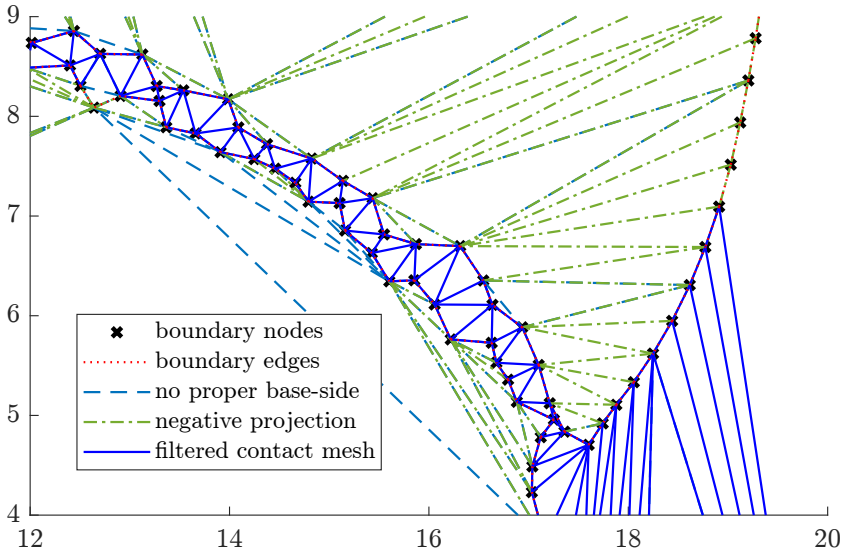

Figure 4.22: Section of mesh with crack and self-contact. The generation of the contact mesh for boundary nodes on the shrunken coordinates is extended by a filter operation to exclude elements without a proper base side and elements where the third node does not lie outside the base side (negative projection).

4.3.5 Treatment of self-contact

As soon as the material separation leads to a chip separation and the chip comes close to the base material again, self-contact elements have to be created. The deletion of elements by the α-shape automatically leads to a change in the boundary polygon when the new boundary is extracted from the connectivity. In such a way, the crack surfaces automatically are part of the new boundary and thus also subjected to the shrinkage of the boundary nodes for contact mesh generation which is described in the previous section. However, the bulk mesh of the two contacting bodies is created in two separate triangulations, whereas the base body and the separated material are still part of the

same body and therefore meshed together. As soon as self-contact is present, elements of zero thickness or even slight edge intersections will make the CDT of the bulk impossible. Therefore, a treatment of possible self-contact nodes is applied similar to the shrinkage within the contact meshing.

Self-contact candidates are detected from the contact mesh of the previous time step. All contact elements consisting of nodes from only one body are self-contact candidates and their nodes are stored in a corresponding list. Within the bulk mesh generation, the self-contact candidate nodes are moved along the negative vertex normal vector for 5% of the underlying bulk element height. All required information is provided by the previous mesh in the boundary information and is therefore also transferred in the case of point insertion or removal. A recalculation based on the new mesh is generally also possible by assuming the boundary edges of the old mesh and detecting the respective underlying bulk element from the connectivity list. Figure 4.23 shows an example of the movement of the self-contact candidates and the generated mesh on the real coordinates. The shrinkage of the self contact candidates makes room for a correct mesh generation of the bulk mesh. The intermediate elements in the crack are removed by the α-shape or the refinement and the contact mesh is fully generated later in the contact mesh generation as explained in the previous section.

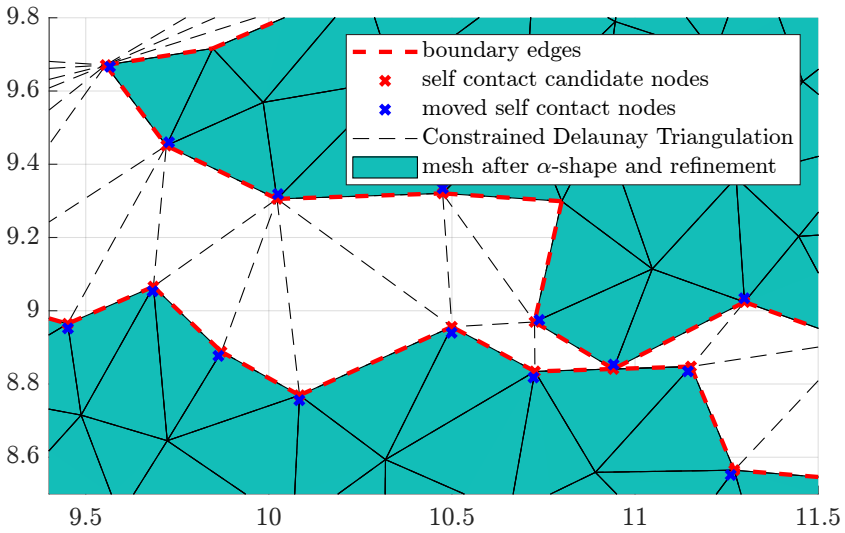

Figure 4.23: Section of mesh with crack and self-contact. Generation of bulk mesh CDT with manipulated positions of self-contact candidate nodes. Intermediate elements are removed by α-shape and boundary refinement, then the contact mesh is generated separately.

4.4 Elastoplastic material model

For the simulation of large shear deformations of steel, a Huber-Mises type elastoplastic material model with isotropic hardening is considered. A multiplicative split of the deformation gradient is defined as

$$\boldsymbol{F} = \boldsymbol{F}_\mathrm{e} \cdot \boldsymbol{F}_\mathrm{p} \tag{4.50}$$

The volume-specific Helmholtz free energy density is defined as

$$\psi(\boldsymbol{C}_\mathrm{e}, k) = \psi_\mathrm{e}(\boldsymbol{C}_\mathrm{e}) + \psi_\mathrm{p}(k) \tag{4.51}$$

with the elastic right Cauchy Green tensor $\boldsymbol{C}_\mathrm{e} = \boldsymbol{F}_\mathrm{e}^\mathrm{t} \cdot \boldsymbol{F}_\mathrm{e}$ and the hardening variable k. Following the Coleman and Noll procedure proposed in [33] the dissipation inequality for the reversible case yields the Piola stress tensor

$$\boldsymbol{P} = \frac{\partial \psi}{\partial \boldsymbol{F}_\mathrm{e}} \cdot \boldsymbol{F}_\mathrm{p}^{-\mathrm{t}} \tag{4.52}$$

with $\psi = \rho_0 \Psi$. Assuming that this relation also holds in the irreversible case leads to the reduced dissipation inequality

$$\mathcal{D}_\mathrm{mec}^\mathrm{red} = \underbrace{\left[\boldsymbol{F}_\mathrm{e}^\mathrm{t} \cdot \frac{\partial \psi}{\partial \boldsymbol{F}_\mathrm{e}}\right]}_{=:\,\boldsymbol{M}_\mathrm{p}} : \boldsymbol{L}_\mathrm{p} \underbrace{- \frac{\partial \psi}{\partial k}}_{=:\,Q} \dot{k} \geq 0 \tag{4.53}$$

where $\boldsymbol{L}_\mathrm{p} = \dot{\boldsymbol{F}}_\mathrm{p} \cdot \boldsymbol{F}_\mathrm{p}^{-1}$ is the plastic velocity gradient, $\boldsymbol{M}_\mathrm{p}$ is the work conjugate Mandel stress tensor and Q is the thermodynamic stress-like quantity which drives the hardening evolution. A Huber-Mises type yield function is defined to describe the plastic flow with

$$\Phi = \| \operatorname{dev}(\boldsymbol{M}_\mathrm{p}) \| - [Q_0 - Q] \leq 0 \tag{4.54}$$

where Q_0 is the initial yield limit and $\operatorname{dev}(\boldsymbol{M}_\mathrm{p}) = \boldsymbol{M}_\mathrm{p} - \operatorname{tr}(\boldsymbol{M}_\mathrm{p})\, \boldsymbol{I} \,/\, 3$. The postulate of maximum dissipation constraint by fulfilment of the yield function leads to a Lagrange function

$$\mathcal{L}(\boldsymbol{M}_\mathrm{p}, Q, \lambda_\mathrm{p}) = -\mathcal{D}_\mathrm{mec}^\mathrm{red} + \lambda_\mathrm{p}\, \Phi \tag{4.55}$$

with Lagrange multiplier λ_p and which is to be minimised. The necessary conditions yield the associated evolution equations

$$\boldsymbol{L}_\mathrm{p} = \lambda_\mathrm{p} \frac{\partial \Phi}{\partial \boldsymbol{M}_\mathrm{p}} \qquad \text{and} \qquad \dot{k} = \lambda_\mathrm{p} \frac{\partial \Phi}{\partial Q} \tag{4.56}$$

Hereby, the isotropic hardening contribution in (4.54) yields a direct equivalence of $\dot{k} = \lambda_\mathrm{p}$ such that k also represents the accumulated plastic strain. Furthermore, the flow

direction follows as $\partial\Phi/\partial\boldsymbol{M}_\mathrm{p} = \mathrm{dev}(\boldsymbol{M}_\mathrm{p})/\|\,\mathrm{dev}(\boldsymbol{M}_\mathrm{p})\|$. For the time-discrete solution of the evolution equations (4.56) with a time step Δt, Backward Euler time integration is applied for k resulting in

$$k_{n+1} = k_n + \underbrace{\Delta t\ [\lambda_\mathrm{p}]_{n+1}}_{=:\,\Delta\lambda} \tag{4.57}$$

In order to achieve the preservation of a volume conserving evolution of the plastic deformation $\boldsymbol{F}_\mathrm{p}$, i.e. $\det(\boldsymbol{F}_\mathrm{p}) = 1$, exponential time integration is applied as discussed in [42] according to

$$\dot{\boldsymbol{T}} = \boldsymbol{A}\cdot\boldsymbol{T} \quad \Rightarrow \quad \boldsymbol{T}_{n+1} = \exp(\Delta t\,\boldsymbol{A})\cdot\boldsymbol{T}_n \tag{4.58}$$

Application to the rearranged evolution equation $(4.56)_1$, i.e.

$$\dot{\boldsymbol{F}}_\mathrm{p} = \lambda_\mathrm{p}\,\frac{\partial\Phi}{\partial\boldsymbol{M}_\mathrm{p}}\,\boldsymbol{F}_\mathrm{p} \tag{4.59}$$

leads to the discrete update equation

$$[\boldsymbol{F}_\mathrm{p}]_{n+1} = \exp\left(\Delta\lambda_\mathrm{p}\frac{\partial\Phi}{\partial\boldsymbol{M}_\mathrm{p}}\right)\cdot[\boldsymbol{F}_\mathrm{p}]_n \tag{4.60}$$

Algorithmically, in the case of a violation of the yield function (4.54) within the elastic trial step, the coupled system of equations $\Phi = 0$ and (4.60) is solved for the 10 unknown coefficients $\{\boldsymbol{F}_\mathrm{p}, \Delta\lambda_\mathrm{p}\}$ with a Newton-Raphson scheme. As this is a standard model for finite elastoplasticity, the reader is referred to the cited literature for further details.

The specific energy density used in this work includes a standard Neo-Hooke function of the form

$$\psi_\mathrm{e}(\boldsymbol{C}_\mathrm{e}) = \frac{1}{2}\,\mu\ [\boldsymbol{C}_\mathrm{e}\colon\boldsymbol{I} - 3] + \lambda\,\frac{J_\mathrm{e}^2 - 1}{4} - \left[\frac{\lambda}{2} + \mu\right]\ \ln(J_\mathrm{e}) \tag{4.61}$$

from which the Mandel stress tensor derives as

$$\boldsymbol{M}_\mathrm{p} = \lambda\,\frac{J_\mathrm{e}^2 - 1}{2}\,\boldsymbol{I} + \mu\ [\boldsymbol{C}_\mathrm{e} - \boldsymbol{I}] \tag{4.62}$$

Moreover, the Piola stresses can be calculated by

$$\boldsymbol{P} = \boldsymbol{F}_\mathrm{e}^{-\mathrm{t}}\cdot\boldsymbol{M}_\mathrm{p}\cdot\boldsymbol{F}_\mathrm{p}^{-\mathrm{t}} = \lambda\,\frac{J_\mathrm{e}^2 - 1}{2}\,\boldsymbol{F}^{-\mathrm{t}} + \mu\ \left[\boldsymbol{F}_\mathrm{e}\cdot\boldsymbol{F}_\mathrm{p}^{-\mathrm{t}} - \boldsymbol{F}^{-\mathrm{t}}\right] \tag{4.63}$$

Furthermore, a linear hardening contribution is defined as

$$\psi_\mathrm{p}(k) = \frac{1}{2}\,H_\mathrm{lin}\,k^2 \tag{4.64}$$

resulting in $Q = H_{\text{lin}}\, k$.

Remark: In contrast to Section 2.2 analytical linearisation is applied for the algorithmic tangent of the elastoplastic material in this section, which is necessary for the global Jacobian matrix of the Finite Element formulation (2.24). Due to the dependence of $\boldsymbol{P}$ on both the total deformation gradient $\boldsymbol{F}$ and the plastic evolution $\boldsymbol{F}_{\text{p}}$, the total derivative reads

$$\mathrm{d}\boldsymbol{P} = \frac{\partial \boldsymbol{P}}{\partial \boldsymbol{F}} : \mathrm{d}\boldsymbol{F} + \frac{\partial \boldsymbol{P}}{\partial \boldsymbol{F}_{\text{p}}} : \frac{\partial \boldsymbol{F}_{\text{p}}}{\partial \boldsymbol{F}} : \mathrm{d}\boldsymbol{F} \tag{4.65}$$

whereby $\partial \boldsymbol{F}_{\text{p}} / \partial \boldsymbol{F}$ can be derived from the local Newton tangent of the converged state.

4.5 Numerical examples for plasticity, contact and material separation

Modelling of the shearing of a surface asperity is the main objective of this chapter. Since the performance of the P1P1 and the TRI6 element formulations is only studied for quasi-incompressible hyperelastic material behaviour in PFEM in Section 4.1, a benchmark example for incompressible plastic flow is presented first.

4.5.1 Element comparison for incompressible plastic flow

In this section, a short comparison is made for the presented elastoplastic material model in order to compare the element behaviour for incompressible plastic flow. The classic Cook's membrane problem is analysed based on similar parameters as in [112] with a higher load in order to introduce more plastic flow and a lower Poisson ratio which clearly focusses on plastic incompressibility. The specific parameters are Young's modulus $E = 70\,\text{MPa}$, Poisson ratio $\nu = 0.3$, hardening modulus $H_{\text{lin}} = 0.135\,\text{MPa}$ and initial yield limit $Q_0 = 0.243\,\text{MPa}$. The total applied force of 3 N is applied on the right edge, where vertical nodal forces on the equidistant 16×16 grid can be calculated as 1/16 for middle nodes and 0.5/16 for corner nodes to represent the total loading. The dimensions of the membrane are defined by the corner points (0,0), (48,44), (48,60) and (0,44) in mm, where the first component is the horizontal direction and the second is the vertical direction. The load is applied in 100 time steps.

Figure 4.24 shows a comparison of the displacement-force curves for a linear triangular element TRI3, a quadratic triangular element TRI6 and a mixed P1P1 formulation. As expected, the TRI3 element shows the stiffest behaviour, whereas the TRI6 and P1P1 show similar performance under severe isochoric plastic deformation. The TRI6 element is thereby slightly softer than the P1P1 element and no differences regarding the stabilisation factor α_{s}^{ϕ} of the P1P1 element are visible in this figure. A further analysis of α_{s}^{ϕ} is therefore shown in Figure 4.25 which reveals only a very small increase in softness

with increasing the stabilisation factor. The stabilisation factor $\alpha_s^\phi = K/10 = 58.33\,\text{MPa}$, which yields best results in the study for elasticity in Section 4.1, still works well, whereas a further increase to $\alpha_s^\phi = K$ or higher values leads to numerical divergence of the FEM solver. Since no significant influence is visible in the case of isochoric plastic flow with volumetric elastic deformations due to $\nu = 0.3$, a value of $\alpha_s^\phi = 2$ is chosen in order to prevent numerical instabilities. The element properties are furthermore illustrated in Figure 4.26 where the severe volumetric locking is evident in the checkerboard pressure patterns in Figure 4.26a. The two advanced element formulations perform significantly better. However, the P1P1 element retains slight pressure oscillations, see Figure 4.26b, while the TRI6 element shows a smooth distribution, Figure 4.26c. The plots thereby show one value per element, i.e. a volume weighted average of the quadrature point values per element. A projection and averaging of the quadrature point values on the nodes would yield a smoother representation, but the element-wise values are preferred in order to see the pressure jumps.

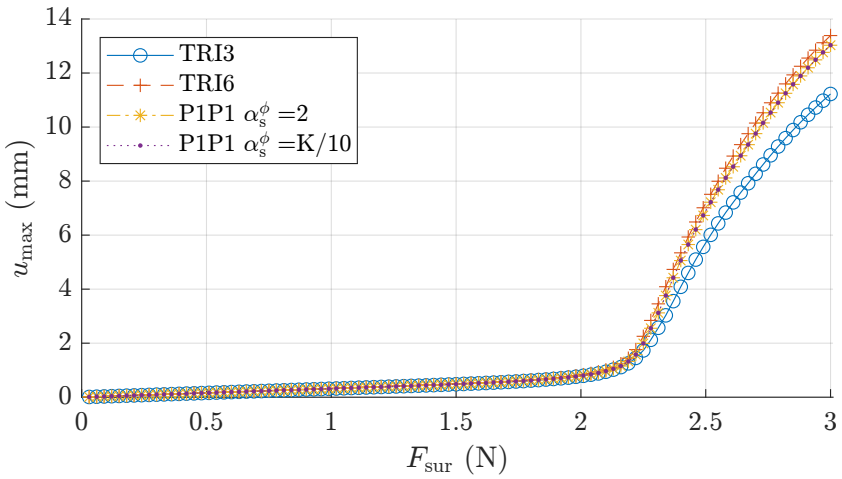

Figure 4.24: Displacement response of elastoplastic Cook's membrane problem for different element types in PFEM. After similar response in the elastic regime, the curves diverge during incompressible plastic flow. The TRI3 element gives a stiff behaviour due to locking while both TRI6 and P1P1 show a softer response. An influence on α_s^ϕ in the P1P1 element is not visible in this figure.

4.5.2 Shearing of surface asperities

In order to analyse the applicability of the PFEM in the simulation of material abrasion, an example where two surface elevations shear off against each other is analysed in the following. On a microscopic level, these surface elevations represent a cut-out of the surface asperities of two contact partners which are approximated by a sinusoidal wave geometry. The dimensions and boundary conditions of the boundary value problem are visualised in Figure 4.27. The units are g − mm − ms and the dimensions of the problem are chosen arbitrarily for a general proof of concept. Periodic boundary conditions

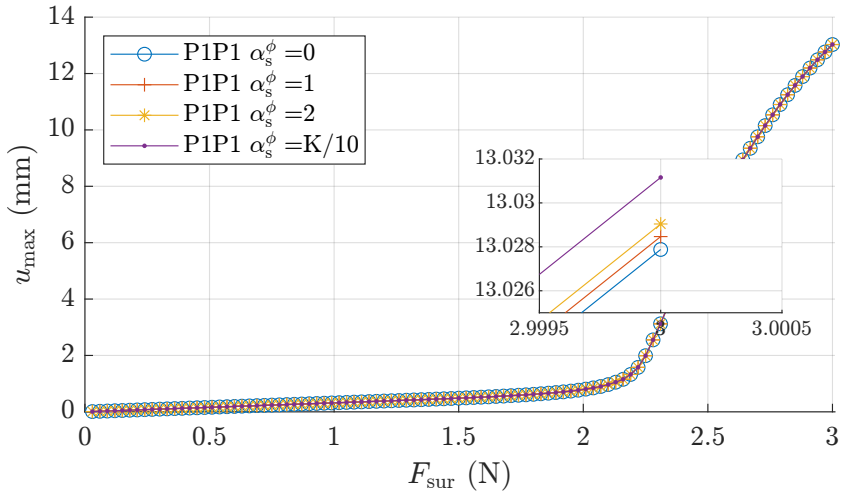

Figure 4.25: Displacement response of elastoplastic Cook's membrane problem for different stabilisation factors α_s^ϕ for the P1P1 element in PFEM. Only the detailed view shows slightly softer behaviour for increasing stability parameters. Further increase leads to numerical divergence of the FEM solver.

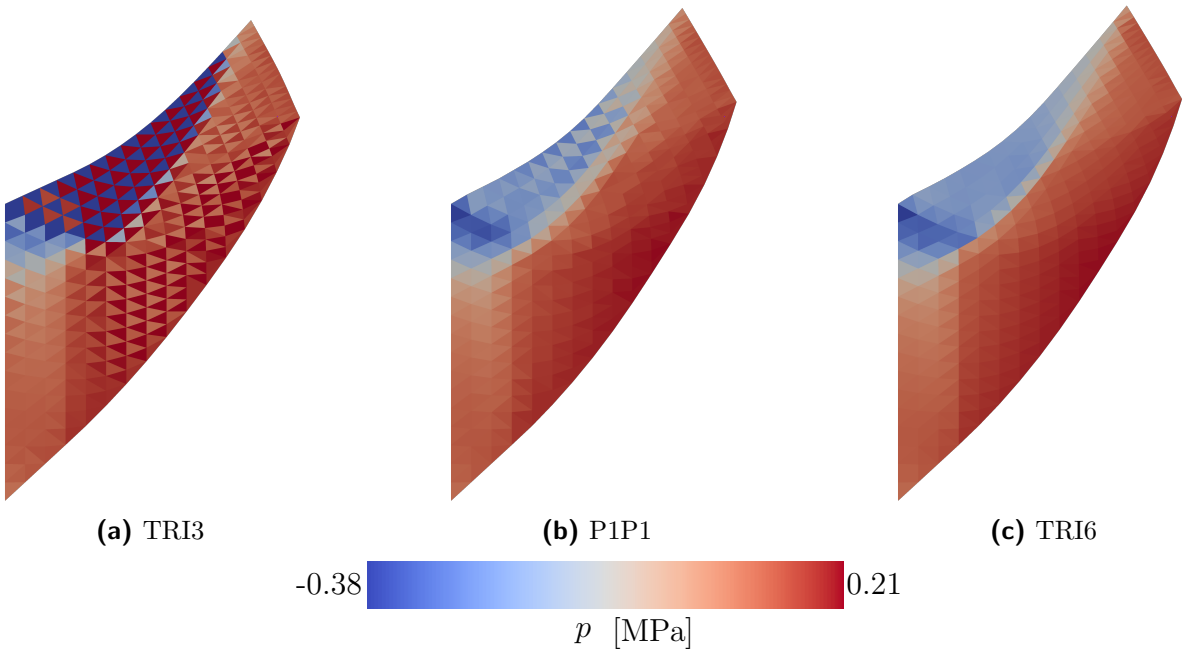

(a) TRI3 **(b)** P1P1 **(c)** TRI6

Figure 4.26: Pressure plots for elastoplastic Cook's membrane test for three element formulations in PFEM. The TRI3 element shows strong locking, the P1P1 element performs much better, but some oscillations remain, whereas the TRI6 element shows a smooth distribution.

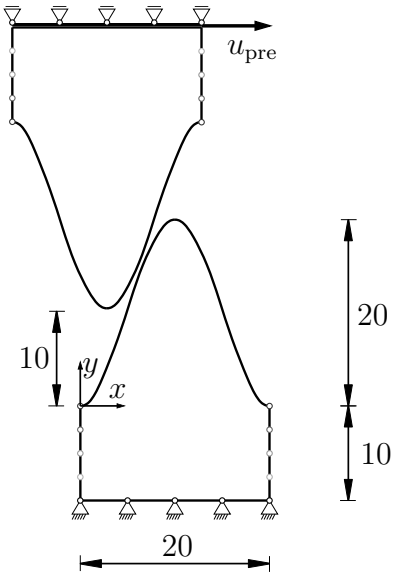

Figure 4.27: Periodic cut out of sinusoidal surface asperities shearing off against each other by a prescribed displacement u_{pre} applied on the top edge. The side edges of both bodies are subjected to linear constraints on opposing nodes.

on the side edges of the lower and upper bodies are realised with linear constraints in order to model the support from the neighbouring material. A global seed size of $l_{\mathrm{seed}} = 0.5\,\mathrm{mm}$ is applied with coarser seeds of 2 mm on the edges of the substrate resulting in a slightly graded mesh density. The initial mesh consists of 3908 triangular elements which increases to approximately 4150 elements for both considered element types due to mesh adaptivity. Steel-like material parameters are assumed for both surfaces with identical elastic properties of $E = 210\,\mathrm{GPa}$ and $\nu = 0.3$. The upper body possesses a very high yield limit such that its response results in hyperelastic behaviour for the examples considered in the following. The lower body represents a low-alloyed steel with $Q_0 = 110\,\mathrm{MPa}$ and a very small linear hardening modulus of $H_{\mathrm{lin}} = E/10000$. This almost perfect plastic behaviour is chosen for significant strain localisation in the region where the material separation shall occur. Dynamic contributions as well as volume forces are considered, where the mass density is $\rho_0 = 7.81 \times 10^{-3}\,\mathrm{g/mm^3}$ and the gravity constant $g = 9.81 \times 10^{-3}\,\mathrm{mm/ms^2}$ leading to a body force vector $\boldsymbol{b} = [0 \;\; -g]^{\mathrm{t}}$. The top edge of the upper asperity is moved to the right with a prescribed displacement of $\dot{u}_{\mathrm{pre}} = 4 \times 10^{-3}\,\mathrm{mm/ms}$. The time step for writing output files is $\Delta t_{\mathrm{out}} = 2\,\mathrm{ms}$, where time step adaptivity reduces the calculation time step to a minimum of $\Delta t = 3 \times 10^{-5}\,\mathrm{ms}$ for short periods of the simulation. The remeshing parameters are chosen as follows: Point insertion is based on the test radius $r_{\mathrm{c}}^{\mathrm{max}} = \alpha^{\mathrm{ins}}\, l_{\mathrm{seed}}$ with α^{ins} depending on $\overline{\varepsilon}_{\mathrm{p}}^{\mathrm{eq}}$ according to Figure 4.16. Here, the global approximate $l_{\mathrm{seed}} = 0.5\,\mathrm{mm}$ is inserted and point adaptivity is only activated for the lower body and therein only the upper part with vertical position $y > 3\,\mathrm{mm}$. The point removal parameters are chosen as the default values

in Algorithm 1. A point-density dependent α-shape detection is applied with a linearly decreasing α-factor as specified in Figure 4.20. The interior stabilisation parameter of the contact model is chosen as $\alpha_{\text{stab}} = 0.01$, see (4.41). As Coulomb friction is a constitutive model representing asperity shear and adhesive forces, frictionless contact is simulated at the asperity level, i.e. $\mu = 0$.

Figure 4.28 shows the force-displacement diagram of the summed up horizontal reaction forces in the upper body. A linear increase in force can be seen after contact closure at step 18. The evolution of the plastic deformation leads to a plateau of the force required to maintain the shear. The force decreases slightly before cracking and the softening becomes more pronounced after crack initiation at around step 500. When the asperity material finally separates around step 800, the force drops to zero. Both element formulations behave rather similarly in the force-displacement plot where the main difference is a slightly faster crack propagation for the TRI6 element.

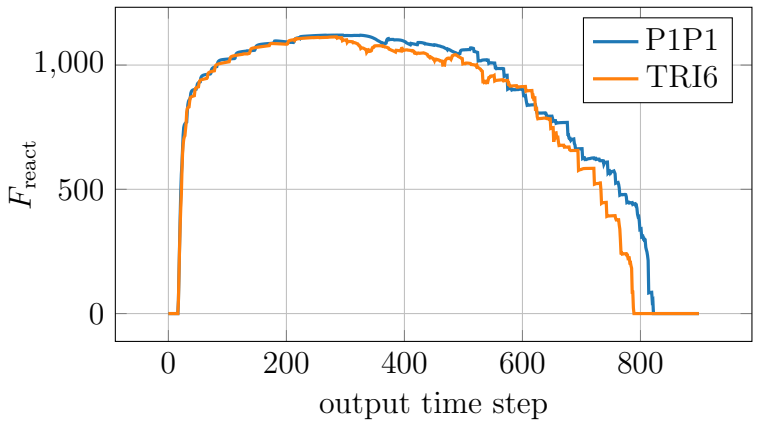

Figure 4.28: Force displacement diagram for shearing of surface asperities with two different element formulations. First crack initiation is at step = 500 for the TRI6 element and at step = 518 for the P1P1 element. The output time step size is $\Delta t_{\text{out}} = 2\,\text{ms}$.

Figure 4.29 shows a sequence of time steps for both the TRI6 and the P1P1 elements. The asperity contact induces large plastic deformations leading to a pronounced shear band formation in Figures 4.29a and 4.29g. The mesh density is also mirrored in the field of the hardening variable k since this quantity is directly related to the locally averaged equivalent plastic strain $\overline{\varepsilon}_{\text{p}}^{\text{eq}}$ for isotropic hardening. Conceptually speaking, $\overline{\varepsilon}_{\text{p}}^{\text{eq}}$ is responsible for the reduction of the point insertion parameter α^{ins} according to Figure 4.16, which serves as an adaptive remeshing criterion. In Figures 4.29b and 4.29h the region of maximum plastic deformation reaches the value of $k = 1.5$, where the α-shape parameter begins to be reduced by the linear function given in Figure 4.20 as a fracture criterion. This increases the sensitivity to topology changes and thus triggers the modelling of crack initiation. The crack propagates in the subsequent figures until the material completely separates at step 790 for the TRI6 element and at step 822 for the P1P1 element. The last two time frames in each series show self-contact situations

where the sides of the crack come back into contact after separation as the chip is pushed aside. Figure 4.30 shows the driving stress of the plastic evolution, $\| \operatorname{dev}(\boldsymbol{M}_{\mathrm{p}}) \|$, to visualise a scalar-valued measure of the stress distribution. Due to the low hardening modulus a very wide zone of maximum stresses can be seen. Upon crack initiation, the material below the crack releases the stresses while the upper part is still loaded by the contact situation. Complete material separation leaves the separated part with residual stresses. These result from incompatible plastic deformations, mainly caused by the deletion of elements in the crack modelling. The two element formulations show significant differences in the quality of the stress distributions. Strong stress oscillations are visible in the P1P1 element, as expected from the Cook's membrane example in the previous section. An element-wise constant value is plotted here as a volume-weighted average of the three element quadrature points for both element formulations. No nodal smoothing is performed for the visualisation, which would significantly improve the visual appeal of the stress field. The observation is even more pronounced in the pressure plot of the hydrostatic stresses in Figure 4.31 for the lower right part of the P1P1 model, see for example Figures 4.31g and 4.31h. In contrast, a smoother stress distribution can be observed for the TRI6 element, for example in Figures 4.31a and 4.31b. Only in the contact region, the P1P1 element shows a slightly smoother pressure distribution, where the TRI6 element in Figures 4.31a and 4.31b shows slight inhomogeneity.

4.6 Modelling and simulation of material separation – Conclusion

This chapter presented a framework for the simulation of shearing and material separation with severe isochoric plastic deformations modelled with the Particle Finite Element Method. Thereby, two advanced element formulations are extensively compared regarding their performance in cases prone for volumetric locking of standard linear triangular elements. Furthermore, the PFEM remeshing methodologies are extended for the modelling of material separation with an enrichment of the α-shape detection with a fracture criterion based on the equivalent plastic strain. In addition, self-contact is modelled with proposing a movement of the self contact candidate nodes to allow for mesh generation as well as by adding filtering operations for the generated contact domain mesh. The following conclusions can be drawn from this work.

- TRI6 is an alternative to the P1P1 element formulation for PFEM.
- In contrast to [114], the modelling of material separation cannot be solely based on the α-shape technique if the deformation is not tension dominated. As soon as shear deformation leads to rebuilding of the connectivities and, furthermore, large deformations are modelled with mesh adaptivity, the element deformation is no longer a measure for material deformation. Thus, a physical fracture criterion is

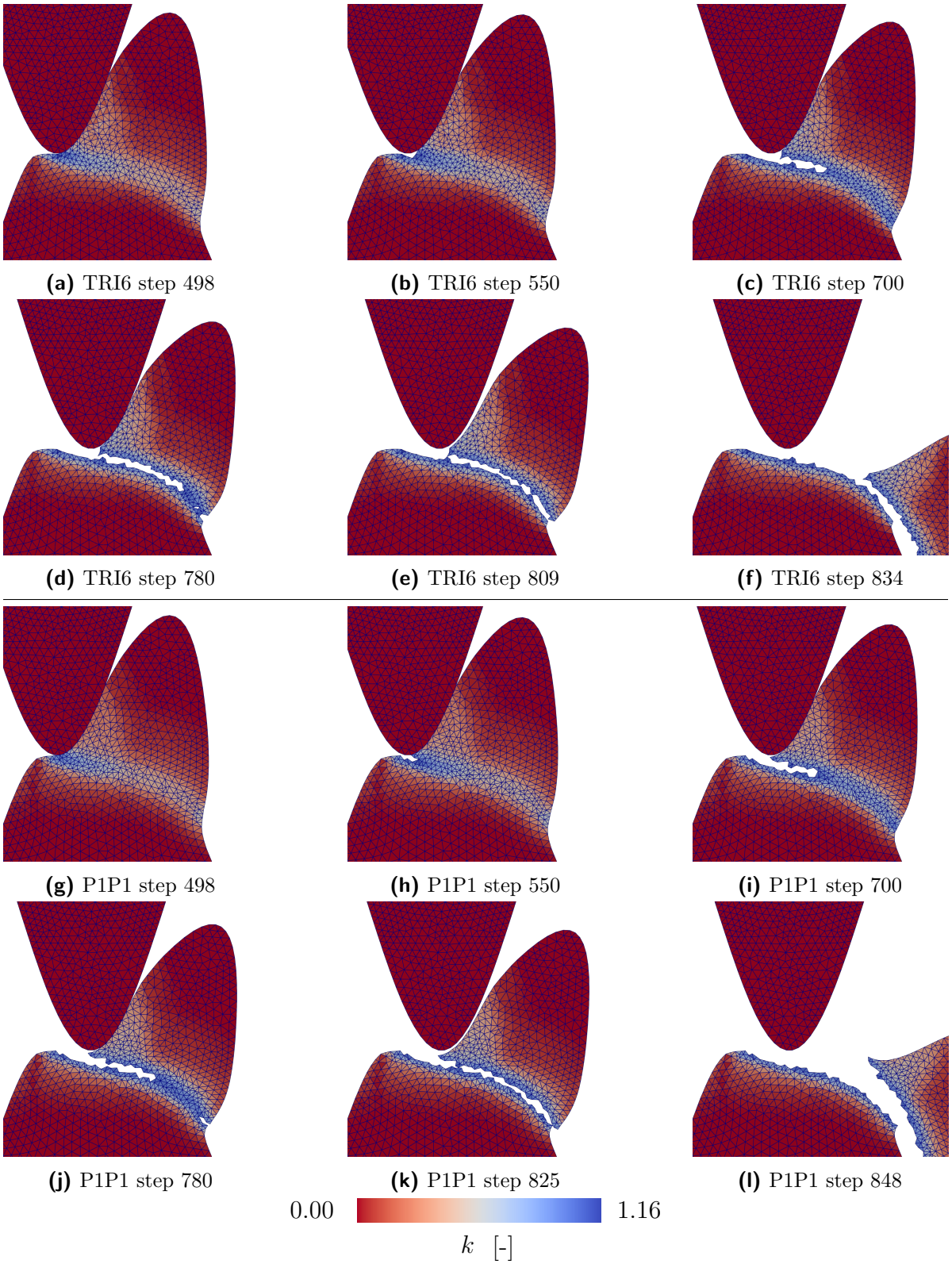

(a) TRI6 step 498 **(b)** TRI6 step 550 **(c)** TRI6 step 700

(d) TRI6 step 780 **(e)** TRI6 step 809 **(f)** TRI6 step 834

(g) P1P1 step 498 **(h)** P1P1 step 550 **(i)** P1P1 step 700

(j) P1P1 step 780 **(k)** P1P1 step 825 **(l)** P1P1 step 848

Figure 4.29: Contour plots of asperity shearing for TRI6 element (a) to (f) and P1P1 element (g) to (l). The last frames (e), (f) and (k), (l) show self-contact situations of the separated chip, where the time steps here do not coincide due to earlier separation for the TRI6 element.

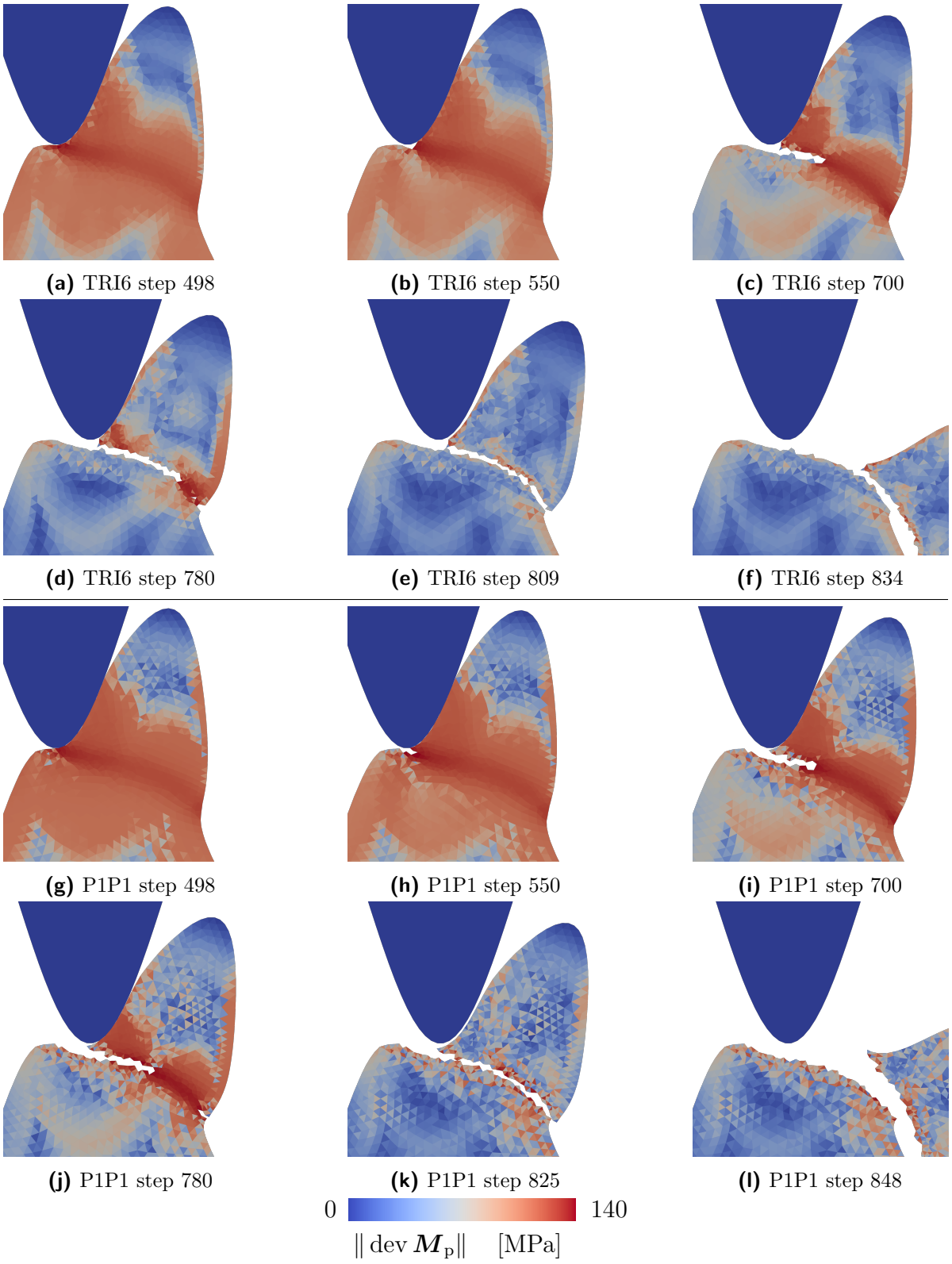

(a) TRI6 step 498 **(b)** TRI6 step 550 **(c)** TRI6 step 700

(d) TRI6 step 780 **(e)** TRI6 step 809 **(f)** TRI6 step 834

(g) P1P1 step 498 **(h)** P1P1 step 550 **(i)** P1P1 step 700

(j) P1P1 step 780 **(k)** P1P1 step 825 **(l)** P1P1 step 848

Figure 4.30: Contour plots of asperity shearing for TRI6 element (a) to (f) and P1P1 element (g) to (l). The last frames (e), (f) and (k), (l) show self-contact situations of the separated chip, where the time steps here do not coincide due to earlier separation for the TRI6 element.

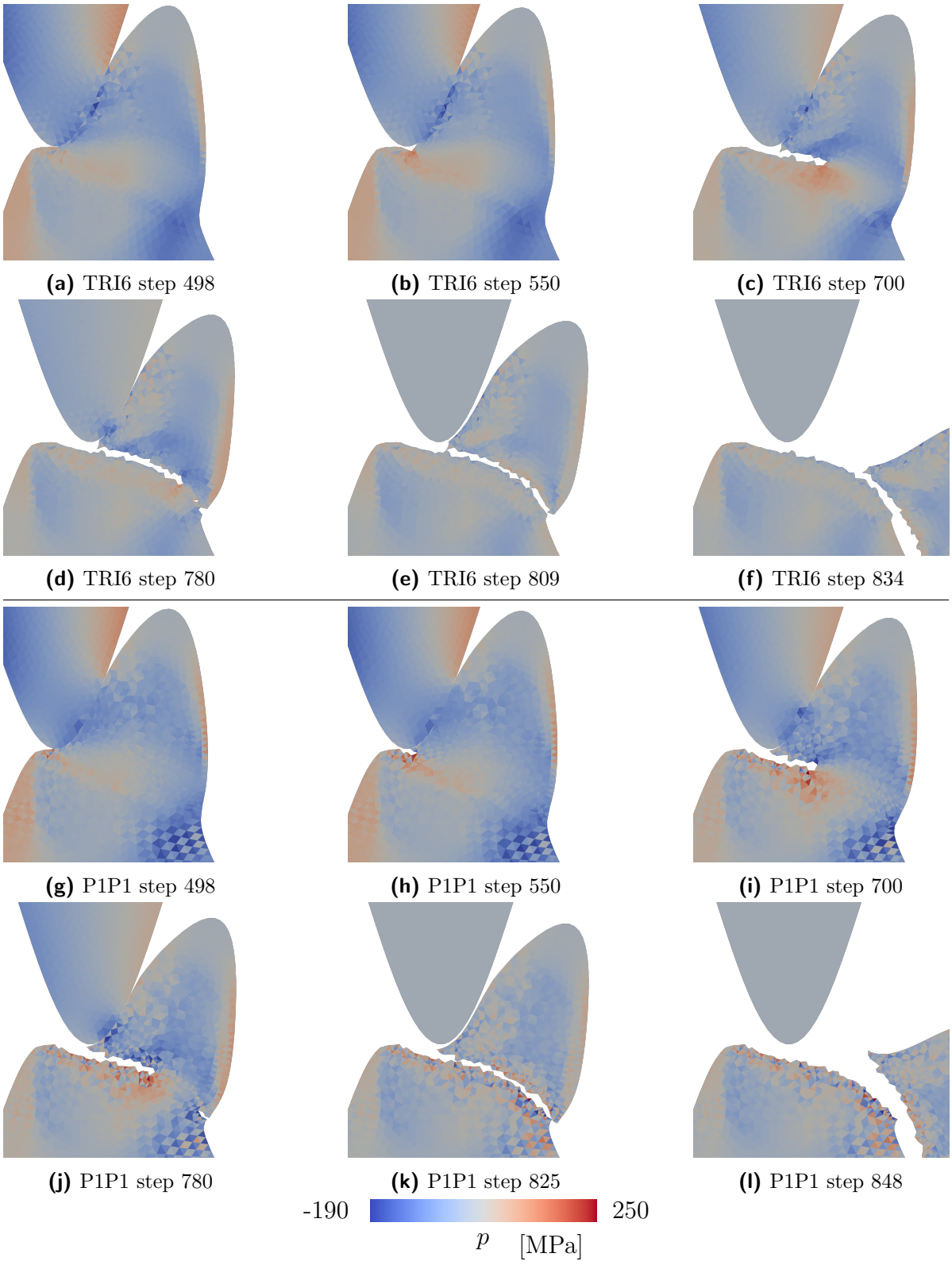

(a) TRI6 step 498 **(b)** TRI6 step 550 **(c)** TRI6 step 700

(d) TRI6 step 780 **(e)** TRI6 step 809 **(f)** TRI6 step 834

(g) P1P1 step 498 **(h)** P1P1 step 550 **(i)** P1P1 step 700

(j) P1P1 step 780 **(k)** P1P1 step 825 **(l)** P1P1 step 848

Figure 4.31: Contour plots of asperity shearing for TRI6 element (a) to (f) and P1P1 element (g) to (l). The last frames (e), (f) and (k), (l) show self-contact situations of the separated chip, where the time steps here do not coincide due to earlier separation for the TRI6 element.

proposed and, as a more elegant element deletion approach, the shape detection method is made more sensitive in regions of high material degradation.

- Self contact is modelled with an extension of the bulk mesh generation with a slight relocation of the self contact candidate nodes in order to prevent edge intersections in the Constrained Delaunay Triangulation for closed self-contact. Although the original contact domain is automatically capable of self-contact, see [58], their model does not include PFEM remeshing and thus the regeneration of the bulk mesh does not pose problems in the case of closed contact.

- In future work, the pressure oscillations for plastic incompressibility for the P1P1 should be further investigated since the author of this thesis is not aware of discussions of this problem in the respective literature. Furthermore, the contact modelling for the TRI6 element currently features a contact mesh which only considers the corner nodes of the quadratic triangles. Although a contact mesh including the edge-mid nodes seems better in terms of contact force distribution, the simulations were significantly less robust. Furthermore, the current solution of meshing only the corner nodes shows slight inhomogeneity of the contact pressures which should be investigated further.

The presented PFEM framework for the modelling of material separation represents a good starting point for microscopic investigations on the wear mechanisms on asperity level, which can supplement the macroscopic wear simulation approach presented in Chapter 3.

5 Modelling and simulation of material deposition

The introduction to this thesis in Section 1.3 introduces key aspects of material deposition processes, such as DED-LB, and their importance in additive manufacturing. Building on the theoretical foundation presented in Chapter 2, this chapter focuses on the theoretical framework required to study the interaction between the deposited hot material and the cold baseplate. The PFEM is used for its remeshing capabilities which are essential for simulating extremely large material flows and modelling residual stresses after deposition and solidification. Emphasis is placed on the phase transformation material model for melt flow and solidification, and the PFEM methods described in Section 2.4 are supplemented by methods related to material bonding. Numerical examples of material behaviour and a 2d application example are given. A conclusion shows how this work contributes to the goal of a full featured simulation model for deposition simulation in DED-LB.

Apart from minor adaptations, this chapter is a textual reproduction of the journal article [120], with directly quoted passages marked in each numbered subsection using $\overset{\text{qtd.}}{_{[120]}}\{$to $\}^{\text{qtd.}}_{[120]}$.

5.1 Material modelling of melt and solidification

$\overset{\text{qtd.}}{_{[120]}}\{$The phase transformation model is based on the small-strain model presented in [95], which is founded on an averaged energy density function and mass phase fractions. While the averaging is adopted from the reference, the phase evolution by energy minimisation is replaced by a temperature based phenomenologically motivated function in the present work and the kinematics are extended to finite strains. This section describes the phase transformation model along with large strain constitutive equations for the solid and fluid phase. $\}^{\text{qtd.}}_{[120]}$

5.1.1 Phase description and homogenisation

qtd. [120] {The microstructural evolution of the phase-mixture is described by volume fractions $\xi_\bullet$ of phase $\bullet$ according to

$$\xi_\bullet = \frac{\mathrm{d}V_\bullet}{\mathrm{d}V} \tag{5.1}$$

which describes the volume contribution $\mathrm{d}V_\bullet$ of phase $\bullet$ related to a reference volume element $\mathrm{d}V$. The symbol $\bullet$ is used as a placeholder for either mel (melt) or sol (solid) whenever an equation holds for the melt and the solid phase. Furthermore, i is used as an index, respectively counter, when a sum over phases mel and sol is conducted. The mass fractions $\zeta_\bullet$ are defined similarly and are related to the volume fractions via

$$\zeta_\bullet = \frac{\mathrm{d}m_\bullet}{\mathrm{d}m} = \frac{\rho_{0\bullet}\,\mathrm{d}V_\bullet}{\rho_0\,\mathrm{d}V} = \frac{\rho_{0\bullet}}{\rho_0}\,\xi_\bullet \tag{5.2}$$

where ρ_0 is the referential mass density, $\rho_{0\bullet}$ refers to the respective referential phase mass densities and where $\mathrm{d}m_\bullet$ denotes the mass contribution of phase $\bullet$ in the mass element $\mathrm{d}m$. The phase fractions have to fulfil mass conservation which can be expressed as

$$\sum_i \mathrm{d}m_i = \mathrm{d}m \qquad \Longleftrightarrow \qquad \sum_i \zeta_i = 1 \tag{5.3}$$

The mass-specific free energy density Ψ of the phase-mixture is specified as

$$\Psi = \sum_i \zeta_i\,\Psi_i \tag{5.4}$$

as a basis for the constitutive modelling. For the use as elastic potential, the conversion to volume-specific energy densities via $\Psi_\bullet = \psi_\bullet/\rho_{0\bullet}$ is made. A multiplication with ρ_0 yields a volume-specific description of the energy mixture as

$$\rho_0\,\Psi = \rho_0 \sum_i \frac{\zeta_i}{\rho_{0i}}\,\psi_i = \sum_i \xi_i\,\psi_i \tag{5.5}$$

where the conversion to volume fractions is based on (5.2). The components of the phase-wise energy densities can furthermore be specified by

$$\psi_\bullet = \psi_\bullet^{\mathrm{mec}}(\boldsymbol{C}_\bullet) + \psi_\bullet^{\mathrm{cal}}(\theta) \tag{5.6}$$

where the mechanical part $\psi_\bullet^{\mathrm{mec}}(\boldsymbol{C}_\bullet)$ will be specified in Section 5.1.2 and the caloric part $\psi_\bullet^{\mathrm{cal}}(\theta)$ will be specified in Section 5.1.3.

In [95], an energy-minimisation approach forms the foundation of the homogenisation technique. To account for the more complex kinematics in the present large strain formulation, a Voigt-type homogenisation technique is applied as a simplification. The

homogenisation approach affects stresses and effective material properties during solidification, but does not couple to the transformation itself, which is modelled as purely temperature dependent. Consequently, the influence is limited to the narrow solidification temperature range and is assumed to have no significant effect on the results. This justifies the adoption of the simplest homogenisation assumption of identical deformation in both phases, i.e.

$$\boldsymbol{F} = \boldsymbol{F}_{\mathrm{mel}} = \boldsymbol{F}_{\mathrm{sol}} \tag{5.7}$$

Based on the hyperelastic format specified in (2.6), Piola stresses are now derived from the averaged energy density according to

$$\boldsymbol{P} = \frac{\partial \rho_0 \Psi}{\partial \boldsymbol{F}} = \sum_i \xi_i \frac{\partial \psi_i}{\partial \boldsymbol{F}_i} = \sum_i \xi_i \boldsymbol{P}_i \tag{5.8}$$

where the Voigt assumption (5.7) allows for an uncoupled calculation of the phase-wise Piola stresses $\boldsymbol{P}_\bullet = \partial \psi_\bullet / \partial \boldsymbol{F}_\bullet$. Likewise, the averaged heat capacity c_0 is calculated from (2.6) and (5.5) as

$$c_0 = -\theta \frac{\partial^2 \rho_0 \Psi}{\partial \theta \, \partial \theta} = -\theta \sum_i \xi_i \frac{\partial^2 \psi_i}{\partial \theta \, \partial \theta} \tag{5.9}$$

Phase evolution equation

The energy-based homogenisation approach in [95] shows that temperature is the main influence on the solidification of melt in AM processes. Therefore, in the present work a purely temperature based evolution equation for the melt mass fraction ζ_{mel} is applied. A smoothed step function is applied to describe the phase transition similar to [73, 113] as

$$\zeta_{\mathrm{mel}}(\theta) = \frac{1}{2}\left[\tanh\left(\frac{2}{\Delta\theta}\left[\theta - \theta^{\mathrm{mlt}}\right]\right) + 1\right] \tag{5.10}$$

close to the melt temperature θ^{mlt}. The temperature range factor $\Delta\theta$ is used to adapt the transformation behaviour to the physical behaviour. The transformation function is illustrated in Figure 5.1 for different range factors. Due to the closed format, an explicit equation for the transformation rate $\dot{\zeta}_{\mathrm{mel}}$ can be derived as

$$\dot{\zeta}_{\mathrm{mel}}(\theta, \dot{\theta}) = \frac{1}{\Delta\theta} \operatorname{sech}^2\left(\frac{2}{\Delta\theta}\left[\theta - \theta^{\mathrm{mlt}}\right]\right) \dot{\theta} \tag{5.11}$$

} qtd. [120]

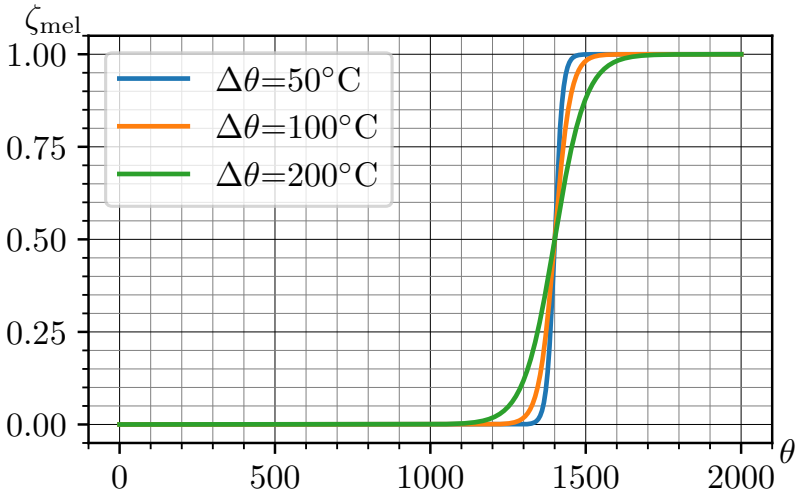

Figure 5.1: Phenomenological melt-evolution function $\zeta_{\mathrm{mel}}(\theta)$ defined in (5.10) as smoothed step function of tanh-type. The melt-temperature $\theta^{\mathrm{mlt}} = 1400\,°\mathrm{C}$ and the temperature range factor $\Delta\theta$ govern the transformation behaviour. Reprinted from [120], licensed under CC BY 4.0.

5.1.2 Mechanical constitutive model of the phase mixture

qtd. [120]{The mechanical constitutive equations for the balance of linear momentum (2.4) are defined in this section. Thereby, a prototype model for the solidification and re-melting of metal is derived. The number of phases is restricted to one melt and one solid phase. The deformation splits into a deformation path of the solid phase fraction ζ_{sol} and the melt phase fraction ζ_{mel}. The melt phase additionally features unbounded isochoric viscous deformation similar to a Maxwell fluid to allow for the description of the fluid-like melt behaviour. The multiplicative decomposition of the deformation gradient for the melt phase is

$$\boldsymbol{F}_{\mathrm{mel}} = \boldsymbol{F}^{\mathrm{iso}}_{\mathrm{mel,e}} \cdot \boldsymbol{F}^{\mathrm{iso}}_{\mathrm{mel,v}} \cdot \boldsymbol{F}^{\mathrm{vol}}_{\mathrm{mel,e}} \cdot \boldsymbol{F}^{\mathrm{thm}}_{\mathrm{mel}} \cdot \boldsymbol{F}^{\mathrm{tra}}_{\mathrm{mel}} \tag{5.12}$$

with the instantaneous elastic deformation $\boldsymbol{F}^{\mathrm{iso}}_{\mathrm{mel,e}}$ which occurs upon fast loading when the viscous deformation $\boldsymbol{F}^{\mathrm{iso}}_{\mathrm{mel,v}}$ has no time to evolve, and with a decomposition of the volumetric deformation into the elastic part $\boldsymbol{F}^{\mathrm{vol}}_{\mathrm{mel,e}}$ and the irreversible parts for thermal expansion $\boldsymbol{F}^{\mathrm{thm}}_{\mathrm{mel}}$ and transformation stretches $\boldsymbol{F}^{\mathrm{tra}}_{\mathrm{mel}}$. The solid phase is modelled by an elastic constitutive relation extended by thermal expansion and transformation stretches. Moreover, the irreversible viscous deformation upon phase transformation is fully inherited to the solid phase, such that the multiplicative decomposition reads

$$\boldsymbol{F}_{\mathrm{sol}} = \boldsymbol{F}^{\mathrm{iso}}_{\mathrm{sol,e}} \cdot \left[\boldsymbol{F}^{\mathrm{iso}}_{\mathrm{mel,v}}\right]_n \cdot \boldsymbol{F}^{\mathrm{vol}}_{\mathrm{sol,e}} \cdot \boldsymbol{F}^{\mathrm{thm}}_{\mathrm{sol}} \cdot \boldsymbol{F}^{\mathrm{tra}}_{\mathrm{sol}} \tag{5.13}$$

Here, $\boldsymbol{F}^{\mathrm{iso}}_{\mathrm{sol,e}}$ is the isochoric elastic deformation, whereas $\left[\boldsymbol{F}^{\mathrm{iso}}_{\mathrm{mel,v}}\right]_n$ does not evolve in the solid phase but is inherited from the value in the melt phase from the last time

step. Furthermore, the volumetric contributions $\boldsymbol{F}_{\mathrm{sol,e}}^{\mathrm{vol}}$, $\boldsymbol{F}_{\mathrm{sol}}^{\mathrm{thm}}$ and $\boldsymbol{F}_{\mathrm{sol}}^{\mathrm{tra}}$ are equivalent to the ones the melt phase. Upon remelting, the previous viscous deformations are also to be inherited back to the melt phase. Both constitutive relations are detailed in the subsequent sections. The total deformation is identical for both phases due to the Voigt assumption (5.7). The model can be identically used for solidification and re-melting of the material, as the phase evolution equation (5.10) uniquely defines the microstructural state. The initial state of the material has to be known in order to correctly calculate transformation stretches and thermal expansion.

Transformation stretches and thermal expansion

Transformation stretch and thermal expansion are inelastic deformation contributions and assumed to be volumetric. The volumetric stretches are given in terms of the determinant $J_\bullet = \det(\boldsymbol{F}_\bullet)$ which defines the volumetric part of the deformation gradient as $\boldsymbol{F}_\bullet^{\mathrm{vol}} = J_\bullet^{1/3}\,\boldsymbol{I}$. Therefore, the volumetric part of the decompositions (5.12) and (5.13) can be expressed as a decomposition of the Jacobians as

$$\boldsymbol{F}_\bullet^{\mathrm{vol}} = \boldsymbol{F}_{\bullet,\mathrm{e}}^{\mathrm{vol}} \cdot \boldsymbol{F}_\bullet^{\mathrm{thm}} \cdot \boldsymbol{F}_\bullet^{\mathrm{tra}} = \left[J_{\bullet,\mathrm{e}}\, J_\bullet^{\mathrm{thm}}\, J_\bullet^{\mathrm{tra}}\right]^{1/3} \boldsymbol{I} \tag{5.14}$$

such that the elastic part follows as $J_{\bullet,\mathrm{e}} = J_\bullet \left[J_\bullet^{\mathrm{thm}}\, J_\bullet^{\mathrm{tra}}\right]^{-1}$ and where the inelastic contributions are defined in the following. As the melt and the solid phases possess different mass densities, the transformation induces a volumetric transformation stretch $J_\bullet^{\mathrm{tra}}$ which can be derived from mass conservation. In contrast to (5.3), where the total mass of the phase mixture is preserved, a transforming mass element is compared between the initial state $\mathrm{d}m_1$ and the transformed state $\mathrm{d}m_2$ as

$$\mathrm{d}m_1 = \mathrm{d}m_2 \quad \Longleftrightarrow \quad \rho_{01}\,\mathrm{d}V_1 = \rho_{02}\,\mathrm{d}V_2 \quad \Longrightarrow \quad J_\bullet^{\mathrm{tra}} = \frac{\mathrm{d}V_2}{\mathrm{d}V_1} = \frac{\rho_{01}}{\rho_{02}} \tag{5.15}$$

As mentioned above, different initial states can be considered in this model. Therefore, the transformation stretch only occurs in the phase that is not present in the initial state of the part under consideration. Furthermore, the initial and transformed mass densities are considered at liquidus temperature θ^{lqd} as $\rho_{0\mathrm{lqd}}$ and solidus temperature θ^{sld} as $\rho_{0\mathrm{sld}}$ in order to clearly differentiate between heat expansion and transformation stretches.

The remaining inelastic volumetric deformation contribution is thermal expansion. According to [80], thermal expansion can be introduced by a nonlinear temperature dependent stretch function

$$J_\bullet^{\mathrm{thm}}(\theta) = \exp\left(\int_{\theta_\bullet^{\mathrm{ref}}}^{\theta} \alpha_\bullet^{\mathrm{thm}}(\vartheta)\,\mathrm{d}\vartheta\right) \tag{5.16}$$

with the temperature dependent expansion coefficient $\alpha_\bullet^{\mathrm{thm}}$ being integrated with integration variable ϑ from reference temperature $\theta_\bullet^{\mathrm{ref}}$ to current temperature θ. Assuming a temperature independent α^{thm}, this simplifies to

$$J_\bullet^{\mathrm{thm}}(\theta) = \exp\left(\alpha_\bullet^{\mathrm{thm}}\left[\theta - \theta_\bullet^{\mathrm{ref}}\right]\right) \tag{5.17}$$

In the case of a temperature dependent heat expansion coefficient it is more convenient to replace (5.16) with a, e.g., standard linear relation to circumvent the path dependence of the expansion. However, as the present work focuses on establishing the basic simulation framework, the exponential relation with a constant expansion coefficient is chosen. For the reference temperature $\theta_\bullet^{\mathrm{ref}}$, a distinction has to be made depending on the initial material state. Starting from the initial phase, the initial temperature θ^{ini} can often directly be related to a stress-free configuration such that $\theta_\bullet^{\mathrm{ref}} = \theta^{\mathrm{ini}}$. Upon transformation from solid to liquid, the liquidus temperature represents the stress free initial state, i.e. $\theta_\bullet^{\mathrm{ref}} = \theta^{\mathrm{lqd}}$. Similarly upon transformation from liquid to solid, the solidus temperature is the reference, i.e. $\theta_\bullet^{\mathrm{ref}} = \theta^{\mathrm{sld}}$, which is one important source of residual stresses after phase transformation.

Melt material model

The deformation path of the molten material is governed by a viscoelastic constitutive relation based on [4, 44] which is adapted as a Maxwell fluid to allow for unbounded isochoric viscous strains $\boldsymbol{F}^{\mathrm{iso}}_{\mathrm{mel,v}}$. Despite the unbounded isochoric flow, a contribution from $\boldsymbol{F}^{\mathrm{iso}}_{\mathrm{mel,e}}$ is present in the Helmholtz free energy density which describes the instantaneously stored elastic energy driving the rate dependent evolution of $\boldsymbol{F}^{\mathrm{iso}}_{\mathrm{mel,v}}$. Furthermore, the melt is considered to be compressible with an elastic volume dilatation $J_{\mathrm{mel,e}}$. The mechanical energy density is expressed as

$$\psi^{\mathrm{mec}}_{\mathrm{mel}} = \underbrace{\frac{1}{2}\, G_{\mathrm{mel}} \left[\boldsymbol{C}^{\mathrm{iso}}_{\mathrm{mel,e}} \colon \boldsymbol{I} - 3 \right]}_{\psi^{\mathrm{iso}}_{\mathrm{mel}}} + \underbrace{\frac{1}{4}\, K_{\mathrm{mel}} \left[\left[{J_{\mathrm{mel,e}}}^2 - 1 \right] - 2 \ln(J_{\mathrm{mel,e}}) \right]}_{\psi^{\mathrm{vol}}_{\mathrm{mel}}} \tag{5.18}$$

with the shear modulus G_{mel} and with the compression modulus K_{mel}. The elastic part of the volume dilatation, i.e. $J_{\mathrm{mel,e}}$, is defined in Section 5.1.2. In view of the elastic isochoric deformation, the first related invariant can be expressed according to

$$\boldsymbol{C}^{\mathrm{iso}}_{\mathrm{mel,e}} \colon \boldsymbol{I} = \boldsymbol{C}^{\mathrm{iso}}_{\mathrm{mel}} \colon \left[\boldsymbol{C}^{\mathrm{iso}}_{\mathrm{mel,v}} \right]^{-1} \tag{5.19}$$

where $\boldsymbol{C}^{\mathrm{iso}}_{\mathrm{mel,v}}$ is chosen as internal variable of the viscous evolution. The Piola stress tensor consequently reads

$$\begin{aligned} \boldsymbol{P}_\bullet &= \frac{\partial \psi^{\mathrm{mec}}_\bullet}{\partial \boldsymbol{F}_\bullet} \\ &= G_\bullet\, J_\bullet^{-2/3} \left[\boldsymbol{F}_\bullet \cdot \left[\boldsymbol{C}^{\mathrm{iso}}_{\bullet,\mathrm{v}} \right]^{-1} - \frac{1}{3} \left[\boldsymbol{C}_\bullet \colon \left[\boldsymbol{C}^{\mathrm{iso}}_{\bullet,\mathrm{v}} \right]^{-1} \right] \boldsymbol{F}_\bullet^{-\mathrm{t}} \right] + \frac{1}{2} K_\bullet \left[J^2_{\bullet,\mathrm{e}} - 1 \right] \boldsymbol{F}_\bullet^{-\mathrm{t}} \end{aligned} \tag{5.20}$$

The $\bullet$ indicates that this equation is valid for both the melt and the solid phases since the viscous contribution is also present in the solid due to inheritance, see Section 5.1.2 for further details.

Viscous evolution equation The evolution of the isochoric viscous flow $\boldsymbol{C}^{\text{iso}}_{\text{mel,v}}$ is introduced in a thermodynamically consistent way based on the dissipation inequality, see [4, 44]. A Mandel type stress-tensor is derived as

$$\boldsymbol{M}_{\text{v}} = \frac{\partial \psi_{\text{mel}}}{\partial \left[\boldsymbol{C}^{\text{iso}}_{\text{mel,v}}\right]^{-1}} \cdot \left[\boldsymbol{C}^{\text{iso}}_{\text{mel,v}}\right]^{-1} = -\,\boldsymbol{C}^{\text{iso}}_{\text{mel,v}} \cdot \frac{\partial \psi_{\text{mel}}}{\partial \boldsymbol{C}^{\text{iso}}_{\text{mel,v}}} \tag{5.21}$$

which is used to reformulate the reduced mechanical dissipation inequality (2.7) as

$$\mathcal{D}^{\text{red}}_{\text{mec}} = -\,\frac{\partial \psi_{\text{mel}}}{\partial \boldsymbol{C}^{\text{iso}}_{\text{mel,v}}} : \dot{\boldsymbol{C}}^{\text{iso}}_{\text{mel,v}} \geq 0 \quad \Longleftrightarrow \quad \boldsymbol{M}_{\text{v}} : \left[\left[\boldsymbol{C}^{\text{iso}}_{\text{mel,v}}\right]^{-1} \cdot \dot{\boldsymbol{C}}^{\text{iso}}_{\text{mel,v}}\right] \geq 0 \tag{5.22}$$

Thermodynamical consistence is thereby guaranteed by defining

$$\left[\boldsymbol{C}^{\text{iso}}_{\text{mel,v}}\right]^{-1} \cdot \dot{\boldsymbol{C}}^{\text{iso}}_{\text{mel,v}} \propto \frac{\partial \Phi_{\text{v}}}{\partial \boldsymbol{M}_{\text{v}}} \quad \Longrightarrow \quad \dot{\boldsymbol{C}}^{\text{iso}}_{\text{mel,v}} = \dot{\gamma}\, \boldsymbol{C}^{\text{iso}}_{\text{mel,v}} \cdot \frac{\partial \Phi_{\text{v}}}{\partial \boldsymbol{M}_{\text{v}}} \tag{5.23}$$

where proportionality factor $\dot{\gamma} \geq 0$ is a viscous rate multiplier and where flow potential Φ_{v} is introduced similar to v. Mises plasticity but without a threshold as

$$\Phi_{\text{v}} = \left[\boldsymbol{M}^{\text{dev}}_{\text{v}} : \boldsymbol{M}^{\text{dev}}_{\text{v}}\right]^{1/2} \quad \Longrightarrow \quad \frac{\partial \Phi_{\text{v}}}{\partial \boldsymbol{M}_{\text{v}}} = \frac{\boldsymbol{M}^{\text{dev\,t}}_{\text{v}}}{\Phi_{\text{v}}} \tag{5.24}$$

The resulting pre-factor of the evolution equation is furthermore abbreviated as

$$\frac{1}{\eta_{\text{v}}} = \frac{\dot{\gamma}}{\Phi_{\text{v}}} \tag{5.25}$$

which leads to the evolution equation in the form

$$\dot{\boldsymbol{C}}^{\text{iso}}_{\text{mel,v}} = \frac{1}{\eta_{\text{v}}}\, \boldsymbol{C}^{\text{iso}}_{\text{mel,v}} \cdot \boldsymbol{M}^{\text{dev\,t}}_{\text{v}} \tag{5.26}$$

where η_{v} is the viscosity of the melt. For the specific energy function (5.18), the driving stress tensor follows as

$$\boldsymbol{M}^{\text{dev}}_{\text{v}} = \frac{1}{2}\, G_{\text{mel}} \left[\boldsymbol{C}^{\text{iso}}_{\text{mel}} \cdot \left[\boldsymbol{C}^{\text{iso}}_{\text{mel,v}}\right]^{-1} - \frac{1}{3}\, \boldsymbol{C}^{\text{iso}}_{\text{mel}} : \left[\boldsymbol{C}^{\text{iso}}_{\text{mel,v}}\right]^{-1} \boldsymbol{I}\right] \tag{5.27}$$

For a more general introduction relating the pre-factor to Perzyna-type viscoplastic laws, the reader is referred to [4, 44]. The purely isochoric evolution is to be guaranteed in the numerical solution of (5.26). As this work proceeds, this is explicitly enforced by adding an equality constraint $\det(\boldsymbol{C}^{\text{iso}}_{\text{mel,v}}) = 1$, cf. [44], yielding the local system of equations

$$\boldsymbol{r}_{\text{v}} = \dot{\boldsymbol{C}}^{\text{iso}}_{\text{mel,v}} - \frac{1}{\eta_{\text{v}}}\, \boldsymbol{C}^{\text{iso}}_{\text{mel,v}} \cdot \boldsymbol{M}^{\text{dev\,t}}_{\text{v}} - \Lambda_{\text{v}}\, \frac{\partial h_{\text{v}}}{\partial \boldsymbol{C}^{\text{iso}}_{\text{mel,v}}} = \boldsymbol{0} \tag{5.28}$$

$$h_{\text{v}} = \det(\boldsymbol{C}^{\text{iso}}_{\text{mel,v}}) - 1 = 0 \tag{5.29}$$

where Λ_v is the Lagrange multiplier controlling the fulfilment of the equality constraint $h_\mathrm{v} = 0$. By applying this additional constraint equation, an implicit Euler time integration

$$\dot{\boldsymbol{C}}^{\mathrm{iso}}_{\mathrm{mel,v}} = \frac{\boldsymbol{C}^{\mathrm{iso}}_{\mathrm{mel,v}} - \left[\boldsymbol{C}^{\mathrm{iso}}_{\mathrm{mel,v}}\right]_n}{\Delta t} \tag{5.30}$$

of time step Δt is sufficient to preserve the fully isochoric evolution of $\boldsymbol{C}^{\mathrm{iso}}_{\mathrm{mel,v}}$. The viscous deformation tensor $\boldsymbol{C}^{\mathrm{iso}}_{\mathrm{mel,v}}$ of the last time step n is stored as a state-variable and is also passed to the solid phase for inheritance and back in case of remelting, i.e. both phases share only one viscous state-variable which solely evolves within the melt phase.

Solid material model

The deformation path of the solid material is governed by an elastic constitutive equation, which is further extended to incorporate inelastic transformation stretches and thermal stretches, both assumed to be volumetric contributions. The mechanical energy-density is similar to the melt model and, based on [4, 44], is chosen as

$$\psi^{\mathrm{mec}}_{\mathrm{sol}} = \underbrace{\frac{1}{2}\, G_{\mathrm{sol}} \left[\boldsymbol{C}^{\mathrm{iso}}_{\mathrm{sol,e}} : \boldsymbol{I} - 3\right]}_{\psi^{\mathrm{iso}}_{\mathrm{sol}}} + \underbrace{\frac{1}{4}\, K_{\mathrm{sol}} \left[\left[{J_{\mathrm{sol,e}}}^2 - 1\right] - 2\,\ln(J_{\mathrm{sol,e}})\right]}_{\psi^{\mathrm{vol}}_{\mathrm{sol}}} \tag{5.31}$$

with the shear modulus G_{sol} and with the compression modulus K_{sol}. The elastic part of the volume dilatation $J_{\mathrm{sol,e}}$ is defined by deducting the inelastic contributions from the full volume dilatation as presented in Section 5.1.2. At the current state, the isochoric deformation of the solid is purely elastic as no plasticity is considered. However, during transformation the irreversible viscous deformations are inherited from the melt phase. Similar to (5.19), the elastic isochoric deformation of the solid phase is described in terms of the first invariant as

$$\boldsymbol{C}^{\mathrm{iso}}_{\mathrm{sol,e}} : \boldsymbol{I} = \boldsymbol{C}^{\mathrm{iso}}_{\mathrm{sol}} : \left[\left[\boldsymbol{C}^{\mathrm{iso}}_{\mathrm{mel,v}}\right]_n\right]^{-1} \tag{5.32}$$

by deducting the inherited viscous melt deformation from the full isochoric deformation of the solid. The inheritance is thereby computed based on the converged value from the previous time step n in order to prevent unwanted coupling of the viscous melt evolution to the solid phase stresses. Due to the inheritance and the similar energy densities, the Piola stress tensor $\boldsymbol{P}_{\mathrm{sol}}$ is computed analogously to the melt phase via (5.20). }$^{\mathrm{qtd.}}_{[120]}$

5.1.3 Thermal constitutive model of the phase mixture

qtd. [120]{The thermal constitutive relations to further complete the energy balance (2.5) are introduced in the sequel alongside the contributions which define the thermomechanical coupling. The caloric energy contributions are defined similar to [95] as

$$\psi^{\mathrm{cal}}_{\mathrm{mel}}(\theta) = -\, c_{0\mathrm{mel}}\, \theta\, \ln(\theta) \tag{5.33}$$

$$\psi^{\mathrm{cal}}_{\mathrm{sol}}(\theta) = -\, c_{0\mathrm{sol}}\, \theta\, \ln(\theta) + L_{\mathrm{sol}}\, \frac{\theta - \theta^{\mathrm{ref}}_{\mathrm{sol}}}{\theta^{\mathrm{ref}}_{\mathrm{sol}}} \tag{5.34}$$

with the heat capacities of the phases $c_{0\mathrm{mel}}$ and $c_{0\mathrm{sol}}$ and the latent heat L_{sol} which represents the gain of stored thermal energy upon phase transformation, calibrated to the reference temperature $\theta^{\mathrm{ref}}_{\mathrm{sol}}$ at which the phase transformation starts to evolve.

Heat sources

Although the evolution equation is chosen in a phenomenological manner according to (5.10), the dissipation still enters the energy balance (2.5) as part of the coupling heat source r^{mec}, cf. (2.8). The first term in (2.8), i.e. $\theta\, \partial_\theta \boldsymbol{P} \colon \dot{\boldsymbol{F}}$, describes the thermoelastic heat source. Based on (5.8) and by keeping the deformation gradient as well as the internal variables constant, the derivation results in

$$\frac{\partial \boldsymbol{P}}{\partial \theta} = \rho_0 \sum_i \frac{\zeta_i}{\rho_{0i}}\, \frac{\partial \boldsymbol{P}_i}{\partial \theta} \qquad \text{with} \qquad \frac{\partial \boldsymbol{P}_\bullet}{\partial \theta} = K_\bullet\, \alpha^{\mathrm{thm}}_\bullet\, \exp\left(\alpha^{\mathrm{thm}}_\bullet\, [\theta - \theta^{\mathrm{ref}}_\bullet]\right) \tag{5.35}$$

for the nonlinear heat expansion model (5.17). This thermoelastic coupling (5.35) is only given for completeness but neglected in the numerical examples in the present work due to its small influence on simulation results in comparison to other effects.

The dissipative heat sources in (2.8), i.e. $\mathcal{D}^{\mathrm{red}}_{\mathrm{mec}} - \theta\, \partial_\theta \mathcal{D}^{\mathrm{red}}_{\mathrm{mec}}$, depend on the internal variables $\mathcal{V} = \{\zeta_{\mathrm{mel}}, \boldsymbol{C}^{\mathrm{iso}}_{\mathrm{mel,v}}\}$. Thereby, ζ_{mel} is chosen as internal variable of the phase transformation which directly also defines $\zeta_{\mathrm{sol}} = 1 - \zeta_{\mathrm{mel}}$ via the mass balance (5.3). The dissipation contribution follows as

$$\mathcal{D}^{\mathrm{red}}_{\mathrm{mec}} = \underbrace{-\, \rho_0\, \frac{\partial \Psi}{\partial \zeta_{\mathrm{mel}}}\, \dot{\zeta}_{\mathrm{mel}}}_{\mathcal{D}_{\zeta_{\mathrm{mel}}}} \underbrace{-\, \rho_0\, \frac{\partial \Psi}{\partial \boldsymbol{C}^{\mathrm{iso}}_{\mathrm{mel,v}}} \colon \dot{\boldsymbol{C}}^{\mathrm{iso}}_{\mathrm{mel,v}}}_{\mathcal{D}_{\boldsymbol{C}^{\mathrm{iso}}_{\mathrm{mel,v}}}} \tag{5.36}$$

As this work proceeds, the dissipation of the viscous evolution in the melt phase $\mathcal{D}_{\boldsymbol{C}^{\mathrm{iso}}_{\mathrm{mel,v}}}$ is neglected in the heat source, as the resulting temperature increase is negligible compared to the overall high temperature of the melt. The heat generated by the phase transformation plays a more significant role in the thermal balance. The specification of $\mathcal{D}_{\zeta_{\mathrm{mel}}}$ follows from the averaged energy density (5.5) as

$$\mathcal{D}_{\zeta_{\mathrm{mel}}} = \rho_0 \left[\frac{\psi_{\mathrm{sol}}}{\rho_{0\mathrm{sol}}} - \frac{\psi_{\mathrm{mel}}}{\rho_{0\mathrm{mel}}}\right] \dot{\zeta}_{\mathrm{mel}} \tag{5.37}$$

where the solid energy enters via the mass balance (5.3). The derivative with respect to temperature results in

$$\begin{aligned}\frac{\partial \mathcal{D}_{\zeta_{\mathrm{mel}}}}{\partial \theta} = \quad & \rho_0 \left[\left[\frac{c_{0\mathrm{mel}}}{\rho_{0\mathrm{mel}}} - \frac{c_{0\mathrm{sol}}}{\rho_{0\mathrm{sol}}} \right] [1 + \ln(\theta)] + \frac{L_{\mathrm{sol}}}{\rho_{0\mathrm{sol}}\, \theta_{\mathrm{sol}}^{\mathrm{ref}}} \right] \dot{\zeta}_{\mathrm{mel}} \\ & + \rho_0 \left[\frac{1}{\rho_{0\mathrm{sol}}} \frac{\partial \psi_{\mathrm{sol}}^{\mathrm{mec}}}{\partial \theta} - \frac{1}{\rho_{0\mathrm{mel}}} \frac{\partial \psi_{\mathrm{mel}}^{\mathrm{mec}}}{\partial \theta} \right] \dot{\zeta}_{\mathrm{mel}}\end{aligned} \tag{5.38}$$

The transformation rate $\dot{\zeta}_{\mathrm{mel}}$ is specified explicitly by the phenomenological evolution equation in (5.11). Furthermore, the energy densities are given for the melt phase in (5.18) and (5.33), and for the solid phase in (5.31) and (5.34), where the inheritance of viscous melt deformation (5.32) has to be used. In view of the derivative of the mechanical energy density with respect to temperature one obtains

$$\frac{\partial \psi_{\bullet}^{\mathrm{mec}}}{\partial \theta} = \frac{\partial \psi_{\bullet}^{\mathrm{mec}}}{\partial J_{\bullet,\mathrm{e}}} \frac{\partial J_{\bullet,\mathrm{e}}}{\partial \theta} = \frac{1}{2} K_{\bullet} \left[J_{\bullet,\mathrm{e}} - J_{\bullet,\mathrm{e}}^{-1} \right] \left[-\alpha_{\bullet}^{\mathrm{thm}} J_{\bullet,\mathrm{e}} \right] \tag{5.39}$$

Remark: For a more intuitive interpretation of the dissipative heat sources from (5.37) and (5.38), the part of the dissipation stemming from the latent heat $\mathcal{D}_{\zeta_{\mathrm{mel}}}^{\mathrm{lat}}$ is further detailed in the following. The contribution related to latent heat in (5.37) is

$$\mathcal{D}_{\zeta_{\mathrm{mel}}}^{\mathrm{lat}} = \frac{\rho_0}{\rho_{0\mathrm{sol}}} L_{\mathrm{sol}} \frac{\theta - \theta_{\mathrm{sol}}^{\mathrm{ref}}}{\theta_{\mathrm{sol}}^{\mathrm{ref}}} \dot{\zeta}_{\mathrm{mel}} \tag{5.40}$$

and the dissipative heat source due to latent heat follows as

$$r^{\mathrm{lat}} = \mathcal{D}_{\zeta_{\mathrm{mel}}}^{\mathrm{lat}} - \theta \frac{\partial \mathcal{D}_{\zeta_{\mathrm{mel}}}^{\mathrm{lat}}}{\partial \theta} = - \frac{\rho_0}{\rho_{0\mathrm{sol}}} L_{\mathrm{sol}} \dot{\zeta}_{\mathrm{mel}} \tag{5.41}$$

This equation shows the expected effects of heating upon solidification and cooling upon liquification. Although the dissipation (5.40) itself can be negative for parts of the evolution due to the phenomenological evolution equation, the heat source is still well motivated and physically meaningful throughout the transformation. The full dissipative heat source of the phase transformation from (5.37) and (5.38) furthermore contains contributions from differences in the mechanical energy densities and the heat capacities of the phases.

Effective heat capacity

The effective heat capacity (5.9) is derived for the specific model at hand as

$$c_0 = -\theta \sum_i \xi_i \frac{\partial^2 \psi_i}{\partial \theta \partial \theta} = \sum_i \xi_i \left[c_{0i} \; - \; \underbrace{\theta \left[\alpha_i^{\mathrm{thm}} \right]^2 K_i \, J_{i,\mathrm{e}}^2}_{\chi} \right] \tag{5.42}$$

The quantity χ stems from the thermoelastic contribution and can be neglected due to the squared heat expansion coefficient.

Heat conduction of the phase mixture

Heat conduction is defined with a referential isotropic Fourier law to fulfil the dissipation restriction (2.7) as

$$\boldsymbol{Q} = -\,k_0\,\nabla_{\boldsymbol{X}}\theta \tag{5.43}$$

with the referential heat transfer coefficient k_0. Following the Voigt assumption used for the kinematics in (5.7), the averaged heat conduction is modelled based on a parallel configuration of two heat conductors which are also modelled via a Fourier law, i.e. $\boldsymbol{Q}_\bullet = -\,k_{0\bullet}\,\nabla_{\boldsymbol{X}}\theta$, with the phase-wise conduction coefficients $k_{0\bullet}$. The total heat flow $\boldsymbol{Q}\,\mathrm{d}V = \boldsymbol{Q}_{\mathrm{sol}}\,\mathrm{d}V_{\mathrm{sol}} + \boldsymbol{Q}_{\mathrm{mel}}\,\mathrm{d}V_{\mathrm{mel}}$ yields, together with (5.1), the averaged referential heat conductivity

$$k_0 = \xi_{\mathrm{sol}}\,k_{0\mathrm{sol}} + \xi_{\mathrm{mel}}\,k_{0\mathrm{mel}} \tag{5.44}$$

Surface heat flux

On the surface, convective and radiative heat flux is considered, see e.g. [15] also in view of aspects of implementation. The heat flux in configuration $\mathcal{B}_n$ is related to the referential heat flux via $\boldsymbol{Q}_n = \boldsymbol{Q}\cdot\mathrm{cof}^{-1}(\boldsymbol{F}_n)$, where the scalar surface heat flux follows as $Q_n = -\,\boldsymbol{Q}_n\cdot\boldsymbol{N}_n$ with the surface normal unit vector $\boldsymbol{N}_n$. For simplicity, the surface heat flux is directly defined with respect to configuration $\mathcal{B}_n$ as $Q_{n,\mathrm{sur}} = Q_{n,\mathrm{con}} + Q_{n,\mathrm{rad}}$ with

$$Q_{n,\mathrm{con}} = -\,h_c\,[\theta - \theta^\infty] \qquad\qquad Q_{n,\mathrm{rad}} = -\,\varepsilon\,\sigma\,[\theta^4 - [\theta^\infty]^4] \tag{5.45}$$

including the heat transfer coefficient h_c, the emissivity ε and the Stefan Boltzmann constant σ. Due to the frequent remeshing considered in the numerical examples as this work proceeds, the formulation is similar to a spatial definition of the surface heat flux. }$^{\mathrm{qtd.}}_{[120]}$

5.1.4 Numerical example of the material behaviour

$^{\mathrm{qtd.}}_{[120]}${In order to illustrate the behaviour of the material model, a simple one-element boundary value problem is considered as shown in Figure 5.2. The geometry and boundary conditions are visualised in Figure 5.2a. The implementation of the thermomechanical material model for melt flow and solidification, as presented in the previous sections, is summarised in Algorithm 3 for, say, the quadrature point level of a continuum element.

The material parameters are similar to those used in the main numerical examples in Section 5.3, compare Table 5.1. The data related to the baseplate is selected for this example from Table 5.2, with $r^{\mathrm{mec}} = 0$ for simplicity. Heating applied by a volumetric heat source until $t = 100\,\mathrm{ms}$ leads to thermal expansion and liquidation along with transformation stretches. The prescribed curve of the heat source r^{ext} as well as the solution of θ and ζ_{mel} are shown in Figure 5.2b along with outlines of the deformed

Algorithm 3: Phase transformation material model for melt flow and solidification. Reprinted from [120], licensed under CC BY 4.0.

Input: Deformation gradient $\boldsymbol{F}$, current and previous temperature θ, θ_n, temperature gradient $\nabla_{\boldsymbol{X}}\theta$, history variable $\left[\boldsymbol{C}^{\mathrm{iso}}_{\mathrm{mel,v}}\right]_n$, time step Δt, element group index Igpe, material parameters from Table 5.1 for both phases, part related parameters from Table 5.2

Output: Piola stresses $\boldsymbol{P}$, updated history variable $\boldsymbol{C}^{\mathrm{iso}}_{\mathrm{mel,v}}$, heat flux $\boldsymbol{Q}$, mechanical heat source r^{mec}, averaged heat capacity c_0, part related mass density ρ_0

Voigt assumption: $\boldsymbol{F} = \boldsymbol{F}_{\mathrm{sol}} = \boldsymbol{F}_{\mathrm{mel}}$

Assign part related parameters:

if Igpe *is 1 (baseplate material)* **then**

$J^{\mathrm{tra}}_{\mathrm{sol}} = 1, \quad J^{\mathrm{tra}}_{\mathrm{mel}} = \rho_{0\mathrm{sld}}/\rho_{0\mathrm{lqd}}, \quad \theta^{\mathrm{ref}}_{\mathrm{sol}} = \theta^{\mathrm{ini}}, \quad \rho_0 = \rho_{0\mathrm{sol}}$

else if Igpe *is 2 (stream material)* **or** *3 (connection zone material)* **then**

$J^{\mathrm{tra}}_{\mathrm{sol}} = \rho_{0\mathrm{lqd}}/\rho_{0\mathrm{sld}}, \quad J^{\mathrm{tra}}_{\mathrm{mel}} = 1, \quad \theta^{\mathrm{ref}}_{\mathrm{sol}} = \theta^{\mathrm{mlt}} - \Delta\theta, \quad \rho_0 = \rho_{0\mathrm{mel}}$

Calculate phase evolution:

$\zeta_{\mathrm{mel}} = 1/2 \left[\tanh\left(2 \left[\theta - \theta^{\mathrm{mlt}}\right]/\Delta\theta\right) + 1\right]$,
$\dot{\zeta}_{\mathrm{mel}} = 1/\Delta\theta \left[\mathrm{sech}^2\left(2\left[\theta - \theta^{\mathrm{mlt}}\right]/\Delta\theta\right)\right] \left[\theta - \theta_n\right]/\Delta t$

mass conservation $\zeta_{\mathrm{sol}} = 1 - \zeta_{\mathrm{mel}}$

Volumetric deformation:

$J^{\mathrm{thm}}_{\mathrm{sol}} = \exp\left(\alpha^{\mathrm{thm}}_{\mathrm{sol}}\left[\theta - \theta^{\mathrm{ref}}_{\mathrm{sol}}\right]\right) , \qquad J^{\mathrm{thm}}_{\mathrm{mel}} = 1 ,$
resulting elastic contributions: $J_{\bullet,\mathrm{e}} = J \left[J^{\mathrm{thm}}_{\bullet}\, J^{\mathrm{tra}}\right]^{-1}$

Viscous evolution in melt phase:

if $\zeta_{\mathrm{mel}} > 0$ **or** $|\dot{\zeta}_{\mathrm{mel}}| > 0$ **then**

Solve local Newton scheme for $\boldsymbol{C}^{\mathrm{iso}}_{\mathrm{mel,v}}$ and Λ_{v}

Initialise $\boldsymbol{C}^{\mathrm{iso}}_{\mathrm{mel,v}} = \left[\boldsymbol{C}^{\mathrm{iso}}_{\mathrm{mel,v}}\right]_n$ and residual equations

$\boldsymbol{r}_{\mathrm{v}} = \boldsymbol{C}^{\mathrm{iso}}_{\mathrm{mel,v}} - \left[\boldsymbol{C}^{\mathrm{iso}}_{\mathrm{mel,v}}\right]_n - \frac{1}{\eta_{\mathrm{v}}}\,\Delta t\, \boldsymbol{C}^{\mathrm{iso}}_{\mathrm{mel,v}} \cdot \boldsymbol{M}^{\mathrm{dev\,t}}_{\mathrm{v}} - \Delta t\, \Lambda_{\mathrm{v}}\, \partial h_{\mathrm{v}}/\partial \boldsymbol{C}^{\mathrm{iso}}_{\mathrm{mel,v}} = \boldsymbol{0}$

$h_{\mathrm{v}} = \det(\boldsymbol{C}^{\mathrm{iso}}_{\mathrm{mel,v}}) - 1 = 0$

while *residuum norm > tol* **do**

Newton update for $\boldsymbol{C}^{\mathrm{iso}}_{\mathrm{mel,v}}$ and Λ_{v}

Recalculate $\boldsymbol{r}_{\mathrm{v}}$, h_{v} and residuum norm

Piola stresses of the melt phase

$$\boldsymbol{P}_{\mathrm{mel}} = G_{\mathrm{mel}}\, J^{-2/3} \left[\boldsymbol{F} \cdot \left[\boldsymbol{C}^{\mathrm{iso}}_{\mathrm{mel,v}}\right]^{-1} - \frac{1}{3}\left[\boldsymbol{C} : \left[\boldsymbol{C}^{\mathrm{iso}}_{\mathrm{mel,v}}\right]^{-1}\right] \boldsymbol{F}^{-\mathrm{t}}\right] + \frac{1}{2}\, K_{\mathrm{mel}} \left[J^2_{\mathrm{mel,e}} - 1\right] \boldsymbol{F}^{-\mathrm{t}}$$

Solid material model: Inheritance of irreversible viscous deformation from melt phase

$$\boldsymbol{P}_{\mathrm{sol}} = G_{\mathrm{sol}}\, J^{-2/3} \left[\boldsymbol{F} \cdot \left[\boldsymbol{C}^{\mathrm{iso}}_{\mathrm{mel,v}}\right]^{-1}_n - \frac{1}{3}\left[\boldsymbol{C} : \left[\boldsymbol{C}^{\mathrm{iso}}_{\mathrm{mel,v}}\right]^{-1}_n\right] \boldsymbol{F}^{-\mathrm{t}}\right] + \frac{1}{2}\, K_{\mathrm{sol}} \left[J^2_{\mathrm{sol,e}} - 1\right] \boldsymbol{F}^{-\mathrm{t}}$$

Phase homogenisation: volume fractions $\xi_{\mathrm{mel}} = \zeta_{\mathrm{mel}}\, \rho_0/\rho_{0\mathrm{mel}}, \quad \xi_{\mathrm{sol}} = \zeta_{\mathrm{sol}}\, \rho_0/\rho_{0\mathrm{sol}}$

Effective Piola stresses $\boldsymbol{P} = \xi_{\mathrm{sol}}\, \boldsymbol{P}_{\mathrm{sol}} + \xi_{\mathrm{mel}}\, \boldsymbol{P}_{\mathrm{mel}}$

Effective heat flux $\boldsymbol{Q} = -\left[\xi_{\mathrm{sol}}\, k_{0\mathrm{sol}} + \xi_{\mathrm{mel}}\, k_{0\mathrm{mel}}\right] \nabla_{\boldsymbol{X}}\theta$

Effective heat capacity $c_0 = \xi_{\mathrm{sol}}\, c_{0\mathrm{sol}} + \xi_{\mathrm{mel}}\, c_{0\mathrm{mel}}$

Mechanical heat source $r^{\mathrm{mec}} = \mathcal{D}_{\zeta_{\mathrm{mel}}} - \theta\, \dfrac{\partial \mathcal{D}_{\zeta_{\mathrm{mel}}}}{\partial \theta}$ based on (5.37) and (5.38)

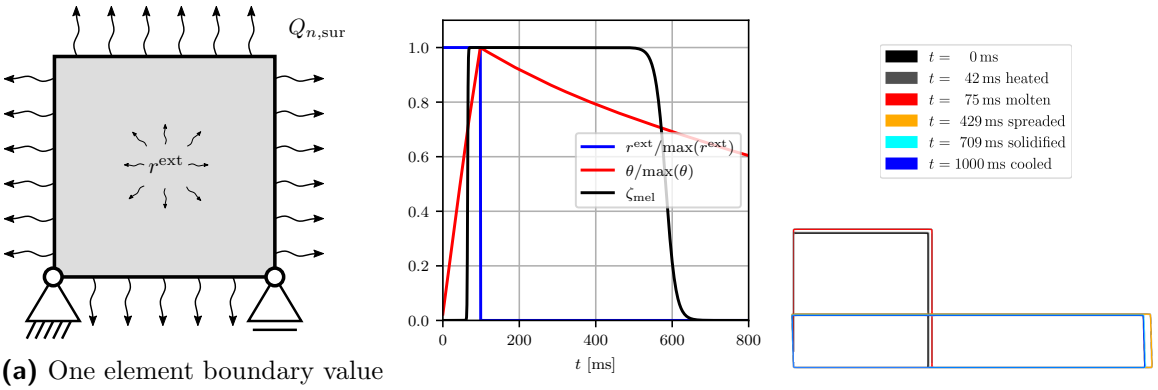

(a) One element boundary value problem

(b) Time evolution

(c) Outlines at different times

Figure 5.2: One element example for melting, flowing and solidification. Volumetric heat source $\max(r^{\mathrm{ext}}) = 50\,\mathrm{W/mm^3}$ leads to homogeneous heating until rapid melting occurs at $\theta^{\mathrm{mlt}} = 1400\,^{\circ}\mathrm{C} = 0.7\,\max(\theta)$. Cooling via surface convection and radiation under ambient temperature of $\theta^{\infty} = 25\,^{\circ}\mathrm{C}$ leads to solidification. Two pairs of contours in (c) which show thermal expansion and contraction are barely distinguishable from each other (black and grey, blue and turquoise). Reprinted from [120], licensed under CC BY 4.0.

element at important points in time in Figure 5.2c. The material flows under gravity until surface cooling induces re-solidification along with transformation stretches, followed by small thermal contractions. }$^{\text{qtd.}}_{[120]}$

5.2 Remeshing methods for material bonding

The general PFEM methods introduced in Section 2.4 are extended below to also consider the connection of two materials. $^{\text{qtd.}}_{[120]}${The α-shape method is adapted for the deposition problem by using individual α-parameter values for different regions of the process. In this context, three element groups are defined based on the nodal group index Igpn, which takes value 1 for the baseplate points and 2 for the stream points. The element group indices Igpe are deducted from the sum of the Igpn of the three element node points p, i.e.

$$\mathrm{Igpe} = \begin{cases} 1\ \text{(baseplate element)} & \texttt{if}\ \ \sum_p \mathrm{Igpn} = 3 \\ 2\ \text{(stream element)} & \texttt{if}\ \ \sum_p \mathrm{Igpn} = 6 \\ 3\ \text{(connection element)} & \texttt{if}\ \ \sum_p \mathrm{Igpn} = 4 \text{ or } 5 \end{cases} \tag{5.46}$$

The basic idea of the deposition remeshing framework is to work with one common Delaunay triangulation for both bodies and to let the α-shape technique decide as to when the bodies are so close that they can be considered to be bonded. The bonding thereby imposes a non-slip behaviour of the liquid-solid interface. A thin connection zone is desirable since the formation of the connection elements adds mass to the simulation. Three arguments can justify the formation of connection elements: for dense meshes

the mass addition is neglectable (A1); in an additive manufacturing process there is a constant inflow of mass and the connection layer is only a small shift in the inflow process (A2); the connection elements are very useful for describing the extremely large temperature gradients between metal stream and base plate (A3). The thinner the connection zone can be made, the stronger arguments A1 and A2 become. However, argument A3 makes a complete suppression of the connection layer undesirable. For example, in [108], the nodes of two concrete printing layers are merged when they come close to each other. This approach is not applicable for different temperatures of the two nodes, as it is the case in the DED-LB simulation. A thermomechanical contact formulation would be applicable, but would add significant complexity for imposing non-penetration and stick conditions along with challenges for the numerical robustness of the formulation. Therefore, the connection zone is accepted as this work proceeds and methods to restrict the thickness of this zone are developed. To be specific, three approaches are presented for limiting the thickness of the connection zone.

- *Reduced-α-method*: the group index Igpe of each element from (5.46) is used in order to choose a smaller value α for the connection zone, allowing the algorithm to connect the bodies only when the distance is smaller.

- *Threshold-method*: a height-distance threshold h_{gap} for the gap height is applied instead of the α-shape method of the connection elements. Only connection elements which consist of nodes which all lie below h_{gap} are accepted in the triangulation. This method is similar to the creation of the contact elements in [106].

- *Progression-method*: a height-distance threshold h_{gap} is enforced only for the progression front of the connection zone. A standard α-test with an α value similar to the continua is applied for all connection elements which lie behind the progression front. In the case of a 2d simulation of metal deposition, the threshold criterion is checked first and the maximum distance of a connection point from the center line of the beam $d_{\text{max}}^{\text{prog}}$ is stored. Afterwards, all connection elements are checked again. If all their related distances are smaller than $d_{\text{max}}^{\text{prog}}$ and they pass the α-test, they are kept in the triangulation.

These approaches will be compared in the numerical examples Section 5.3.3. $\}_{[120]}^{\text{qtd.}}$

5.3 Numerical examples – melt flow and material deposition

$_{[120]}^{\text{qtd.}}\{$For the simulation of the metal deposition of the directed energy deposition process, a cylindrical beam of molten metal is considered which left the cylindrical nozzle at a previous point in time. The melting of the powder is therefore not considered in the model. Moreover, the simulation model assumes a continuous fluid stream of molten

metal, whereas in reality it is possible that droplets of melt or unmolten powder particles are mixed with shielding gas or air. In order to focus on establishing the material modelling as well as on the PFEM methods for the flow and connection of the material, a 2d framework is developed in the current work. In this section, firstly the shape of the 2d beam cross section is derived and the material and process parameters are summarised. The meshing methods for the connection zone as well as the influence of point insertion and removal are then analysed and illustrated. The final deposition simulation is presented and two parameter studies show the influence of the viscosity and the impact velocity. }$^{\text{qtd.}}_{[120]}$

5.3.1 Derivation of a 2d cross section model for DED-LB

$^{\text{qtd.}}_{[120]}${For the 2d simulation, a cross section of the 3d beam material in a 2d cutting plane is derived as illustrated in Figure 5.3a. It is assumed that this shape of material will be deposited in any y–z cross section of the process. As soon as the material reaches the weld bead, a plane strain assumption can be justified by the large thickness of the bead in feed direction. For simplicity, the plane strain assumption is used throughout the whole simulation. A constant beam velocity consisting of the horizontal feed velocity v_x and the vertical beam velocity v_z, and the beam diameter d_b define the kinematics and geometry of the deposition. Since $v_x \neq 0$, the beam geometry results in an inclined cylinder where the velocity ratio defines the inclination angle. The height h_e and width w_e of the ellipse

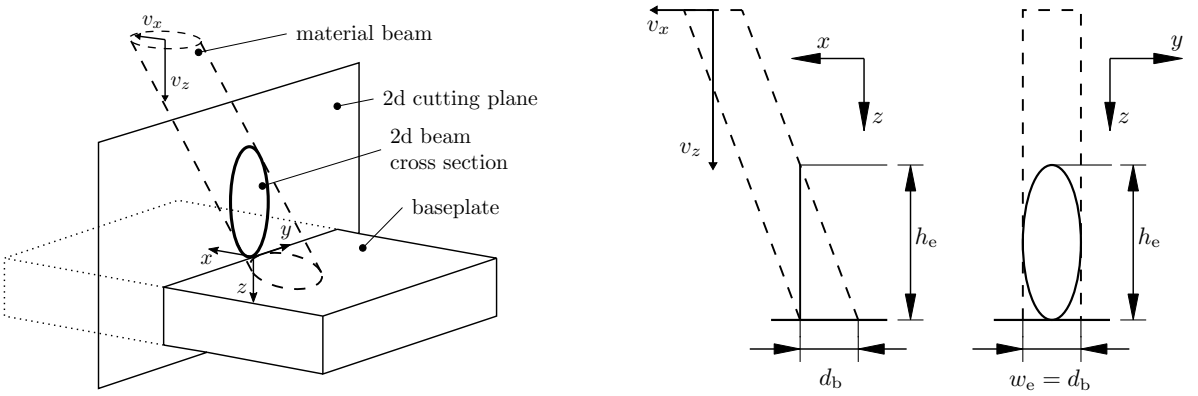

(a) Isometric view. **(b)** Side views in the x–z and y–z planes.

Figure 5.3: Illustration of the 2d beam cross section from an inclined cylinder describing the material beam and for constant beam velocities v_x and v_y. Side views in two planes show the geometrical measurements. Reprinted from [120], licensed under CC BY 4.0.

representing the cutting plane can be derived from the side views visualised in Figure 5.3b according to

$$h_\mathrm{e} = d_\mathrm{b}\,\frac{v_z}{v_x} \qquad\qquad w_\mathrm{e} = d_\mathrm{b} \tag{5.47}$$

where h_e follows from the velocity ratio and where w_e is identical to the beam diameter because the widest point of the ellipse is defined by the outer envelope of the beam. The beam diameter of the simulated fluid stream does not coincide with the real diameter of the nozzle in the process since only a continuous fluid stream of molten metal is considered rather than a mixture of droplets and shielding gas. which is e.g. 3 mm. Instead, the beam diameter is calculated from the mass-flow rate $\dot{m}_\mathrm{f}$ of the process. With the melt density $\rho_{0\mathrm{mel}}$ this translates to the feed volume-rate

$$\dot{V}_\mathrm{f} = \frac{\dot{m}_\mathrm{f}}{\rho_{0\mathrm{mel}}} \tag{5.48}$$

of melt coming from the nozzle. The volume of an oblique cylinder is the same as a standard cylinder, i.e.

$$V_\mathrm{b} = \frac{\pi\, d_\mathrm{b}^2}{4}\, h_\mathrm{b} \quad \Longrightarrow \quad \dot{V}_\mathrm{b} = \frac{\pi\, d_\mathrm{b}^2}{4}\, v_z \tag{5.49}$$

where the volume-rate of the beam is calculated by inserting the vertical beam velocity v_z as the rate of the beam height h_b. The unknown beam diameter d_b is therefore calculated from setting $\dot{V}_\mathrm{f} = \dot{V}_\mathrm{b}$ by using (5.48) and (5.49) as

$$d_\mathrm{b} = 2\sqrt{\frac{\dot{m}_\mathrm{f}}{\pi\, v_z\, \rho_{0\mathrm{mel}}}} \tag{5.50}$$

The volume rate and hence the beam diameter is not influenced by the inclination angle of the oblique cylinder and therefore also not by the feed velocity v_x. The feed velocity only changes the height of the cutting ellipse according to (5.47), as this becomes shorter with a more inclined stream. The simulation uses a beam velocity of $v_z = 3.58\,\mathrm{m/s}$ measured at the Institute of Forming Technology and Lightweight Components at TU Dortmund University by evaluating high-speed camera images of powder particles without activating the laser beam. For the feed velocity, $v_x = 24\,\mathrm{m/min}$ is assumed as well as $\dot{m}_\mathrm{f} = 290\,\mathrm{g/min}$ for the mass flow rate. These process parameters result in a beam diameter of $d_\mathrm{b} = 0.5\,\mathrm{mm}$ and an ellipse height of $h_\mathrm{e} = 4.5\,\mathrm{mm}$.

The boundary value problem is depicted in Figure 5.4, where only half of the $y-z$ cross section is considered with a symmetry boundary condition. Only a section of the original $10\,\mathrm{mm} \times 100\,\mathrm{mm}$ cross section is taken into account for the baseplate and the bottom of the cut-out is mechanically fixed and simulated as a heat sink. Heat conduction and deformation of the baseplate are still fully considered in the model. The phase transformation model also allows for a remelting of the baseplate, which, however, does not occur in this example.

Remark: The feed velocity in the real process is $v_x = 1\,\mathrm{m/min}$ and the mass flow rate is $\dot{m}_\mathrm{f} = 12\,\mathrm{g/min}$. However, these values yield an extremely long and thin elliptical cross section with $d_\mathrm{b} = 0.1\,\mathrm{mm}$ and $h_\mathrm{e} = 22\,\mathrm{mm}$, which complicates the mesh generation and

makes an extremely fine mesh necessary. In order to establish the simulation framework with a reasonably shaped ellipsoid and a manageable mesh density, these parameters are mitigated. The cross section area of the selected 0.5 mm × 4.5 mm ellipse is thereby similar to the 0.1 mm × 22 mm shape, such that the amount of deposited material per cross section is still comparable. }[120]qtd.

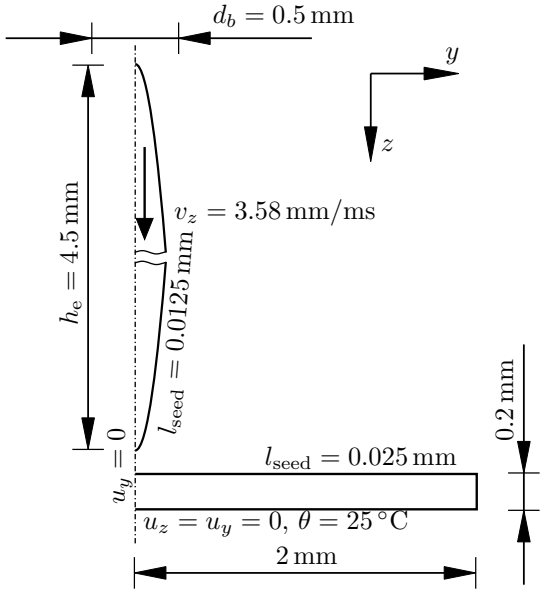

Figure 5.4: Sketch of the boundary value problem for the simulation of an elliptical 2d cross section of the deposition process derived from Figure 5.3 and with a symmetry boundary condition. The initial mesh consists of 406 points and 643 elements for the baseplate and 6338 points and 11950 elements for the stream, generated with a characteristic element seed size of $l_{\mathrm{seed}} = 0.0125\,\mathrm{mm}$ for the stream and $l_{\mathrm{seed}} = 0.025\,\mathrm{mm}$ for the baseplate. Reprinted from [120], licensed under CC BY 4.0.

5.3.2 Material and process parameters

{The material parameters for the two phases are mainly extracted from [88] for AISI 316 austenitic steel, see Table 5.1. Most temperature dependencies are neglected in the present work since the phase transformation model covers the main property changes, and further refinement of the material behaviour to the real process conditions is not in the focus of this work. A representative value for each phase is therefore extracted from the reference data. One exception is the Young's modulus of the solid phase, which is modelled with a thermal softening in order to reduce the stiffness increase that occurs upon solidification. This is especially important since plastic deformation contributions in the solid are, at the present stage, not included in the model. Young's modulus data from [23, 94] indicates that the Young's Modulus reduces linearly from around 195 GPa at room temperature to 130 GPa at 820 °C for AISI 316. Afterwards, [94] shows a drastic

decrease in the curve which is not further specified beyond that temperature range. Therefore, a linear function

$$E_{\mathrm{sol}}(\theta) = -\,81.66\,\frac{\mathrm{MPa}}{^{\circ}\mathrm{C}}\,[\theta - 24\,^{\circ}\mathrm{C}] + 195 \times 10^{3}\,\mathrm{MPa} \tag{5.51}$$

is assumed for the complete solid regime which yields a final value of $E_{\mathrm{sol}}(1350\,^{\circ}\mathrm{C}) = 86.7\,\mathrm{GPa}$ at the solidus temperature. Additional sensitivities which arise in (5.35) and (5.42) due to this temperature dependence are neglected in this work. The shear modulus $G_{\bullet} = E_{\bullet}/[2 + 2\,\nu_{\bullet}]$ and the compression modulus $K_{\bullet} = E_{\bullet}/[3 - 6\,\nu_{\bullet}]$ are derived from the Young's modulus and the Poisson ratio of the respective phases.

Besides the phase-wise properties, some parameters differ with respect to the initial state of the material and are therefore distinguished with respect to the stream and the baseplate part in Table 5.2. This is the case for thermal properties such as the initial temperature, the reference temperature for heat expansion, the surface quality dependent convection and radiation coefficients, as well as for the transformation stretch. }$^{\text{qtd.}}_{[120]}$

Table 5.1: Phase related material parameters of AISI 316 based on [88]. The estimated viscosity η_{v} has been increased by factor 100 based on test simulations, whereas the value for Young's modulus of the melt has been assumed. Reprinted from [120], licensed under CC BY 4.0.

	mm-g-ms	Melt	Solid
Mass density ρ_0	[g/mm^3]	6.8×10^{-3}	7.8×10^{-3}
Poisson ratio ν	[-]	0.26	0.26
Young's modulus E	[MPa]	2×10^{3}	$-\,81.66\,(\theta/^{\circ}\mathrm{C} - 24) + 195 \times 10^{3}$
Heat expansion α^{thm}	[-]	-	1.4×10^{-5}
Viscosity η_{v}	[MPa ms]	800×10^{-6}	-
Heat capacity c_0/ρ_0	[mJ/(g K)]	830	750
Latent heat L/ρ_0	[mJ/g]	-	260×10^{3}
Heat conduction k_0	[W/(mm K)]	30.5×10^{-3}	23.4×10^{-3}
Melt temperature θ^{mlt}	[°C]	-	1400
Melt range factor $\Delta\theta$	[K]	-	50

5.3.3 Analysis of PFEM remeshing methods

$^{\text{qtd.}}_{[120]}${The present work adapts PFEM remeshing methods to the specific DED-LB process, where the mesh generation for the connection zone and the adaptivity of the point cloud play an important role. Therefore, these aspects are analysed in the following. For the mesh generation of the *connection zone*, i.e. those elements which contain nodes from both the baseplate and the stream, three methods have been described in Section 5.2. Figure 5.5 shows a comparison of simulation results based on these methods for the identical simulation time $t = 0.4375\,\mathrm{ms}$. It becomes evident that the α-shape method with a reduced α parameter alone does not provide a thin and closed mesh in the

Table 5.2: Part related parameters based on the initial material state and real process conditions. Heat transfer coefficient is based on [137] and increased in the stream to account for forced convection under shielding gas flow, emissivity from therein is applied for the baseplate, whereas a higher emissivity based on [15] is assumed for the rough stream surface. Reprinted from [120], licensed under CC BY 4.0.

	mm-g-ms	Stream	Baseplate
Initial temperature θ^{ini}	[°C]	1738	25
Expansion ref. temp. $\theta^{\text{ref}}_{\text{sol}}$	[°C]	$\theta^{\text{mlt}} - \Delta\theta$	θ^{ini}
Heat convection h_c	[W/(mm^{2}K]	800×10^{-6}	80×10^{-6}
Emissivity ε	[-]	0.81	0.4
Stefan-Boltzmann constant σ	[W/mm^{2}K^4]	5.6704×10^{-14}	5.6704×10^{-14}
Ambient temperature θ^{∞}	[°C]	25	25
Transformation stretch $J^{\text{tra}}_{\text{mel}}$	[-]	1	$\rho_{0\text{sld}}/\rho_{0\text{lqd}} = 1.058$
Transformation stretch $J^{\text{tra}}_{\text{sol}}$	[-]	$\rho_{0\text{lqd}}/\rho_{0\text{sld}} = 0.945$	1

connection zone. Either the zone becomes thinner for a very small α-parameter, which is accompanied by holes appearing between the elements, see Figure 5.5a, or with a larger α-parameter the connection zone becomes very thick and holes remain a problem along with a deterioration of the aspect ratio, see Figure 5.5b. The use of a fixed gap threshold significantly reduces the thickness, but in several positions the initially closed elements provide sufficient support to the adjacent liquid melt stream so that the melt does not fill the remaining holes, see Figure 5.5c. Finally, the progression-method results in a thin and fully closed connection zone, where the method uses the standard α-parameter of $\alpha = 1.4$ for both the continua and the connection zone – but restricted to elements which lie behind the progression front of the connection. The final result is visualised in Figure 5.5d.

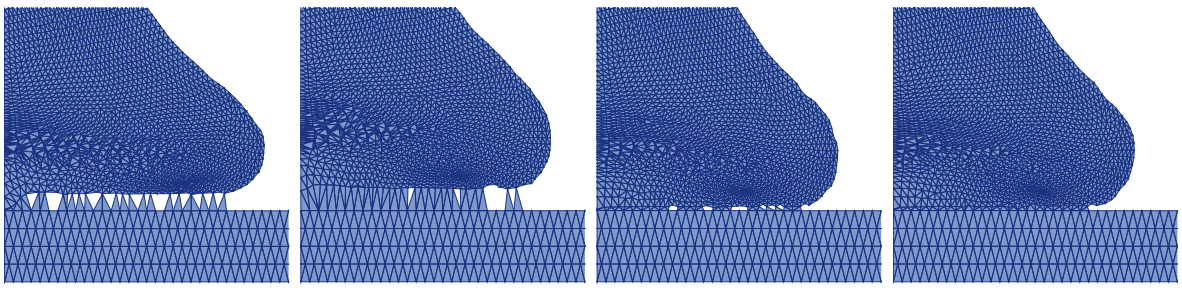

(a) Reduced-α-method $\alpha_3 = 0.8$ **(b)** Reduced-α-method $\alpha_3 = 1.0$ **(c)** Threshold-method **(d)** Progression-method

Figure 5.5: Comparison of meshing methods for the connection zone: a) and b) use reduced α-parameters for connection elements (Igpe = 3), resulting in either many holes or very thick elements. c) applies a gap threshold of $h_{\text{gap}} = l_{\text{seed}}$, reducing thickness but leaving holes due to support of neighbouring elements. d) uses a gap threshold at the front and a standard α-shape behind, creating a closed, thin connection zone. Reprinted from [120], licensed under CC BY 4.0.

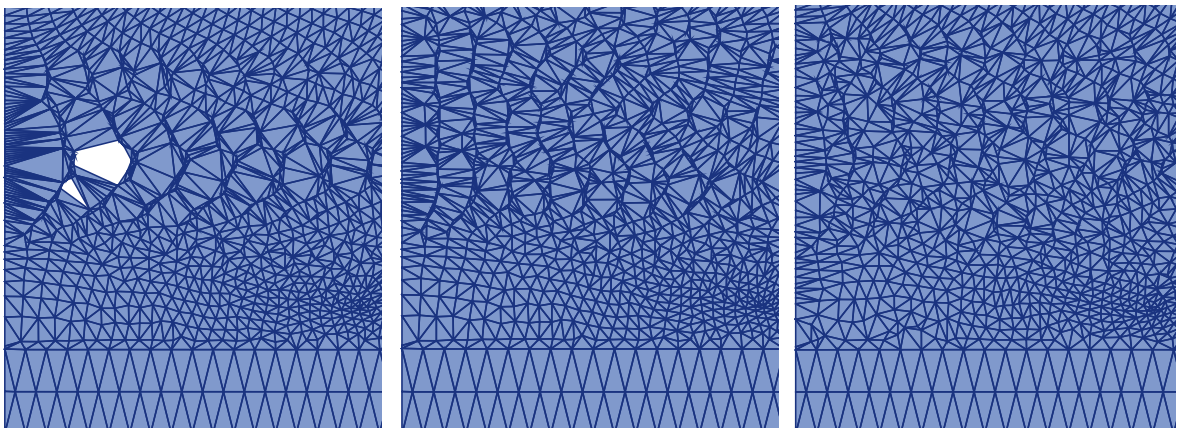

(a) No point adaption leads to holes and point accumulation.

(b) Point insertion prevents holes.

(c) Additional point removal prevents point accumulation.

Figure 5.6: Comparison of a section of the mesh at $t = 0.875\,\text{ms}$ for no mesh adaptivity (a), for utilising point insertion in large elements (b) and for additional collapsing short edges to a single mid-point (c), leading to sufficient mesh quality. Reprinted from [120], licensed under CC BY 4.0.

The mesh adaptivity methods of *point insertion and removal* are tested for the first phase of deposition and Figure 5.6 shows a comparison. Figure 5.6a shows extreme accumulation of points in vertical direction due to the compression of the material, while large flow in horizontal direction leads to very large and distorted elements. The α-shape method deletes some very large and distorted elements, such that holes appear in the discretisation. The simple geometrical point insertion scheme discussed in Section 2.4.3 leads to a significantly improved point distribution and mesh quality, as visualised in Figure 5.6b. In order to additionally overcome the local accumulation of points, for example at the left symmetry boundary edge, Figure 5.6c shows the effect of collapsing edges which are shorter than a prescribed global tolerance to a common mid-point. With the help of these methods, the mesh quality is sufficiently preserved throughout the simulation. }$^{\text{qtd.}}_{[120]}$

5.3.4 Simulation of the elliptical beam cross section

$^{\text{qtd.}}_{[120]}${The DED-LB process is simulated in a simplified 2d cross section model as shown in Figure 5.4 with the parameters specified in Tables 5.1 and 5.2. The initial point cloud is generated with an unstructured triangular mesh generator with a global seed size of $l_{\text{seed}} = 0.0125\,\text{mm}$, whereas the baseplate features $l_{\text{seed}} = 0.025\,\text{mm}$ on the deposition surface and $l_{\text{seed}} = 0.05\,\text{mm}$ in vertical direction with a structured mesh. The unstructured mesh of the melt stream is beneficial because it has more regular angles and less tendency to edge flips during the deformation. With respect to the meshing methods discussed in the previous section, the advantageous methods are used here, i.e. the progression method

for connection meshing and both point insertion and removal with the parameters given in Algorithm 1.

The deposition simulation is visualised in Figure 5.7 which shows the melt phase fraction ζ_{mel} for representative time steps during the deposition phase, the solidification phase and the cooling phase. Due to the high stream velocity of $v_z = 3.58\,\mathrm{ms}$, the *deposition stage* takes place until approximately $t = 3.0\,\mathrm{ms}$, see Figures 5.7a to 5.7d, when the motion of the stream ends. The movement is thereby slowed down by the bonding to the baseplate, the viscous material behaviour and the fast solidification of the bottom element layers of the stream. The fast solidification is caused by the cold baseplate and the heat sink at the bottom of the baseplate, which leads to the formation of a large wetting angle. Due to gravity, the fluid part of the stream can still flow, but the timescale of the solidification is faster than the flow under gravity. The *solidification stage* consists of cooling the complete weld bead below the solidus temperature $\theta^{\mathrm{sld}} = 1350\,^{\circ}\mathrm{C}$, which takes a longer time period until $t = 237\,\mathrm{ms}$ and is visualised in Figures 5.7e to 5.7h. The final *cooling stage* is finished at $t \approx 2000\,\mathrm{ms}$ when the weld bead reaches room temperature throughout, whereas the shape is indistinguishable from Figures 5.7h to 5.7i. The shrinkage of the weld bead throughout all stages is further illustrated in Figure 5.8 with outlines of the geometry for different time steps. The inclined solidification front in Figure 5.7f and 5.7e is mirrored in the roughening of the surface due to the transformation stretches and the influence of mapping of variables in the still fluid melt part during remeshing. Nonetheless, a pure FEM without remeshing is not able to resolve this phase of the simulation and leads to a highly distorted mesh. Figure 5.8 highlights that the final cooling stage does not significantly add to the shrinkage of the weld bead, since the thermal expansion is much smaller than the transformation stretch. The final geometry shows a significant tip-shape of the top of the weld bead. The temperature evolution during the stages of the deposition simulation are visualised in Figure 5.9, closely mirroring the phase fraction plots in Figure 5.7 due to the temperature dependence of ζ_{mel} via (5.10). Figures 5.9a to 5.9g show that the heat mainly flows into the baseplate and that no temperature gradient on the surface due to convection and radiation is visible, because these effects do not significantly contribute due to the short time period. Furthermore, Figures 5.7h and 5.7i show that the final cooling stage is the longest stage until the complete weld bead reaches room temperature. The presented results strongly depend on the viscosity parameter η_{v} of the melt phase and the impact velocity v_z of the melt on the baseplate. Both influences are analysed in B. Furthermore, a mesh convergence study is presented in C and the stress distribution is analysed in C.

Remark: The results presented in this section all are generated with the symmetry boundary condition depicted in Figure 5.4. In order to test the validity of this symmetry condition, the results have been reproduced without applying the symmetry boundary condition. Apart from slight differences due to the mesh asymmetry of the full model, the resulting geometry remains consistent. This confirms that the symmetry boundary condition is justified here.

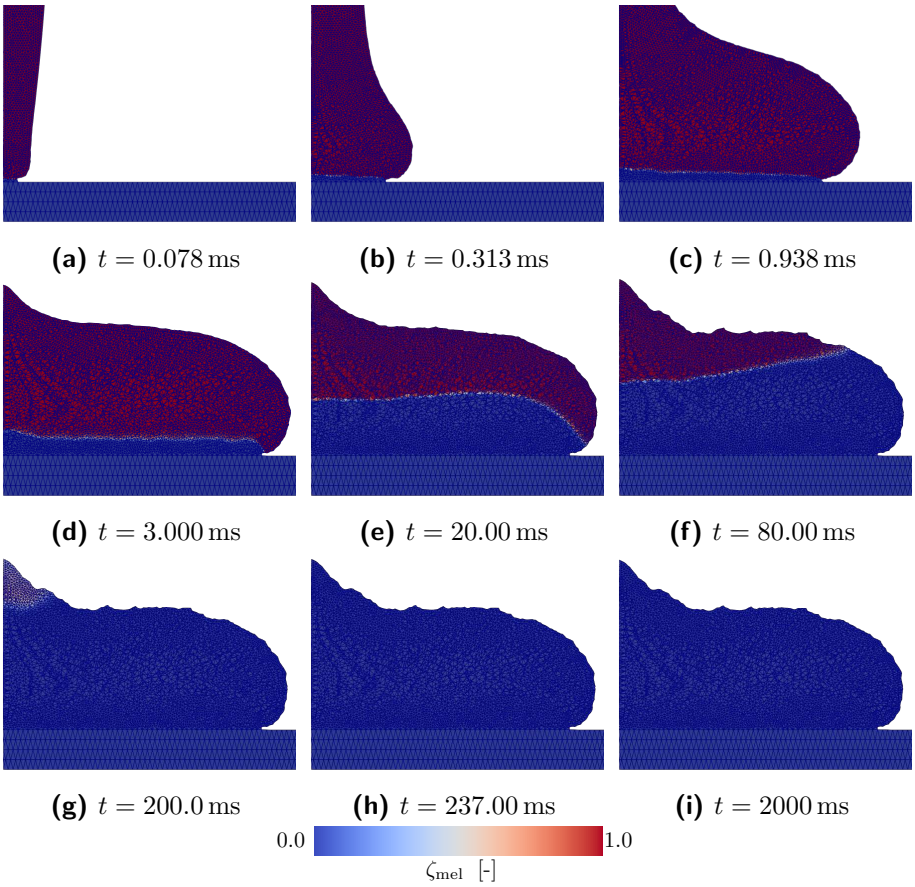

Figure 5.7: Deposition of the elliptical stream cross section. The cold base plate leads to immediate solidification of the bottom part of the stream and at $t = 3.000\,\mathrm{ms}$ the deposition stage ends (d) with no further significant motion. At $t = 237.00\,\mathrm{ms}$, the solidification is finished and ζ_{mel} falls below 0.01 % (h) while the maximum temperature is still $\theta = 1200\,^{\circ}\mathrm{C}$. The weld bead is fully cooled down to room temperature at $t = 2000\,\mathrm{ms}$ (i). Reprinted from [120], licensed under CC BY 4.0.

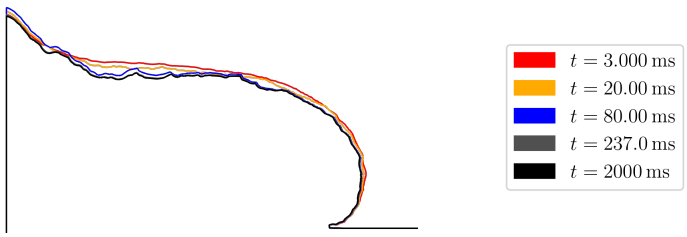

Figure 5.8: Outlines of the weld bead during solidification. Contraction induced by transformation stretches between $t = 3\,\mathrm{ms}$ and $t = 237\,\mathrm{ms}$ leads to rough surface and significant shrinkage, whereas pure cooling from maximum temperature $\theta(t = 237\,\mathrm{ms}) = 1200\,^{\circ}\mathrm{C}$ until thermal equilibrium at $t = 2000\,\mathrm{ms}$ only induces an almost indistinguishable thermal contraction. Reprinted from [120], licensed under CC BY 4.0.

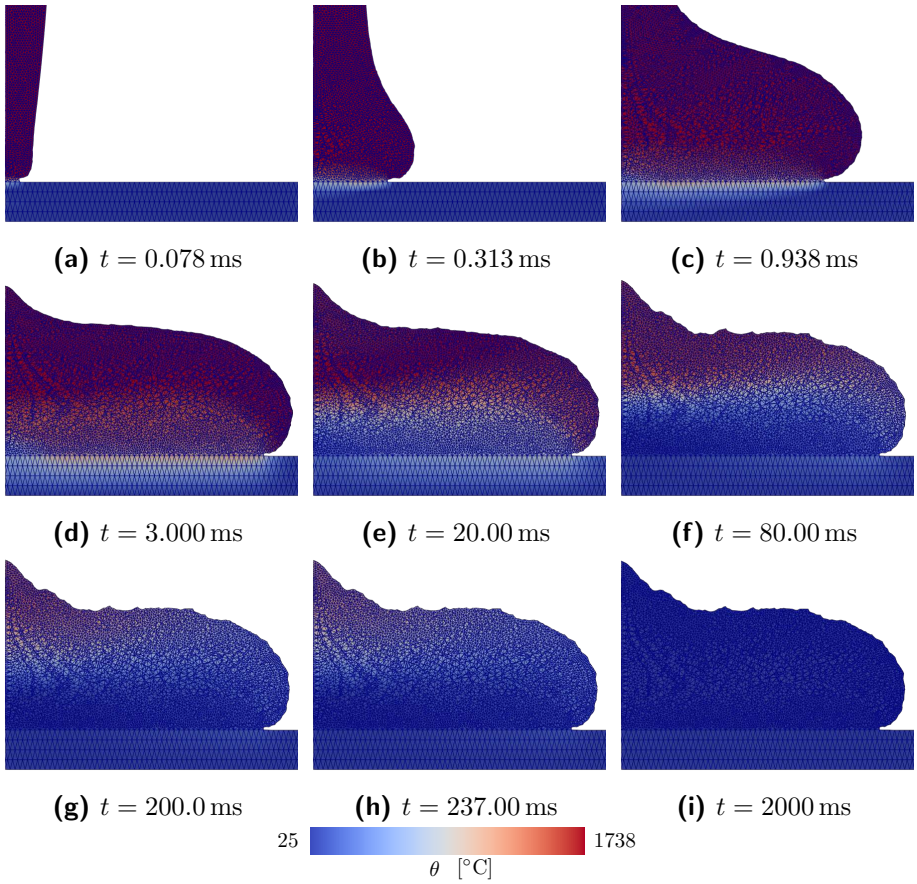

Figure 5.9: Temperature evolution of the deposition process. The cooling directly mirrors the phase transformation distribution because of the temperature based evolution equation (5.10). The surface heat flux does not show any visible influence on the cooling within the short deposition time period. Reprinted from [120], licensed under CC BY 4.0.

Remark: The computational problem in this section consists of initially 6744 nodes, which results in approximately 20000 global degrees of freedom that are solved within a MATLAB implementation. To give exemplary numbers, a total of 3700 output steps until the total simulation time of $t = 2000\,\mathrm{ms}$ were calculated in 4830 actual calculation steps due to the time step adaptation scheme discussed in Section 2.2. Thereby, the element routine and the implementation of constitutive equations are precompiled into C code with MEX-functions and, moreover, the element loop is parallelised with a PARFOR loop. The resulting simulation time was 25 hours on four processors of an Intel® Xeon® Gold 6134 CPU. The relation of remeshing time to finite element solution time is approximately 7% to 93%, highlighting that the computational effort is primarily dominated by the element loop and the solution of the system of equations. Approximately 60% of the remeshing time is spent in the transfer of state variables, which involves background triangulation and tensor decomposition, and 40% are spent in point adaptivity, triangulation, α-shape

detection and boundary detection. In summary, PFEM remeshing constitutes only a minor fraction of the overall computational cost. }[120]qtd.

5.4 Modelling and simulation of material deposition – Conclusion

[120]qtd.{This work establishes an extensible 2d framework for the simulation of the DED-LB process, combining the remeshing techniques of PFEM with a large strain phase transformation material model for melt flow and solidification. The phase transformation model is based on a temperature dependent smoothed step function defining the phase transition and therewith the averaged energy density. The Voigt-type homogenisation allows the calculation of phase-wise Piola stresses for a Maxwell-type viscoelasticity in the fluid and hyperelasticity in the solid, where the irreversible viscous strains are inherited from the melt phase. The approach includes thermal and transformation-induced volumetric deformation as well as a consistent transformation heat source including the latent heat and changes in the mechanical and caloric energy. The large material flows are resolved with an Updated-Lagrangian description within the PFEM, where the quality of the point cloud is improved by point insertion and removal and where the connectivities are rebuilt along with the α-shape detection of the surface. Particular emphasis is placed on the mesh generation of the connection zone which consists of elements formed between the nodes of the substrate and the stream. These elements violate mass conservation but prove to be useful for describing the large temperature gradients between the materials. Therefore, special remeshing techniques for keeping the connection zone as thin as possible are presented in this work.
Several conclusions can be drawn from the investigations:

- PFEM remeshing by rebuilding the connectivity of an unchanged point cloud is not sufficient because the quality of the point cloud decreases. Well established point insertion and removal techniques from [111] are combined with recent ideas on how to collapse small edges from [78] in order to provide sufficient mesh quality for the numerical examples in this chapter. However, further improvements are advisable, including e.g. a Laplacian smoothing of the point positions, see [26].

- The surface roughness of the weld bead in the numerical examples is considered to be a numerical artefact stemming from the state-variable mapping and from the absence of a plasticity model in the solid phase which leads to an overestimation of stresses. For a real process simulation, a plasticity model can straightforwardly be added to the solid phase. Furthermore, the influence of the state variable mapping should be investigated, e.g. by varying the remeshing frequency during the solidification stage, where the deformations are significantly smaller than in the deposition stage. Additionally, a surface tension contribution could further improve the surface by favouring a smooth surface shape.

- The pointed top of the weld bead in the numerical examples is not visible in experimental examples of DED-LB, for example in [38]. This indicates that the 2d cross section simulation is not sufficient for a precise process simulation because it neglects drag effects in the feed direction which could remove the tip-shape. Since 2d is nonetheless only an intermediate step in developing a comprehensive modelling framework, the 3d extension is an essential next step. The computational effort necessary for a 3d simulation makes a more efficient implementation necessary, e.g. with C++.

- Similarly, the large wetting angle is not visible in experiments, cf. [38], indicating that the solidification of the base layers of the weld bead is too fast. Therefore, a more realistic heat model is necessary, taking into account a larger part of the base plate as well as a laser heat source that also effects the substrate instead of only providing a fluid melt stream. Laser heat source models from, e.g., [56] should therefore be included in the model for a more realistic wetting angle. In addition, surface contributions that penalise curvature of the boundary polygon could introduce wetting forces into the model, leading to further improvement.

- The current model overestimates the stresses such that an extension of the solid material model by plasticity contributions is important in order to realistically simulate residual stresses after the deposition. A calibration of material parameters, including the compression modulus of the melt, will further improve the quality of the model based prediction. Moreover, in the quasi-incompressible limit case, special element technology will be necessary for the melt material, see Section 4.1.

- The material model presents a valuable large strain extension of established simulation approaches for melt and solidification in small strain settings, e.g. [24, 54, 95]. It also applies a thermodynamically consistent viscous evolution in the melt phase and inheritance of viscous deformations to the solid phase, which extends the simplified approaches to stress relaxation by deletion of stresses, e.g. [138]. In addition, the temperature dependent phase transition function keeps the numerical cost low compared to energy convexification approaches in [10, 95] and the transition is applied to the complete thermomechanical constitutive model rather than only to parts of the model or only to the material parameters as in, e.g., [17, 71, 73, 113]. Further validation of the model needs to be addressed in future research by, e.g., comparing the predicted weld bead geometry and the stress-induced baseplate distortion with experimental data, as well as validating the thermal problem based on temperature measurements.

In summary, this contribution presents a broad basis for the simulation of deposition and solidification of DED-LB processes and shows necessary steps towards a full featured process simulation that allows the investigation of process induced part properties such as residual stresses and distortion. }$^{\text{qtd.}}_{[120]}$

B Appendix – Parameter studies for the deposition simulation

$\overset{\text{qtd.}}{[120]}\{$The shape of the weld bead is significantly influenced by the viscosity parameter η_v of the melt phase and the impact velocity v_z. Both influences are analysed in this section.

Influence of the viscosity parameter

Figure 5.10 shows a comparison of weld bead shapes for different viscosities based around the value $\eta_\text{v}^\text{ref} = 800 \times 10^{-6}\,\text{MPa}\,\text{ms}$ that has been applied in the main example. Different viscosities yield a significantly different spreading of the molten stream because the flow of the unsolidified upper part of the weld bead is influenced by the viscosity. The phase evolution is compared for three different viscosities in Figure 5.11. The base layers of the weld bead solidify very fast due to the cold baseplate for all viscosity parameters, because the thermal and microstructural properties are unchanged. At higher viscosities, the reduced flowability of the material results in a faster stopping of the deposition. This can be seen in Figures 5.11h and 5.11i where no further motion is visible in contrast to Figures 5.11e and 5.11f.

Influence of the impact velocity

The vertical beam velocity v_z also has an important influence on the final shape of the weld bead. The effect is analysed in this section with a constant elliptical cross section area, although a higher vertical velocity theoretically also leads to a more elongated ellipsoid shape following the derivation in Section 5.3.1. However, the focus of this example is to show the influence of different impact velocities which can be best compared for similar geometries. The resulting outlines of the weld bead geometry after the deposition stage are visualised in Figure 5.12. The effect is similar to the variation of the viscosities in the previous section, however, the formation of the connection zone is more important in this example. A high impact velocity leads to a faster spreading of the material and the motion is slowed down much faster due to the bonding and solidification in the connection region. As the viscosity of the material is identical in all variations, the flowability of the upper part of the weld bead does not make a difference here. The different deposition and solidification behaviour is visualised in Figure 5.13, where the comparison of Figures 5.13h and 5.13i shows how fast the deposition stops for high impact velocities compared to Figures 5.13e and 5.13f or Figures 5.13b and 5.13c, where the spreading continues. Effects such as a spring back of the melt or the detachment of drops from the streams are not present for simulations up to $v_z = 10\,v_z^\text{ref}$, only the spreading speed and range increase. $\}^{\text{qtd.}}_{[120]}$

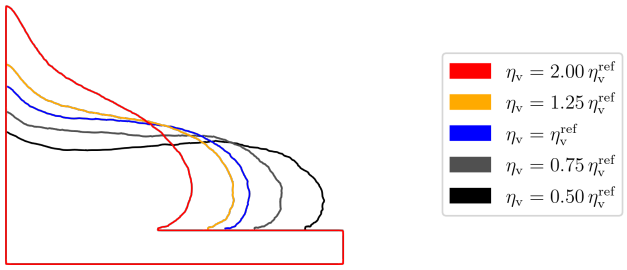

Figure 5.10: Outlines of the weld bead for different viscosity parameters at $t = 3.0\,\text{ms}$, where each deposition has come to a rest. The reference viscosity parameter is $\eta_v^{ref} = 800 \times 10^{-6}\,\text{MPa ms}$ and the initial velocity is $v_z = 3.58\,\text{m/s}$ as in the previous examples. Reprinted from [120], licensed under CC BY 4.0.

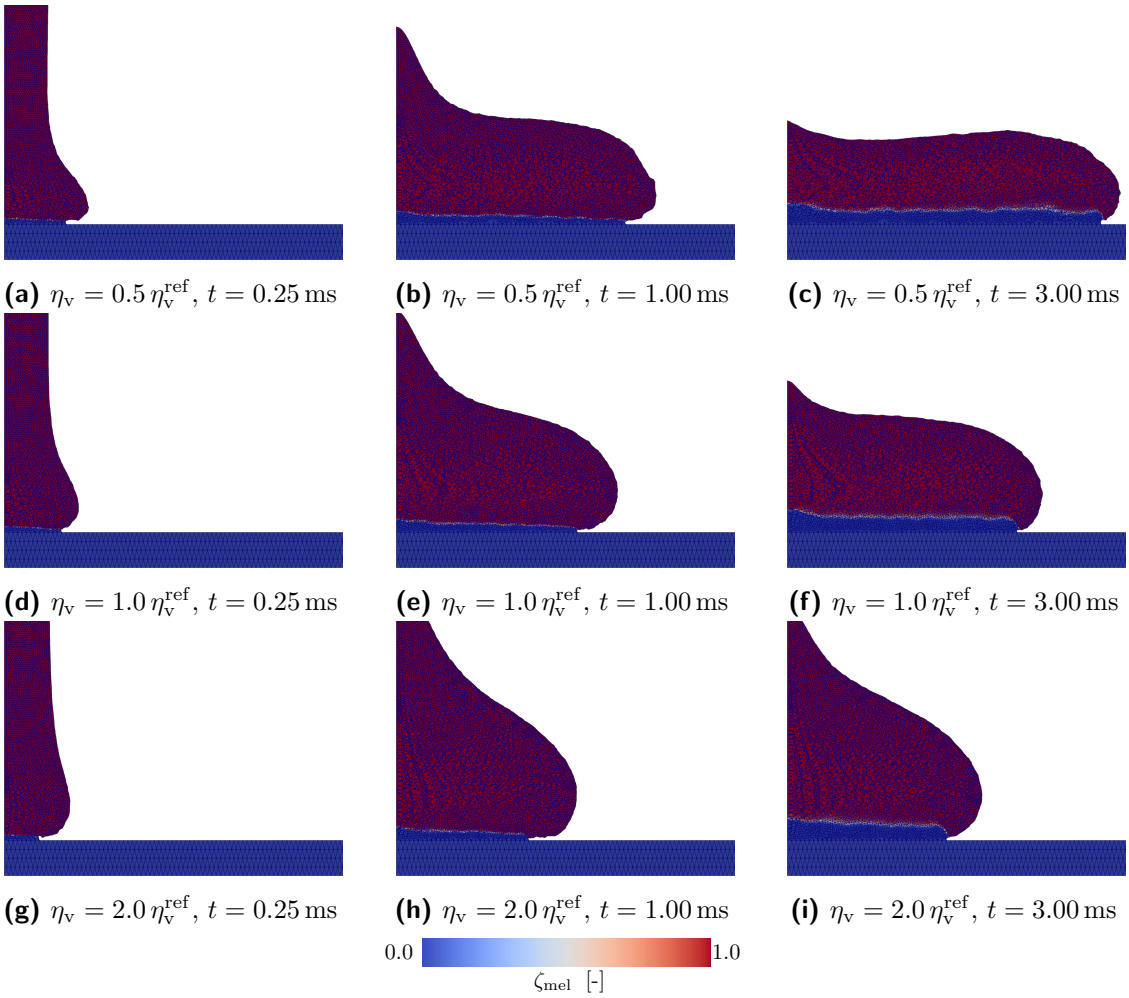

Figure 5.11: Deposition for different viscosities in relation to $\eta_v^{ref} = 800 \times 10^{-6}\,\text{MPa ms}$. The solidification of the connection zone and the bottom layers of the weld bead is similar for different viscosity parameters. The viscosity significantly influences the spreading of the material through the flowability of the upper part of the weld bead. Reprinted from [120], licensed under CC BY 4.0.

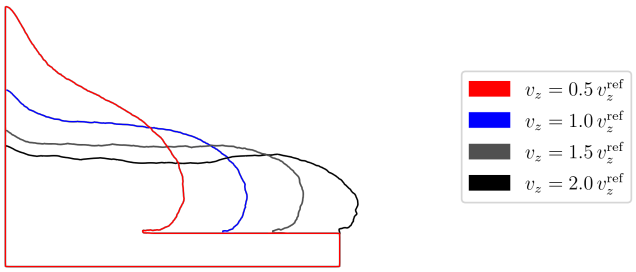

Figure 5.12: Outlines of the weld bead for different initial beam velocities at $t = 3.0\,\mathrm{ms}$, where each deposition has come to a rest. The reference initial velocity is $v_z^{\mathrm{ref}} = 3.58\,\mathrm{m/s}$ and the viscosity is $\eta_{\mathrm{v}} = 800 \times 10^{-6}\,\mathrm{MPa\,ms}$ as in the previous examples. Reprinted from [120], licensed under CC BY 4.0.

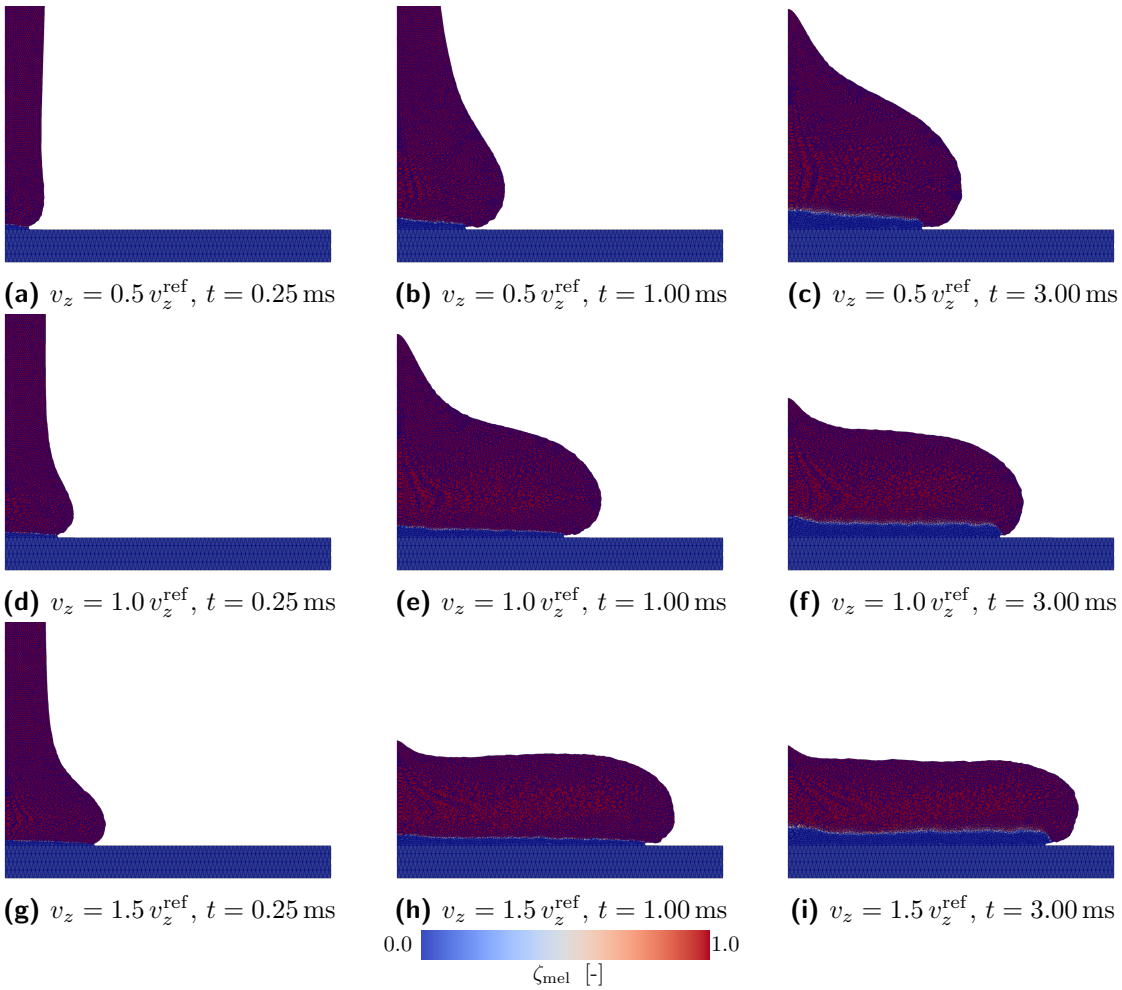

Figure 5.13: Deposition for different initial beam velocities in relation to $v_z^{\mathrm{ref}} = 3.58\,\mathrm{m/s}$. The higher velocity leads to a faster deposition and the deceleration of the bonded material brings the weld bead to a rest in less time. Reprinted from [120], licensed under CC BY 4.0.

C Appendix – Mesh convergence study and stress analysis

qtd. [120]{Based on the detailed deposition example discussed in Section 5.3.4, this appendix evaluates the influence of the discretisation and examines the resulting stresses in the solidifying weld bead.

Mesh convergence study

In order to analyse the influence of the mesh density, Figure 5.14 shows results for three different meshes, whereby the comparison of results is focussed on surface contour and melt volume fraction distribution. The coarsest discretisation ($l_{\text{seed}} = 18.75\,\mu\text{m}$) shows slightly reduced flow whereas the two finer discretisations yield very similar results, with only a small improvement of the surface smoothness for the finest ($l_{\text{seed}} = 10.00\,\mu\text{m}$) discretisation. Therefore, the chosen discretisation with $l_{\text{seed}} = 12.50\,\mu\text{m}$ represents a reasonable compromise of accuracy and computational efficiency.

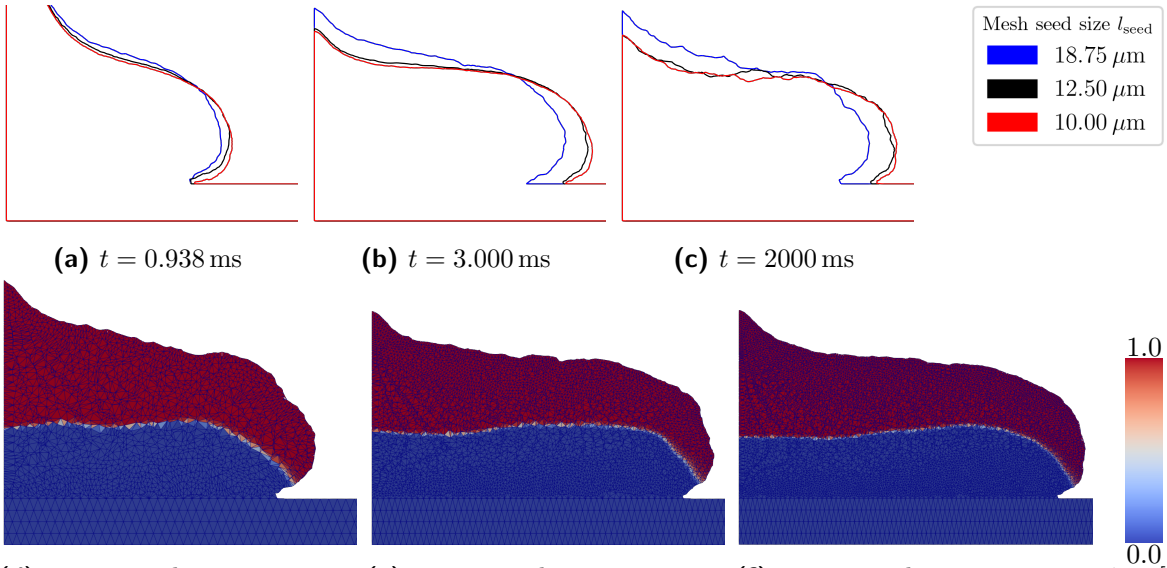

(a) $t = 0.938\,\text{ms}$ **(b)** $t = 3.000\,\text{ms}$ **(c)** $t = 2000\,\text{ms}$

(d) $t = 20\,\text{ms}$, $l_{\text{seed}} = 18.75\,\mu\text{m}$ **(e)** $t = 20\,\text{ms}$, $l_{\text{seed}} = 12.50\,\mu\text{m}$ **(f)** $t = 20\,\text{ms}$, $l_{\text{seed}} = 10.00\,\mu\text{m}$

Figure 5.14: Mesh convergence study: initial melt flow in (a) is similar, but as flow stops in (b) and the material cools down in (c), the coarse mesh predicts less flow, while the medium and fine meshes closely agree. Contour plots (d)-(f) analyse a time step during the solidification phase. Finer meshes lead to a smoother surface and phase boundary where again the medium (e) and fine (f) discretisations show good agreement. Reprinted from [120], licensed under CC BY 4.0.

Qualitative stress analysis

A representative stress evolution in the solidifying material is depicted in Figure 5.15. The von Mises equivalent stress predicted by the model significantly exceeds realistic yield limit values – in view of more reliable simulation results, particularly the material model for the solid needs to be further extended. However, qualitative deductions can be made based on the model proposed within this work. To be specific, the stress distribution is smooth as expected for the compressible material behaviour assumed – the only exception being the connection zone and nearby substrate elements, where high gradients, e.g. of temperature, as well as different sizes of neighbouring elements occur. The stresses are mainly stemming from incompatible transformations and thermal deformations which especially occur in the bonding region and show maximum values in the connection elements and near the edge of the connection zone. }[qtd. [120]]

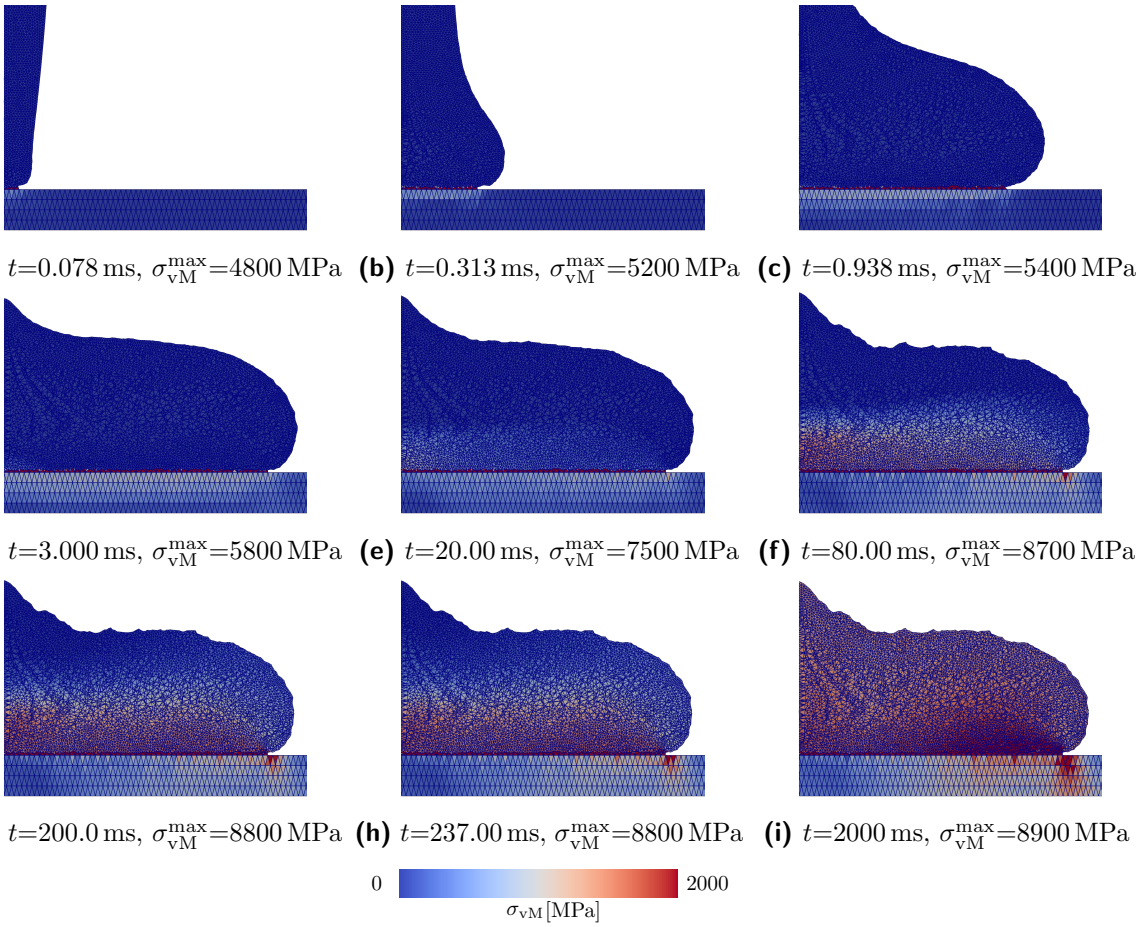

Figure 5.15: Evolution of the von Mises equivalent stress during the deposition process. The stress vastly exceeds realistic yield limit values of the solidified material due to the thermo-elastic material law so that the results only give qualitative insight in the smoothness and distribution of the stress field. Reprinted from [120], licensed under CC BY 4.0.

6 Summary and Conclusions

This thesis develops numerical modelling approaches for simulating shape changes induced by surface interactions, addressing three critical applications: wear mechanisms, material separation processes, and material deposition technologies. By advancing methods such as dissipation-based wear models in friction homogenisation, Particle Finite Element Method (PFEM) adaptations and material modelling for melt flow and solidification, this work advances simulation capabilities across multiple domains while identifying open challenges for future research.

For *wear modelling*, a Coulomb friction model with a shear-stress limit is applied alongside an Archard law based on dissipated frictional work. This approach demonstrates superior accuracy compared to pressure-based formulations when friction coefficients vary, which is important for the modelling of high-pressure metal forming applications. Simulations conducted on microstructured tool surfaces highlight their potential for tailoring directional friction properties while wear resistance during operation can be investigated. Quasi-isotropic scarab beetle-inspired structures exhibited predictable wear patterns under different sliding directions compared to a wear experiment. However, certain limitations remain: steady-state behaviour was only captured over short intervals due to strain hardening effects of the sheet material and due to contact closing and opening times. Future investigations should explore longer cut-outs and more refined experimental set-ups, e.g. finished probes, to validate dissipation-based Archard coefficients quantitatively.

In terms of *material separation*, PFEM was adapted for simulating adhesion-free asperity shearing at microscopic scales allowing to study wear mechanisms at asperity levels. The study revealed that utilising quadratic displacement-elements provides smoother stress distributions under elastoplastic conditions compared to mixed formulation elements traditionally used in PFEM simulations, while the mixed elements show superior numerical robustness for hyperelastic test cases. Additionally, an improved local state-variable transfer scheme significantly enhanced numerical robustness during remeshing operations compared to the conventional closest-point mapping for coarse discretisations. Adaptive meshing strategies based on equivalent plastic strain allowed better resolution of deformed regions while enabling crack modelling through enriched α-shape detection criteria targeting highly plastically deformed zones. Despite these

advancements, challenges remain regarding pressure oscillations under plastic incompressibility for the mixed element as well as achieving robust contact force distribution for the quadratic element formulation.

For *material deposition*, thermo-mechanical PFEM was adapted to simulate Directed Energy Deposition with Laser Beam (DED-LB), a process involving high-speed melt streams deposited onto cold substrates followed by solidification-induced residual stresses during cooling. A mesh generation criterion specific to the material bonding zone ensured accurate representation of material progression fronts without holes or overly large elements. Furthermore, a large-strain constitutive model based on deformation measures with temperature-dependent phase transitions established a profound framework for realistic predictions of residual stresses caused by incompatible deformations between molten and solidified phases. However, additional refinements are needed: extending simulations from 2d cross-sections into full 3d geometries will improve accuracy by capturing drag effects along feed direction as well as the full interactions. Similarly, incorporating calibrated laser heat sources capable of affecting both substrate material and melt stream could yield more realistic wetting angles observed experimentally. With these further steps, key insights relevant for optimising additive manufacturing processes such as DED-LB technology can be made possible in future work.

Collectively, these contributions represent significant advancements over existing state-of-the-art methods in tribology and additive manufacturing research:

- Dissipation-based wear models applied in representative surface cut-outs provide new tools for designing microstructured surfaces tailored toward specific operational requirements.
- PFEM adaptations provide a robust framework for investigating microscale failure mechanisms that underlie macroscale wear phenomena.
- Thermomechanical PFEM modelling progresses towards a modelling approach for process optimisation which links deposition parameters directly with part properties such as residual stresses or distortion.

Despite these achievements, several challenges remain open for future exploration: validating proposed models against larger experimental datasets – extending PFEM frameworks beyond 2d geometries – investigating thermal boundary conditions and loads during the deposition simulation – or integrating multi-material interactions within additive manufacturing models involving dissimilar substrate and deposition material.

In summary, this thesis bridges gaps between fundamental research on surface interactions and practical engineering applications across multiple disciplines, including tribology, contact mechanics, and additive manufacturing technologies. It lays a strong foundation for further innovations aimed at improving performance and reliability across diverse industrial processes.

Bibliography

[1] R. Ambati, X. Pan, H. Yuan, and X. Zhang. Application of material point methods for cutting process simulations. *Computational Materials Science*, 57:102–110, 2012. doi:10.1016/j.commatsci.2011.06.018.

[2] J. F. Archard. Contact and Rubbing of Flat Surfaces. *Journal of Applied Physics*, 24(8):981–988, 1953. doi:10.1063/1.1721448.

[3] M. Arroyo and M. Ortiz. Local *maximum-entropy* approximation schemes: a seamless bridge between finite elements and meshfree methods. *International Journal for Numerical Methods in Engineering*, 65(13):2167–2202, 2006. doi:10.1002/nme.1534.

[4] A. Ask, A. Menzel, and M. Ristinmaa. Electrostriction in electro-viscoelastic polymers. *Mechanics of Materials*, 50:9–21, 2012. doi:10.1016/j.mechmat.2012.01.009.

[5] A. Ask, A. Menzel, and M. Ristinmaa. Phenomenological modeling of viscous electrostrictive polymers. *International Journal of Non-Linear Mechanics*, 47: 156–165, 2012. doi:10.1016/j.ijnonlinmec.2011.03.020.

[6] M. Bagheri, M. Mohammadi, and M. Riazi. A review of smoothed particle hydrodynamics. *Computational Particle Mechanics*, 11(3):1163–1219, 2024. doi:10.1007/s40571-023-00679-7.

[7] H. Bakhshan, E. Oñate, and J. M. Carbonell. Modeling of ultrasonic vibration-assisted micromachining using the particle finite element method. *Computational Particle Mechanics*, 2024. doi:10.1007/s40571-024-00791-2. Publisher: Springer Science and Business Media LLC.

[8] O. Barro, F. Arias-Gonzalez, F. Lusquinos, R. Comesana, J. Del Val, A. Riveiro, A. Badaoui, F. Gomez-Bano, and J. Pou. Improved Commercially Pure Titanium Obtained by Laser Directed Energy Deposition for Dental Prosthetic Applications. *Metals*, 11(1):70, 2020. doi:10.3390/met11010070.

[9] T. Bartel and K. Hackl. A micromechanical model for martensitic phase-transformations in shape-memory alloys based on energy-relaxation. *ZAMM - Journal of Applied Mathematics and Mechanics / Zeitschrift für Angewandte Mathematik und Mechanik*, 89(10):792–809, 2009. doi:10.1002/zamm.200900244.

[10] T. Bartel, I. Guschke, and A. Menzel. Towards the simulation of Selective Laser Melting processes via phase transformation models. *Computers & Mathematics with Applications*, 78(7):2267–2281, 2019. doi:10.1016/j.camwa.2018.08.032.

[11] B.-A. Behrens, A. Bouguecha, M. Vucetic, and A. Chugreev. Advanced Wear Simulation for Bulk Metal Forming Processes. *MATEC Web of Conferences*, 80: 04003, 2016. doi:10.1051/matecconf/20168004003.

[12] B.-A. Behrens, A. Bouguecha, M. Vucetic, A. Chugreev, and D. Rosenbusch. Advanced finite element analysis of die wear in sheet-bulk metal forming processes. *AIP Conference Proceedings*, 1769(1):130010, 2016. doi:10.1063/1.4963529.

[13] B.-A. Behrens, D. Biermann, A. Menzel, W. Tillmann, R. Krimm, A. Meijer, M. Schewe, D. Stangier, O. Commichau, P. Müller, S. Hübner, and D. Rosenbusch. Untersuchungen strukturierter Werkzeugflächen und der Einfluss auf den Werkzeugverschleiß. In M. Merklein, B.-A. Behrens, and A. E. Tekkaya, editors, *4. Workshop Blechmassivumformung: Umformtechnische Herstellung von komplexen Funktionsbauteilen mit Nebenformelementen aus Feinblechen*, pages 7–30, Hannover, 2020. FAU University Press. doi:10.25593/978-3-96147-280-2.

[14] T. Belytschko. *Nonlinear Finite Elements for Continua and Structures*. New York Academy of Sciences Series. John Wiley & Sons, Incorporated, New York, 1st edition, 2014. ISBN 978-1-118-63270-3.

[15] R. Berthelsen, D. Tomath, R. Denzer, and A. Menzel. Finite element simulation of coating-induced heat transfer: application to thermal spraying processes. *Meccanica*, 51(2):291–307, 2016. doi:10.1007/s11012-015-0236-7.

[16] R. Berthelsen, H. Wilbuer, R. Holtermann, and A. Menzel. Computational modelling of wear - application to structured surfaces of elastoplastic tools. *GAMM-Mitteilungen*, 39(2):210–228, 2016. doi:10.1002/gamm.201610013.

[17] B.-J. Bobach. *Towards a unified formulation for the simulation of thermo-fluid-solid problems with phase change*. PhD thesis, ULiege - University of Liege, Liege, Belgium, 2023. URL `https://hdl.handle.net/2268/304838`.

[18] B.-J. Bobach, R. Boman, D. Celentano, V. E. Terrapon, and J.-P. Ponthot. Simulation of the Marangoni Effect and Phase Change Using the Particle Finite Element Method. *Applied Sciences*, 11(24):11893, 2021. doi:10.3390/app112411893.

[19] B.-J. Bobach, R. Boman, J. M. Carbonell, L. Papeleux, E. Fernandez, and J.-P. Ponthot. A Unified Thermo-Fluid–Solid Formulation for FSI and Phase Change Problems Based on the Particle Finite Element Method. *International Journal of Computational Methods*, page 2342008, 2024. doi:10.1142/S0219876223420082.

[20] P. B. Bochev, C. R. Dohrmann, and M. D. Gunzburger. Stabilization of Low-order Mixed Finite Elements for the Stokes Equations. *SIAM Journal on Numerical Analysis*, 44(1):82–101, 2006. doi:10.1137/S0036142905444482.

[21] E. F. I. Boerner and P. Wriggers. A macro-element for incompressible finite deformations based on a volume averaged deformation gradient. *Computational Mechanics*, 42(3):407–416, 2008. doi:10.1007/s00466-008-0250-x.

[22] J. Bonet and R. D. Wood. *Nonlinear continuum mechanics for finite element analysis*. Cambridge University Press, Cambridge, 2 edition, 2008. doi:10.1017/CBO9780511755446.

[23] British stainless stell association. Elevated temperature physical properties of stainless steels, n.d. URL `https://bssa.org.uk/bssa_articles/elevated-temperature-physical-properties-of-stainless-steels/`.

[24] C. Burkhardt, D. Soldner, and J. Mergheim. A comparison of material models for the simulation of selective beam melting processes. *Procedia CIRP*, 94:52–57, 2020. doi:10.1016/j.procir.2020.09.011.

[25] G. Camacho and M. Ortiz. Adaptive Lagrangian modelling of ballistic penetration of metallic targets. *Computer Methods in Applied Mechanics and Engineering*, 142 (3-4):269–301, 1997. doi:10.1016/S0045-7825(96)01134-6.

[26] J. M. Carbonell, J. M. Rodríguez, and E. Oñate. Modelling 3D metal cutting problems with the particle finite element method. *Computational Mechanics*, 66 (3):603–624, 2020. doi:10.1007/s00466-020-01867-5.

[27] J. M. Carbonell, E. Oñate, and B. Suárez. Modelling of tunnelling processes and rock cutting tool wear with the particle finite element method. *Computational Mechanics*, 52(3):607–629, 2013. doi:10.1007/s00466-013-0835-x.

[28] J. M. Carbonell, L. Monforte, M. O. Ciantia, M. Arroyo, and A. Gens. Geotechnical particle finite element method for modeling of soil-structure interaction under large deformation conditions. *Journal of Rock Mechanics and Geotechnical Engineering*, 14(3):967–983, 2022. doi:10.1016/j.jrmge.2021.12.006.

[29] J. C. Cavendish, D. A. Field, and W. H. Frey. An approach to automatic three-dimensional finite element mesh generation. *International Journal for Numerical Methods in Engineering*, 21(2):329–347, 1985. doi:10.1002/nme.1620210210.

[30] I. Caylak and R. Mahnken. Mixed finite element formulations with volume bubble functions for triangular elements. *Computers & Structures*, 89(21-22):1844–1851, 2011. doi:10.1016/j.compstruc.2011.07.004.

[31] W.-G. Cha, T. Hammer, F. Gutknecht, R. Golle, A. E. Tekkaya, and W. Volk. Adaptive wear model for shear-cutting simulation with open cutting line. *Wear*, 386-387:17–28, 2017. doi:10.1016/j.wear.2017.05.019.

[32] Y. Chew, J. H. L. Pang, G. Bi, and B. Song. Thermo-mechanical model for simulating laser cladding induced residual stresses with single and multiple clad beads. *Journal of Materials Processing Technology*, 224:89–101, 2015. doi:10.1016/j.jmatprotec.2015.04.031.

[33] B. D. Coleman and W. Noll. The thermodynamics of elastic materials with heat conduction and viscosity. *Archive for Rational Mechanics and Analysis*, 13(1): 167–178, 1963. doi:10.1007/BF01262690.

[34] M. Cremonesi, A. Franci, S. Idelsohn, and E. Oñate. A State of the Art Review of the Particle Finite Element Method (PFEM). *Archives of Computational Methods in Engineering*, 27(5):1709–1735, 2020. doi:10.1007/s11831-020-09468-4.

[35] M. H. Dao and J. Lou. Simulations of Laser Assisted Additive Manufacturing by Smoothed Particle Hydrodynamics. *Computer Methods in Applied Mechanics and Engineering*, 373:113491, 2021. doi:10.1016/j.cma.2020.113491.

[36] M. H. Dao and J. Lou. Simulations of directed energy deposition additive manufacturing process by smoothed particle hydrodynamics methods. *The International Journal of Advanced Manufacturing Technology*, 120(7-8):4755–4774, 2022. doi:10.1007/s00170-022-09050-1.

[37] H. Dardaei Joghan, M. Hahn, and A. E. Tekkaya. Effect of preheating during laser metal deposition on the properties of laminated bending dies. *The International Journal of Advanced Manufacturing Technology*, 125(1-2):157–168, 2023. doi:10.1007/s00170-022-10697-z.

[38] H. Dardaei Joghan, R. Hölker-Jäger, A. Komodromos, and A. E. Tekkaya. Hybrid Additive Manufacturing of Forming Tools. *Automotive Innovation*, 6(3):311–323, 2023. doi:10.1007/s42154-023-00239-y.

[39] Dassault Systèmes. Simulia Abaqus Manual, 2018. URL `https://help.3ds.com/2018/English/DSSIMULIA_Established/SIMULIA_Established_FrontmatterMap/DSDocAbaqus.htm?ContextScope=all`.

[40] Dassault Systèmes. Simulia Abaqus Manual, 2025. URL `https://help.3ds.com/2025/English/DSSIMULIA_Established/SIMULIA_Established_FrontmatterMap/DSDocHome.htm?contextscope=all`.

[41] L. De Lorenzis and P. Wriggers. Computational homogenization of rubber friction on rough rigid surfaces. *Computational Materials Science*, 77:264–280, 2013. doi:10.1016/j.commatsci.2013.04.049.

[42] E. A. de Souza Neto, D. Perić, and D. R. J. Owen. *Computational Methods for Plasticity: Theory and Applications*. Wiley, 1 edition, 2008. doi:10.1002/9780470694626.

[43] B. Delaunay. Sur la sphere vide. *Bulletin of the Academy of Sciences of the U. S. S. R. Classe des Sciences Mathematiques et Naturelles*, 7:793–800, 1934. URL `https://cir.nii.ac.jp/crid/1573105974067499264`.

[44] R. Denzer and A. Menzel. Configurational forces for quasi-incompressible large strain electro-viscoelasticity – Application to fracture mechanics. *European Journal of Mechanics - A/Solids*, 48:3–15, 2014. doi:10.1016/j.euromechsol.2014.05.012.

[45] E. Doege and B.-A. Behrens. *Handbuch Umformtechnik: Grundlagen, Technologien, Maschinen*. VDI. Springer, Berlin, 2007. doi:10.1007/978-3-540-48924-5.

[46] H. Edelsbrunner and E. P. Mücke. Three-dimensional alpha shapes. *ACM Transactions on Graphics (TOG)*, 13(1):43–72, 1994. doi:10.1145/174462.156635.

[47] K. Ersoy-Nürnberg, G. Nürnberg, M. Golle, and H. Hoffmann. Simulation of wear on sheet metal forming tools—An energy approach. *Wear*, 265(11-12):1801–1807, 2008. doi:10.1016/j.wear.2008.04.039.

[48] E. Falconnet, H. Makich, J. Chambert, G. Monteil, and P. Picart. Numerical and experimental analyses of punch wear in the blanking of copper alloy thin sheet. *Wear*, 296(1-2):598–606, 2012. doi:10.1016/j.wear.2012.07.031.

[49] R. Falla, B.-J. Bobach, R. Boman, J.-P. Ponthot, and V. E. Terrapon. Mesh adaption for two-dimensional bounded and free-surface flows with the particle finite element method. *Computational Particle Mechanics*, 10(5):1049–1076, 2023. doi:10.1007/s40571-022-00541-2.

[50] P. Farah, W. A. Wall, and A. Popp. An implicit finite wear contact formulation based on dual mortar methods: An implicit finite wear contact formulation based on dual mortar methods. *International Journal for Numerical Methods in Engineering*, 111(4):325–353, 2017. doi:10.1002/nme.5464.

[51] P. Farahmand and R. Kovacevic. An experimental–numerical investigation of heat distribution and stress field in single- and multi-track laser cladding by a high-power direct diode laser. *Optics & Laser Technology*, 63:154–168, 2014. doi:10.1016/j.optlastec.2014.04.016.

[52] K. Fischer. *Introduction to Alpha Shapes*. Script, Eidgenössische Technische Hochschule Zürich, Abteilung für Informatik, 2000. URL `https://graphics.stanford.edu/courses/cs268-11-spring/handouts/AlphaShapes/as_fisher.pdf`.

[53] S. Fouvry, P. Kapsa, and L. Vincent. Quantification of fretting damage. *Wear*, 200 (1-2):186–205, 1996. doi:10.1016/S0043-1648(96)07306-1.

[54] A. Franci, E. Oñate, J. M. Carbonell, and M. Chiumenti. PFEM formulation for thermo-coupled FSI analysis. Application to nuclear core melt accident. *Computer Methods in Applied Mechanics and Engineering*, 325:711–732, 2017. doi:10.1016/j.cma.2017.07.028.

[55] T. Furlan, M. Schewe, P. Scherm, P. Retzl, E. Kozeschnik, and A. Menzel. Modelling and finite element simulation of martensite and bainite phase transformations during quenching under consideration of carbon repartitioning. *Mechanics of Materials*, 204:105275, 2025. doi:10.1016/j.mechmat.2025.105275.

[56] J. Goldak, A. Chakravarti, and M. Bibby. A new finite element model for welding heat sources. *Metallurgical Transactions B*, 15(2):299–305, 1984. doi:10.1007/BF02667333.

[57] R. Hambli. Blanking tool wear modeling using the finite element method. *International Journal of Machine Tools and Manufacture*, 41(12):1815–1829, 2001. doi:10.1016/S0890-6955(01)00024-4.

[58] S. Hartmann, J. Oliver, R. Weyler, J. Cante, and J. Hernández. A contact domain method for large deformation frictional contact problems. Part 2: Numerical aspects. *Computer Methods in Applied Mechanics and Engineering*, 198(33-36):2607–2631, 2009. doi:10.1016/j.cma.2009.03.009.

[59] S. Hartmann, R. Weyler, J. Oliver, J. C. Cante, and J. A. Hernández. A 3D Frictionless Contact Domain Method for Large Deformation Problems. *Computer Modeling in Engineering and Sciences*, 55(3):211–270, 2010. doi:10.3970/cmes.2010.055.211.

[60] L. Hauser and H. F. Schweiger. Numerical study on undrained cone penetration in structured soil using G-PFEM. *Computers and Geotechnics*, 133:104061, 2021. doi:10.1016/j.compgeo.2021.104061.

[61] V. Hegadekatte, N. Huber, and O. Kraft. Finite element based simulation of dry sliding wear. *Modelling and Simulation in Materials Science and Engineering*, 13 (1):57–75, 2005. doi:10.1088/0965-0393/13/1/005.

[62] V. Hegadekatte, J. Hilgert, O. Kraft, and N. Huber. Multi time scale simulations for wear prediction in micro-gears. *Wear*, 268(1-2):316–324, 2010. doi:10.1016/j.wear.2009.08.017.

[63] H. Hoffmann, C. Hwang, and K. Ersoy. Advanced Wear Simulation in Sheet Metal Forming. *CIRP Annals*, 54(1):217–220, 2005. doi:10.1016/S0007-8506(07)60087-0.

[64] C. Hortig. *Local and non-local thermomechanical modeling and finite-element simulation of high-speed cutting*. PhD thesis, Technische Universität Dortmund, 2010. URL `https://doi.org/10.17877/DE290R-15992`.

[65] Y. Hu and M. F. Randolph. A practical numerical approach for large deformation problems in soil. *International Journal for Numerical and Analytical Methods in Geomechanics*, 22(5):327–350, 1998. doi:10.1002/(SICI)1096-9853(199805)22:5<327::AID-NAG920>3.0.CO;2-X.

[66] K. Isik, G. Gerstein, F. Gutknecht, T. Clausmeyer, F. Nürnberger, H. J. Maier, and A. E. Tekkaya. Investigations of ductile damage in DP600 and DC04 deep drawing steel sheets during punching. *Procedia Structural Integrity*, 2:673–680, 2016. doi:10.1016/j.prostr.2016.06.087.

[67] Y. Jin, W. Yuan, Z. Yin, and Y. Cheng. An edge-based strain smoothing particle finite element method for large deformation problems in geotechnical engineering. *International Journal for Numerical and Analytical Methods in Geomechanics*, 44 (7):923–941, 2020. doi:10.1002/nag.3016.

[68] G. R. Johnson and W. H. Cook. Fracture characteristics of three metals subjected to various strains, strain rates, temperatures and pressures. *Engineering Fracture Mechanics*, 21(1):31–48, 1985. doi:10.1016/0013-7944(85)90052-9.

[69] P. Kersting, D. Gröbel, M. Merklein, P. Sieczkarek, S. Wernicke, A. E. Tekkaya, E. Krebs, D. Freiburg, D. Biermann, T. Weikert, S. Tremmel, D. Stangier, W. Tillmann, S. Matthias, E. Reithmeier, M. Löffler, F. Beyer, and K. Willner. Ex-

perimental and numerical analysis of tribological effective surfaces for forming tools in Sheet-Bulk Metal Forming. *Production Engineering*, 10(1):37–50, 2016. doi:10.1007/s11740-015-0651-6.

[70] B. M. Klingner and J. R. Shewchuk. Aggressive Tetrahedral Mesh Improvement. In M. L. Brewer and D. Marcum, editors, *Proceedings of the 16th International Meshing Roundtable*, pages 3–23. Springer, Berlin, Heidelberg, 2008. doi:10.1007/978-3-540-75103-8_1.

[71] S. Kollmannsberger, M. Carraturo, A. Reali, and F. Auricchio. Accurate Prediction of Melt Pool Shapes in Laser Powder Bed Fusion by the Non-Linear Temperature Equation Including Phase Changes: Model validity: isotropic versus anisotropic conductivity to capture AM Benchmark Test AMB2018-02. *Integrating Materials and Manufacturing Innovation*, 8(2):167–177, 2019. doi:10.1007/s40192-019-00132-9.

[72] K. Komvopoulos and S. A. Erpenbeck. Finite Element Modeling of Orthogonal Metal Cutting. *Journal of Engineering for Industry*, 113(3):253–267, 1991. doi:10.1115/1.2899695.

[73] P. Kopp, V. Calo, E. Rank, and S. Kollmannsberger. Space-time hp-finite elements for heat evolution in laser powder bed fusion additive manufacturing. *Engineering with Computers*, 38(6):4879–4893, 2022. doi:10.1007/s00366-022-01719-1.

[74] S. Kumar, K. Danas, and D. M. Kochmann. Enhanced local maximum-entropy approximation for stable meshfree simulations. *Computer Methods in Applied Mechanics and Engineering*, 344:858–886, 2019. doi:10.1016/j.cma.2018.10.030.

[75] C. Körner, M. Markl, and J. A. Koepf. Modeling and Simulation of Microstructure Evolution for Additive Manufacturing of Metals: A Critical Review. *Metallurgical and Materials Transactions A*, 51(10):4970–4983, 2020. doi:10.1007/s11661-020-05946-3.

[76] T. A. Laursen. *Computational Contact and Impact Mechanics*. Springer Berlin Heidelberg, Berlin, Heidelberg, 2003. doi:10.1007/978-3-662-04864-1.

[77] J. Lengiewicz and S. Stupkiewicz. Continuum framework for finite element modelling of finite wear. *Computer Methods in Applied Mechanics and Engineering*, 205-208: 178–188, 2012. doi:10.1016/j.cma.2010.12.020.

[78] T. Leyssens, M. Henry, J. Lambrechts, and J. Remacle. A Delaunay refinement algorithm for the particle finite element method applied to free surface flows. *International Journal for Numerical Methods in Engineering*, 125(18):e7554, 2024. doi:10.1002/nme.7554.

[79] I.-S. Liu. *Continuum Mechanics*. Advanced Texts in Physics. Springer, Berlin, Heidelberg, 2002. doi:10.1007/978-3-662-05056-9.

[80] S. Lu and K. Pister. Decomposition of deformation and representation of the free energy function for isotropic thermoelastic solids. *International Journal of Solids*

and Structures, 11(7-8):927–934, 1975. doi:10.1016/0020-7683(75)90015-3.

[81] M. Löffler, K. Andreas, U. Engel, R. Schulte, D. Groebel, E. Krebs, D. Freiburg, D. Biermann, D. Stangier, W. Tillmann, T. Weikert, S. Wartzack, S. Tremmel, H. Lucas, B. Denkena, and M. Merklein. Tribological measures for controlling material flow in sheet-bulk metal forming. *Production Engineering*, 10(4-5):459–470, 2016. doi:10.1007/s11740-016-0695-2.

[82] L. Malvern. *Introduction to the Mechanics of a Continuous Medium*. Prentice-Hall series in engineering of the physical sciences. Prentice-Hall, 1969. ISBN 9780134876030.

[83] T. D. Marusich and M. Ortiz. Modelling and simulation of high-speed machining. *International Journal for Numerical Methods in Engineering*, 38(21):3675–3694, 1995. doi:10.1002/nme.1620382108.

[84] A. Masud and T. J. Truster. A framework for residual-based stabilization of incompressible finite elasticity: Stabilized formulations and $\overline{F}$ methods for linear triangles and tetrahedra. *Computer Methods in Applied Mechanics and Engineering*, 267:359–399, 2013. doi:10.1016/j.cma.2013.08.010.

[85] S. Meduri, M. Cremonesi, and U. Perego. An efficient runtime mesh smoothing technique for 3D explicit Lagrangian free-surface fluid flow simulations. *International Journal for Numerical Methods in Engineering*, 117(4):430–452, 2019. doi:10.1002/nme.5962.

[86] C. Meier, S. L. Fuchs, A. J. Hart, and W. A. Wall. A novel smoothed particle hydrodynamics formulation for thermo-capillary phase change problems with focus on metal additive manufacturing melt pool modeling. *Computer Methods in Applied Mechanics and Engineering*, 381:113812, 2021. doi:10.1016/j.cma.2021.113812.

[87] M. Merklein, J. Allwood, B.-A. Behrens, A. Brosius, H. Hagenah, K. Kuzman, K. Mori, A. Tekkaya, and A. Weckenmann. Bulk forming of sheet metal. *CIRP Annals*, 61(2):725–745, 2012. doi:10.1016/j.cirp.2012.05.007.

[88] K. C. Mills. *Recommended values of thermophysical properties for selected commercial alloys*. Woodhead, Cambridge, 2002. doi:10.1108/aeat.2002.12774eae.001.

[89] J.-F. Molinari, R. Aghababaei, T. Brink, L. Frérot, and E. Milanese. Adhesive wear mechanisms uncovered by atomistic simulations. *Friction*, 6(3):245–259, 2018. doi:10.1007/s40544-018-0234-6.

[90] L. Monforte, J. M. Carbonell, M. Arroyo, and A. Gens. Performance of mixed formulations for the particle finite element method in soil mechanics problems. *Computational Particle Mechanics*, 4(3):269–284, 2017. doi:10.1007/s40571-016-0145-0.

[91] D. Montoya-Zapata, J. M. Rodríguez, A. Moreno, O. Ruiz-Salguero, and J. Posada. Nonlinear thermal simulation of laser metal deposition. *Australian Journal of Mechanical Engineering*, 19(5):653–668, 2021. doi:10.1080/14484846.2021.1988435.

[92] D. Mulvihill, M. Kartal, D. Nowell, and D. Hills. An elastic–plastic asperity interaction model for sliding friction. *Tribology International*, 44(12):1679–1694, 2011. doi:10.1016/j.triboint.2011.06.018.

[93] P. Müller, D. Rosenbusch, J. Wehmeyer, S. Hübner, and B.-A. Behrens. Investigations of forming force, friction values and surface qualities in ring compression tests using oscillating tools: Untersuchungen zur Umformkraft, Reibwerten und Oberflächengüten bei Ringstauchversuchen mit oszillierenden Werkzeugen. In J. P. Wulfsberg, W. Hintze, and B.-A. Behrens, editors, *Production at the leading edge of technology*, pages 73–81. Springer, Berlin, Heidelberg, 2019. doi:10.1007/978-3-662-60417-5_7.

[94] Nickel-Development-Institute. High-temperature characteristics of stainless steels, n.d. URL `https://nickelinstitute.org/media/1699/high_temperaturecharacteristicsofstainlesssteel_9004_.pdf`.

[95] I. Noll, T. Bartel, and A. Menzel. A computational phase transformation model for selective laser melting processes. *Computational Mechanics*, 66(6):1321–1342, 2020. doi:10.1007/s00466-020-01903-4.

[96] J. Oliver, J. C. Cante, R. Weyler, C. González, and J. Hernandez. Particle Finite Element Methods in Solid Mechanics Problems. In E. Oñate and R. Owen, editors, *Computational Plasticity*, volume 7, pages 87–103. Springer Netherlands, Dordrecht, 2007. doi:10.1007/978-1-4020-6577-4_6.

[97] J. Oliver, S. Hartmann, J. Cante, R. Weyler, and J. Hernández. A contact domain method for large deformation frictional contact problems. Part 1: Theoretical basis. *Computer Methods in Applied Mechanics and Engineering*, 198(33-36):2591–2606, 2009. doi:10.1016/j.cma.2009.03.006.

[98] E. Oñate, S. R. Idelsohn, F. Del Pin, and R. Aubry. The particle finite element method - an overview. *International Journal of Computational Methods*, 01(02): 267–307, 2004. doi:10.1142/S0219876204000204.

[99] V. L. Popov and R. Pohrt. Adhesive wear and particle emission: Numerical approach based on asperity-free formulation of Rabinowicz criterion. *Friction*, 6 (3):260–273, 2018. doi:10.1007/s40544-018-0236-4.

[100] S. D. Proell, P. Munch, M. t. Kronbichler, W. A. Wall, and C. Meier. A highly efficient computational approach for fast scan-resolved simulations of metal additive manufacturing processes on the scale of real parts. *Additive Manufacturing*, 79: 103921, 2024. doi:10.1016/j.addma.2023.103921.

[101] G. Qiu, S. Henke, and J. Grabe. Application of a Coupled Eulerian–Lagrangian approach on geomechanical problems involving large deformations. *Computers and Geotechnics*, 38(1):30–39, 2011. doi:10.1016/j.compgeo.2010.09.002.

[102] E. Rabinowicz. The effect of size on the looseness of wear fragments. *Wear*, 2(1): 4–8, 1958. doi:10.1016/0043-1648(58)90335-1.

[103] R. Raj, L. N. S. Chiu, D. Marla, and A. Huang. Development and validation of a fully coupled thermo-mechanical model for in-situ micro-rolling in laser-directed energy deposition: Single-track multi-layer case. *Materials & Design*, 245:113210, 2024. doi:10.1016/j.matdes.2024.113210.

[104] A. Ramalho and J. Miranda. The relationship between wear and dissipated energy in sliding systems. *Wear*, 260(4-5):361–367, 2006. doi:10.1016/j.wear.2005.02.121.

[105] J. Reinold and G. Meschke. A mixed u–p edge-based smoothed particle finite element formulation for viscous flow simulations. *Computational Mechanics*, 69(4): 891–910, 2022. doi:10.1007/s00466-021-02119-w.

[106] J. Reinold, V. N. Nerella, V. Mechtcherine, and G. Meschke. Extrusion process simulation and layer shape prediction during 3D-concrete-printing using the Particle Finite Element Method. *Automation in Construction*, 136:104173, 2022. doi:10.1016/j.autcon.2022.104173.

[107] D. Riedlbauer, T. Scharowsky, R. F. Singer, P. Steinmann, C. Körner, and J. Mergheim. Macroscopic simulation and experimental measurement of melt pool characteristics in selective electron beam melting of Ti-6Al-4V. *The International Journal of Advanced Manufacturing Technology*, 88(5-8):1309–1317, 2017. doi:10.1007/s00170-016-8819-6.

[108] G. Rizzieri, L. Ferrara, and M. Cremonesi. Numerical simulation of the extrusion and layer deposition processes in 3D concrete printing with the Particle Finite Element Method. *Computational Mechanics*, 73(2):277–295, February 2024. doi:10.1007/s00466-023-02367-y.

[109] G. Rizzieri, L. Ferrara, and M. Cremonesi. Simulation of viscoelastic free-surface flows with the Particle Finite Element Method. *Computational Particle Mechanics*, March 2024. doi:10.1007/s40571-024-00730-1.

[110] J. M. Rodríguez, J. M. Carbonell, and P. Jonsén. Numerical Methods for the Modelling of Chip Formation. *Archives of Computational Methods in Engineering*, 27(2):387–412, 2020. doi:10.1007/s11831-018-09313-9.

[111] J. Rodríguez, J. Carbonell, J. Cante, and J. Oliver. Continuous chip formation in metal cutting processes using the Particle Finite Element Method (PFEM). *International Journal of Solids and Structures*, 120:81–102, 2017. doi:10.1016/j.ijsolstr.2017.04.030.

[112] J. M. Rodríguez Prieto. *Numerical modeling of metal cutting processes using the Particle Finite Element Method*. PhD thesis, Universitat Politècnica de Catalunya, 2014. URL `https://doi.org/10.5821/dissertation-2117-95349`.

[113] S. Roy, M. Juha, M. S. Shephard, and A. M. Maniatty. Heat transfer model and finite element formulation for simulation of selective laser melting. *Computational Mechanics*, 62(3):273–284, 2018. doi:10.1007/s00466-017-1496-y.

[114] M. Sabel, C. Sator, T. I. Zohdi, and R. Müller. Application of the Particle Finite Element Method in Machining Simulation Discussion of the Alpha-Shape Method in the Context of Strength of Materials. *Journal of Computing and Information Science in Engineering*, 17(1):011002, 2017. doi:10.1115/1.4034434.

[115] M. Schewe and A. Menzel. The Particle Finite Element Method for the modelling and simulation of solid body interactions. *Proceedings in Applied Mathematics and Mechanics*, 18(1):e201800110, 2018. doi:10.1002/pamm.201800110.

[116] M. Schewe and A. Menzel. Aspects of the Particle Finite Element Method applied to contact problems. *Proceedings in Applied Mathematics and Mechanics*, 19(1): e201900403, 2019. doi:10.1002/pamm.201900403.

[117] M. Schewe and A. Menzel. Mechanism-Based Modelling of Wear in Sheet-Bulk Metal Forming. In M. Merklein, A. E. Tekkaya, and B.-A. Behrens, editors, *Sheet Bulk Metal Forming – Research Results of the TCRC73*, pages 434–457. Springer International Publishing, Cham, 2021. doi:10.1007/978-3-030-61902-2_19.

[118] M. Schewe, H. Wilbuer, and A. Menzel. Simulation of wear and effective friction properties of microstructured surfaces. *Wear*, 464-465:203491, 2021. doi:10.1016/j.wear.2020.203491.

[119] M. Schewe, T. Bartel, and A. Menzel. Comparison of elements and state-variable transfer methods for quasi-incompressible material behaviour in the particle finite element method. *Computational Mechanics*, 75:755–773, 2025. doi:10.1007/s00466-024-02531-y.

[120] M. Schewe, I. Noll, T. Bartel, and A. Menzel. Towards the simulation of metal deposition with the Particle Finite Element Method and a phase transformation model. *Computer Methods in Applied Mechanics and Engineering*, 437:117730, 2025. doi:10.1016/j.cma.2025.117730.

[121] H. Si. TetGen, a Delaunay-Based Quality Tetrahedral Mesh Generator. *ACM Transactions on Mathematical Software*, 41(2):1–36, 2015. doi:10.1145/2629697.

[122] P. Sieczkarek, S. Wernicke, S. Gies, A. Tekkaya, E. Krebs, P. Wiederkehr, D. Biermann, W. Tillmann, and D. Stangier. Wear behavior of tribologically optimized tool surfaces for incremental forming processes. *Tribology International*, 104:64–72, 2016. doi:10.1016/j.triboint.2016.08.028.

[123] G. Straffelini. *Friction and Wear: Methodologies for Design and Control*. Springer Tracts in Mechanical Engineering. Springer International Publishing, Cham, 2015. doi:10.1007/978-3-319-05894-8.

[124] J. S. Strenkowski and J. T. Carroll. A Finite Element Model of Orthogonal Metal Cutting. *Journal of Engineering for Industry*, 107(4):349–354, 1985. doi:10.1115/1.3186008.

[125] S. Stupkiewicz. *Micromechanics of Contact and Interphase Layers*, volume 30 of *Lecture Notes in Applied and Computational Mechanics*. Springer, Berlin,

Heidelberg, 2007. doi:10.1007/978-3-540-49717-2.

[126] S. Stupkiewicz. An ALE formulation for implicit time integration of quasi-steady-state wear problems. *Computer Methods in Applied Mechanics and Engineering*, 260:130–142, 2013. doi:10.1016/j.cma.2013.03.023.

[127] S. Stupkiewicz. Finite Wear and Soft Elasto-Hydrodynamic Lubrication: Beyond the Classical Frictional Contact of Soft Solids. In A. Popp and P. Wriggers, editors, *Contact Modeling for Solids and Particles*, volume 585, pages 125–176. Springer International Publishing, Cham, 2018. doi:10.1007/978-3-319-90155-8_3.

[128] S. Stupkiewicz, M. J. Lewandowski, and J. Lengiewicz. Micromechanical analysis of friction anisotropy in rough elastic contacts. *International Journal of Solids and Structures*, 51(23-24):3931–3943, 2014. doi:10.1016/j.ijsolstr.2014.07.013.

[129] M. Tanaka, M. Fujikawa, D. Balzani, and J. Schröder. Robust numerical calculation of tangent moduli at finite strains based on complex-step derivative approximation and its application to localization analysis. *Computer Methods in Applied Mechanics and Engineering*, 269:454–470, 2014. doi:10.1016/j.cma.2013.11.005.

[130] F. A. Tavarez and M. E. Plesha. Discrete element method for modelling solid and particulate materials. *International Journal for Numerical Methods in Engineering*, 70(4):379–404, 2007. doi:10.1002/nme.1881.

[131] I. Temizer and P. Wriggers. A multiscale contact homogenization technique for the modeling of third bodies in the contact interface. *Computer Methods in Applied Mechanics and Engineering*, 198(3-4):377–396, 2008. doi:10.1016/j.cma.2008.08.008.

[132] W. Tillmann, L. Hagen, D. Stangier, I.-A. Laemmerhirt, D. Biermann, P. Kersting, and E. Krebs. Wear behavior of bio-inspired and technologically structured HVOF sprayed NiCrBSiFe coatings. *Surface and Coatings Technology*, 280:16–26, 2015. doi:10.1016/j.surfcoat.2015.08.055.

[133] W. Volk, P. Groche, A. Brosius, A. Ghiotti, B. L. Kinsey, M. Liewald, L. Madej, J. Min, and J. Yanagimoto. Models and modelling for process limits in metal forming. *CIRP Annals*, 68(2):775–798, 2019. doi:10.1016/j.cirp.2019.05.007.

[134] C. Wang, J. Chen, Z. C. Xia, and F. Ren. Die wear prediction by defining three-stage coefficient K for AHSS sheet metal forming process. *The International Journal of Advanced Manufacturing Technology*, 69(1-4):797–803, 2013. doi:10.1007/s00170-013-5069-8.

[135] L. Wang, X. Zhang, S. Zhang, and S. Tinti. A generalized Hellinger-Reissner variational principle and its PFEM formulation for dynamic analysis of saturated porous media. *Computers and Geotechnics*, 132:103994, 2021. doi:10.1016/j.compgeo.2020.103994.

[136] L. Wang, X. Zhang, Q. Lei, S. Panayides, and S. Tinti. A three-dimensional particle finite element model for simulating soil flow with elastoplasticity. *Acta Geotechnica*, 17(12):5639–5653, 2022. doi:10.1007/s11440-022-01618-1.

[137] Y. Wang and H. L. Tsai. Effects of surface active elements on weld pool fluid flow and weld penetration in gas metal arc welding. *Metallurgical and Materials Transactions B*, 32(3):501–515, 2001. doi:10.1007/s11663-001-0035-5.

[138] H. Wessels, C. Weißenfels, and P. Wriggers. Metal particle fusion analysis for additive manufacturing using the stabilized optimal transportation meshfree method. *Computer Methods in Applied Mechanics and Engineering*, 339:91–114, 2018. doi:10.1016/j.cma.2018.04.042.

[139] R. Weyler, J. Oliver, T. Sain, and J. Cante. On the contact domain method: A comparison of penalty and Lagrange multiplier implementations. *Computer Methods in Applied Mechanics and Engineering*, 205-208:68–82, 2012. doi:10.1016/j.cma.2011.01.011.

[140] P. Wriggers. *Nonlinear finite element methods*. Springer, Berlin, 2008. doi:10.1007/978-3-540-71001-1.

[141] P. Wriggers. *Computational contact mechanics*. Springer, Wien, New York, 2007. doi:10.1007/978-3-540-32609-0.

[142] P. Wriggers. Advanced Discretization Methods for Contact Mechanics. In A. Popp and P. Wriggers, editors, *Contact Modeling for Solids and Particles*, volume 585, pages 87–123. Springer International Publishing, Cham, 2018. doi:10.1007/978-3-319-90155-8_2. Series Title: CISM International Centre for Mechanical Sciences.

[143] D. Zhang, J. M. Rodriguez, X. Ye, and R. Müller. A Particle Finite Element Method for Additive Manufacturing Simulations. *Journal of Computing and Information Science in Engineering*, 23(5):051008, 2023. doi:10.1115/1.4062143.

[144] H. Zhang and I. Etsion. An advanced efficient model for adhesive wear in elastic—plastic spherical contact. *Friction*, 10(8):1276–1284, 2022. doi:10.1007/s40544-021-0569-2.

[145] H. Zhang, R. Goltsberg, and I. Etsion. Modeling Adhesive Wear in Asperity and Rough Surface Contacts: A Review. *Materials*, 15(19):6855, 2022. doi:10.3390/ma15196855.

[146] W. Zhang, W. Yuan, and B. Dai. Smoothed Particle Finite-Element Method for Large-Deformation Problems in Geomechanics. *International Journal of Geomechanics*, 18(4):04018010, 2018. doi:10.1061/(ASCE)GM.1943-5622.0001079.

[147] X. Zhang, K. Krabbenhoft, D. Sheng, and W. Li. Numerical simulation of a flow-like landslide using the particle finite element method. *Computational Mechanics*, 55 (1):167–177, 2015. doi:10.1007/s00466-014-1088-z.

[148] K. Zhao and R. Aghababaei. Adhesive wear law at the single asperity level. *Journal of the Mechanics and Physics of Solids*, 143:104069, 2020. doi:10.1016/j.jmps.2020.104069.

[149] Z. Zhao, Q. Zhu, and J. Yan. A thermal multi-phase flow model for directed energy deposition processes via a moving signed distance function. *Computer Methods in Applied Mechanics and Engineering*, 373:113518, 2021. doi:10.1016/j.cma.2020.113518.

[150] Z. Zheng, M. Zang, S. Chen, and C. Zhao. An improved 3D DEM-FEM contact detection algorithm for the interaction simulations between particles and structures. *Powder Technology*, 305:308–322, 2017. doi:10.1016/j.powtec.2016.09.076.

[151] J. Zhong, J. B. Adams, and L. G. Hector. Molecular dynamics simulations of asperity shear in aluminum. *Journal of Applied Physics*, 94(7):4306–4314, 2003. doi:10.1063/1.1558966.

[152] H. Zhou, L. Chen, W. Wang, L. Ren, H. Shan, and Z. Zhang. Abrasive particle wear behavior of 3Cr2W8V steel processed to bionic non-smooth surface by laser. *Materials Science and Engineering: A*, 412(1-2):323–327, 2005. doi:10.1016/j.msea.2005.09.042.

[153] O. C. Zienkiewicz, R. L. Taylor, and J. Z. Zhu. *The finite element method: its basis and fundamentals*. Elsevier, Amsterdam Heidelberg, 6. ed., reprint., transferred to digital print edition, 2010. ISBN 978-0-7506-6320-5.

[154] M. Öqvist. Numerical simulations of mild wear using updated geometry with different step size approaches. *Wear*, 249(1-2):6–11, 2001. doi:10.1016/S0043-1648(00)00548-2.

Publication series of the Institute of Mechanics

published to date:

2010/01 Palnau, V.: Implementierung eines netzfreien Diskretisierungsverfahrens und seine Anwendung auf die Scherbandanalyse.
ISBN 978-3-921823-51-4

2010/02 Klusemann, B.: Application of homogenization methods and crystal plasticity to the modeling of heterogeneous materials of technological interest.
ISBN 978-3-921823-53-8

2011/01 Hortig, C.: Local and non-local thermomechanical modeling and finite-element simulation of high-speed cutting.
ISBN 978-3-921823-54-5

2011/02 Parvizian, F.: Modeling of microstructure evolution in aluminum alloys during hot extrusion.
ISBN 978-3-921823-56-9

2011/03 Noman, M.: Characterization and model identification for the simulation of the forming behavior of ferritic steels.
ISBN 978-3-921823-55-2

2011/04 Kayser, T.: Characterization of microstructure in aluminum alloys based on electron backscatter diffraction.
ISBN 978-3-921823-57-6

2011/05 Bargmann, S.: Computational modeling of material behavior on different scales based on continuum mechanics.
ISBN 978-3-921823-58-3

2013/01 Waffenschmidt, T.: Modelling and simulation of adaptation and degradation in anisotropic biological tissues.
ISBN 978-3-921823-61-3

2015/01 Ostwald, R.: Modelling and simulation of phase-transformations in elastoplastic polycrystals.
ISBN 978-3-921823-66-8

2016/01 Subramanian, M.: Phenomenological modelling and simulation of ferroelectric ceramics.
ISBN 978-3-921823-74-3

2016/02 Clausmeyer, T.: Evolution of plastic anisotropy in metals.
ISBN 978-3-921823-76-7

2017/01 Holtermann, R.: Computational multiscale modelling of grinding processes.
ISBN 978-3-921823-86-6

2017/02 Bartels, A.: Modelling of evolving microstructures at different scales.
ISBN 978-3-921823-93-4

2017/03 Dusthakar Kumar Rao, D. K.: Computational modelling of single and polycrystalline ferroelectric materials.
ISBN 978-3-921823-94-1

2019/01 Buckmann, K.: Microstructure evolution in functional magnetic materials.
ISBN 978-3-947323-09-8

2019/02 Kaiser, T.: Computational modelling of non-simple and anisotropic materials.
ISBN 978-3-947323-14-2

2019/03 Heitbreder, T.: Modelling of material interfaces at different length scales.
ISBN 978-3-947323-18-0

2020/01 Berthelsen, R.: Computational homogenisation of thermomechanical problems.
ISBN 978-3-947323-19-7

2020/02 Sievers, C.: Describing the macroscopic behavior of surfaces based on atomistic models.
ISBN 978-3-947323-24-1

2022/01 Rose, L.: Optimisation based parameter identification using optical field measurements.
ISBN 978-3-947323-31-9

2023/01 Langenfeld, K.: Continuum modeling of brittle and ductile damage: theory and computational frameworks.
ISBN 978-3-947323-41-8

2023/02 Schulte, R.: Parameter identification approaches with application to different classes of materials.
ISBN 978-3-947323-45-6

2023/03 Kaiser, T.: Multiscale multiphysics material modelling.
ISBN 978-3-947323-46-3

2024/01 Noll, I.: Thermomechanical modelling and simulation of laser powder bed fusion processes.
ISBN 978-3-947323-49-4

2024/02 Witt, C.: Isogeometric analysis of anisotropic mechanical and electromechanical higher-gradient continua.
ISBN 978-3-947323-50-0

2025/01 Kurzeja, P.: Modeling, control and opportunities of mechanical interfaces across the scales.
ISBN 978-3-947323-51-7

2025/02 Lammen, H.: Modeling and simulation of general imperfect interfaces using phase-field-theory.
ISBN 978-3-947323-52-4

2025/03 Sprave, L.: Computational modelling and simulation of ductile damage in metals.
ISBN 978-3-947323-54-8

2025/04 Schewe, M.: Computational modelling of surface interactions – wear, material separation and deposition.
ISBN 978-3-947323-55-5